Investigation of Resistive Switching in Fe-doped $SrTiO_3$ by Advanced Spectroscopy

Von der Fakultät für Georessourcen und Materialtechnik der
Rheinisch -Westfälischen Technischen Hochschule Aachen

zur Erlangung des akademischen Grades eines

Doktors der Naturwissenschaften

genehmigte Dissertation

vorgelegt von **M.Sc.**

Christian Lenser

aus Oberhausen

Berichter: Univ.-Prof. Dr. rer. nat. Georg Roth
Univ.-Prof. Dr. rer. nat. Rainer Waser
Prof. Dr. rer. nat. Regina Dittmann

Tag der mündlichen Prüfung: 13. Februar 2013

Diese Dissertation ist auf den Internetseiten der Hochschulbibliothek online verfügbar

Abstract

Resistive Random Access Memory (ReRAM) technology is a promising candidate for future non-volatile, highly scalable and energy efficient data storage concepts. A typical ReRAM cell consists of a transition metal oxide sandwiched between two metallic electrodes in a metal-insulator-metal (MIM) cell, and can be fabricated into conceptually simple crossbar arrays suitable for high integration densities. The high switching speeds, large resistance windows, high endurance, low energy demand and good scalability highlights ReRAM as a potential replacement of FLASH memories below the 10 nm node, and utilization as a "universal" memory is also theoretically possible.

However, a major obstacle to be overcome for the commercialization of ReRAM is the elucidation and detailed understanding of the switching mechanism, which is still not completely clear despite increasing scientific interest in the field in the last decade. The focus of this thesis is therefore the investigation of ReRAM cells fabricated from Fe-doped $SrTiO_3$ thin films by advanced spectroscopy, in order to gain more information about the physical and chemical state of the material before and after electrical treatment.

For many ReRAM systems, an initial DC voltage treatment is necessary to electroform the cell. The chemical and structural changes induced locally by this treatment are analyzed with spatially resolved spectroscopy, and a mapping of the oxygen vacancy distribution in a switched cell yields some insights into the mechanism of electroforming and the defect structure of the conducting filament. In addition, evidence for voltage-induced redox-reactions and chemical decomposition at the nanometer-scale can be observed with chemically sensitive electron spectromicroscopy.

The necessity of a dedicated DC electroforming step is removed when the thickness of the $SrTiO_3$ film is scaled down, or the film is pre-reduced through a reactive electrode. Electron spectroscopy shows that the latter is due to a redox-reaction at the metal-insulator interface, reducing the $SrTiO_3$ and partially oxidizing the electrode. In this way, the need for electrical forming is removed through a chemical reduction.

Thin films that do not require DC-forming show desirable properties such as high reliability and continuously tunable resistance. With temperature-dependent current-voltage characteristics and photoemission data obtained on large arrays of switched MIM cells, a switching model for these films is suggested based on the modulation of the width of a tunneling barrier located at the top electrode interface. The asymmetric barrier is modified by the movement of oxygen vacancies under applied bias, creating a vacancy-depleted region of variable thickness near the top electrode that acts as the tunneling barrier.

Kurzfassung

Die Resistive Random Access Memory (ReRAM) Technologie gilt als vielversprechender Kandidat für zukünftige, nicht-flüchtige Datenspeicher, die sich durch sehr gute Skalierbarkeit und Energieeffizienz auszeichnen. Eine typische ReRAM Zelle besteht aus einem Übergangsmetalloxid zwischen zwei metallischen Elektroden in sogenannten Metall - Isolator - Metall (MIM) Strukturen, die sich zur dichten Integration in konzeptionell einfachen Crossbar-Strukturen eignen. Neben den sehr schnellen Schaltgeschwindigkeiten und hohen Widerstandsänderungen macht die hohe Anzahl an Schreibzyklen ReRAM zu einem potentiellen Nachfolger von FLASH-Speichern unterhalb der 10 nm Technologie.
Zur Kommerzialisierung von ReRAM fehlt allerdings das Verständnis des atomistischen Schaltmechanismus, welcher trotz stark wachsendem wissenschaftlichem Interesse an diesem Forschungsthema in den letzten zehn Jahren noch nicht klar erarbeitet ist. Der Schwerpunkt dieser Arbeit ist daher die Untersuchung von resistiv schaltenden ReRAM Zellen aus Fe-dotierten $SrTiO_3$ Dünnschichten mit Hilfe moderner spektroskopischer Techniken, um mehr Informationen über den physikalischen und chemischen Zustand des geschalteten Materials zu gewinnen.
Für viele ReRAM Systeme ist eine Elektroformierung durch eine Gleichspannung notwendig. Die chemischen und strukturellen Änderungen, die beim Formieren lokal entstehen, werden mit räumlich aufgelöster Spektroskopie untersucht und die Verteilung von Sauerstoffleerstellen in einer geschalteten Zelle gemessen. Daraus ergeben sich wichtige Einsichten in den Mechanismus der Formierung und Erkenntnisse über die Defektstruktur des leitenden Filaments. Hinweise auf eine spannungsgetriebende Redox-Reaktion und chemische Entmischung auf der Nanometer-Skala können mit chemisch sensitiver Elektronen-Spektromikroskopie beobachtet werden.
Die Notwendigkeit des Elektroformierens verschwindet, wenn die Schichtdicke des $SrTiO_3$ verringert oder die Schicht durch reaktive Elektroden chemisch reduziert wird. Letzteres kann durch Elektronenspektroskopie einer Redox-Reaktion an der Grenzfläche zugeordnet werden, die das $SrTiO_3$ reduziert und die Elektrode partiell oxidiert. Das Elektroformieren wird so durch chemische Reduktion ersetzt.
Solche dünnen Schichten zeigen interessante Eigenschaften wie hohe Verlässlichkeit und kontinuierlich veränderbaren Widerstand. Basierend auf Photoemissionsdaten geschalteter Zellen und Temperatur-abhängiger elektrischer Charakteristik wird ein Model präsentiert, welches auf der Modulation der Breite einer Tunnelbarriere nahe der oberen Elektrode basiert. Die asymmetrische Barriere kann durch die Bewegung von Sauerstoffleerstellen in einem elektrischen Feld verändert werden, womit eine Leerstellen-verarmte Zone unterhalb der oberen Elektrode erzeugt wird, die als Tunnelbarriere für Ladungsträger wirkt.

Contents

1 Introduction **3**

2 Background **5**
2.1 Resistive Switching 5
2.1.1 Oxides as Resisitive Memories 6
2.2 $SrTiO_3$ 7
2.2.1 Defect Chemistry 7
2.2.2 Resistive Switching in $SrTiO_3$ 8
2.2.3 Dopants as Tracer-ions for Valence Change 9

3 Experimental Techniques **11**
3.1 Pulsed Laser Deposition 11
3.2 X-ray Diffraction 12
3.2.1 X-ray Reflectivity 13
3.3 Atomic Force Microscopy 14
3.4 Solid State Spectroscopy - Fundamental Considerations 15
3.4.1 Binding Energy and Chemical Shifts 16
3.4.2 Satellites and Line Splitting 17
3.4.3 Information Depth 19
3.4.4 Radiation Sources 20
3.4.5 Nomenclature in Spectroscopy 21
3.5 Photoemission Spectroscopy 22
3.5.1 X-ray Photoelectron Spectroscopy - XPS 22
3.5.2 Hard X-ray Photoelectron Spectroscopy - HAXPES 22
3.6 X-ray Absorption Spectroscopy 24
3.6.1 X-ray Absorption Fine Structure - XAFS 25
3.6.2 Extended X-ray Absorption Fine Structure - EXAFS 26
3.6.3 X-ray absorption Near Edge Structure - XANES 27

4 Epitaxial Oxide Growth **29**
4.1 Heteroepitaxy on $NdGaO_3$ 29
4.1.1 Influence of Deposition Parameters 31
4.1.2 Strain Relaxation 35
4.1.3 Strain Engineering: Influence of the Substrate 40
4.2 Homoepitaxy: Influence of Iron Concentration 42

5 Influence of Fe-Doping in $SrTiO_3$ **45**
5.1 Fe-doped Single Crystal after Electrocoloration 45
5.1.1 Raman Spectroscopy 47
5.1.2 X-ray Absorption Near Edge Structure - XANES 48
5.1.3 Extended X-ray Absorption Fine Structure - EXAFS 50
5.1.4 Electron Paramagnetic Resonance - EPR 51

5.1.5 Discussion . . . 54
5.2 Thick Epitaxial Films . . . 55
5.2.1 X-ray Absorption Fine Structure - XAFS . . . 55
5.2.2 Raman Spectroscopy . . . 59
5.3 Thin Epitaxial Films . . . 59
5.3.1 Hard X-ray Photoelectron Spectroscopy - HAXPES . . . 59
5.4 Conclusions . . . 68

6 Resistive Switching of Fe-doped $SrTiO_3$ thin films 71
6.1 Thick Films (≥100 nm) . . . 71
6.1.1 Voltage-Time Relation . . . 73
6.1.2 Current Control . . . 74
6.1.3 Influence of Screw Dislocations . . . 75
6.1.4 Correlation of Forming Parameters . . . 79
6.1.5 Summary . . . 81
6.2 Thin Films (≤20 nm) . . . 81
6.2.1 Virgin Cells . . . 82
6.2.2 Resistive Switching - Thickness Dependence . . . 86
6.2.3 Resistive Switching - Reliability Improvement . . . 88
6.2.4 Multilevel Capability . . . 89
6.2.5 Temperature Dependence . . . 90
6.2.6 Switching Model . . . 93
6.3 Switching Polarity - Thickness Dependence . . . 96
6.4 Forming-free Thin Film Devices . . . 97

7 Bulk-Sensitive Spectroscopy on MIM Cells: Thick Films 101
7.1 μ - X-ray Absorption Fine Structure - μXAFS . . . 101

8 Surface-Sensitive Spectroscopy on MIM Cells: Thin Films 107
8.1 Photoemission Electron Microscopy - PEEM . . . 107
8.1.1 Sample Preparation . . . 107
8.1.2 X-ray Absoprtion Spectroscopy - XAS . . . 109
8.1.3 Structural Considerations . . . 112
8.1.4 Consequences for the Switching Mechanism . . . 116
8.2 Hard X-ray Photoelectron Spectroscopy . . . 119
8.2.1 Sample preparation . . . 119
8.2.2 Interfacial Band Line-Up . . . 120
8.2.3 Ti Electrodes . . . 123
8.2.4 Pt Electrodes . . . 125
8.2.5 Rh electrodes . . . 128

9 Conclusions and Outlook 139

Appendix **145**

Bibliography **151**

Acknowledgements **159**

Chapter 1

Introduction

The prediction of a physical scaling limit of existing FLASH memory technology has precipitated scientific activity in recent years to find novel concepts for non-volatile data storage [1]. Today, the memory class of 'Resistive Random Access Memory' (ReRAM) is being considered not only as a replacement for FLASH, but also as a basis for novel computing concepts [2]. The ITRS roadmap 2011 lists redox-based ReRAM as the most promising candidate for future non-volatile memory devices [3], but also lists the limited understanding of the physical SET and RESET processes in the memory devices as the most important challenge to be overcome for commercialization. One key ingredient for the development of quantitative models is the identification of the physico-chemical changes that occur in the material during switching, which can be achieved through suitable spectroscopy techniques.

For most oxide-based ReRAM materials, the resistive switching process is attributed to the movement of oxygen vacancies under electric field and temperature gradients on the nanometer scale, and the formation of nanometer-sized conducting channels in an insulating matrix [4]. An ideally suited technique to investigate such phenomena needs a spatial resolution of several nanometers, as well as a depth-resolution on the same scale, chemical sensitivity of less than 0.1% and simultaneously structural information to correctly interpret any observed changes. At the same time, the requirements for sample preparation should be minimal, since the ideal investigation would be performed on a working device during memory operation. Obviously, such a technique does not exist, and despite the vast amount of scientific publications related to resistive switching in the last decade, only a few groups attempt an investigation by spectroscopic means.

However, several recent works demonstrate the application of promising novel spectroscopies on resistive switching systems, among them μ-focused x-ray absorption spectroscopy [5, 6], x-ray photoemission electron microscopy [7, 8], transmission x-ray spectromicroscopy [9] and hard x-ray photoemission spectroscopy [10, 11]. The core challenge is to develop sample geometries and measurement techniques that either exploit the advantages or circumvent the limitations that are unique to each spectroscopy technique. The main topic of this thesis is to adress these issues for a selection of different spectroscopy techniques and to evaluate them with respect to the information that can be gained from each of them.

The structure of this thesis is as follows: after a brief excursion into the background knowledge of resistive switching and $SrTiO_3$ in chapter 2, the physical basics of electron emission and x-ray absorption spectroscopy is covered in chapter 3, along with a short description of other experimental techniques that were used for this work.

Chapter 4 deals with the homo- and heteroepitaxial growth of $SrTi_{1-x}Fe_xO_3$ films on $NdGaO_3$ substrates, and the relation of the c-axis expansion to deposition parameters like laser energy density and ambient pressure. Furthermore, the miscut angle and the corresponding step-length of the reconstructed substrate surface is shown to influence the relaxation of growth strain induced by the lattice mismatch of the heteroepitaxial interface.
Investigations concerning the resistive switching properties of $SrTi_{1-x}Fe_xO_3$ film are discussed in chapter 6, which is divided into two parts. The first part deals with thick $SrTi_{1-x}Fe_xO_3$ films with a thickness $\geq$100 nm, and focuses on the influence of screw dislocations on the DC hardforming that is necessary to break down the initially high resistance of the films. The second part deals with thin films ($\leq$20 nm) that show favorable properties with regard to switching reliability and uniformity. The electrical properties of electrically untreated MIM-cells (the so-called Virgin state) are evaluated in terms of thermionic emission over an interfacial barrier, and the influence of the Fe-dopant concentration on junction properties are discussed.
The incorporation of Fe-acceptors into $SrTiO_3$ is discussed in chapter 5, on the example of an electrocolored single-crystal and thin films with different Fe concentrations. Investigations on the single-crystal provide an excellent framework for the interpretation of thin film experiments by establishing a spectroscopic footprint of the Fe - oxygen vacancy associate and the valence states of Fe in $SrTiO_3$. Within this framework, the structural and electronic properties of $SrTi_{1-x}Fe_xO_3$ thin films are investigated. Despite Fe concentrations above the expected solubility limit for single crystals, no segregation effects or phase separation can be found even for 5% site fraction of Fe.
The electron concentration in the $SrTi_{1-x}Fe_xO_3$ films is found to decrease with increasing Fe-concentration. Chapters 6 and 5 provide the basis for the application of spectroscopy techniques on Virgin and switched MIM-cells, which is the topic of chapter 8. Two techniques providing spatial resolution and chemical sensitivity are used to characterize single MIM-cells, whereas an area-averaging technique is used to investigate large arrays of switched MIM-cells. The presence of a conductive filament is shown by μ-focused x-ray absorption fine structure (μXAFS) spectroscopy, and a basic understanding of the Fe-related defect structure is developed. Photoemission electron miscroscopy (PEEM) is used to characterize the area of a switched MIM-pad where the thin Au electrodes was locally removed by Joule heating and analyze local changes in surface structure and chemistry. Large arrays of switched MIM-cells with different top electrode materials are investigated by hard x-ray photoemission spectroscopy (HAXPES) to characterize the metal/insulator interface in the Virgin state and after resistive switching.
Finally, the main conclusions from this thesis are presented in a brief discussion in chapter 9, and the spectroscopy applied in this thesis are evaluated with regard to their suitability for the investigation of resistive switching MIM-structures.

Chapter 2

Background

2.1 Resistive Switching

The term 'Resistive Switching' is used to describe the non-volatile and reversible change of the electrical resistance in a given material system by an external voltage or current stimulus. After first examinations of the phenomenon (e.g by Simmons and Verderber [12]) failed to attract attention, scientific interest in the resistive switching effect has been renewed in the last decade because of the potential for application as non-volatile memories [13]. Resistive memories can be classified into several classes according to the physical and chemical effects that influence the resistivity [1], for example phase change memories (PCM), electrochemical metalization cells (ECM), thermochemical (TCM) or valence change memories (VCM). A further distinction can be made with respect to the polarity of the switching voltage, where materials switching in a *non−* or *unipolar* manner are distinguished from materials switching in a *bipolar* way [1]. Unipolar switches are generally based on the formation and dissolution of a conductive filament through an insulating matrix, whereas bipolar switches can exhibit a filamentary and a homogeneous mechanism [14]. VCM materials generally exhibit bipolar resistive switching, where the low resistance state is known as SET and the high resistance state as RESET. The SET and RESET state can be used to represent the logic states '0' and '1'. However, several material systems enable a continuous tuning of the resistance with applied voltage, enabling multilevel programming of a memory cell. Since the resistance ratio of the two resistive states, R_{RESET}/R_{SET} , should be larger than 10 for a clear separation of the logic states, a large resistance ratio is strongly desirable for application [1].
Recently, it was demonstrated that VCM memories can generally be classified as 'memristors' or memristive devices, a term that was introduced by L. Chua [15] to describe a 'memory resistor' that changes its resistance according to the history of its electrical treatment. Strukov *et* al. demonstrated how Pt/ TiO_2/ Pt MIM-structures can be characterized as memristors, and attributed the 'state variable' that is the key parameter for the mathematical description of memristors to the width of the tunneling gap between the active electrode and the conducting filament in the TiO_2.

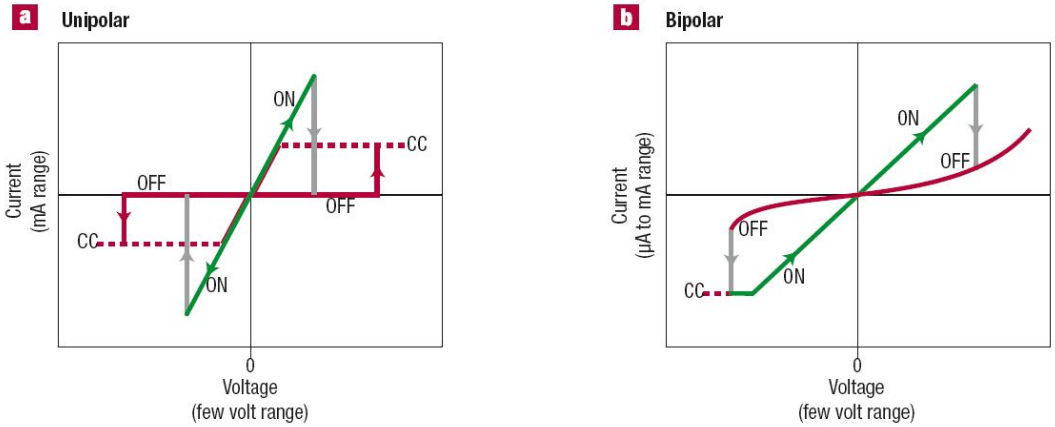

Figure 2.1: Schematic classification of uni- and bipolar switches according to the current-voltage behavior during switching. Reproduced from [14].

2.1.1 Oxides as Resisitive Memories

A large number of oxides are classified as VCM, including binary oxides TiO_2, HfO_2, and TaO_x, and complex oxides such as $Pr_{0.7}Ca_{0.3}MnO_3$ (PCMO), $SrTiO_3$, $SrZrO_3$, and various others [7, 9, 13, 16, 17]. $SrTiO_3$ has been proposed as a model system of a complex oxide for resistive switching due to the deep understanding of defect-chemical processes and oxygen vacancy self-doping in this material, e.g. [18–20]. Investigations into the local nature of the resistive switching process have shown that in addition to point defects, structural defects such as dislocations have to be considered as possible sources of a resistance change under applied bias [21]. The resistive switching process is based on a perturbation of the resistance of a stoichiometric oxide, whether insulating or conducting, and the introduction of defects that modify the resistance. For $SrTiO_3$, the oxygen stoichiometry is well-known to sensitively influence the conductivity because removal of oxygen from the $SrTiO_3$ lattice introduces two electrons that can populate states in the conduction band. Furthermore, oxygen vacancies are known to be highly mobile at low temperatures, and contribute significantly to the ionic conductivity in $SrTiO_3$ since they are charged defects and are subject to drift in an electric field [18, 20]. It was recently demonstrated that the local temperature due to Joule heating contributes significantly to the switching process in VCM materials, narrowing the boundary to TCM systems [22, 23]. Indeed, the possibility to achieve unipolar and bipolar resistive switching in identical MIM-stacks was demonstrated for multiple oxide systems, e.g. TiO_2 [24] and HfO_2 [25]. Since both thermochemical and electric-field mediated processes take place in most resistive switching oxides, the ITRS 2011 no longer distinguishes between 'Thermochemical' memory and 'Nano-ionic' memory, and combines both groups into 'Redox' memory [3].

2.2 $SrTiO_3$

$SrTiO_3$ is a ternary oxide that crystallizes in the perovskite structure, with corner-sharing Ti-O_6 octahedra forming a framework for the anticuboctahedrally coordinated Sr ions. The lattice parameter of the cubic unit cell is 3.903Å at room temperature. $SrTiO_3$ undergoes an antiferrodistortive phase transition from a cubic to a tetragonal crystal structure below 105 K. The high dielectric constant $\epsilon_r = 300$ at room-temperature have made $SrTiO_3$ an attractive candidate for application as a dielectric, especially for DRAM applications [26]. The optical band-gap in $SrTiO_3$ is determined to ∼3.75 eV, while the indirect band-gap is slightly smaller with 3.25 eV [27]. The top of the $SrTiO_3$ valence band is composed mainly of states with Ti 3d and O 2p character, with Sr 4d states present at lower energy, whereas the bottom of the conduction band shows mainly Ti 3d - O 2p character [27, 28].

2.2.1 Defect Chemistry

The introduction of small concentrations of point defects in stoichiometric $SrTiO_3$ can be described by defect chemistry [18]. Using the Kröger-Vink notation [29], substitutional defects in $SrTiO_3$ can be described by their electronic charge with respect to the perfect lattice. For example, Nb^{5+} substituted for Ti^{4+} is written as $Nb_{Ti}^{\bullet}$, where $\bullet$ indicates the positive charge of the defect with respect to the perfect lattice (' indicates a negative charge, whereas x indicates neutrality). Due to the charge neutrality condition, the positive charge of the Nb-dopant is compensated by an electron in the conduction band. Therefore, sufficiently high doping of Nb (e.g. 0.5wt-%) induces metallic conductivity in $SrTiO_3$ making it an ideal candidate for a bottom electrode with an ohmic contact to resistive switching $SrTiO_3$ films.
In the defect chemical description, acceptor-type dopants like Al or Fe are compensated by oxygen vacancies for intermediate oxygen pressures, and only for very high oxygen pressure by holes in the valence band. The defect equilibria for the intrinsic regime in Fe-doped $SrTiO_3$ are given by [19]:

$$\begin{aligned} 1/2\ O_2 + V_O^{\bullet\bullet} &\rightleftharpoons O_O^x + 2\ h^{\bullet} \\ Fe_{Ti}^x &\rightleftharpoons Fe_{Ti}^{'} + h^{\bullet} \\ 0 &\rightleftharpoons e^{'} + h^{\bullet} \\ [Fe]_{tot} &= [Fe_{Ti}^x] + [Fe_{Ti}^{'}] \\ 2[V_O^{\bullet\bullet}] + [h^{\bullet}] &= [Fe_{Ti}^{'}] + [e^{'}] \end{aligned}$$

Due to the weak band-gap excitation in $SrTiO_3$ the last equation - called the charge neutrality condition - can be rewritten as:

$$2[V_O^{\bullet\bullet}] \approx [Fe'_{Ti}] \tag{2.1}$$

Equation 2.1 is valid for intrinsic conditions (not for strongly reducing conditions) and indicates that it is advisable to intentionally dope $SrTiO_3$ in order to have a defined oxygen non-stoichiometry in the material [19]. Because the incorporated Fe is mostly compensated by oxygen vacancies, a known Fe concentration defines the amount of oxygen vacancies in the material. At the same time, the term 'acceptor'-dopant is slightly misleading because Fe is not electronically compensated by a hole in the valence band (as is the case for acceptor-doped Si), but by oxygen vacancies and therefore no free charge carriers are introduced by the doping. Only for very high oxygen partial pressures and temperatures that allow sufficient oxygen exchange with the environment, the oxygen vacancies are 'filled' and the Fe dopants are compensated by $h^{\bullet}$.
The description of point-defect equilibria by defect chemistry is very useful for single crystals and ceramics that are close to thermodynamic equilibrium conditions. However, thin films grown by pulsed laser deposition (PLD) are grown under kinetic constraints from the surface diffusion length on the one hand and also the influence of the plasma plume chemistry, on the other hand. It has been shown that the ratio of cationic defects (V_{Sr} and V_{Ti}) can be influenced by the laser energy used for the ablation at substrate temperatures of 800°C, which indicates that defect chemistry is not the dominant driving force for defect formation in PLD grown thin films [30].

2.2.2 Resistive Switching in $SrTiO_3$

$SrTiO_3$ is counted among the valence change memory (VCM) materials and can be fabricated into MIM-structures switching in a bipolar way [1, 13, 14]. Investigations with high-resolution local conductivity atomic force microscopy (LC-AFM) on $SrTiO_3$ single crystals revealed the possibility to electrically modify the resistance of single dislocations, implying that the switched volume can be as small as a single crystal defect [21]. Similar investigations on PLD grown $SrTiO_3$ thin films show that the conductivity of the thin film surface can be modified with a conductive tip much in the same way as the dislocation in the single crystal [31]. With the same technique, Münstermann *et* al. demonstrated the co-existence of two switching polarities under the same electrode pad in MIM-structures fabricated from Nb:STO/ Fe:STO/ Pt after removal of the Pt electrode [32]. The two regions were spatially separated into a 'crater' regions showing a 'filamentary' or 'counter-eightwise' polarity and a 'halo' regions showing a 'homogeneous' or 'eightwise' polarity. The names are given with respect to the sense of rotation of the

current hysteresis: the eightwise polarity switches in the SET state in the positive voltage branch, whereas the counter-eightwise polarity switches into the SET state in the negative voltage branch (bias applied to the top electrode).
Menke *et* al. demonstrate that unformed or 'virgin' Nb:STO/ Fe:STO/ Pt devices show two contributions to the complex impedance, and that one of these vanishes during electroforming [33]. The thickness dependence of this analysis revealed that this contribution to the impedance is connected to the Pt/ Fe:STO interface, and the depletion layer width is estimated to 200 nm. Electroforming is interpreted as a local bypassing of the interface barrier through the local removal of oxygen from the Fe:STO.

2.2.3 Dopants as Tracer-ions for Valence Change

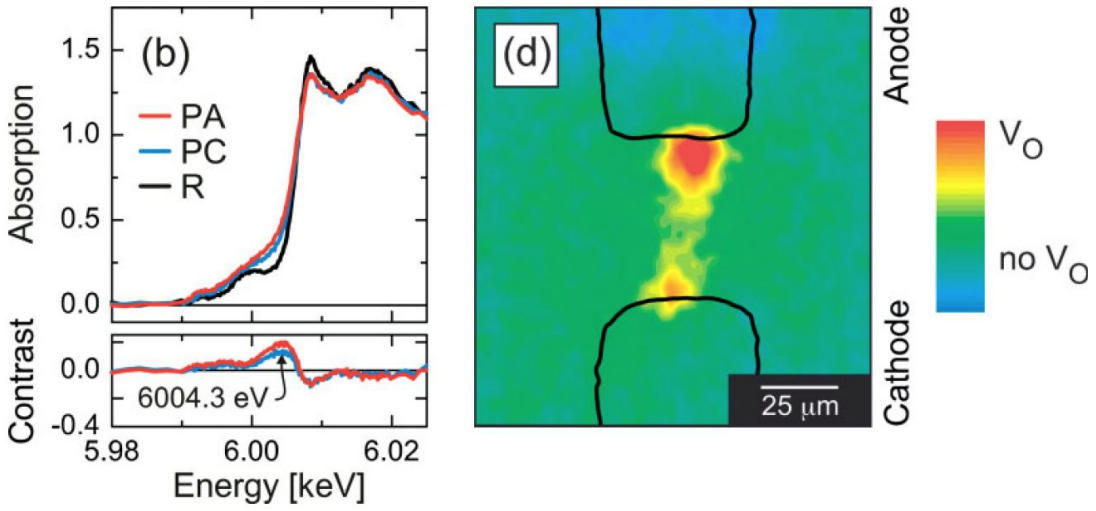

Figure 2.2: Cr K-edge XANES showing the trace of Cr-V_O in the pre-edge region, and the intensity mapping at the corresponding energy showing a vacancy enriched channel between the electrodes. Reproduced from [5].

In the case of single crystals, oxygen vacancy concentrations as small as 10^{18} cm^{-3} are sufficient to induce appreciable conductivity in the material. The conduction electrons populate states in the conduction band with Ti 3d character, inducing the presence of Ti^{3+} ions in undoped material. For $[V_O]$ of 10^{18} cm^{-3} the $[Ti^{3+}]/[Ti^{4+}]$ ratio is smaller than 10^{-4}, which is extremely hard to detect with any kind of spectroscopy.
However, oxygen vacancies preferentially associate to transition metal dopants in the material, such as Fe or Cr [34–36]. The preferential association of V_O to TM-dopants can be used to trace the movement of V_O in $SrTiO_3$ by optical means

under applied electric fields, which leads to so-called 'electrocoloration' in Fe-doped $SrTiO_3$ since Fe^{4+} absorbs in the deep red part of the visible spectrum [20]. Since the association enthalpy $\Delta\ H_{ass}$ is more negative for Fe-$V_O^{\bullet\bullet}$ than for Ti-$V_O^{\bullet\bullet}$ (in other words, the Ti - O bond is 'stronger' than the Fe - O bond [34]), small changes in the total oxygen vacancy concentration lead to large changes at the TM-dopant since their concentration is also small. For the above example, introducing $[V_O]$ of 10^{18} cm^{-3} in the presence of 10^{19} cm^{-3} Fe ions, the change of Fe will be as large as 10%.
This fact was exploited to study the distribution of oxygen vacancies in a planar MIM-structure on a Cr-doped $SrTiO_3$ single crystal with a μ-focused x-ray beam by Janousch *et* al. [5]. They found a characteristic increase in the pre-edge of the Cr K-edge XANES, which they attributed to the presence of an oxygen vacancy in the first coordination shell around Cr. This revealed the presence of an oxygen vacancy enriched channel between the two electrodes, as shown in figure 2.2.

Chapter 3

Experimental Techniques

3.1 Pulsed Laser Deposition

One of the most commonly used techniques for the epitaxial growth of complex oxides is Pulsed Laser Deposition (PLD) due to its simplicity and versatility for deposition of a wide range of materials. The near-stoichiometric deposition of a target material onto the substrate enables the deposition of multi-component compounds in a controlled and reproducible manner. A comprehensive review of this technique is given in [37]. The operation principle of PLD is simple: a pulsed laser is focused through a window onto a rotating target inside a vacuum chamber. The substrate is positioned on a heater facing the target. Process gases can be provided to control the ambient pressure and chemical activity of the atmosphere (O_2, Ar, Ar/H_2).
Excimer lasers are popular tools for PLD due to their short pulse duration and high energy output. The laser used in this work is a KrF excimer laser with a wavelength of $\lambda = 248$ nm, a pulse duration of 25 ns (FWHM) and a maximum laser pulse energy of 1.3 J. Excimer lasers rely on the ionization of the active components in the laser gas through a high-voltage pulse applied by two electrodes inside the resonator. The ionized species Kr^+ and F^- form metastable KrF dimers that dissociate spontaneously as the laser gas relaxes back into the stable ground state. This association under an electric field creates the population inversion necessary to produce a laser pulse, and the wavelength of the laser can be adjusted through the choice of active laser gas (KrF, ArF, XeF, etc.). The pulsed laser provides a short (ns) pulse of monochromatic radiation with a pulse power in the MW-range due to the short pulse duration, at a repetition rate that is generally between 1 and 50 Hz.
The key to the stoichiometric transfer from target to substrate is the non-equilibrium ablation of the target material by the laser pulse. The thermal conductivity of the target materials does not play a significant role since the laser pulse is too short, and therefore the absorbing material is transfered directly into a non-equilibrium plasma. Since equilibrium processes like melting or evaporation are suppressed, the laser plume can have the same stoichiometry as the target material.
In this work, the process parameters for all films grown for resistive switching are kept constant at a substrate temperature of 700°C, a O_2 pressure of 0.25 mbar, a laser energy (measured in front of the lens) of 80 mJ at a repetition rate of 5 Hz. The substrate was attached to the heater with silver paste and heated with a ramp of 90°C/min, and cooled down in 500 mbar O_2 atmosphere after deposition.

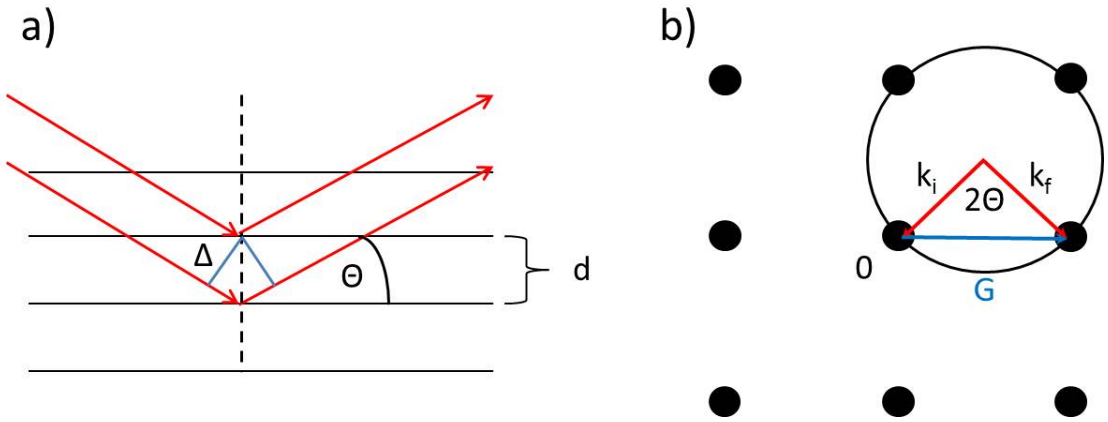

Figure 3.1: a): graphic illustration of Bragg's Law. b) Exemplary construction of Ewald's sphere in a simple cubic reciprocal lattice.

The laser spot size on the target was determined in an optical microscope to 1.5 x 4 mm^2.

3.2 X-ray Diffraction

X-ray diffraction (XRD) is a commonly used technique for the characterization of crystalline materials with respect to crystallinity, space group and, in the case of thin films, orientation and epitaxial relations. The basic models of X-ray diffraction were developed by William Lawrence Bragg and Paul Peter Ewald. Most simple diffraction experiments can be described by Bragg's Law:

$$\lambda = 2d_{hkl}\ sin(\Theta) \tag{3.1}$$

where λ is the wavelength of the x-ray radiation, d_{hkl} is the lattice constant of the respective crystal plane with hkl being the Miller-indices of this plane, and Θ the diffraction angle. The physical model is based on the crystal plane acting as a diffraction grating, where the diffracted beams interfere constructively with each other when equation 3.1 is satisfied (see figure 3.2 a)). When the path difference 2Δ of the parallel, reflected beams equals the wavelength of the radiation, the two beams interfere constructively and diffraction is observed. Contrary to optical interference, the interference is generally assumed to be of first order ($n = 1$) and higher order interferences are attributed to higher index crystal planes. This distinction is important since certain reflections of a family of lattice plains {hkl} can be symmetry forbidden for a given crystal system. For a given wavelength and known crystal system, the observed diffration angle of a specific lattice plane (hkl) can be used to evaluate the lattice constant of a crystal through equation 3.1.

A more sophisticated description of X-ray diffraction is given by the concept of Ewald's sphere. Each set of real-space lattice vectors $\vec{a}$, $\vec{b}$, $\vec{c}$ defining a crystal can be related to a set of reciprocal lattice vectors $\vec{a}'$, $\vec{b}'$, $\vec{c}'$:

$$\vec{a}' = 2\pi \frac{\vec{b} \times \vec{c}}{\vec{a} \bullet (\vec{b} \times \vec{c})} \qquad \vec{b}' = 2\pi \frac{\vec{c} \times \vec{a}}{\vec{b} \bullet (\vec{c} \times \vec{a})} \qquad \vec{c}\,' = 2\pi \frac{\vec{a} \times \vec{b}}{\vec{c} \bullet (\vec{a} \times \vec{b})} \tag{3.2}$$

Each lattice vector describing a lattice plane of a real-space crystal is correlated to a point in reciprocal space. The crystal lattice can therefore be represented by a reciprocal lattice consisting of a point for each lattice plane of the crystal. The real or 'direct' lattice and the reciprocal lattice have the same space group and symmetry. Ewald's sphere is constructed in reciprocal space: a sphere of radius $k = 2\pi/\lambda$ is superimposed over a representation of the reciprocal lattice. Reciprocal lattice points that intersect the Ewald sphere produce diffraction under the angle 2Θ, which is the angle between the reciprocal vectors k_i and k_f describing the initial state of the incident photon and the final state of the photons after diffraction, respectively. Since the scattering is elastic, $|\vec{k_i}| = |\vec{k_f}|$, and the reciprocal vector $\vec{G}$ linking the two vectors $\vec{k_f} = \vec{k_i} + \vec{G}$ is a reciprocal lattice vector of the diffracting crystal. An exemplary, 2-dimensional cut through the Ewald sphere of a simple cubic lattice is shown in figure 3.2 b).
The concept of the Ewald sphere is employed for reciprocal space mapping (RSM) of hetero- and homoepitaxial structures. Growing a thin film epitaxially on top of a single crystal gives rise to diffraction from both lattices since the absorption length of Cu Kα radiation is on the order of several μm. In reciprocal space, both lattices are superimposed and it is possible to record a map of reciprocal space containing diffraction points from both substrate and film. This is especially useful when recording asymmetric (e.g h≠l for a (h0l)-cut through reciprocal space) reflections since the in-plane lattice constant is accessible and the strain state of the thin film can be evaluated. For simplicity, the reciprocal space map is often presented using the reciprocal vectors $q_\perp$ and $q_\parallel$, which are referenced with respect to the sample orientation and can describe any diffracted radiation through a summation of its out-of-plane ($q_\perp$) and in-plane ($q_\parallel$) component given in reciprocal length units $2\pi/\lambda$. For (h0l) and (0kl) diffraction of a (001) oriented crystal, $q_\perp$ and $q_\parallel$ correspond directly to the reciprocal lattice vectors of the crystal, which can be converted to a real-space length via equation 3.2. In this way, the RSM can be shown with the real-space length coordinates that correspond to the observed reciprocal space points, which is the preferred way of presentation in this thesis.

3.2.1 X-ray Reflectivity

A convenient way of determining film thickness and surface / interface roughness for stacked layer systems is X-ray Reflectivity (XRR) [38]. The experimental

geometry is very similar to that used for XRD, the only difference being that XRR is measured close to the regime of specular reflectivity. For hard x-rays, the index of refraction is $n < 1$ for most materials and there exists a regime of total external reflection where the incident radiation is completely reflected into the vacuum. This is a consequence of the fact that the refractive index of vacuum is larger than the refractive index of matter, and therefore radiation that enters into the matter from vacuum is refracted towards the vaccum according to Snell's Law. The critical angle of total external reflection is given by $cos\Theta_c = n_2/n_1$ (with $n_2 < n_1$) and is generally between 0.1° and 0.6° for most materials. For incident angles Θ_i slightly larger than Θ_c, the Fresnel reflectivity R of the surface can be approximated by

$$R = (2\Theta/\Theta_c)^{-4} \tag{3.3}$$

In the case of a thin film on a thick substrate, the reflectivity above the critical angle is additionally modulated with the interference of radiation that is reflected at the surface and radiation that is reflected at the interface and passes into vacuum again. For a thin film deposited on a (infinitely thick) substrate, the condition of constructive interference in dependence of the incident angle Θ_i is given by [39]:

$$\begin{aligned} m\lambda &= 2d\sqrt{\Theta_{i,m}^2 - \Theta_c^2} \quad for\ n_2 > n_3 \\ (m+1/2)\lambda &= 2d\sqrt{\Theta_{i,m}^2 - \Theta_c^2} \quad for\ n_2 < n_3 \end{aligned} \tag{3.4}$$

The factor 1/2 is a product of the phase shift induced at the film-substrate interface when the electron density δ of the film is higher than that of the substrate. Since most films are either grown homoepitaxially (where δ_{film} is almost always slightly smaller than $\delta_{substrate}$) or on a denser substrate, this phase shift is generally not encountered for the XRR measurements in this thesis. The presence of surface and interface roughness can be treated as a perturbation [38] or a systematic deviation from an ideal surface [39], and can be evaluated to give at least a qualitative impression of the roughness values. Even if absolute values depend on the respective models used and can deviate from those determined by other techniques (e.g. AFM for surface roughness), a comparative analysis of the damping of the reflectivity can yield insights into the roughness at surface and, more interestingly, interfaces.

3.3 Atomic Force Microscopy

Since its invention by Binnig, Quate and Gerber [40], atomic force microscopy (AFM) has become a widely used tool for surface characterization on the nanometer-scale. For this work, only tapping-mode AFM has been employed since it offers

superior spatial resolution and minimizes damage to surface and tip [41]. A sharp tip fixed to a stiff cantilever - usually made from Si - oscillates with its resonance frequency ω_0 and amplitude A_0. When the tip encounters repulsive or attractive interaction with a sample surface, the frequency and amplitude of the reflected oscillation can be evaluated. In addition, the change in frequency causes a phase-shift between the excited and the reflected oscillation, which yields another information channel that can be used to gain information about the surface. For epitaxial oxide layers, the most important information is the height (or amplitude) image since thin films grown epitaxially on stepped single crystal surfaces are atomically smooth when grown in layer-by-layer mode. AFM is therefore a powerful tool to control the surface roughness of a thin film.
Signal detection techniques for AFM are usually based on a laser beam that is reflected of the top of the cantilever. A position-sensitive detector (either a segmented diode or sometimes an interferometer) is used to record the cantilever deflection.

3.4 Solid State Spectroscopy - Fundamental Considerations

The physical and chemical properties of a solid are determined by the interaction of the electron shells of each constituent atom or ion. In solid state physics, spectroscopy is used to study the electronic structure of solids by exciting electronic transitions from a ground state to an excited state, which can be induced by irradiation of the sample with particles of a suitable energy. As we will focus on spectroscopy using photons as exciting particles, two types of spectroscopy can be distinguished: emission (ES) and absorption (AS) spectroscopy, which probe the occupied and unoccupied density of states (DOS), respectively.
In a solid, electronic states can roughly be distinguished by their binding energy into core-level states and valence states. The tightly bound core-level electrons are localized in sharp energy levels (orbitals) that resemble those found in an isolated atom or a molecule, while the valence electrons experience significant interaction with those of the neighboring atoms and form the valence band. Spectroscopy techniques can be conveniently classified (see table 3.1) into those investigating the valence electrons (e.g. UV-VIS, UPS, ARPES, SXPS) and those that investigate the core-levels (e.g. XAS, XPS, HAXPES). More precisely, the techniques are distinguished by the excitation energy of the respective probe, ranging from several eV (UPS) to several keV (HAXPES, XAFS). Additionally, techniques commomly applied in materials science can be distinguished by whether they provide information about the chemistry or the structure of a material. As a side remark,

Table 3.1: A rough classification of selected spectroscopies commonly used in materials science, the criteria being energy and information.

Energy \ Information	Chemical or **Structural**
Low Energy (< 100 eV)	Ultraviolett PS (UPS) **Electron paramagnetic resonance (EPR)** Ultraviolett - Visual spectroscopy (UV-VIS) Angular-resolved PES (ARPES) Soft x-ray PS (SXPS)
High Energy (> 100 eV)	X-ray PS (XPS) **X-ray absorption fine structure (XAFS)** Hard X-ray PES (HAXPES) X-ray absorption spectroscopy (XAS)

the abbreviation for photoelectron spectroscopy is frequently used as both PS and PES, therefore both are used here.

In the following, some basic considerations concerning the application of spectroscopy on solids to materials science will be given, followed by the description of the spectroscopy techniques employed in this work.

3.4.1 Binding Energy and Chemical Shifts

A detailed understanding of the electronic structure and electron - photon interaction is a prerequisite for the interpretation of any emission or absorption spectrum. The exact definition of the binding energy E_{bind} of an electron is given by [42]

$$E_{bind} = E_f^{N-1} - E_i^N \tag{3.5}$$

where E_i^N denotes the energy of the initial state with N electrons, and E_f^{N-1} that of the final state with $N-1$ electrons. In practice, E_{bind} is referenced to the Fermi level E_F for solids. In investigations related to material properties, it is usually the change of E_{bind} that is of interest, and not the absolute position. The value of E_{bind} depends strongly on the chemical state of the material. Chemical bonds in (partially) ionic materials reduce the electron density on the cations, which in turn reduces the screening of the core-potential for the remaining electrons. This change in E_{bind} is called the *chemical* shift. In oxidic materials, the magnitude of the chemical shift is a direct measure for the oxidation state of the probed anion. In addition, it is possible to induce an energy shift in a given material through the

introduction of charge carriers and a corresponding shift of the Fermi level E_F. A good example is the doping of a Si crystal with a donor such as P. The donors introduce electrons into the Si conduction band, without actually changing the chemical state of the Si atoms. Low doping levels of 10^{16}-10^{18} cm^{-3} are sufficient to shift the Fermi level from its intrinsic position (the middle of the band -gap for an ideal semiconductor at 0 K) closer to the conduction band. Since Si has band-gap of 1.1 eV, energy shifts of $\sim$1 eV in Si core-level emission lines can be observed between donor or acceptor doped material. Since the chemical environment of the Si lattice does not change appreciably and the main issue is the introduction of free charge carriers, these shifts can be called *electronic* shifts. The observed shift of the emission lines is essentially a consequence of the shift of the reference level E_F.

3.4.2 Satellites and Line Splitting

An important fact is that in any experiment, the binding energy (or absorption edge position) that is measured does not correspond to the ground state energy of the probed atom, but to the excited, final state. In many-body systems, such as atoms with $Z > 1$ and solids, there can be multiple configurations of the final state. Since these final states are described as quantum-mechanical wave-functions, they interfere with each other in what is called configuration-interaction (CI), which can include spin-dependent configurations, such as core-polarization, and charge-transfer (CT) processes [42].
For the specific case of transition-metal oxides (TMO), the charge transfer from ligand to metal gives rise to so-called *satellite* lines. While the phyiscal origin of CT-satellites in early (Sc, Ti, V) and late (Ni, Cu) TM oxides is considered to be somewhat different in nature due to the weaker correlation in early TMOs [43], satellite structures of varying complexity can be observed for all TMO 2p emission lines. A schematic description of the ligand-to-metal charge-transfer in an insulator is depicted in figure 3.2 a). In the ground state, E_F is located at the top of the filled ligand *p*-band, while the metal *d*-states and *sp*-band are unocuppied. Upon excitation, a core-hole c^{-1} causes the metal energy levels to relax, enabling charge-transfer from the ligand *p*-band into the metal *sp*-band (final states configuration "1") or the metal *d*-states (final state configuration "2"). The difference in screening strength of the two configurations results in different energy positions of the respective emission lines. Note that the third possibility (no CT) is not depicted.
A prominent example are the CT-satellites found in $SrTiO_3$ (and other Ti-O containing compounds). To a first approximantion, the ground state of the Ti^{4+} ion in $SrTiO_3$ is $2p^6 3d^0 L$, where L stands for the electronic configuration of the ligand ($2p^6$ in the case of oxygen). For the excited state, we can write $2p^5 3d^0 L$ and

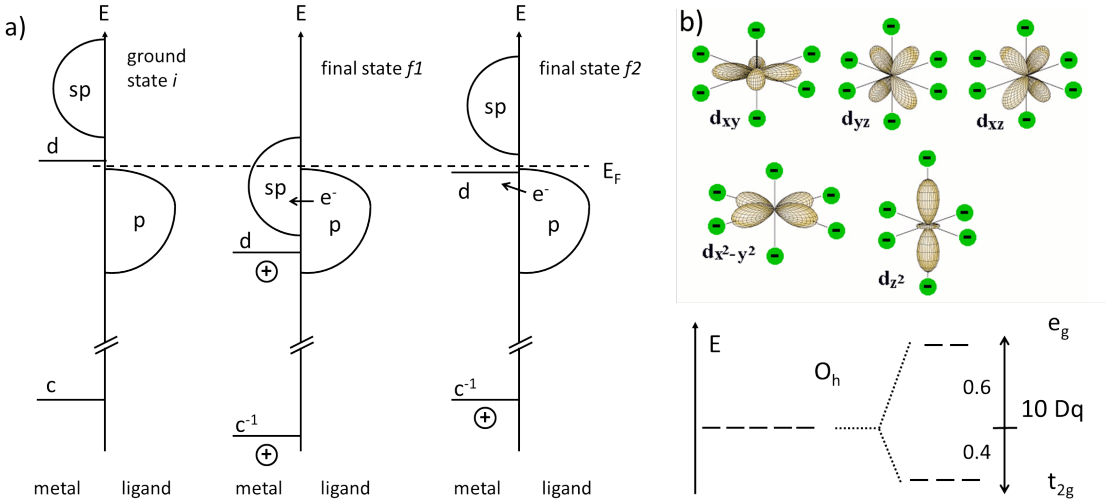

Figure 3.2: a) Schematic energy diagram of the ligand-to-metal charge-transfer (LMCT) reproduced from [42]. b) Graphic representation of the orientation of *d*-orbitals in space. The presence of increased electron density along the crystal axes lifts the five-fold degeneracy of the energy levels [44].

$2p^5 3d^1 \mathrm{L}^{-1}$ for the CT-case. One of these final states is usually favored strongly, such that the other final state contributes significantly less intensity to the measured spectrum and is observed as weak satellites with an energy shift compared to the main line.
In real solids, this simplified description proves insufficient to reproduce the experimental spectra with theoretical calculations, and admixtures of additional configurations (for example $2p^6 3d^1 \mathrm{L}^{-1}$, $2p^6 3d^2 \mathrm{L}^{-2}$) have to be mixed to the ground state [43]. From an experimental point of view, this is rather intuitive since the XPS valence band spectrum of $SrTiO_3$ is composed of contributions from both O $2p$ and Ti $3d$ orbitals, despite the fact that for Ti^{4+}, the $3d$ orbitals are nominally empty ($3d^0$). This demonstrates at the same time that the rather simple concept of assigning charge to an ion according to the valence state has to be treated with caution.
Orbitals with $l > 0$ (p,d,f) have an orbital angular momentum, which couples to the angular momentum of the electrons (spin) and lifts the energetic degeneracy of the respective orbitals. The magnitude of the spin-orbit splitting depends on the nuclear charge and the electron configuration, and can therefore serve as an additional way to assign a doublet to an element. In addition, there is a weak dependence of the spin-orbit splitting on the oxidation state, since the reduction of electron density results in weaker screening of the core-levels.
The crystal-field-splitting is a direct consequence of the nearest neighbor interaction in a solid and can be observed in compounds containing transition metals. In the case of $SrTiO_3$, the five-fold degeneracy of the Ti $3d$-orbitals is lifted by

the presence of six oxygen ions along the crystallographic axes of the cubic unit cell. Since the Ti-O bond is strongly ionic in nature, the electron density located on the oxygen repulses the electrons in the $3d$ orbitals "pointing" along the cubic axes of the unit cell (d_{z^2}, $d_{x^2-y^2}$), whereas the orbitals that have the probability density located between the cubic axes are repulsed less strongly and therefore are energetically favorable (d_{xy}, d_{yz}, d_{xz}). The strength of this crystal-field-splitting is denominated as 10Dq and depends on the type of ligand, and the interatomic distance between the metal ion and the ligand. Crystal-field-effects are not restricted to compounds containing octahedrally coordinated TM ions and can be observed for other coordination polyhedra as well, although the number of split states increases with decreasing symmetry of the polyhedra.

3.4.3 Information Depth

For investigations of vertically stacked samples such as MIM-structures, knowledge of the information depth is of paramount importance and usually depends on the signal-detection technique that is used in a specific experiment. Experimental techniques that detect fluorescence radiation are generally considered bulk-sensitive, since the attenuation length of the radiation is usually on the order of several μm for K-edge and several hundred nm for L-edge fluorescence [45]. Fluorescence detection is a popular technique when investigating low concentrations of absorbers, such as dopants [46].
Compared to photon-based techniques, spectroscopies detecting electrons can be considered surface-sensitive because of the much larger scattering cross-section of electrons. The average distance between two scattering events - the inelastic mean free path (IMFP) - of an electron depends stronlgy on its kinetic energy, which is schematically shown in figure 3.3 a). Since photoelectrons from several 10 to several 100 eV kinetic energy E_{kin} have IMFP values on the order of a few Å, they are frequently used for the analysis of adsorbants and of the first few monolayers of a crystal surface. Secondary electrons generally have lower scattering cross-sections and therefore longer IMFP values, which makes techniques like XAS (using total-electron-yield (TEY) detection) less sensitive to surface phenomena. With respect to topics investigated in materials science, IMFP of the order of 50 Å are desirable for the investigation of material stacks and interfaces. This can be achieved by HAXPES, increasing the photon-energy of the exciting radiation up to several keV and resulting in increasing E_{kin} and larger IMFP values.
In practice, the IMFP is not a suitable value to use for information depth evaluation since in addition to electro-electron scattering, scattering events at the surface (plasmons) or elastic scattering can occur, and therefore the experimentally more accessible effective attenuation length (EAL) is used. Following the definition suggested by Jablonski and Powell [48], the information depth (ID) is the "maximum

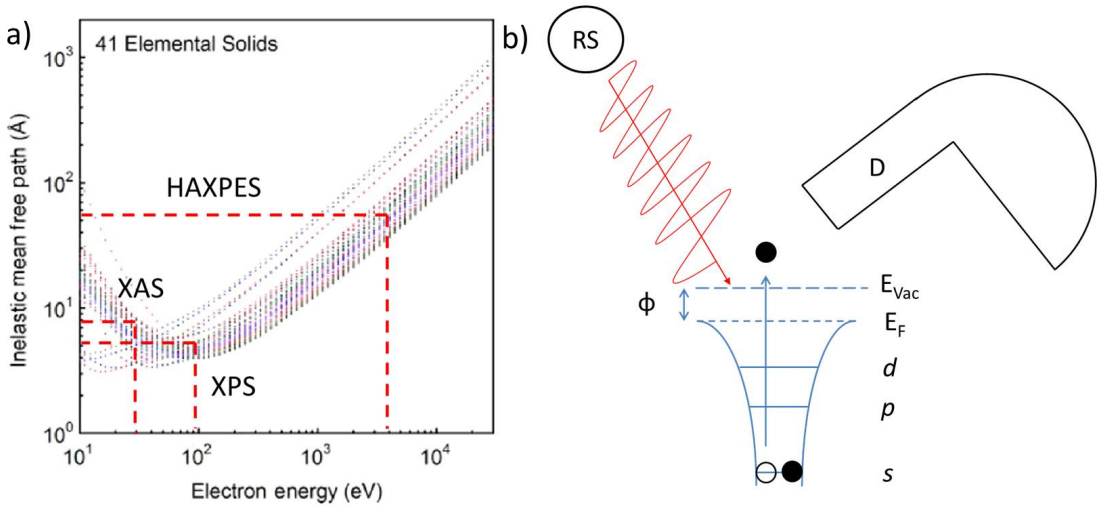

Figure 3.3: a): Calculations of IMFP values for 41 elemental solids, with the energy ranges for XPS, XAS and HAXPES indicated. Adopted from [47]. b): Schematic illustration of photoemission spectroscopy. Abbreviations are RS = radiation source, D = detector, E_{Vac} = vacuum level, E_F = Fermi level, ϕ = work function of the material.

depth, normal to the specimen surface, from which a useful signal information is obtained", and the EAL can be defined as the average decay length of the emission depth distribution function (EDDF), provided the EDDF is sufficiently described by an exponential function. In this framework, the EAL can be calculated by measuring the signal intensity of a given photoemission line from a substrate S through an overlayer

$$I_S = I_S^0 \; exp(-\frac{t}{\lambda_i^S cos\ \alpha}) \tag{3.6}$$

where I_S and I_S^0 denote the intensity of a substrate emission line through and overlayer of thickness t and the intensity of the bare substrate, respectively, α is the emission angle and λ_i^S is the EAL. It is readily apparent from equation 3.6 that the EAL can be experimentally determined through a variation of the overlayer thickness or the emission angle.

3.4.4 Radiation Sources

The information that is accessible via spectroscopy depends on the type of radiation that is used to excite the electronic system. He-, Ne- or Hg- gas lamps or UV-lasers can be used to obtain information about the valence electrons and the band structure of a solid, with excitation energies in the range 1 - 50 eV. X-rays

are the preferential radiation used for core-level analysis, and can be either generated in a x-ray tube or using a synchrotron light source. While a state-of-the-art x-ray anode source can provide monochromatized radiation with a photon flux $I_{ph} \sim 10^9$ $photons/s$ at the sample, modern insertion devices (ID) can provide upward of 10^{12} $photons/s$ and are therefore preferred for flux-hungry experiments such as photoemission electron microscopy (PEEM) or HAXPES. An additional advantage for synchrotron radiation is the tunability of the photon energy, which is a prerequisite for x-ray absorption spectroscopy.
The simplest radiation source at a synchrotron is a bending magnet, which is simply a magnetic dipole that forces electrons passing through the magnetic field onto a circular path. The emitted radiation covers a broad spectrum with a maximum depending on device characteristics such as the radius of the electrons in the magnetic field, and delivers moderate photon fluxes.
Undulator sources are long, static arrays of magnets of alternating field direction through which an electron-beam at relativistic energies is guided. Each magnet forces the electron beam to bend in the magnet field, emitting radiation of a defined wavelength depending on the radius of curvature. Relativistic effects cause the emitted radiation to be strongly forward-focused, and the undulator-gap (separation of the magnetic poles) can be adjusted to tune the energy of the emitted radiation. The brightness of the radiation produced by an undulator can be up to N^2 larger than that of a bending magnet, where N is number of magnetic poles, and at the same time the source size of an undulator is very small due to the small opening angle of the radiation cone.
The small source size is useful for a number of experiments, especially those requiring focused beams. Since x-rays interact only weakly with matter, x-ray optics are usually very complex. A simple way to achieve x-ray beams focused to several μm on the specimen are polished Si-mirror mounted on a piezo-crystal controlling the bending radius of the mirror (Kirckpatrick-Baez [KB] mirrors).

3.4.5 Nomenclature in Spectroscopy

Since the nomenclature used in emission and absorption spectroscopies is different, table 3.2 gives a brief overview of the most important emission lines and absorption edges discussed in the later sections.

Table 3.2: Overview of the nomenclature commonly used in photoemission and x-ray absorption spectroscopy, up to the M-shell.

Orbital	$\|j\| = \|l \pm 1/2\|$	Emission line	Absorption edge
$1s$	1/2	1s	K
$2s$	1/2	2s	L_1
$2p$	3/2	$2p_{3/2}$	L_3
	1/2	$2p_{1/2}$	L_2
$3s$	1/2	3s	M_1
$3p$	3/2	$3p_{3/2}$	M_3
	1/2	$3p_{1/2}$	M_2
$3d$	5/2	$3d_{5/2}$	M_5
	3/2	$3d_{3/2}$	M_4

3.5 Photoemission Spectroscopy

3.5.1 X-ray Photoelectron Spectroscopy - XPS

XPS is a popular tool in materials science for the analysis of the chemical state and composition of materials. The basic principle is illustrated in Figure 3.3 b): a core-level electron is excited by an incident photon, which provides the electron with sufficient energy to leave the atomic potential well and overcome the surface barrier of the solid and escape into the vacuum. The photoelectron is now "free" and can be detected via a photoelectron analyzer D that measures the kinetic energy E_{kin} of the photoelectron. Using monochromatic radiation of a known wavelength ν, the binding energy E_{bind} of the electron can be calculated:

$$E_{bind} = h\nu - E_{kin} - W \tag{3.7}$$

where W denotes the work function of the spectrometer. Whereas the value of E_{bind} permits the identification of the emitting atom, the major interest to materials science is the energy shift that is induced by the chemical state of the probed atom, called the chemical shift (see section 3.4.1).

3.5.2 Hard X-ray Photoelectron Spectroscopy - HAXPES

As a tool for materials science, XPS suffers from severe limitations because the small EAL restricts the information depth to the near-surface region. To gain access to "buried" interfaces, like the metal-oxide interface in a MIM-stack, it is

necessary to significantly increase the EAL. An increasingly popular way to do so is using hard x-rays to increase the photoelectron kinetic energies to values of several keV, resulting in EAL values of several nm. The IMFP values of photoelectrons (and correspondingly, the EAL) have been shown to increase with E^n, with $n = 0.75$, by experiments and theory [47]. This universal behavior reflects a general trend, and EAL values can be very different for various materials, but the implication that high kinetic energy gives access to buried layers and provides information depth of up to 200 Å has been validated [49, 50].
In addition to the increased EAL values, the use of hard x-rays is accompanied by several physical phenomena that either have consequences on the measured spectra or necessitate the use of special equipment. A general overview can be gained from [51], but some specific aspects deserve closer examination.
The use of synchrotron radiation for HAXPES is favorable because of the tunability of the excitation energy, but also because the photoelectric scattering cross-sections σ of the electrons decays with increasing energy. Notably, $\sigma \propto E^{-7/2}$ for orbitals with s character and $\sigma \propto E^{-9/2}$ for orbitals with p, d, f character, and in consequence the spectral shape of the valence band in particular can change with photon energy. In general, the intensity of emission lines deriving from orbits with high n and low l values will decay more slowly. The overall intensity loss is more than compensated by modern, high-brightness undulator sources. Another consequence of the high photon energies is the non-negligible momentum transfer from the photon to the excited electron, which makes non-dipole corrections necessary for some calculations. If the momentum of the photoelectron $|k_{hv}|$ is not much smaller than the size of the first Brillouin-zone (BZ), the momentum of the photoelectron looses its information concerning the band structure of the material, and the valence band is measured as a matrix-element weighted density-of-states (DOS) [52]. In addition, the small acceptance angles of the photoelectron analyzer produces some BZ-averaging as well.
Yet another effect of high E_{kin} is that the elastic scattering at the surface is much less pronounced than for soft x-ray PS, leading to a simpler interpretation of angle-resolved core-level spectra and a generally low background. It has been demonstrated that using angles of incidence just above the critical angle of total external reflection ϕ_c, the inelastic contribution to the background can be significantly reduced [53].
An beneficial effect of the high kinetic energies is the decreased surface-sensitivity, which removes the need for surface cleaning or $in-situ$ sample preparation. Sacchi *et* al. calculate that at an electron kinetic energy of 6000 eV, a 5Å surface layer contributes only 7% of the total signal intensity, compared with 46% at 600 eV kinetic energy [49].

3.6 X-ray Absorption Spectroscopy

The linear absorption coefficient μ_t is defined as the amount that a beam of primary intensity I_0 is attenuated by a sample of thickness x

$$dI = \mu_t I_0 dx \tag{3.8}$$

or in the integrated form

$$I = I_0 \; exp(-\mu_t x) \tag{3.9}$$

with

$$\mu_t = \mu_A + \mu_b, \tag{3.10}$$

where μ_t, μ_A and μ_b denote the total (linear) absorption coffecient (the measured quantity), the absorption coefficient of species A and the background, respectively. The schematic setup of an absorption experiment is shown in figure 3.4. The simplest way to measure μ_t is a transmission experiment, where the intensity of the x-ray beam is measured in front of and behind the sample, and μ_tx can be calculated according to equation 3.9. The desirable sample thickness for transmission experiments is $x = 1/\mu$, corresponding to an absorption step of $log(I/I_0) = 1$. For practical reasons, transmission experiments are most commonly used in combination with hard x-rays since x is of the order of a few μm, facilitating sample preparation. In addition, photons with $h\nu > 5$ keV are only weakly attenuated by air, removing the need for a vacuum sample environment. Transmission experiments are commonly done on concentrated, powdered samples.
The absorption coefficient μ can also be measured by secondary processes, such as fluorescence radiation and secondary electrons. Fluorescence detection offers advantages over transmission for the detection of small concentrations of A, because the statistical precision for fluorescence $\delta\mu_A/\mu_A \propto (1/\mu_A)^{1/2}$ and for transmission $\delta\mu_A/\mu_A \propto 1/\mu_A$ [54]. As a consequence, fluorescence is preferable to transmission

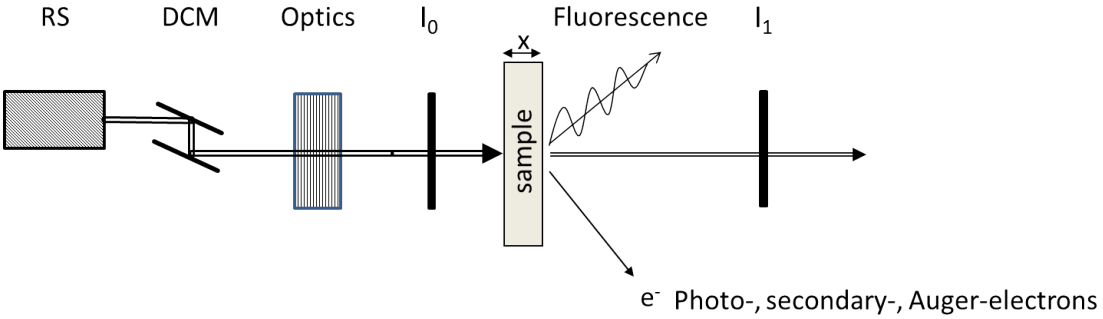

Figure 3.4: Schematic setup of an x-ray absorption experiment. Abbreviations: RS = radiation source, DCM = double crystal monochromator.

for thick, diluted samples (dopants) or thin, concentrated samples (thin films). Fluorescence detectors are compact and mobile, which offers experimental advantages to the fixed position of the ionization chambers commonly used for transmission.
For soft x-ray absorption, an evacuated x-ray guide and sample environment are necessary to minimize intensity losses. Under UHV conditions, the detection of photo-, Auger- or secondary electrons can be used to measure μ_A, either by electron optics or the sample current. The latter technique, known as total electron yield (TEY), essentially uses secondary electrons since the creation of these is much more likely than photo- or Auger-electrons, and can therefore be considered surface sensitive with escape depths of several nm (see section 3.4.3).

3.6.1 X-ray Absorption Fine Structure - XAFS

X-ray absorption fine structure (XAFS) refers to the oscillatory behavior of the absorption coefficient μ_A above an absorption edge. For hard x-ray radiation, the main absorption mechanism is photoionization of core-levels, which can be described by the one-electron approximation of Fermi's golden rule

$$\mu \propto \sum_f |\langle \Psi_f | \mathbf{p} \cdot \mathbf{A(r)} | \Psi_i \rangle|^2 \, \delta(E_f - E_i - \hbar\omega) \tag{3.11}$$

where the Ψ_i and Ψ_f stand for the intial and final eigenstages of the effective one-electron Hamiltonian, respectively, and $\mathbf{p}$ and $\mathbf{A(r)}$ are the momentum operator and the vector potential of the incident electromagnetic field [55]. In a solid, the transition matrix elements are influenced by the neighboring atoms, resulting in the oscillatory structure. In the picture of a quantum-mechanical wave, the outgoing photoelectron wave is reflected off the surrounding atoms, and the oscillatory structure is a product of the interference of the outgoing and the reflected waves. Put differently, the intial state $|\Psi_i\rangle$ describes a localized state of the absorber, and the final state $\langle \Psi_f |$ is the sum of the outgoing photoelectron wave and the reflected waves from the surrounding atoms. Since this interference depends on the strength and distance of the scattering centers, the crystallographic structure and coordination polyhedra of a crystalline solid can be investigated. Nevertheless, XAFS is a local probe due to the limited lifetime of the excited state and the mean free path inside the material. Since XAFS has now been used for many decades, there is extensive literature on the subject; e.g. a recent review by Rehr and Albers [55] or Teo's book [56]. The following paragraphs generally follow both of these sources.
In the post-edge structure, the energy region just above the edge up to ~ 50 eV is refered to as x-ray absorption near-edge spectroscopy (XANES), while the region

from 50 eV up to 1000 eV beyond the edge is called extended x-ray absorption fine structure (EXAFS).

3.6.2 Extended X-ray Absorption Fine Structure - EXAFS

The term EXAFS refers to the high energy part of oscillatory structure, generally beginning 40-60 eV above the absorption edge. The onset of the EXAFS regime is connected to the photoelectron kinetic energy being large enough to be considered a "free" electron moving through the solid, at which point the spatial variations of the interatomic potential have negligible influence on the photoelectron. This means that in the energy regime of EXAFS, the electronic structure of the absorber (bonding state, electronic configuration) does not influence the photoelectron, and the oscillations can be described by the model of the interference of outgoing and incoming photoelectron waves. EXAFS is therefore suited to investigate structural parameters such as bond distance and the disorder therein, coordination numbers and species of the surrounding atoms.
Through the particle-wave dualism of electrons, the wave vector k of a photoelectron is given by

$$k = \frac{2\pi}{\lambda} \tag{3.12}$$

which is related to the energy via

$$k = \sqrt{\frac{2m}{\hbar^2}(E - E_0)} \tag{3.13}$$

where $\hbar = h/2\pi$, h is Planck's constant and m is the mass of an electron, and E_0 is the threshold energy of the absorption edge.
The measured absorption coefficient μ(E) consists of a background μ_B (from lower-lying edges and inelastic scattering), an atomic-like absorption coefficient μ_0 (corresponding to a step function of the absorption coefficient) and the oscillatory modulations $\chi(E)$

$$\mu(E) = \mu_B + \mu_0(1 + \chi(E)). \tag{3.14}$$

While raw data is measured vs. energy, it is necessary to convert the $\chi(E)$ into $\chi(k)$ via equation 3.13 in order to interpret the structural parameters contributing to the EXAFS in the *short-range single-electron single-scattering* theory (as summarized in [56]). The oscillatory structure can be interpreted as the sum of j plane-waves $sin(2kr_j)$ with a phase shift ϕ_{ij}, where the index i denotes the absorber and the index j runs through all adjacent atoms:

$$\chi(k) = \sum_j N_j S_i(k) F_j(k)\ e^{-2\sigma_j^2 k^2}\ e^{-2r_j/\lambda_j(k)}\ \frac{(sin(2kr_j + \phi_{ij}(k))}{kr_j^2} \tag{3.15}$$

where N is the coordination number, S is the amplitude reduction factor of the absorber, F is the backscattering amplitude, $e^{-2\sigma_j^2 k^2}$ an attenuation factor due to disorder σ (which corresponds to the Debye-Waller factor for pure thermal disorder, but includes structural disorder also) and $e^{-2r_j/\lambda_j(k)}$ is an attenuation factor due to the limited mean free path of the photoelectron.
This parameterized equation is the basis for structural analysis of EXAFS. In practice, EXAFS analysis software (like the Horae software package [57]) uses scattering paths calculated by the $ab-initio$ method IFEFFIT ([58]) to fit the extracted EXAFS signal. Since multiple scattering and non-linear scattering paths are generally hard to model accurately - especially with respect to the Debye-Waller factor - the first coordination shell yields the most accurate results.

3.6.3 X-ray absorption Near Edge Structure - XANES

The term XANES refers to the energy range of the actual absorption edge, usually a few ten eV before the white line up to 40-60 eV above the edge. Due to the low kinetic energy of the photoelectron, the mean free path can be quite large and is a strong function of E_{kin}, and the XANES region is dominated by strong multiple scattering effects. The simplified assumption that the electron is not influenced by the variations of the interatomic potential cannot be made for XANES, and therefore modelling of XANES is still relatively undeveloped compared to EXAFS. However, there are approaches to model XANES by either DFT calculations of the DOS or full multiple-scattering $ab-initio$ calculations [59, 60]. Due to the sensitivity of the XANES to structural parameters such as disorder or interatomic distances, comparisons between the XANES of the same element in different environments (e.g. Fe in $SrFeO_3$ and as a dopant in $SrTiO_3$) have to be treated with caution.

Chapter 4

Epitaxial Oxide Growth

In this chapter, the influence of growth parameters and substrate-induced strain ϵ on the epitaxial growth of $SrTi_{1-x}Fe_xO_3$ is examined. In the first part, the strain relaxation of $SrTi_{1-x}Fe_xO_3$ films grown heteroexpitaxially on $NdGaO_3$ will be examined with regard to sample thickness, deposition pressure, laser energy and substrate influence. In the second part, the influence of Fe on the c-axis elongation will be demonstrated for a given set of process parameters, and a set of optimized parameters established that is used for the growth of resistive switching samples. As a global definition for this work, the substrate temperature corresponds to that set at the heater unit and the laser energy density (on the target) is calculated using a spot size on the target of 6 mm^2, and assuming a transmission of 60% through the quartz-glas window. A KrF excimer laser ($\lambda = 248$ nm) with a pulse duration of 25 nanoseconds (FWHM) was used to ablate the target material.

4.1 Heteroepitaxy on $NdGaO_3$

$NdGaO_3$ is a rare-earth oxide crystallizing in the orthorombic space group *Pbnm* ($GdFeO_3$-type), with a melting point of $T_{melt} \approx 1900$ K and a density of 7.57 g/cm^3, and orthorombic lattice constants of $a = 5.433$ Å, $b = 5.503$ Å and $c = 7.716$ Å. The $NdGaO_3$ crystal structure is a distorted perovskite structure, with Nd occupying the A-site in 12-fold oxygen coordination, but the Ga-O_6 octahedra are tilted with respect to each other. Using a simple coordinate transformation, $NdGaO_3$ can be described as a pseudo-cubic system with lattice parameters a', b' and c'

$$\begin{aligned} a' &= c/2 = 3.858 \text{ Å} \\ b' &= \sqrt{a^2 + b^2}/2 = 3.867 \text{ Å} \\ c' &= \sqrt{a^2 + b^2}/2 = 3.867 \text{ Å} \end{aligned} \tag{4.1}$$

In this way, $NdGaO_3$ crystals cut along the (110) plane can be used to grow cubic oxides since the pseudo-cubic lattice parameters in the $(001)'$ plane are identical to within 0.01 Å, according to the coordinate transformation (see figure 4.1. The difference in unit cell parameters between the $NdGaO_3$ and $SrTiO_3$ crystal structure is ~ 0.05 Å, therefore growing $SrTiO_3$ on $NdGaO_3$ induces strain in the epitaxial oxide.

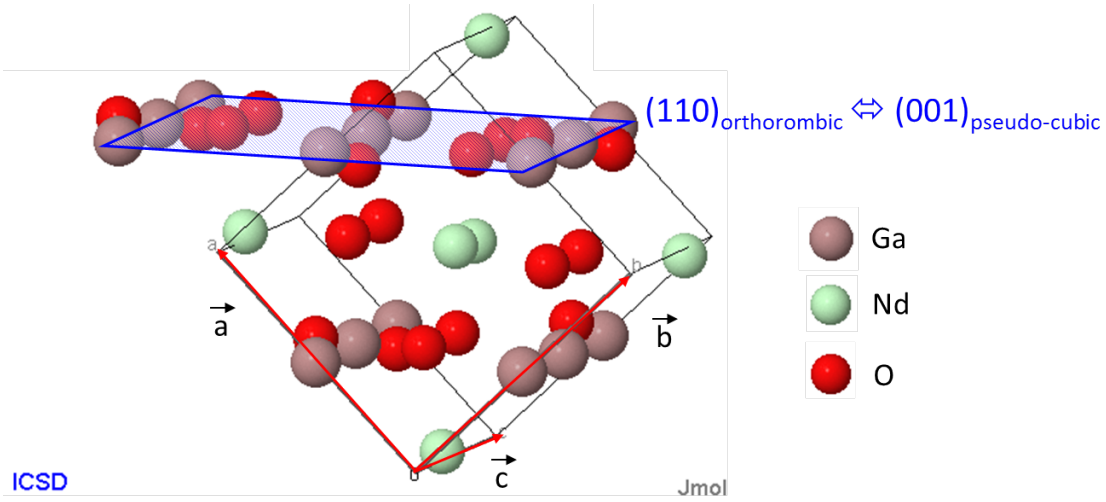

Figure 4.1: Illustration of the pseudo-cubic (001) plane in $NdGaO_3$ crystals. Model exported from [61].

Since the commercially available $NdGaO_3$ crystals (Crystec GmbH, Berlin) were delivered with polished crystal surface, an annealing step in air is necessary to obtain a crystal surface with atomic (110) termination. Low-index crystal planes have the lowest surface enthalpy ΔG_s, and the polished crystal surface restructures into terraces with (110) termination, forming a stepped surface with a step height of one unit cell. For crystals with a miscut-angle of $< 0.05°$, an annealing step at 1000°C for 2 hours in air yielded the best results. The miscut-angle α is defined as the angle between the surface normal of the crystal surface, $\bar{n}_{sur}$, and the normal with respect to the lattice plane, $\bar{n}_{lat}$. This is schematically depicted in figure 4.2 a), along with an atomic force microscope (AFM) image of a polished, as-received crystal in b) and a crystal showing a stepped surface structure after annealing, c). In contrast to $SrTiO_3$, the surface of $NdGaO_3$ after annealing is A-site terminated and consists almost exclusively of NdO planes, which is explained by the high vapor pressure of Ga above 800°C [62]. The miscut angle of a crystal surface can be determined by measuring the average length of the surface steps, l, and calculating α via the geometrical relation $d/l = \tan\alpha$, where d corresponds to the step height. An alternative way to calculate α is to determine the difference between the incident angle in x-ray reflectometry and x-ray diffraction, $\alpha = \omega_{refl}$ - ω_{diff}, corresponding to the orientation of the crystal surface and the lattice planes, respectively.

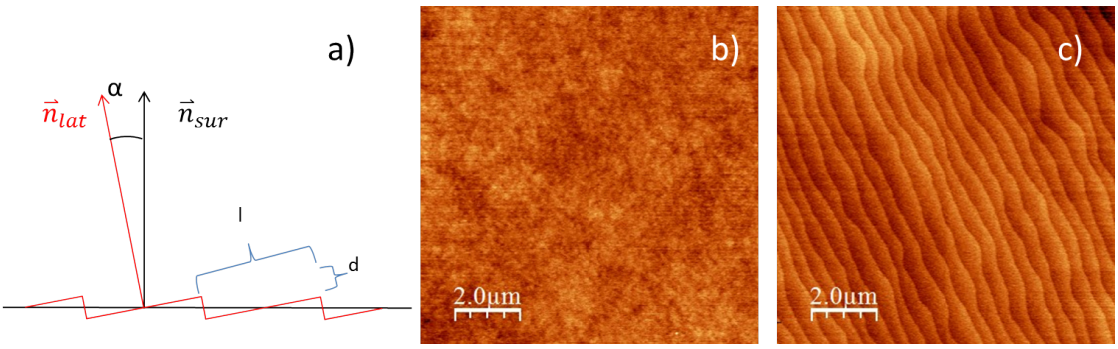

Figure 4.2: a): Schematic illustration of the miscut-angle α. b) and c): as-received and annealed (1000°C, 2h, air) surface of a 110-cut $NdGaO_3$ crystal as observed via AFM.

4.1.1 Influence of Deposition Parameters

The influence of the deposition parameters laser energy density E (J/cm^2) and oxygen pressure p_{O_2} (mbar) on the surface quality and lattice relaxation of $SrTi_{1-x}Fe_xO_3$ grown on (110)-cut $NdGaO_3$ is studied via a systematic variation of the parameters and ensuing characterization by AFM, XRR and XRD. The substrate temperature during growth was kept constant at T = 700°C for all experiments discussed here. The laser energy density E has been shown to influence the stoichiometry of $SrTiO_3$ thin films, with an excess of Sr present at low E and an excess of Ti at high E [30, 63, 64]. The presence of Fe in the target and the thin film, however, causes severe differences to the studies mentioned, and is as yet not understood. In figure 4.3 a)-c), AFM scans of the surface of $SrTi_{0.99}Fe_{0.01}O_3$ films after deposition at p_{O_2} = 0.025 mbar with 2000 pulses of varying energy are presented. A first indication to the film stoichiometry are small, seemingly round particles on the film surface that are generally identified as SrO or Sr-rich exclusions, based on observations on reduced single crystals. These exclusion are observable as "white" spots in the false-color plots in figure 4.3, and the density of these spots varies as a function of energy. For the deposition pressure used (0.025 mbar), the spots do not disappear for any given value of E. The parameter set yielding the highest surface non-stoichiometry also produces the thinnest films, therefore a film-thickness effect is unlikely. XRD scans of the symmetrical (002) diffraction peak show the systematical decrease of the $SrTiO_3$ - (002) diffraction angle with decreasing E (see figure 4.3 d)). The in-plane lattice constant is locked to the value of the substrate, representatively shown by the reciprocal space map (RSM) for the 1.3 J/cm^2 sample in figure 4.3 e). The nominal diffraction angles for the (002) plane is indicated for bulk $SrTiO_3$ (a = 3.9034 Å, dashed line) and for a coherently strained $SrTiO_3$ film assuming a constant unit cell volume (dash-dotted line, $a_{STO} = a'$, $b_{STO} = b'$, c_{STO} = 3.985 Å). Similar to homoepitaxial films, the increase of the unit cell

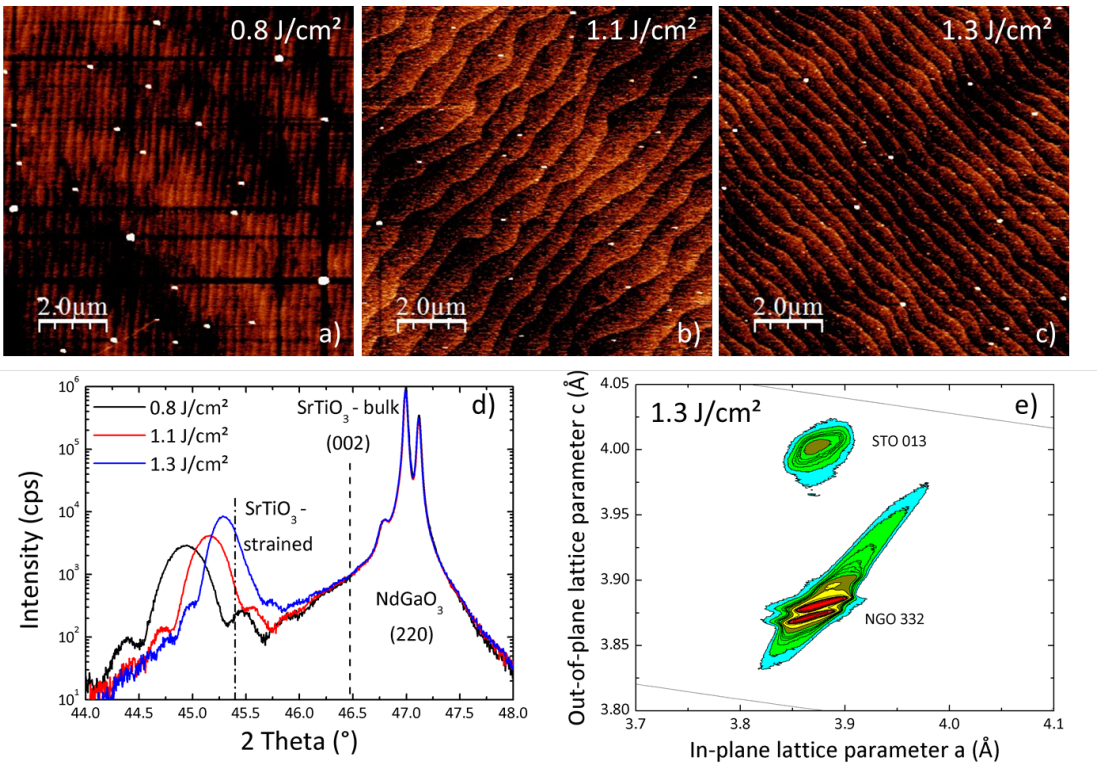

Figure 4.3: a)-c): AFM images of $SrTi_{0.98}Fe_{0.02}O_3$ films grown with a laser energy density of 0.8, 1.1 and 1.3 J/cm^2, respectively. d): Symmetric 00l reflections of the films shown in a)-c). The bulk lattice constant of $SrTiO_3$ and the theoretical lattice constant of coherently strained $SrTiO_3$ on $NdGaO_3$ are indicated with the dashed and the dash-dot line, respectively. e): RSM of the $(013)_{STO}$ and $(332)_{NGO}$ reflections of the film grown at 1.3 J/cm^2. The film thickness is 47.1 nm.

volume with decreasing laser energy indicates the presence on a systematic non-stoichiometry that is induced by the ablation process and/or the particle energy distribution in the ablated plume. The direction of the volume change indicates a Sr-enrichment in the $SrTi_{1-x}Fe_xO_3$ films.

The length of the c-axis can also be influenced by the deposition pressure p_{O_2}, as shown in figure 4.4 a). The film grown at 0.025 mbar has a thickness of 53.8 nm and is identical to the one shown in figure 4.3 d) and e), whereas the one grown at 0.25 mbar is nearly 10 nm thinner (44.7 nm). This excludes a thickness-induced relaxation as the explanation for the relaxed c-axis of the 0.25 mbar film. The generally observed trend is that films grown at 0.25 mbar p_{O_2} have a relaxed crystal structure, whereas lower p_{O_2} yield coherently strained films. The impact of this relaxation on the crystal quality is in figure 4.4 b) in terms of the rocking curve of the $SrTiO_3$ (002) reflection. The half-width of the rocking curve is a measure for the crystal quality of a single crystal: while the reflection condition

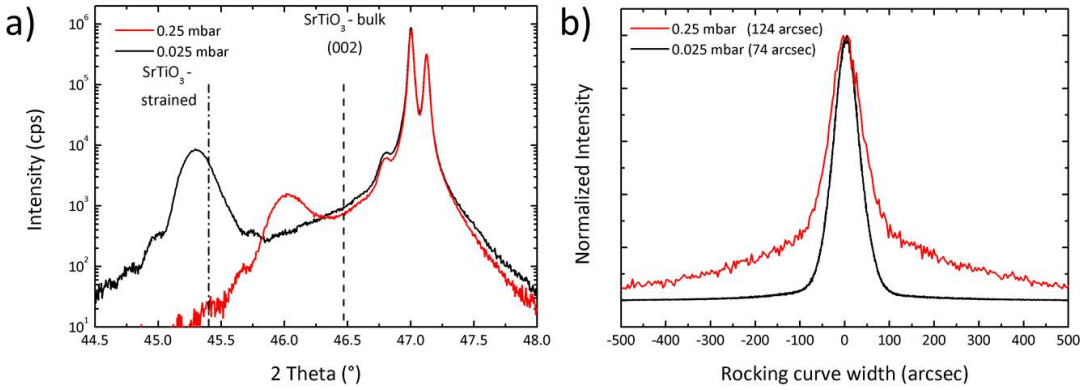

Figure 4.4: a): $(002)_{STO}$ reflections of films grown at a p_{O_2} 0.25 mbar (red) and 0.025 mbar (black). b): The corresponding rocking curves of the $(002)_{STO}$ reflection.

for theoretically perfect crystal lattices is a delta-function, a real crystal contains stacking faults and dislocations that will disturb the long range order and increase the half-width. While the rocking curve of the film grown at 0.025 mbar shows a very narrow half width that corresponds to the experimental resolution of the x-ray setup (∼70 arcsec), the half-width of the 0.25 mbar-grown film is significantly broader. This suggests that relaxation through built-in defects like stacking faults or misfit-dislocations is favored by high deposition pressures. In comparison, the right side of figure 4.5 depicts the rocking curves measured on the $(002)_{STO}$ reflection of the three thin films discussed in figure 4.3. For the three laser energy densities, the half-width of the rocking curve is smaller than the experimental resolution of the x-ray setup, and E does not influence the crystal quality, indicating coherent growth in all three cases. In terms of lattice relaxation, E shows no influence while high p_{O_2} yields films that relax growth stress through a higher defect density. The most likely reason is a transition from a 2-dimensional (layer-by-layer) growth mode at low p_{O_2} to a pseudo 3-dimensional (island growth) at higher p_{O_2}, where the border between intergrowing islands could facilitate the incorporation of higher dimensional defects. The top left side of figure 4.5 demonstrates the systematic influence of E (red and black symbols) and p_{O_2} (blue symbols) on the deposition rate, which is measured $ex - situ$ by XRR and is a simple gauge for the gross mass transfer from target to substrate during growth. The increase of the deposition rate with increasing laser energy density suggests that the amount of ablated material increases in a linear way with laser energy. A linear relation is found for deposition pressure of 0.25 mbar (red symbols) and 0.025 mbar (black symbols). The top x-axis of the same graph shows the dependence of the deposition rate on gas pressure during growth. The observed exponential decay with increasing p_{O_2} is explained by the reduction of the mean free path of the particles in the plume. Increased gas pressure significantly increases particle-particle scat-

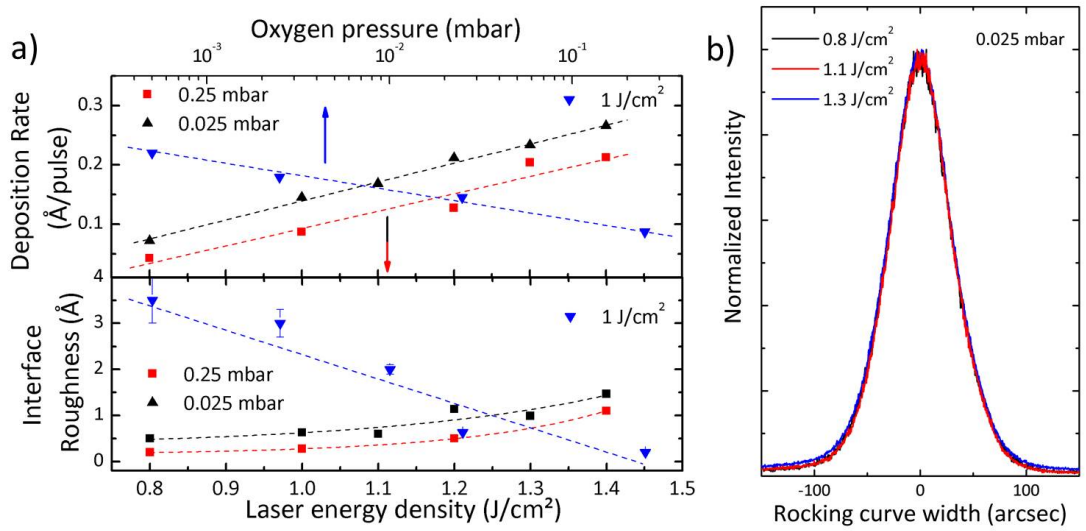

Figure 4.5: a): Influence of laser energy density (red and black symbols) and gas pressure (blue symbols) on the deposition rate of $SrTi_{0.98}Fe_{0.02}O_3$. lower a): interface roughness vs. laser energy density (red and black symbols) for $SrTi_{0.98}Fe_{0.02}O_3$. Dashed lines are a guide to the eye. b): Rocking curves of the $(002)_{STO}$ reflection for $SrTi_{0.98}Fe_{0.02}O_3$ films grown at varying laser energy density at 0.025 mbar p_{O_2}.

tering and reduces the impinging flux on the substrate. The scattering probability is energy dependent, and therefore the stoichiometry of the impinging plume is influenced as well since different particles in the plume (Sr, Fe, Ti, O and clusters of these constituents) have different kinetic energies.
The interfacial roughness $\rho_{interface}$ between substrate and film is a measure for the kinetic energy of the plume, since it is related to the amount of sputtering induced by impinging particles or implantation of the same. The $\rho_{interface}$ as measured by XRR is shown in the bottom left box of figure 4.5 as a function of E at 0.25 mbar (red symbols) and 0.025 mbar (black symbols) p_{O_2}, and the pressure dependence is plotted vs. the top x-axis (blue symbols). For the latter, the observable trend is similar to that of the deposition rate, demonstrating that the mean free path is the pivotal physical parameters as well. In contrast to the deposition rate, $\rho_{interface}$ increases with increasing E in a non-linear way. This can be attributed to the energy transfer from the laser pulse to the plume. While the interface roughness shows a strong dependence on E, the surface roughness is generally low for all samples investigated in this series. As an example, the RMS roughness of the samples showing the highest $\rho_{interface}$ is $\sim$0.3 nm.
Figures 4.3 and 4.5 point out the close correlation between laser energy density and deposition pressure, since both deposition rate and interface roughness are strongly dependent of E and p_{O_2}. The conclusion is that both E and p_{O_2} influ-

ence the energy distribution of the particles leaving the target and traveling to the substrate surface. The interplay between the controllable deposition parameters and the physical quantities governing thin film growth is non-trivial and correlations are strong. The gas pressure determines the amount of molecules which are present in the path from target to substrate which scatter the ablated particles, and increasing p_{O_2} reduces the average particle energy and the flux to the substrate. The laser energy arrives in a pulse with a duration of 25 ns, and therefore interacts with the ablated particles during this time. The energy that is absorbed by the plume increases the average particle velocity, while a higher amount of total energy will at the same time ablate more material. The systematic influence of both E and p_{O_2} can be interpreted in this way. Increasing E and decreasing p_{O_2} leads to a higher deposition rate since more particles are ablated and less particles are scattered during the flight, respectively, while the roughness of the interface as measured by XRR increases.
A simple way to minimize the correlations is to work at high p_{O_2} values (0.25 mbar), since the particle-particle scattering will dominate the energy distribution of the impinging flux. As a coarse estimation of the mean free path $\lambda = 6.7 \cdot 10^{-3}$/p (mbar) can be used, yielding $\lambda(0.25\text{ mbar}) = 0.03$ cm and $\lambda(0.0025\text{ mbar}) = 2.7$ cm. Considering that the distance from target substrate d_{TS} is ~ 6.5 cm, it becomes clear that for 0.25 mbar ($\lambda << d_{TS}$) the impinging particles will be thermalized ($\bar{E}_{kin} \approx$ kT), while for $\lambda \approx d_{TS}$ the kinetic energy will be strongly dependent on the energy transfer from the laser pulse. Changing the laser energy density E shows no measurable effect on crystal quality while inducing changes in the c-axis of the unit cell, which points to the E-dependent incorporation of point-defect like Sr- or Ti-vacancies in the lattice. In contrast, a change from low to high p_{O_2} induces lattice relaxation in homoepitaxial growth that is accompanied by an increase in extended defects such as dislocations or stacking faults that broaden the half-width of the rocking curve. The latter is likely related to a reduction in surface diffusion length of the particles on the substrate surface, and probably also to the degree of association of the plume particles. The high statistical number of particle-particle interaction increases the probability of anion-cation collisions and therefore that of the formation of associates, atomic chains or clusters in the gas phase.

4.1.2 Strain Relaxation

The deformation of the unit cell induced by the coherent growth mode accumulates strain energy in the film as the film thickness increases. A common mechanism to relax growth stress is the inclusion of misfit-dislocations at the film-substrate interface, creating a partially strained interface and a relaxed thin film. The critical thickness t_c depends on the lattice mismatch of substrate and film, the mechanical

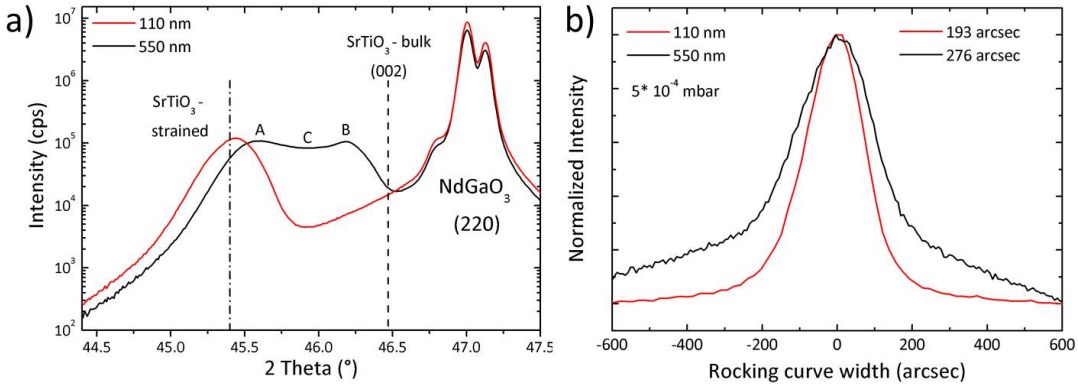

Figure 4.6: a): Diffraction pattern of $(002)_{STO}$ and $(220)_{NGO}$ of films grown at $5{\cdot}10^{-4}$ mbar p_{O_2}. Diffraction angles for coherently strained $SrTiO_3$ and bulk $SrTiO_3$ are indicated by dash-dot and dashed lines, respectively. A, B and C marks different strain states of the lattice. b): rocking curve width of the $(002)_{STO}$ reflections.

properties of the growing film such as Youngs modulus **E**, and also to a certain extend on the growth conditions. Growth temperatures that exceed the activation energy for cation transport enable the movement and formation of dislocations, favoring the relaxation of growth strain, while lower temperatures generally mean that the cation lattice is immobile. In oxidic materials, the movement of dislocations is strongly suppressed due to the high ionicity (and high strength) of the atomic bonds, which results in materials with generally high hardness and low fracture strength. For low growth temperatures, self-healing effects of the lattice through out-of-plane cation diffusion are suppressed, which means that coherently strained layers close to the interface stay strained even when the lattice relaxes close to the surface. This is illustrated in figure 4.6 a) with two films of $SrTi_{0.98}Fe_{0.02}O_3$ grown at a low gas pressure of $p_{O_2} = 5{\cdot}10^{-4}$ mbar. Since the inclusion of higher dimensional defects is not favorable at low pressure, the structure of the $SrTi_{0.98}Fe_{0.02}O_3$ film is dominated by the strain induced through coherent growth even up to a thickness of $\sim$ 110 nm. Increasing the film thickness by a factor of 5 causes the lattice to relax due to the accumulated strain. The diffraction pattern of the relaxed film indicates the presence of two separate regions with a different lattice constant, the first corresponding to a strained lattice ($a_A = 3.941$ Å, labeled A in figure 4.6) and the second to a relaxed lattice ($a_B = 3.926$ Å, labeled B). In addition, the region marked C can be attributed to the presence of a relaxation region with a gradual transition from a_A to a_B.
There are be two possible explanations for the different lattice constants, namely regions in a different strain state or regions that are chemically different. The latter is unlikely since the out-of-plane movement of cations is suppressed at the growth temperature of 700°C, and should also be observed in thinner films, but

this distinction cannot be made based on diffraction experiments alone. One of

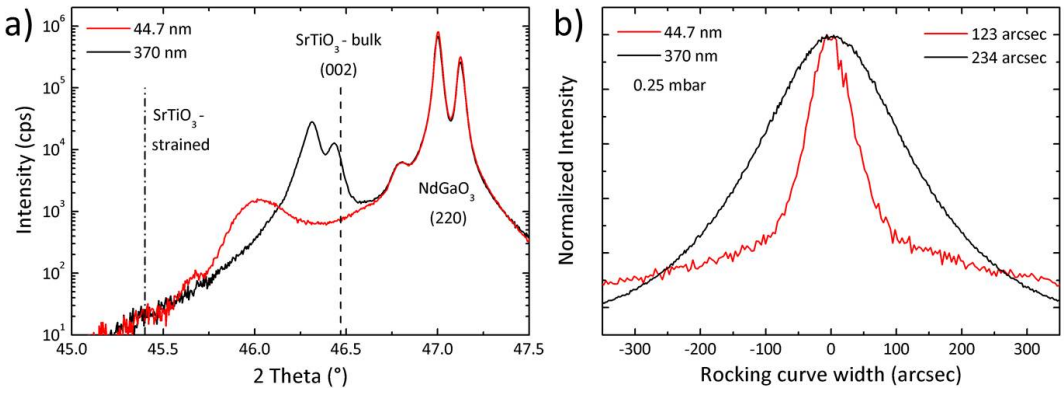

Figure 4.7: a): Diffraction pattern of $(002)_{STO}$ and $(220)_{NGO}$ of films grown at 0.25 mbar p_{O_2}. Diffraction angles for coherently strained $SrTiO_3$ and bulk $SrTiO_3$ are indicated by dash-dot and dashed lines, respectively. b): rocking curve width of the $(002)_{STO}$ reflections.

the arguments in favor of the theory of inhomogeneous strain states in the lattice is that the relaxation can be significantly influenced by the deposition pressure. Figure 4.7 a) shows a similar comparison for a thin (44.7 nm) and a thick (370 nm) film grown at a high p_{O_2} of 0.25 mbar. Already the thinner film grows in a partially relaxed strain state, while the lattice of the thicker film has almost completely relaxed to bulk $SrTiO_3$ values. There is only one strain state present in the lattice, which means that the strain relaxation takes place directly at the interface or within the first few layers of the film. The fact that the film lattice is efficient enough as a diffraction grating to separate the $K\alpha_1$ and $K\alpha_2$ spectral contributions of the x-ray beam also implies that the strain is homogeneous over the whole film thickness (figure 4.7 a)). In comparison, the thick film grown at low pressure (figure 4.6 a)) does not resolve the spectral components, likely because the peak broadening induced by the inhomogeneously distributed strain is too large. For the thinner films grown at both low and high pressure, the film thickness itself is the source of the peak broadening. However, the half-width of the respective rocking curves is smaller for the film grown at high pressure, which is another indication of increased long-range order in the lattice due to a homogeneous strain state.

To assert that out-of-plane cation diffusion truly is suppressed at the growth temperature of 700°C, a $SrTi_{0.99}Fe_{0.01}O_3$ film with an inhomogeneous strain state was subjected to annealing steps of 8 hours duration and subsequently higher temperatures (500°C, 600°C, 700°C, 750°C, 800°C, 850°C, 900°C, 950°C) in air (see figure 9.3 for complete data). After deposition at 0.25 mbar p_{O_2}, the $(002)_{STO}$ reflection (see figure 4.8 a)) is composed of two components, which in turn consist of the contributions from the Cu $K\alpha_1$ and $K\alpha_2$ radiation. This indicates the presence

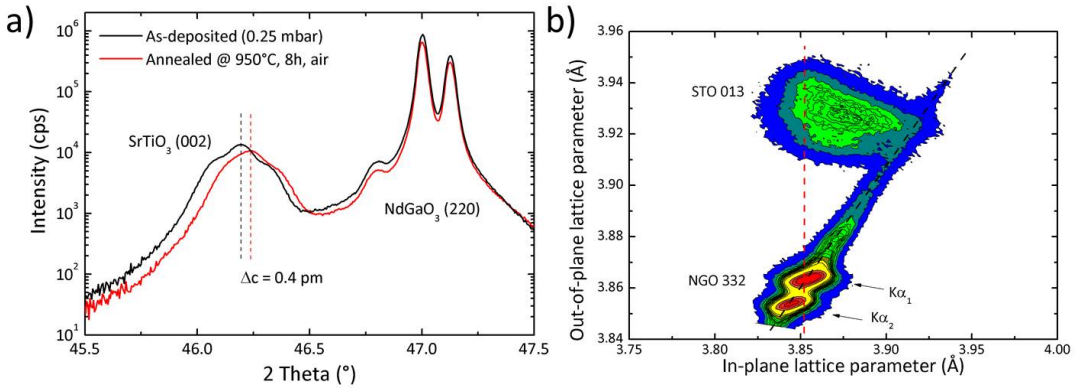

Figure 4.8: Left: Diffraction pattern of $(002)_{STO}$ and $(220)_{NGO}$ of a $SrTi_{0.99}Fe_{0.01}O_3$film grown at 0.25 mbar p_{O_2}, as-deposited (black line) and annealed at 950°C for 8 hours in air (red line). Right: Reciprocal-space map (RSM) of the $(332)_{NGO}$ and $(013)_{STO}$ reflections after deposition.

of at least two regions of different strain ϵ, probably with an intermediate region similar to that visible in figure 4.6 but with smaller differences in ϵ due to the high growth pressure. The inhomogeneity of the strain is confirmed by reciprocal space mapping of the $(013)_{STO}$ reflection (see figure 4.8 b)), which is significantly broadened compared to a coherently strained lattice (refer to figure 4.3 e)). The dashed red line indicates the direction of coherent strain in reciprocal space (a_{STO} = a'_{NGO}), whereas the black dashed line indicates the direction of full strain relaxation in a cubic system (a_{STO} = c_{STO}). It is obvious that the strain in the lattice ranges from the coherently strained values to the fully relaxed values after growth, while being mostly intermediate between the two.

After each annealing step, the out-of-plane lattice parameters was examined by a symmetrical $(00l)$ scan. No change of the position or shape of the $(002)_{STO}$ reflection was found up to an annealing temperature of 900°C. After annealing at 950°C, a small shift of the center of gravity of the diffraction peak is found, corresponding to an average decrease of the c-parameter of $\Delta c = 0.4$ pm. At the same time, the distinct three-pronged shape of the peak appears slightly softened after annealing, indicating a more gradual transition between the strained regions. It follows that for annealing temperatures of 950°C, cationic diffusion takes place in the lattice and can relax growth-induced strain by the annihilation of any Frenkel or Schottky disorder present in the lattice, by the formation of shear-planes or the creation and movement of dislocations.

Since both strain relaxation and chemical demixing are temperature activated processes, it is necessary to examine the film structure in closer detail to establish the dominant process. Figure 4.9 a) shows the diffraction pattern of a $SrTi_{0.9}Fe_{0.1}O_3$ film (t = 270 nm) after deposition (blue) and after annealing in Ar/4% H_2 at 700°C for 1h (black) and at 950°C for 2h (red). The as-deposited film shows a

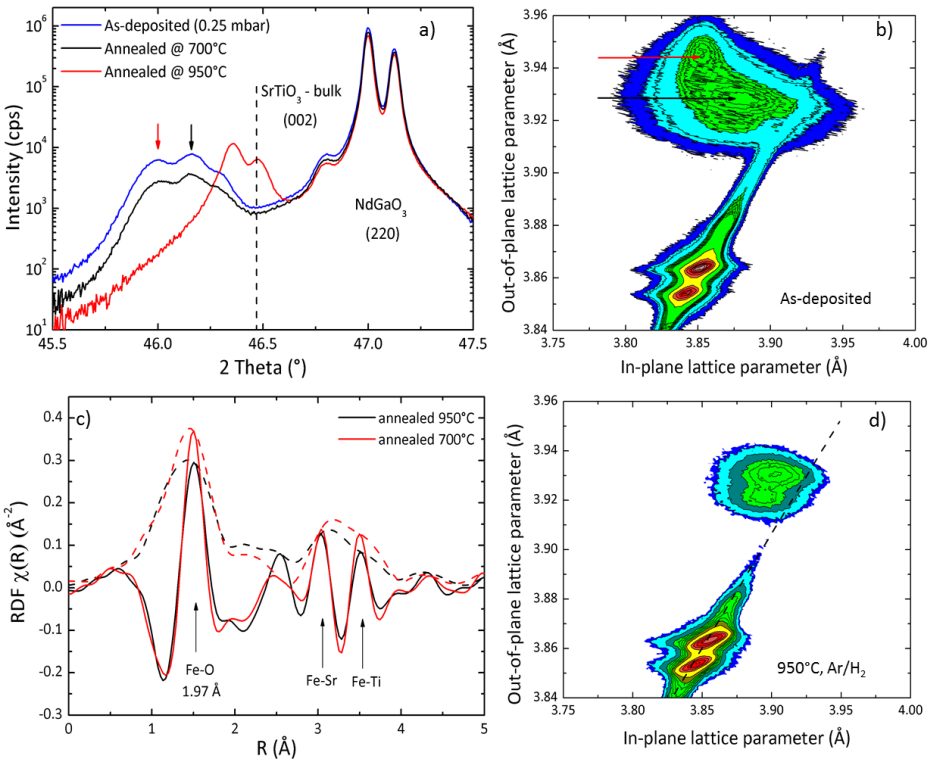

Figure 4.9: a) Diffraction pattern of the $(002)_{STO}$ reflection of $SrTi_{0.9}Fe_{0.1}O_3$ after deposition (blue) and after annealing in Ar/H_2 at 700°C for 1h (black) and 950°C for 2h (red). b) and d): RSM of the $(013)_{STO}$ reciprocal lattice point, showing the strain state after annealing. c): RDF of the Fe K-edge after annealing. The local environment of Fe seems unchanged at least up to the third coordination shell ($\sim$ 4Å).

very similar diffraction pattern as that seen in figure 4.8 for $SrTi_{0.99}Fe_{0.01}O_3$, albeit with a more pronounced contribution of the strained lattice (marked by the blue arrow). The RSM of the $(013)_{STO}$ reflection (figure 4.9 b)) shows one reciprocal lattice point of a strained $SrTi_{0.9}Fe_{0.1}O_3$ state ($a_{STO} = a'_{NGO}$, $c_{STO} = 3.94$ Å), and a relaxed state with $a_{STO} = 3.88$ Å and $c_{STO} = 3.928$ Å. The corresponding features in figure 4.9 a) and b) are marked with a red arrow (strained) and a black arrow (partially relaxed). The significant broadening of these points (compare the sharp $NdGaO_3$ reciprocal lattice points) shows again that the strain is not uniform and shows a broad distribution.
After annealing, the symmetrical diffraction pattern shows a single diffraction peak that is shifted by 0.2° 2Θ (red curve), and the RSM depicted in d) likewise shows only one single reciprocal lattice point. From diffraction, it is readily apparent that the two distinct strain states have been replaced by a single, relaxed strain state with a bulk-like in-plane lattice parameter $a_{STO} = 3.903$ Å and an elongated c-axis with $c_{STO} = 3.93$ Å. To complement the information on the long range

order in the crystal lattice, the Fe K-edge EXAFS has been measured after both annealing steps to obtain information about the short range order. The radial distribution function (RDF) of both samples peak at identical R-values, which is a good indication that the Fe-O, Fe-Sr and Fe-Ti distance in both samples is the same (figure 4.9 c)). The Fe-O distance has been evaluated via a first-shell fit to $d_{Fe-O} = 1.97 \pm 0.008$ Å, which is similar to that found in the cathodic region of an electrocolored single crystal and hints at the presence of Fe^{3+} as the most prominent Fe center. The Fe-O distance does not change after annealing, however, while the lattice parameter is clearly altered. This is proof of the fact that the structure observed with diffraction is a consequence of heteroepitaxial strain in the lattice, and that the change of the lattice parameters after high temperature annealing is related to strain relaxation and not chemical demixing, even for Fe-content as high as 10% site-fraction. A chemical demixing, like a precipitation of an Fe-rich phase, would affect the Fe-O distance since the structure of the precipitate would be different from that of the matrix. The characteristic shape of the Fe K-edge EXAFS in $SrTi_{0.9}Fe_{0.1}O_3$ films is very similar to that of Fe in $SrTiO_3$ single crystals, therefore it seems unlikely that such precipitates exist already after deposition. It should be noted at this point that annealing experiments done in air and Ar/4% H_2 yielded the same lattice relaxation effects, and that subsequent annealing of the same sample in reducing and oxidizing atmosphere did not change the lattice relaxation. Therefore the relaxation is temperature related and not redox-based. The fact that annealing in Ar/4% H_2 at 700°C did not influence the strain state of the lattice at all supports the argument that the lattice relaxation is not dominated by oxygen exchange at the surface, but internal relaxation processes. Annealing of the $SrTi_{0.99}Fe_{0.01}O_3$ films at 1050°C in air did not change the lattice relaxation achieved by a previous anneal at 950°C in Ar/4% H_2.

4.1.3 Strain Engineering: Influence of the Substrate

In any given epitaxial growth process, the substrate quality plays an important role for the quality of the deposited film. Defects in the crystal surface are preferred nucleation sites for growth and will be transfered into the film. In the case of heteroepitaxy, the substrate-film lattice mismatch determines the growth strain and can be tailored by the choice of substrate material. However, using stepped crystal surfaces for epitaxial growth introduces an additional complication. Figure 4.10 shows the symmetric (002) and asymmetric (013) reflexes of two $SrTi_{0.99}Fe_{0.01}O_3$films grown with the same process parameters ($p_{O_2} = 0.25$ mbar, $E = 1.3$ J/cm^2, t $\sim$ 270 nm). It is apparent that one of the films is partially strained due to the heteroepitaxial growth while the other was grown in a relaxed strain state. Both films were grown on (110)-terminated $NdGaO_3$ crystals with a

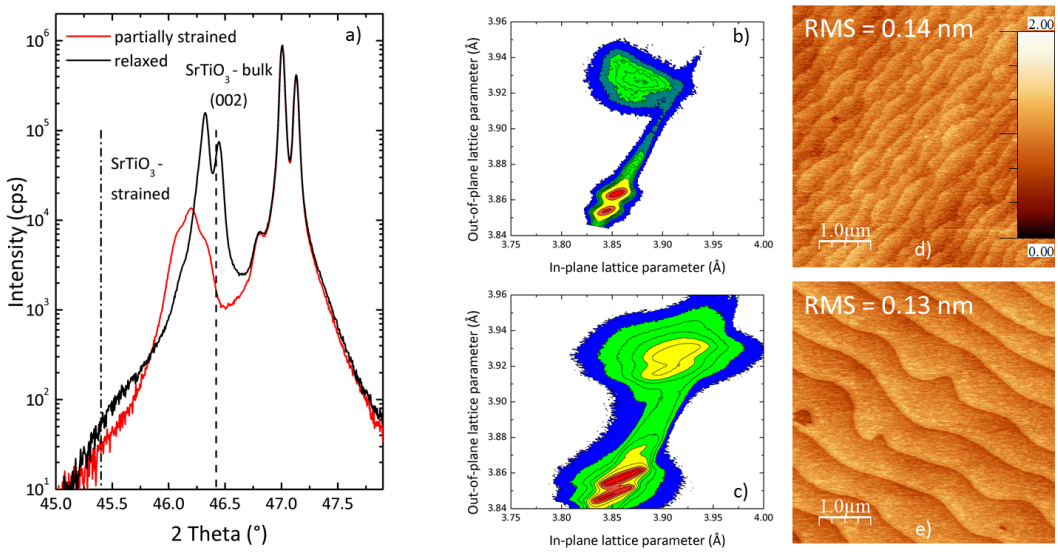

Figure 4.10: a): Diffraction pattern of the $(002)_{STO}$ reflection of two $SrTi_{0.99}Fe_{0.01}O_3$films after deposition at identical process conditions. RSMs of b) the strained and c) the relaxed film, and the corresponding AFM images of the substrate before deposition d) and e), respectively.

stepped surface structure. The miscut-angle α of the two crystals can be evaluated as $\tan\alpha = d/l$, where d and l are the step height and length, respectively. The average step length of the two crystals are 300 nm for the partially strained film and 480 nm for the relaxed film, corresponding to $\alpha = 0.074°$ and $0.047°$, respectively. This phenomenom is observed independent of Fe-concentration or laser energy density, which points to the fact that the step length can have an influence on the lattice relaxation. Without monitoring the atomic processes during growth, it is impossible to establish the exact mechanism. However, the most probable explanation is related to the surface diffusivity of the adatoms and the density of step-sites. Bonding sites with more than one next neighbor are energetically favorable and diffusing adatoms are preferentially trapped there. The length of a terrace determines the probability of an atom impinging at a random location to reach a favorable site at a step edge, and therefore heterogenuous nucleation at step edges is preferred for a high density of step sites. Nucleation at step edges can, in special cases, lead to step-flow growth and favors layer-by-layer growth since the density of nuclei on the steps is smaller. In contrast, large terrace lengths favor homogeneuous nucleation on sites with only one nearest neighbor since fewer adatoms can reach a step site, which in turn favors a 3-dimensional growth mode (island growth). The influence of the step density on the growth mode is not intuitive and hard to quantify without dedicated experiments. How-

ever, it appears that the strain relaxation in the thin film can be influenced by the choice of miscut-angle of the substrate, with high α favoring strained films and low α favoring relaxed films.

4.2 Homoepitaxy: Influence of Iron Concentration

Since Fe is a B-site acceptor dopant in $SrTiO_3$, the dopant concentration influences the electronic structure of the $SrTi_{1-x}Fe_xO_3$ thin films. It will be demonstrated in 5.3.1 that this is indeed the case, although oxygen vacancies remain the dopant with the highest concentration and influence the electronic structure much more strongly than Fe. However, adding Fe to the $SrTiO_3$ targets influences the deposition process of homoepitaxial thin film in a way that will be phenomenologically analyzed.
The laser energy is coupled into the target material via electronic excitations, which are then converted into thermal energy [65]. The energy of a $\lambda = 248$ nm photon can be calculated through $E = hc/\lambda$ (h: Planck's constant, c: speed of light) to E = 5 eV. It is clear that the main mechanism of absorption in $SrTiO_3$ is band-gap excitation across the direct band-gap (3.75 eV according to [27]). Doping Fe into $SrTiO_3$ introduces a variety of states both in the top of the valence band and in the band-gap, increasing the density of occupied states that is within 5 eV of the bottom of the conduction band [36]. A higher DOS enhances the absorption, reducing the attenuation length of the radiation in the target and causing the laser energy to be absorbed in a smaller volume of material. This is visible as a decrease in deposition rate with increasing Fe-content, as seen in figure 4.11 a). The non-linearity of the decrease agrees with a change in the linear absorption coefficient $\mu = d \ln I/dx$. At the same time, the average plume velocity of $SrTi_{0.98}Fe_{0.02}O_3$ ablated targets has been found to be increased with respect to $SrTiO_3$ targets [66]. This confirms a change in the average particle energy in the plume, which is likely due to the increased energy density in the ablated volume, and also to the stronger interaction of the laser beam with the plume.
A second effect of Fe-doping on film growth is shown in figure 4.11 b). The $(002)_{STO}$ reflection of $SrTi_{1-x}Fe_xO_3$(x=0.005, 0.01, 0.02, 0.05) thin films deposited on (001)-cut Nb-doped $SrTiO_3$ at identical process conditions (0.25 mbar, 0.8 J/cm^2, 700°C) demonstrates the increasing elongation of the unit cell c-axis with increasing Fe-content. Interestingly, the unit cell distortion shows two regions, with a steep increase below 1% Fe and a more shallow increase above 1%. This relaxation could be related to a transition from layer-by-layer growth at low x to pseudo-island growth mode at x > 1% [67]. Considering that varying the laser energy density in the deposition of $SrTiO_3$ influences the unit cell volume through the introduction

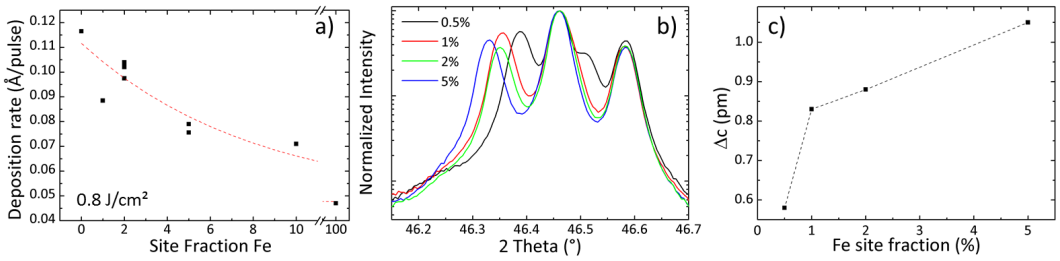

Figure 4.11: a): Deposition rate vs. Fe-concentration in the target, given in % site fraction. The dashed red line is an exponential fit that includes the deposition rate for $SrFeO_3$. b): $(002)_{STO}$ reflections demonstrating the systematic c-axis elongation, with the quantification given in c).

of point defects, and that the above considerations show that the Fe-content directly influences the energy density since less material is ablated with each pulse, it is likely that the c-axis elongation observed is connected to the introduction of point defects through a change in plume chemistry or energy distribution. It might also be worth investigating the opening angle of the plasma plume, since small stoichiometry changes have been found for off-axis and on-axis deposition of $SrTiO_3$ on $NdGaO_3$ [68].

Chapter 5

Influence of Fe-Doping in $SrTiO_3$

According to defect chemistry, the mixed valence (Fe^{3+}/Fe^{4+}) character of Fe in $SrTiO_3$ creates a charge imbalance with respect to the neutral lattice, which is compensated by the creation of oxygen vacancies to conserve charge neutrality [19]. Redox-type reactions of the crystal affect the balance between Fe^{3+} and Fe^{4+}, and therefore the oxygen vacancy concentration in the material. It has been shown that such redox reactions, induced by thermal treatment under oxidizing or reducing atmosphere, influence the X-ray absorption near-edge structure (XANES) of transition metal dopants, while the XANES of the Ti K-edge remains unchanged [34]. The strong ionicity of the constituent species makes $SrTiO_3$ susceptible to chemical changes induced by an electric field [20, 69], resulting in a concentration polarization of oxygen vacancies that is visible as a color-change taking place at anode and cathode (electrocoloration) [70]. Since the oxidation state of Fe is known from optical absorption, such a crystal is ideally suited to study the spectroscopic "footprint" of the valence states of Fe in $SrTiO_3$.
The first part of this chapter was published in Phys. Chem. Chem. Phys. [76]

5.1 Fe-doped Single Crystal after Electrocoloration

A 0.2 wt-% Fe-doped $SrTiO_3$ single crystal was electrocolored using two Au-electrodes evaporated onto the (001)-oriented, polished crystal. A constant current was increased stepwise from 1 nA to 0.1 mA over the duration of 2 weeks, until finally a breakdown in resistance occurred and a current of 10 mA flowed. The crystal was kept at a temperature of 300°C at a vacuum pressure of 10^{-9} mbar. The coloration of the crystal is depicted in Fig. 5.1, along with an indication of the anodic and cathodic regions that were investigated in this work. After XAFS and Raman measurements, the crystal was cut into slices for the EPR spectrometer. The generally accepted model of electrocoloration in Fe-doped $SrTiO_3$ is based on the field-driven migration of oxygen vacancies and the corresponding chemical changes at the Fe centers that give rise to the color change [70]. In the low concentration (dilute) regime where the Fe centers can be considered as isolated, a set of equations can be used to describe the defect equilibria in the ionic crystal. Of special interest for this section are the conservation conditions [19]:

$$[\mathrm{Fe}]_{\mathrm{tot}} = [\mathrm{Fe}^{3+}] + [\mathrm{Fe}^{4+}] \tag{5.1}$$

$$2[\mathrm{V}_{\mathrm{O}}^{\bullet\bullet}] + [h] = [\mathrm{Fe}^{3+}] + [e]. \tag{5.2}$$

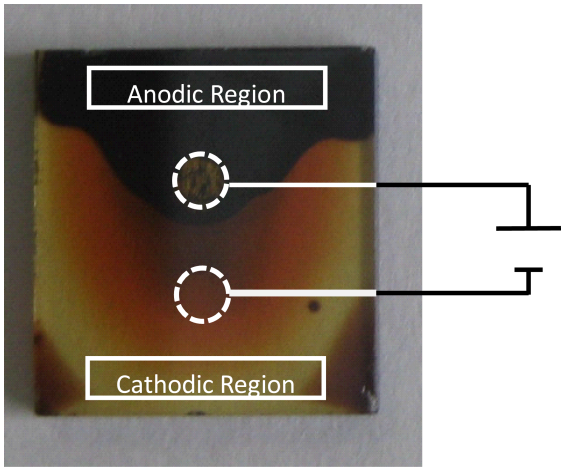

Figure 5.1: Optical photograph of the electrocolored Fe-doped $SrTiO_3$ single crystal. The white rectangles indicate the anodic and cathodic regions used in the analysis.

In particular, the weak band-gap excitation (no free charge carriers) under moderate oxygen partial pressures (intrinsic regime) allows the simplification of eqn (5.2):

$$2[V_O^{\bullet\bullet}] \approx [Fe^{3+}]. \tag{5.3}$$

This charge neutrality condition imposes some constraints on the defect structure that can be present in the material. Most notably, even under completely reduced conditions, eqn (5.3) demands that the oxygen vacancy concentration will not be more than half of the total Fe concentration, assuming that every Fe center has been reduced to Fe^{3+} and that other mechanisms of charge compensation can be neglected. For strongly reduced crystals, the charge neutrality condition has to be expanded to accommodate the compensation of oxygen vacancies by free electrons [71], causing the appearance of Ti^{3+} ions through the occupation of conduction band states. To verify the validity of eqn (5.3) for the present work, it is necessary to monitor the chemical changes induced by the electrocoloration at both the Fe- and Ti-site. Since there is no observable change in the Ti K-edge XANES and the average Ti–O bond distance as extracted from EXAFS data is identical (1.946 ± 0.005 Å) in the anodic and cathodic region within the measurement uncertainty (Fig. 5.2), it follows that the oxidation/reduction process takes place preferentially at the Fe-site and that the changes at the Ti-site are too low to be detectable. Therefore, the following sections are concerned with the structural and chemical changes at the Fe-site induced by the electrocoloration process, and eqn (5.3) will be regarded as valid.

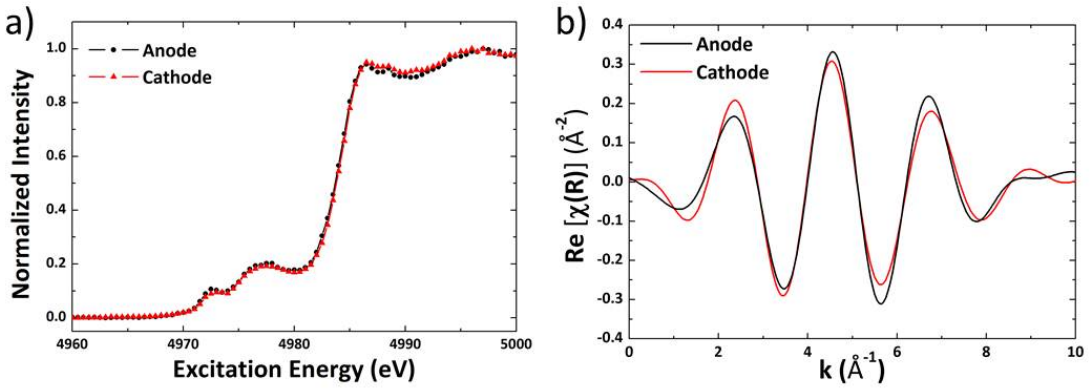

Figure 5.2: a): XANES of the Ti K-edge from the anodic (black circles) and cathodic (red triangles) regions of the electrocolored Fe-doped $SrTiO_3$ single crystal. b) Ti K-edge EXAFS of the 1st shell, isolated by back-Fourier transformation (BFT), of the corresponding regions. EXAFS was isolated via Fourier transformation (FT) in the k-range 2-8.4 Å^{-1}, then BFT in the R-range from 1-2 Å.

5.1.1 Raman Spectroscopy

Micro-Raman spectra were collected by A. Kuzmin, at 20°C using a confocal microscope with spectrometer Nanofinder-S (SOLAR TII, Ltd.).[72] The measurements were performed through a Nikon Plan Fluor 40× (NA = 0.75) optical objective. The Raman spectra were excited by a He-Cd laser (441.6 nm, 50 mW cw power) and dispersed by 600 grooves/mm diffraction grating mounted in the 520 mm focal length monochromator. A Peltier-cooled back-thinned CCD camera (ProScan HS-101H, 1024×58 pixels) was used as a detector. The elastic laser light component was eliminated by an edge filter (Omega, 441.6AELP-GP).
Since $SrTiO_3$ at room temperature has a cubic structure (space group $Pm\bar{3}m$) with a center of inversion, the undoped crystal exhibits no first-order Raman scattering, and only second-order effects are observed in the Raman spectra. An extensive examination of the Raman spectra of oxidized and reduced $SrTi_{1-x}Fe_xO_{3-\delta}$ solid solution powders has been given in ref. [73], and the existence of a first-order Raman peak at 690 cm^{-1} has been attributed to doping with Fe^{4+} ions. In addition, three "forbidden" phonon modes have been weakly visible: LO3, TO4 and LO4 at 475 cm^{-1}, 545 cm^{-1} and 795 cm^{-1}, respectively. On the other hand, Fe^{3+} does not induce any change in the Raman spectrum with regard to that of an undoped crystal. Therefore, the appearance of the strong peak at 690 cm^{-1} can be seen as a "fingerprint" indicating the presence of Fe^{4+} in the crystal.
In the present work, Raman spectroscopy was performed close to the anode and cathode of the Fe-doped $SrTiO_3$ single crystal, using a confocal Raman microscope with a spatial resolution of 1 μm. The recorded spectrum (Fig. 5.3 a)) of

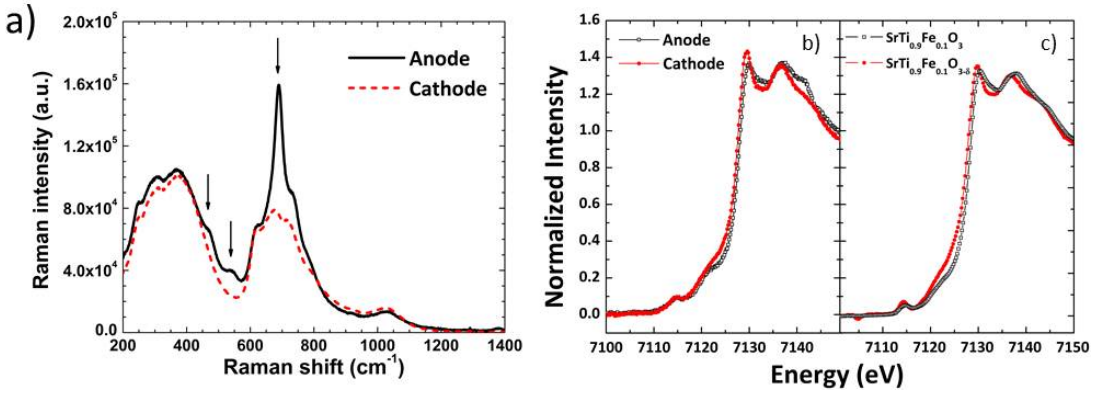

Figure 5.3: a): Raman scattering spectra from the anodic (solid black line) and cathodic (dashed red line) regions of the electrocolored Fe-doped $SrTiO_3$ single crystal. Note the developing shoulders and the pronounced peak indicated by the arrows. b): Fe K-edge XANES spectra from the anodic (black, open squares) and cathodic (red, solid circles) regions of the electrocolored Fe-doped $SrTiO_3$ single crystal. c): Fe K-edge XANES spectra of powder solid solution $SrTi_{0.9}Fe_{0.1}O_3$, fully oxidized (black, open squares) and reduced (red, solid circles) (data from ref. [73]).

the anodic (solid black line) region shows the distinct features that characterize the oxidized $SrTi_{1-x}Fe_xO_3$ powders as described above. In the spectrum of the cathodic region (dashed red line), the additional peak as well as the weak phonon modes are notably absent, indicating that the amount of Fe^{4+} in the cathodic region is too low to be detected by Raman spectroscopy. From the Raman data, we can conclude that the cathodic region does not contain significant amounts of Fe^{4+}, while the anodic region contains predominantly Fe^{4+}.

5.1.2 X-ray Absorption Near Edge Structure - XANES

XAFS experiments were performed at beamlines BM29 (ESRF, Grenoble) and A1 (HASYLAB, Hamburg). X-ray absorption near edge spectroscopy (XANES) and extended X-ray absorption fine structure (EXAFS) were measured in fluorescence step-by-step (single crystal) and transmission mode (powder references) using monochromatic X-ray radiation, using a Si(111) double-crystal monochromator with an energy resolution of $\Delta E/E < 10^{-4}$ at 7000 eV photon energy. The size of the beam at the sample was typically $1{\times}8$ mm^2. XANES of the Fe K-edge (Ti K-edge) spectra were typically recorded within an interval of 100 eV (50 eV) around the absorption edge, with a constant energy step of 0.5 eV (0.2 eV). The Fe K- and Ti K-edge EXAFS spectra were recorded using an optimized energy mesh with a step of 0.2 eV around the absorption edge and a constant Δk step far

above the edge. The EXAFS data treatment and fitting was done using the EDA [74] and the ARTEMIS [57] software packages. The XANES region of the absorption edge was extracted by background subtraction and normalization to 100 eV above the edge. The EXAFS signal was extracted up to $k = 10$ Å^{-1} after standard background subtraction, and the single-scattering contributions of the first shell were isolated by back Fourier transformation (BFT) in the interval 0.8-2.1 Å. The single-shell fitting of the EXAFS spectra was done using the single-scattering curved-wave formalism in k-space after BFT. In this paper, the EXAFS data were analyzed using two different approaches: the backscattering phases and amplitudes were either calculated by the FEFF8 code[75] or obtained experimentally from the polycrystalline reference compound $LaFeO_3$.
A comparison of the experimental Fe K-edge XANES for the cathodic and anodic regions in the Fe-doped $SrTiO_3$ single crystal (Fig. 5.3 b)) indicates that while the pre-edge peak located at 7115 eV is similar in both cases, the fine structure located at higher energies is different. In particular, the shoulder at 7123 eV is more pronounced in the cathodic region, and the main absorption edge shifts by about ∼0.5 eV to higher energies in the anodic region. Reference XANES data (from ref. [73]) of completely oxidized and reduced $SrTi_{1-x}Fe_xO_{3-\delta}$ solid solution powders show an almost identical shift of the main absorption edge (Fig. 5.3 c)). Comparing the XANES data for the single crystal to the reference data, it is obvious that the changes taking place during electrocoloration affect the valence state of the Fe atoms in a reduction/oxidation process, leaving Fe centers predominantly oxidized in the anodic region and reduced in the cathodic region. Deeper understanding of the Fe K-edge XANES signals has been obtained using theoretical simulations, performed by A. Kuzmin (for details see [76]). The results of the XANES calculations are shown in Fig. 5.4 and are compared with the experimental data for the cathodic and anodic regions. There are four features (A, B, C, D) in the XANES signals that can be distinguished below the main absorption edge E . At the Fe K-edge, the $1s$(Fe) core-electron is excited, following dipole selection rules, into empty final-states with p-character, located above the Fermi level and being relaxed due to the presence of the positively charged core-hole. Such transitions give rise to peaks starting from B and above (Fig. 5.4). The transition of the $1s$ electron to the conduction band of cubic Fe-doped $SrTiO_3$ (peak A in Fig. 5.4), composed mainly of the $3d$-states of the Ti(Fe) ions, is forbidden in the dipole approximation. However, it becomes allowed through symmetry lowering due to the Jahn-Teller distortion,[77] the presence of an oxygen vacancy in the first coordination shell of iron or within the quadrupole approximation. Note that generally, the small cross section of the $1s \rightarrow 3d$ quadrupole transition is compensated by a high density of $3d$ states.

To conclude, we attribute a variation of the absorption intensity observed between the two experimental Fe K-edge XANES signals from the anodic and cathodic re-

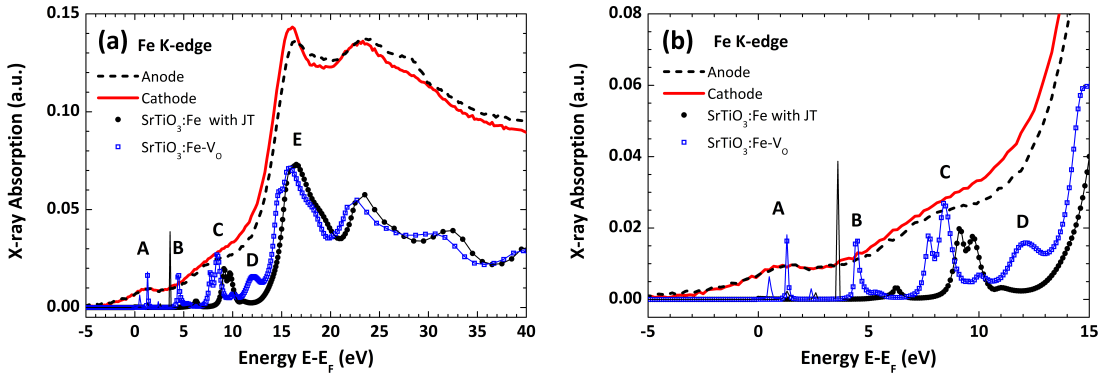

Figure 5.4: (Color online) Comparison of the experimental and calculated Fe K-edge XANES in Fe-doped $SrTiO_3$. The experimental XANES correspond to the cathode (solid red line) and anode (dashed black line) regions of the electrocolored Fe-doped $SrTiO_3$ single crystal. The calculations were performed in the dipole approximation for the two models: JT-distorted iron environment without oxygen vacancies (solid, black circles) and with a single oxygen vacancy V_O in the first coordination shell of unrelaxed iron environment (open, blue squares). The zero of the energy scale corresponds to the theoretical Fermi level E_F. Four features (A, B, C, D), located in the pre-edge region, and the main peak E are indicated. In addition, the results for calculations in the dipole plus quadrupole approximation are shown as solid lines, being completely identical to the dipole approximation except for the range of the feature A (0-4 eV).

gions of the Fe-doped $SrTiO_3$ single crystal to the appearance of an oxygen vacancy in the first coordination shell of Fe. Our interpretation of the Fe K-edge XANES in Fe-doped $SrTiO_3$ agree with that by Janousch et al.[5] for Cr-doped $SrTiO_3$, where it was shown, using density functional theory (DFT) calculations, that the presence of an oxygen vacancy in the octahedron surrounding the chromium atom leads to an increase of the Cr $4p$ density of states and, thus, increases absorption in the chromium K-edge XANES below the main absorption edge.

5.1.3 Extended X-ray Absorption Fine Structure - EXAFS

The experimental EXAFS $\chi(k)k$ spectra for the anodic and cathodic regions are shown in Fig. 5.5 a). Their Fourier transforms (FTs) (Fig. 5.5 b)) indicate a change of the first peak position (better seen in the imaginary part of FTs) at $\sim$1.4 Å due to the first coordination shell of iron. At the same time, the position of the second and third coordination shells (peaks in the region 2.5-4 Å, Fig. 5.5 a)) remains unchanged. This suggests that the electrocoloration process induces a difference in the average Fe–O bond distance in the anodic and cathodic regions of the single crystal.

The fitting results obtained (as described above) with experimental phase and amplitude are presented in table 5.1. As one can expect from the Shannon radii of iron ions ($r(Fe^{3+})$ = 0.645 Å, $r(Fe^{4+})$ = 0.565 Å), the Fe^{3+}–O bond length as extracted from EXAFS of Fe^{3+}–O in $LaFeO_3$ (1.994±0.005 Å) is significantly longer than that of Fe^{4+}–O in $SrFeO_3$ (1.925 Å).[78] Using the experimental phase and amplitude for the fitting procedure, we observe that the Fe–O bond distance in the anodic part of the crystal (1.932 Å) is very close to the distance of the fully oxidized $SrTi_{0.9}Fe_{0.1}O_3$ powder reference (1.931 Å). In addition, the large MSRD value for both spectra is characteristic of the Jahn-Teller distortion around Fe^{4+} (d^4 configuration) in $SrTiO_3$.[73] From the EXAFS and XANES analysis as well as Raman, it follows that Fe is predominantly tetravalent in the anodic region, albeit with a small admixture of Fe^{3+} (cubic center, d^5 configuration) as shown by EPR (see section 5.1.4).

Table 5.1: Best-fit structural parameters (N is the coordination number, R is the interatomic distance, and σ^2 is the mean-square relative displacement (MSRD)) for the first coordination shell of iron obtained from the analysis of the Fe K-edge EXAFS spectra using experimental backscattering phase and amplitude functions extracted from $LaFeO_3$.

	$SrTi_{0.9}Fe^{4+}_{0.1}O_3$	$SrTi_{0.9}Fe^{3+}_{0.1}O_{2.95}$	Anode	Cathode
N	5.4 ± 0.1	5.0 ± 0.1	5.7 ± 0.1	5.4 ± 0.1
R (Å) ±0.005	1.931	1.955	1.932	1.972
σ^2 (Å^2)± 0.0005	0.0094	0.0072	0.0098	0.0056

In contrast, the Fe–O bond length in the cathodic part (1.972 Å) is 4 pm longer than in the anodic region, while the MSRD decreases significantly. The EPR and Raman results show the existence of cubic Fe^{3+} centers in this region, with an admixture of Fe^{3+}–$V_O^{\bullet\bullet}$ complexes, and no Fe^{4+}. The Fe^{3+}–O distance in reduced $SrTi_{0.9}Fe_{0.1}O_{2.95}$ (1.955 Å) is intermediate between that in $SrTi_{0.5}Fe_{0.5}O_{2.5}$ (1.960 Å)[73] and the Ti–O distance in $SrTiO_3$ (1.951 Å), while the Fe–O distance in the cathodic region of the single crystal is significantly longer. In addition, the slightly larger MSRD value observed in $SrTi_{0.9}Fe_{0.1}O_{2.95}$ compared with the cathodic part suggests a larger distortion in the first coordination shell around Fe^{3+} in the reduced solid solution.

5.1.4 Electron Paramagnetic Resonance - EPR

Owing to its strong EPR signal and the fact that Fe is always present in $SrTiO_3$as an impurity, the EPR signal of Fe^{3+} ions in $SrTiO_3$has been the subject of a number of investigations (e.g. [79–81]) and has been analyzed extensively. In particular,

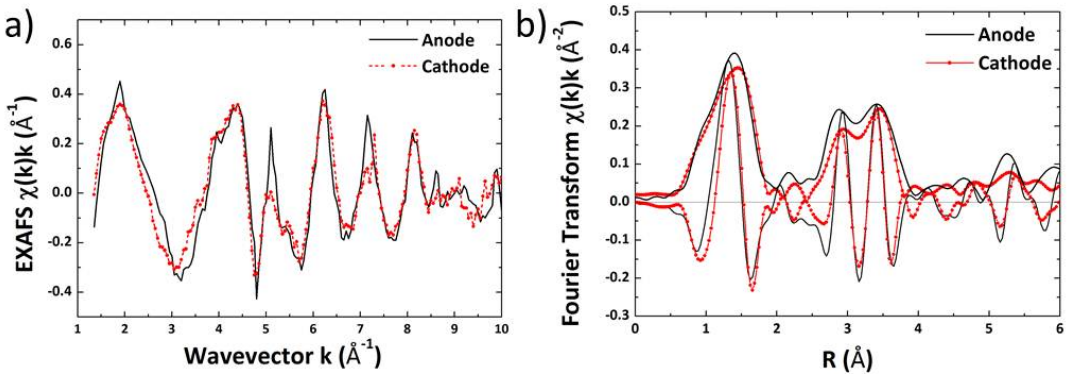

Figure 5.5: a): Experimental Fe K-edge EXAFS spectra from the cathode (solid, black line) and anode (dashed, red line) regions of the electrocolored Fe-doped $SrTiO_3$ single crystal. b): Magnitude and imaginary part of the Fourier transform of the Fe K-edge EXAFS signals shown on the left for the anodic (solid, black lines) and cathodic (red, open circles) regions of the electrocolored Fe-doped $SrTiO_3$ single crystal. The shift of the first peak at ∼1.4 Å, corresponding to the first coordination shell of iron (the Fe–O distance), is clearly visible.

EPR is well suited to distinguish between Fe'_{Ti} ions in octahedral oxygen coordination (cubic site) and Fe'_{Ti}–$V^{\bullet\bullet}_O$ complexes (axial site) because of the tetragonal distortion of the axial site. The correlation between optical absorption and the valence state of the Fe impurities has been demonstrated by Faughnan [81], showing that Fe in $SrTiO_3$is mainly trivalent.
The magnetic properties in oxides are generally governed by the exchange-interaction between magnetic nuclei mediated via the bridging oxygen ions. Prominent Fe-containing examples are the anti-ferromagnetic insulator $LaFeO_3$ (T_N 750K) and the ferri-magnetic Fe_3O_4. As a B-site substituent in $SrTiO_3$, the electronic energy levels of the Fe^{3+} ground state are split by the exchange-interaction, resulting in a high-spin (HS) d^5 configuration so that there are 5 optically allowed transitions in the d-shell: $\pm(5/2 \leftrightarrow 3/2)$, $\pm$ $(3/2 \leftrightarrow 1/2)$, $(-1/2 \leftrightarrow 1/2)$. As shown by Müller [79], the EPR signal of Fe^{3+} in a cubic site shows a strong, isotropic line $(-1/2 \leftrightarrow 1/2)$ with g = 1.979 with a second-order angular dependence, and 2 sets of lines corresponding to the $\pm(5/2 \leftrightarrow 3/2)$ and $\pm(3/2 \leftrightarrow 1/2)$ transitions. The splitting of the latter about the position of the isotropic line varies with the angle between the magnetic field and the crystallographic axis of the single crystals, as well as the crystal orientation.
Kirkpatrick et al. [80] have identified the EPR signal of Fe'_{Ti}–$V^{\bullet\bullet}_O$ complexes by oxidation-reduction experiments of Fe-doped $SrTiO_3$single crystals. They observed additional lines with $g_\perp$=5.993 and $g_\parallel$ = 2.0054 (= 3.3 cm) corresponding to the $-1/2 \leftrightarrow 1/2$ transition of Fe^{3+} in an axial site with strong tetragonal distortion. No other lines are visible due to the strong zero-field splitting induced by the local

crystal field.
The EPR spectra for this work have been recorded by D. Berzins (Riga), with a X-band ($\nu = 9.323$ GHz) spectrometer with a modulation of 100 kHz. In order to study the angular dependence, thin slices of the Fe-doped single crystal were cut along the [010]-axis and aligned with [010] parallel to the rotation axis of the spectrometer. The dimensions of each piece were about $1\times10\times1$ mm^3. The samples were mounted on the xyz orthogonal laboratory frame chosen for the EPR anisotropy pattern and related to the crystallographic axes as follows: $x \parallel [001]$, $z \parallel [010]$, $y \parallel [100]$. The presented measurements were done at room temperature, while additional measurements at liquid nitrogen temperature confirm the presented results.
Figure 5.6 a) shows the EPR spectra of Fe^{3+} of the cathodic (upper, red line) and anodic regions (lower, black line) of the doped $SrTiO_3$ single crystal, with the static magnetic field parallel to the crystallographic [010] direction. The EPR signal in the anodic region consists of a strong, isotropic central line, with 4 symmetrically split satellite lines showing an angular variation identical to that found in Ref.[79], with the isotropic g-factor of 2.00 corresponding to cubic Fe^{3+} centers and with a cubic splitting parameter of $a \sim 0.02$ cm^{-1}. The EPR signal of the cathodic

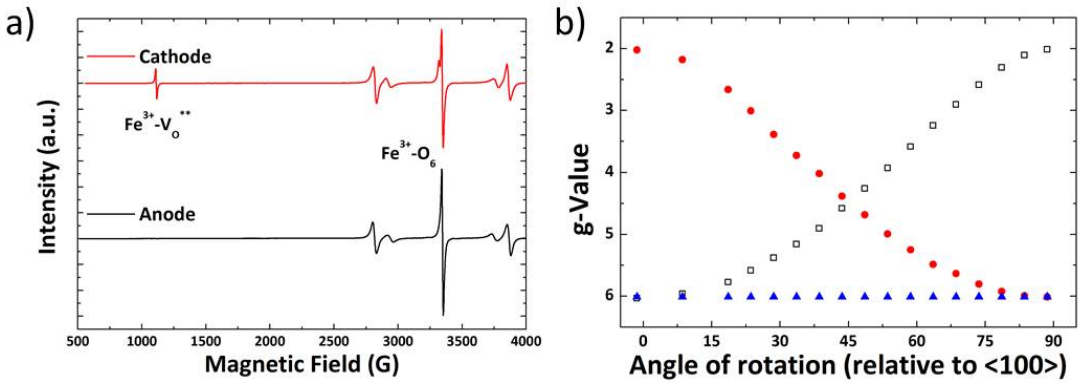

Figure 5.6: a): EPR signals of Fe^{3+} in the anodic (lower, black line) and cathodic (upper, red line) region of the electrocolored Fe-doped $SrTiO_3$ single crystal. The relative amplitude of the EPR signals is normalized to the maximum. Note that the intensity of the normalized spectra is not comparable. b): Angular dependence of the effective g-value of the axial Fe^{3+} center in the cathodic region. The angle of rotation corresponds to the angle between the magnetic field lines and the crystallographic [100] axis.

region consists of two structurally non-equivalent centers, a cubic center equivalent to that in the anodic region and an axial center with a strongly anisotropic g-factor, as is well described in the literature[35, 80]. Kirckpatrick *et* al. [80] found these lines with $g_\perp = 5.993$ and $g_\parallel = 2.0054$ to correspond to the $-1/2 \leftrightarrow 1/2$ transition of Fe^{3+} in an axial site with strong tetragonal distortion. No other

lines are visible due to the strong zero-field splitting induced by the local crystal field. The angular variation of the effective g-factor of the axial center is shown in Fig. 5.6 b), reproducing the angular dependence demonstrated by Kirkpatrick *et* al. remarkably well.
We can conclude that after the electrocoloration process, the axial Fe^{3+} center in the anodic part has disappeared almost completely, while the signal of the cubic Fe^{3+} center is decreased by about a factor of 7 ($\pm$ 1) with respect to the cathodic part. It should be mentioned that the Fe^{4+} center created in the anodic region is a "non-Kramers" ion due to the large contribution of the d^4 configuration to the ground state, and therefore does not appear in the spectra [82]. There are no other EPR-active impurity centers with significant contributions to the EPR spectra.

5.1.5 Discussion

The experimental determination of the Fe^{3+}–$V_O^{\bullet\bullet}$ concentration has been shown to be possible via double-integration EPR techniques,[35] and also attempted via linear combination of XANES spectra.[5] In principle, the relative concentrations of Fe centers can be estimated from linear combination of the Fe–O bond distances using suitable standards. Care has to be taken to determine which type of Fe center is present in the analyzed sample. Following the EPR and Raman results, we can assume that the only defect centers present in the anodic region of the single crystal are 6-fold coordinated Fe^{3+} and Fe^{4+} without any Fe^{3+}–$V_O^{\bullet\bullet}$. Suitable standards are $LaFeO_3$ and $SrFeO_3$ with Fe–O distances of 1.994 Å and 1.925 Å, respectively. For these compounds, it has been shown that A-site substitution of Sr for La decreases the size of the unit cell, despite the smaller Shannon radius of the La^{3+} ion, and the Fe–O bond distance has been shown to decrease continuously with increasing amount of Fe^{4+} going from $LaFeO_3$ to $SrFeO_3$ without systematic deviations from the Vegard's law.[83] Assuming a linear relation of Fe–O distance to concentration, the Fe^{3+} concentration in the anodic part can be estimated to be approximately 10%. Integrating the EPR signals, we can further estimate the ratio (cathode to anode) of Fe^{3+} to be about 7 ($\pm$ 1), which puts the concentration of the cubic Fe^{3+}–O_6 - center at roughly 70% ($\pm$ 10 %) in the cathodic region. Since Raman spectroscopy demonstrates the absence of Fe^{4+} in this region, consequently the amount of Fe^{3+}–$V_O^{\bullet\bullet}$ can be estimated as 30%. Unfortunately, the above estimation cannot be used to gain information on the Fe–O bond lenght in the Fe^{3+}–$V_O^{\bullet\bullet}$ complexes because of the tetragonal distortion of the axial site.
Merkle and Maier [35] demonstrate that the degree of association of Fe and oxygen vacancies shows a tendency to decrease with increasing doping level and temperature. For a similar doping concentration as used in this study, the degree of association at room temperature is given as $\sim$ 25%, while values approaching 50% are only seen for lower concentrations and temperatures below 273 K. Since these

values are in agreement within the error bar specified above, a Fe^{3+}–$V_O^{\bullet\bullet}$ concentration of 30% is a realistic estimation.
From the EXAFS and XANES analysis as well as from EPR data, it is reasonable to conclude that Fe exists mainly as a cubic Fe^{3+} center with Fe–O distance $R = 1.972$ Å in the cathodic region of the single crystal. The concentrations of the cubic Fe^{3+}–O_6 and the axial Fe^{3+}–$V_O^{\bullet\bullet}$ center is in agreement with the defect chemical constraint $[V_O^{\bullet\bullet}]/[Fe^{3+}] < 0.5$ for the dilute regime (eqn (5.3)), with the amount of the Fe^{3+}–$V_O^{\bullet\bullet}$ present around the cathode estimated to be $\sim 30\%$. As $SrTi_{0.9}Fe_{0.1}O_{2.95}$ is far outside the dilute regime [19], the constraints described by eqn (5.3) are no longer valid and Fe^{3+}–$V_O^{\bullet\bullet}$ with an Fe–O distance of $R = 1.955$ Å becomes the predominant Fe center.

5.2 Thick Epitaxial Films

While the bulk system discussed above provides useful references, the physical structure of a thin film can be very different from chemically equivalent bulk material. The chemistry of the single crystal is governed by thermodynamics during the slow and high temperature growth process, while thin film growth is usually limited kinetically and dominated by a very different set of process parameters. Since thin films are technologically more relevant that single crystals, the investigation of the chemical state after growth becomes very important.
In analogy to chapter 6, 'thick' ($\geq$100 nm) and 'thin' ($\leq$20 nm) films are distinguished in the following section. Whereas 'thick' films can be investigated with bulk-sensitive methods (e.g. fluorescence), 'thin' films need more surface sensitivity (e.g. photoemission).

5.2.1 X-ray Absorption Fine Structure - XAFS

$SrTi_{1-x}Fe_xO_3$ films with x = 0.005, 0.01, 0.02 and 0.05 were PLD - grown epitaxially on 0.05% Nb-doped $SrTiO_3$ single crystals using standard deposition conditions (700°C, 0.25 mbar, 0.8 J/cm^2, 5 Hz). The film thickness is 500 nm, calculated form the respective deposition rate. Fe K-edge EXAFS measurements were done on all four samples, as well as on several reference substances containing Fe ions: $SrFeO_3$, $LaFeO_3$, Fe_2O_3 and $FeTiO_3$ containing Fe^{4+}, Fe^{3+}, Fe^{3+} and Fe^{2+} ions, respectively. The Fe K-edge XANES spectra recorded on the Fe concentration series grown on Nb-doped $SrTiO_3$ is shown in figure 5.7 on the left-hand side. There are two features that show a systematic decrease with increasing Fe content, the shoulder 'A' at 7122 eV in the pre-edge region and the intensity of the two white line features 'B' and 'C' relative to the edge jump. Feature 'A' has been identified

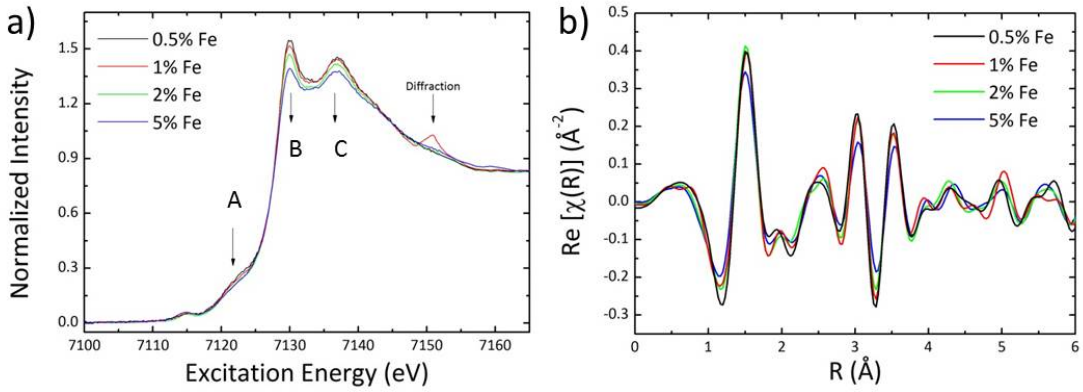

Figure 5.7: a): Fe K-edge XANES of 500 nm $SrTi_{1-x}Fe_xO_3$ films with x= 0.005, 0.01, 0.02 and 0.05. Features A, B and C scale with Fe concentration. All spectra are normalized to an edge-jump of 1. b): Real-part of the Fourier transform of the EXAFS in the k-range 2 - 9 Å^{-1}. No systematic shift in the scattering path length can be identified.

above (figure 5.4) as corresponding to the presence of Fe-$V_O^{\bullet\bullet}$ complexes, whereas the interpretation of the latter is less clear at the present time. One conceivable explanation would be the presence of two inequivalent Fe centers in the films, and as the ratio of these centers changes with Fe-content, the white line changes its shape. However, there is no systematic change apparent in the absorption fine structure, as shown in the right part of figure 5.7 with the example of the real part of the Fourier transform of the EXAFS signals. Plots of the Fourier transform in R-space are sometimes called 'Radial Distribution Function', because the interatomic distances to the surrounding atoms can be approximated and directly compared. It should be noted that the peaks in the RDF do not correspond directly to the bond-length since the absorber phase shift usually causes the scattering paths to peak at shorter R-values than the interatomic distance. The sharp oscillations at 1.5 Å, 3 Å and 3.6 Å correspond to the Fe-O, Fe-Sr and Fe-Ti direct scattering paths. No difference in the R coordinate is visible for the four different Fe concentrations, confirming that the amount of Fe is insufficient to significantly influence the lattice parameters of the perovskite lattice. It is highly relevant to note that, since no structural change with Fe-content is apparent, the presence of lattice-inequivalent Fe centers (such as Fe on A and B sites) is unlikely. The presence of a transition metal substituent on the A-site causes severe changes in the Fourier transform of the EXAFS, as shown for Mn by Levin *et* al. [84]. This means that if there are two non-equivalent Fe-centers present in the films, they are most likely distinguished by the presence of an oxygen vacancy in the first coordination shell. This theory is supported by the systematic decrease of feature 'A', which is indicative of a reduced degree of association for higher Fe concentrations. Merkle and Maier have found that the association enthalpy of Fe'_{Ti} and $V_O^{\bullet\bullet}$ depends on the Fe concentra-

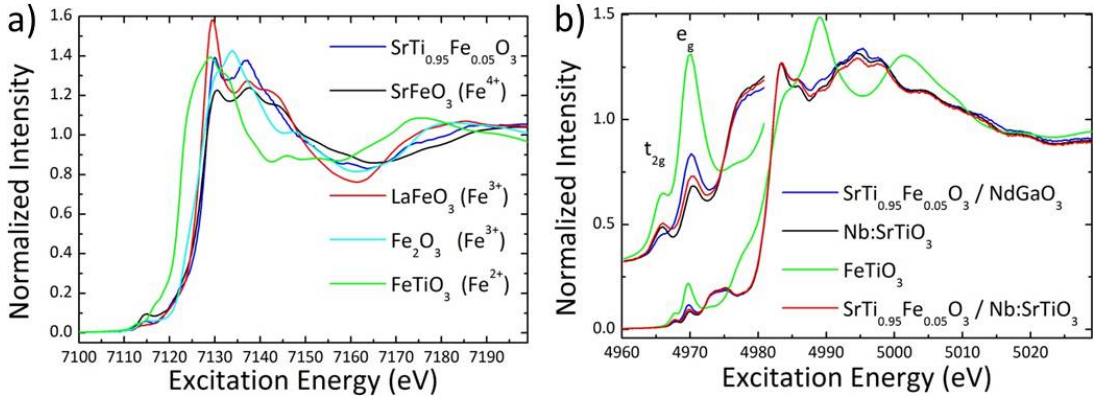

Figure 5.8: a): Fe K-edge XANES of various reference compounds containing Fe^{2+}, Fe^{3+} and Fe^{4+}. A clear shift can be observed between Fe^{3+} and Fe^{2+} compounds. b): Ti K-edge XANES for $FeTiO_3$, a Nb-doped $SrTiO_3$ single crystal and two thin films of $SrTi_{0.95}Fe_{0.05}O_3$ grown homo- and heteroepitaxially. The pre-edge region is sensitive to the tetragonal distortion of the unit cell (see inset).

tion in $SrTiO_3$ single crystals and approaches zero for Fe concentrations exceeding 10^{20} cm^{-3} due to a decrease of the activity coefficient [35], which is in agreement with our experimental observations. Analysis of the plasma-plume during the PLD growth process may suggest that the $V_O^{\bullet\bullet}$ concentration in the films decreases with increasing amount of Fe due to the changes in the plume chemistry and energy distribution in the plume, which could be induced by the modified absorption of the laser pulse during ablation [66].

A different question with regard to the incorporation of Fe into the $SrTiO_3$ lattice concerns the solubility limit. In thermodynamic equilibrium, the substitution of acceptor-type ions (such as Fe^{3+}) for Ti^{4+} will introduce additional oxygen vacancies, which can form ordered defect structures above a certain critical concentration. For acceptor doping of $SrTiO_3$, the solubility limit is given as 2% [85], which corresponds nominally to the $SrTi_{0.98}Fe_{0.02}O_3$ films. From this point of view, we do not expect any structural changes in the thin films up to 2% Fe doping. However, solubility limits are a thermodynamical quantity, whereas the film growth by PLD is governed by kinetic constraints and a supersaturation of Fe could be possible for concentrations far above the thermodynamic limitations. The conclusions from these considerations is that Fe is incorporated into the $SrTiO_3$ lattice as a B-site substituent, and no indication of A-site occupancy can be found in the EXAFS up to a Fe site-fraction of 5%. Since the $SrTi_{0.95}Fe_{0.05}O_3$ XANES is almost identical to that found in the anodic region of the electrocolored single crystal (see section 7.1), we can conclude that Fe mainly has the oxidation state +3 in $SrTi_{1-x}Fe_xO_3$ thin films grown by PLD.

For the sake of comparison, it is useful to examine some reference materials. Figure 5.8 a) shows the Fe K-edge XANES of reference substances containing Fe

ions with nominal oxidation states of +2, +3 and +4. From the structure of the pre-edge region and the shape of the white line, it is clear that a comparison between the respective compounds needs to take into account the different crystal structures and therefore different atomic environments of Fe. As an example, we can compare $LaFeO_3$ and α-Fe_2O_3, both of which contain Fe in the oxidation state +3. Despite the same oxidation state of the Fe ions, and hence a nominally similar electron density on the nuclei, there are pronounced differences between the two XANES which are caused by the differences in atomic coordination. Both compounds contain Fe in octahedral oxygen coordination, but the distortions of these octahedra is small in $LaFeO_3$ and large in Fe_2O_3. Furthermore, the low-energy region of the XANES is very sensitive to multiple scattering effects, which means that the higher coordination spheres become important.
Despite these complications, several points can be derived from the study of the Fe K-edge XANES: i) perovskites and distorted perovskites ($SrFeO_3$, $SrTi_{1-x}Fe_xO_3$, and $LaFeO_3$) show a characteristic twin structure of the white line (the main absorption jump), ii) a small ($\leq$1 eV) shift in energy is visible between Fe^{4+} and Fe^{3+}, whereas a significant shift in energy is visible between Fe^{3+} and Fe^{2+} ($\sim$4 eV), measured at an absorption of unity on the white line. The Fe^{2+} compound - $FeTiO_3$ - is not a perovskite, despite the similar chemical formula, but a rhombohedral compound that consists of Fe and Ti in distorted, face-sharing octahedra. The crystal structure of $FeTiO_3$ is drastically different from a perovskite, which is a stacking of corner-sharing octahedra. The differences in crystal structure are manifest in the Fe K-edge XANES, but are less pronounced at lower energy absorption edges ($L_{2,3}$ edge [86]). Despite these differences, the clear shift of the white line (also visible in FeO, not shown) for the Fe^{2+} compound suggests Fe^{2+} is not present significant amounts in the bulk of the examined films. The measurements on the $SrTi_{1-x}Fe_xO_3$ films and the standards was performed with fluorescence detection and transmission, respectively, therefore both techniques are bulk-sensitive, which can be the explanation why photoemission and soft x-ray absorption data come to a different conclusion (see section 5.3.1, section 8.1, reference [86]).
Figure 5.8 b) shows the Ti K-edge absorption spectra of a Nb-doped $SrTiO_3$ single crystal, two films of $SrTi_{0.95}Fe_{0.05}O_3$ grown on Nb:STO and $NdGaO_3$, respectively, and $FeTiO_3$. All four compounds contain Ti^{4+} ions, which is confirmed by the coincident energy position of the $1s \rightarrow 3d$ dipole transitions in the pre-edge region (labeled e_g and t_{2g} in the inset). The relative weight of the t_{2g} and e_g transitions depends strongly on the crystal structure and the band structure, therefore $FeTiO_3$ is not suitable for a quick comparison. However, a comparison of the other three shows an increased e_g/t_{2g} ratio for the heteroepitaxially-grown $SrTi_{0.95}Fe_{0.05}O_3$ / $NdGaO_3$ film as compared to the single crystal. Variations of the quadropolar transitions at the Ti K-edge can be an indication of a tetragonal distortion of the unit cell [87, 88], reflecting the tetragonal distortion of the $SrTi_{0.95}Fe_{0.05}O_3$ films due to the heteroepitaxial strain(see chapter 4). A similar if much smaller

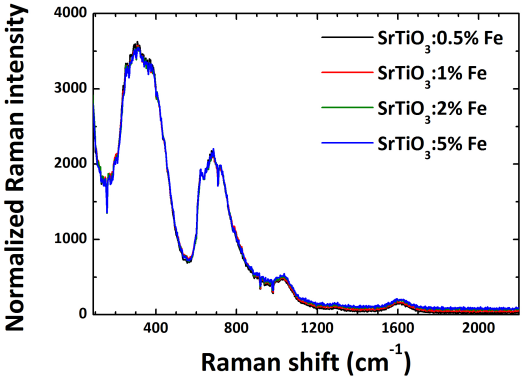

Figure 5.9: Raman spectra of $SrTi_{1-x}Fe_xO_3$ films with x = 0.005, 0.01, 0.02 and 0.05. No difference can be found between the spectra, and the characteristic line at 690 cm^{-1} indicating Fe^{4+} is absent.

effect can be seen in the pre-edge structure of the $SrTi_{0.95}Fe_{0.05}O_3$ film grown on Nb:STO, which could be induced by the small tetragonal distortion of the unit cell that is visible in the c-axis expansion of ∼1 pm (see section 4.2). However, the overall shape of the Ti K-edge XANES (and EXAFS) is very similar for the three perovskite samples, indicating no significant structural distortion is present.

5.2.2 Raman Spectroscopy

Raman spectroscopy was performed by A. Kuzmin (Institute for Solid State Physics, Riga) on the 500 nm $SrTi_{1-x}Fe_xO_3$ films (x = 0.005, 0.01, 0.02 and 0.05) after examination by XAFS, using an excitation wavelength of $\lambda = 532$ nm with a cw-power of 150 mW, and a 600 groves/mm diffraction grating at room temperature. As explained in the single crystal section, Raman spectroscopy can be used to identify Fe^{4+} ions in the thin films. Figure 5.9 shows the normalized Raman spectra of all four thin films. The spectra are identical, and the characteristics Fe^{4+} line at 690 cm^{-1} is missing. This is in agreement with the XAFS results that indicate the presence of Fe^{3+} exclusively.

5.3 Thin Epitaxial Films

5.3.1 Hard X-ray Photoelectron Spectroscopy - HAXPES

The electronic structure and chemical composition of $SrTi_{1-x}Fe_xO_3$ thin films with x = 0, 0.02, 0.05 were investigated by HAXPES at beamline P09 (HASYLAB,

Hamburg) with monochromatic x-ray radiation at a photon energy of $E_{ph} = 5500$ eV, using a Si (311) monochromator crystal and a SPECS hemispherical photoelectron analyzer. The overall energy resolution of the beamline was $\Delta E \leq 350$ meV at analyzer pass energy $E_{pass} = 40$ eV as measured at the Au Fermi edge, and the stability of the photon energy was periodically checked using a Au reference. All spectra in this section were recorded under an angle of incidence close to the critical angle of total external reflection θ_c to minimize the background of the spectra [51] , and the take-off angle was correspondingly close to 90°, in the plane of linear polarization of the synchrotron beam.

For insulating and semiconducting materials, the position of the Fermi level E_F

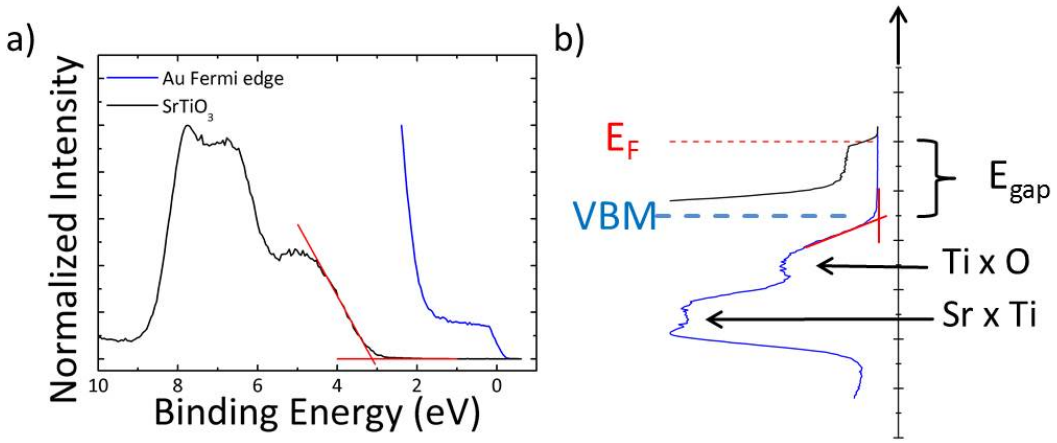

Figure 5.10: a): Valence band of an undoped $SrTiO_3$ film - corresponding to the BZ-averaged density of states - and the Au Fermi edge at $E_{ph} = 5.5$ keV. The VBM is indicated in red. b): Graphic illustration of the scheme to extract the position of E_F in the $SrTiO_3$ films.

in the band gap is an indicator for the type of prevalent charge carriers. In theory, E_F is located in the middle of the forbidden gap at T = 0 K, but the position can be lowered or increased in energy by acceptor or donor doping, respectively. Figure 5.10 illustrates the principle of determining the position of E_F within the band gap of $SrTiO_3$: the leading edge of the valence band is extrapolated with a linear function to intersect the energy axis [89], which is calibrated using the Au Fermi-edge measured on a Au strip. Since the Au strip and the thin film sample are in electrical contact, their respective Fermi level is in the same position with respect to the photoelectron analyzer. Since E_F is the chosen reference point for XPS, the energy position of the VBM yields direct information about the position of E_F within the band gap. For the sample shown in figure 5.10, $E_{VBM} = 3.1$ eV, indicating that the position of E_F is just below the conduction band (with $E_{gap} =$

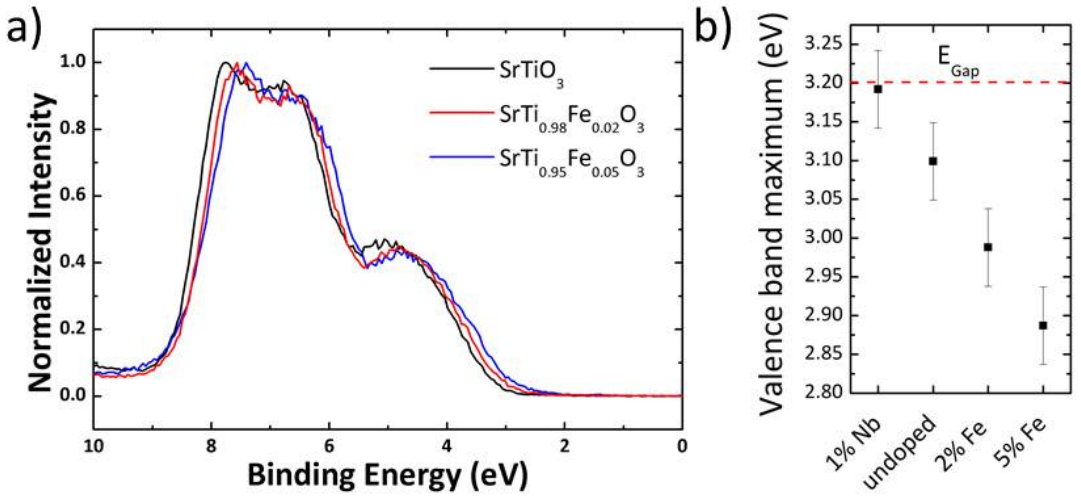

Figure 5.11: a): Valence band spectra recorded at 5.5 keV excitation energy of undoped $SrTiO_3$ (black), $SrTi_{0.98}Fe_{0.02}O_3$ (red) and $SrTi_{0.95}Fe_{0.05}O_3$ (blue). b): Position of the VBM of $SrTi_{1-x}Fe_xO_3$thin films (x = 0, 0.002, 0.005) and additionally of a 1 at-% (0.5 wt-%) Nb-doped $SrTiO_3$ single crystal.

3.2 eV).

Fig. 5.11 a) demonstrates the influence of Fe on the electronic structure of the $SrTi_{1-x}Fe_xO_3$ thin films. The valence band maximum (VBM) of the $SrTi_{1-x}Fe_xO_3$ films is gradually shifted to lower binding energies with increasing Fe-content, while the overall shape of the valence band remains essentially unchanged. The values of the VBM are plotted vs. dopant concentration in figure 5.11 b). There are several possibilities how this shift of the VBM could be interpreted. In the case described by Rothschild *et al.* [36], a solid solution $SrTi_{1-x}Fe_xO_3$ ($0 \leq x \leq 1$) is formed. A direct consequence of this is a narrowing of the band-gap and a broadening of the valence band as the Fe 3*d* states situated at the top of the valence band form an impurity band of increasing bandwidth with increasing Fe-content. However, the width of the valence band is approximately constant, and the reduction of the band gap predicted by this model $\Delta E_g^0 = 3.2 - 1.9x + 0.5x^2\ eV$ is $\sim$ 100 meV for 5% Fe, much smaller than the shift observed between the VBM of the undoped $SrTiO_3$ and the $SrTi_{0.95}Fe_{0.05}O_3$ film. It seems likely that the observed shift of the VBM is in fact caused by an internal shift of E_F, which results in an *observed* shift of the spectra since E_F is the chosen reference for XPS. Such a shift of E_F is plausible if it can be observed in all core-level emission lines as well, and indeed it is, as shown in figure 5.12.

Two explanations can be considered for this shift of E_F, either the formation of a secondary phase of different Fe-content or a decrease of the electron concentration in the conduction band. The formation of ordered structures is, from a thermodynamical point of view, often the preferred reaction of perovskites to increased

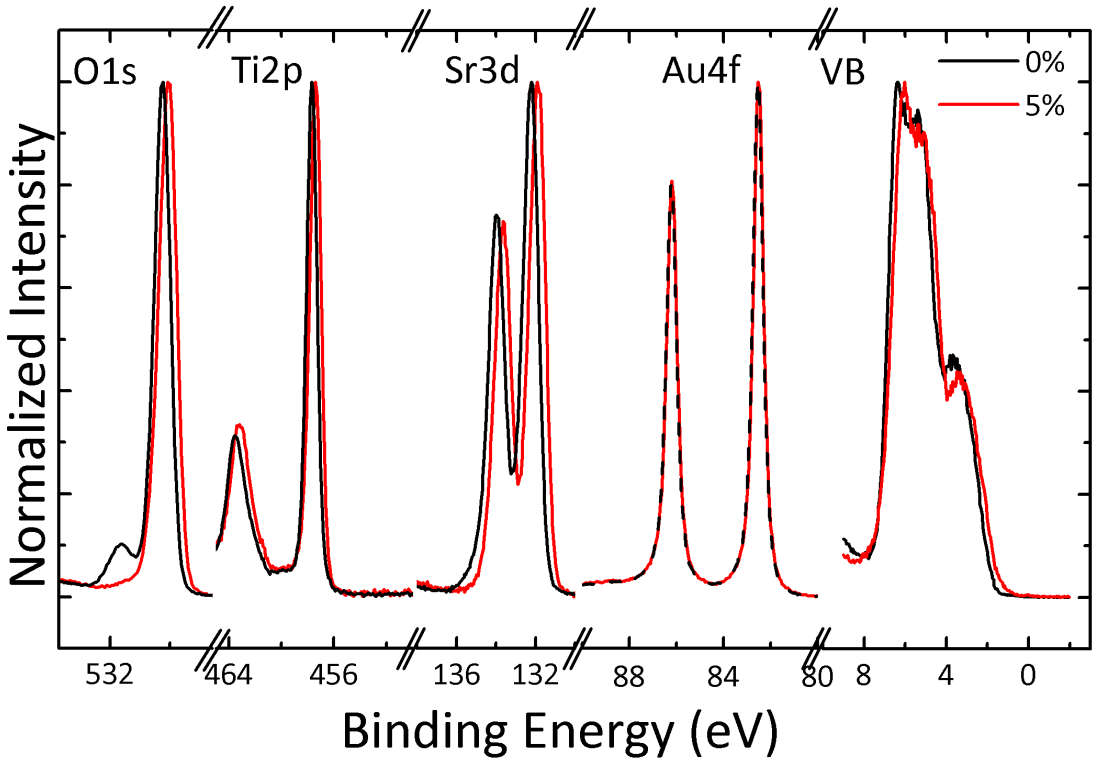

Figure 5.12: Overview of all relevant core-levels - O 1s, Ti 2p, Sr 3d, and the valence band in order of decreasing binding energy - in reference to the energy position of the Au 4f doublet. Note the consistence of the energy shift. The apparent difference in the shift are induced by the different length of the respective energy axis.

non-stoichiometry [85], and the growth of SrO – islands on the surface of reduced $SrTiO_3$ single crystals has been confirmed experimentally and related to the formation of Sr-deficient Magnelli phases [90]. Since the growth process during PLD is kinetically limited, the system is not in a state of thermodynamic equilibrium. In fact, non-stoichiometry in PLD-grown $SrTiO_3$ films has recently been studied and found to depend on process parameters for undoped systems [30]. Recent investigations suggest that this process of V_{Sr} and V_{Ti} incorporation through PLD is significantly complicated by the addition of Fe to the system [66].
To clarify whether or not there are additional phases present in the $SrTi_{1-x}Fe_xO_3$ system, it is useful to reproduce the shape of the measured spectra with single components. Due to the great number of free parameters than can be adjusted during the fitting procedure (and their correlations), the use of a suitable standard is advantageous. A good choice for the standard is a Nb-doped $SrTiO_3$ single crystal (Nb-STO), since there are no charging issues to be overcome and the stoichiometry is very well defined in comparison to a thin film. Fitting the Sr $3d$ lines

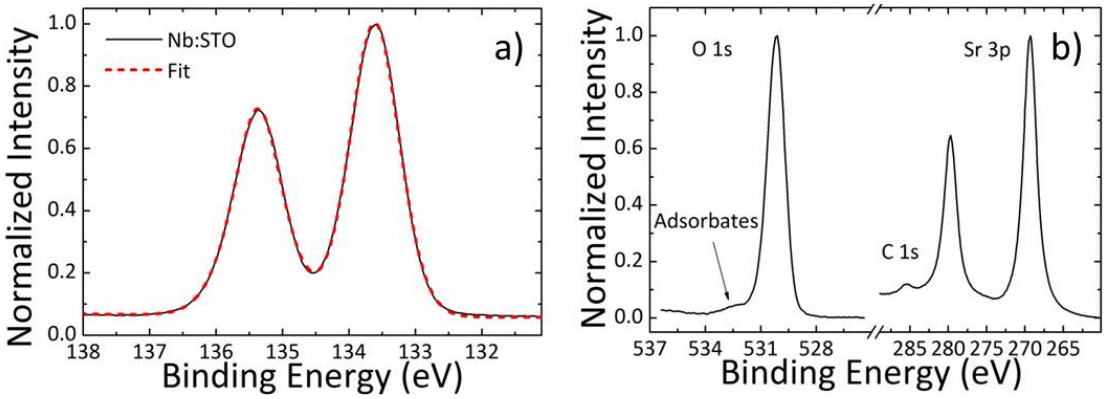

Figure 5.13: a): Measured data (black line) and fit (dashed, red line) for the Sr 3p doublet at E_{ph} = 4203 eV. b): O 1s and Sr 3p spectra of the Nb-STO single crystal, displaying small features related to adsorbates (O 1s line at higher E_{bind} and C 1s line of adventitious carbon. Note that the vacuum in the sample chamber was 10^{-8} mbar and no surface cleaning was used.

with a single doublet yields an excellent fit (see figure 5.13a)), and physically reasonable parameters with respect to the line shape (LG-mix, FWHM) can be extracted from the fit. The background has very little influence on the line shape, and is best approximated with a Tougaard-function for Sr 3d. To illustrate the point made in section 3.4 that HAXPES is insensitive to surface contaminants and therefore does not require sample treatment (such as heating in vacuum or sputter-cleaning), the O 1s, Sr 3p and C 1s spectra recorded on the Nb:STO crystal are shown in figure 5.13 b). The spectral weight of the oxygen-containing adsorbates is not only much smaller than the emission line for the lattice oxygen of Nb-STO, but it is also resolved as a separate peak. The comparison of the integrated peak area of the Sr 3p doublet and the C 1s at E_{bind} = 285 eV yields a carbon contribution to the spectrum of $\sim$ 1.3%, which corresponds to an adsorbate layer of $\sim$ 1 Å thickness when EAL = 50 Å is assumed. The vacuum pressure was $\sim 10^{-8}$ mbar, and no sample treatment was used to clean the surface.
The line-shape parameters obtained in this way (see table 9.1 in the appendix) can be treated as a reference for the peak-fitting of more complicated structures, such as the Sr 3d lines of the undoped $SrTiO_3$ thin film. To correctly fit the constituent lines into the envelope, the LG-mix and FWHM are kept constant for all spectral components, at the value determined for Nb-STO. It is obvious that already the undoped $SrTiO_3$ films exhibits additional spectral components in the Sr 3d lines. Two doublets are insufficient to fit the data in a satisfactory manner, and only with three doublets of the same line-shape can the envelope be reproduced, as seen in figure 5.14 a). The appearance of two additional components on the surface of $SrTiO_3$ single crystals after high-temperature reduction at 1000° C was described by Szot *et al.*, and attributed to a Sr-rich phase in the perovskite and SrO islands

on the surface of the crystal for the doublet shifted by $\Delta E = 0.8$ eV and $\Delta E = 1.5$ eV, respectively [91]. Given the fact that for non-stoichiometric growth conditions, SrO "islands" can be observed by AFM on the surface of $SrTiO_3$thin films, this interpretation seems a reasonable starting point.

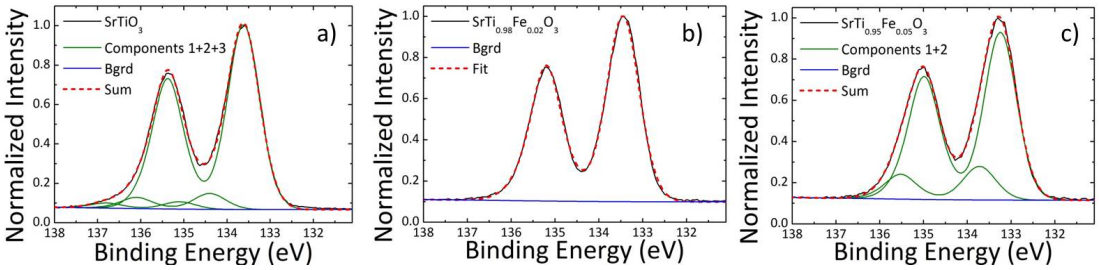

Figure 5.14: Sr 3d doublets for $SrTi_{1-x}Fe_xO_3$with x = 0, 0.02 and 0.05 (a), b) and c), respectively), recorded at 5.5 keV excitation energy (black lines), and the corresponding fits (dashed, red lines). Spectral components are shwon in green.

For $SrTi_{1-x}Fe_xO_3$ films, the spectral contribution of the additional components vanish for 2% Fe, and a satisfactory fit is achieved with only a single doublet, whereas the 5%-$SrTi_{1-x}Fe_xO_3$ film exhibits a significant contribution of the Sr-rich component, but no further components. Since the deposition paramters used for all three films were optimized for $SrTi_{1-x}Fe_xO_3$ with 2% Fe (see chapter 4), the appearance of the Sr-rich component is likely a consequence of non-stoichiometry induced by the choice of deposition parameters. The presence of these additional components does not, however, follow the systematic dependence on Fe-content observed for ΔE_F, and is therefore unlikely as the cause for the observed shifts.
At this point, a brief summary of the literature on the energy positions of the Fe-related defect levels is useful. Prevalent techniques to study the energy position of Fe in the band gap of $SrTiO_3$ are optical absorption and EPR-techniques, a combination of both, or combinations of either with computational methods (e.g. [92–95]). The combined results are summarized in figure 5.15 b), showing a scheme of the Fe-related energy levels for low Fe-concentrations (dilute regime). The notation of the defect levels reads as follows: Fe^{3+} stands for the reaction $Fe^x_{Ti} \rightarrow Fe'_{Ti} + h^\bullet$, meaning that an electron from the valence band is trapped in the Fe^x_{Ti} (Fe^{4+}) acceptor level, leaving the acceptor ionized (Fe^{3+}) and a hole $h^\bullet$ in the valence band. Therefore the notation of the energy levels refers to the ionized state, and the ionization energies indicated on the right side can be understood as the energy to excite an electron from the valence band into the acceptor level. Solid lines denote Fe^{n+}–O_6 centers, whereas the dotted lines underneath refer to the respective Fe^{n+}–$V_O^{\bullet\bullet}$ defect level, the position of which can be significantly relaxed with respect to the former. The first ionization energy of oxygen vacancies

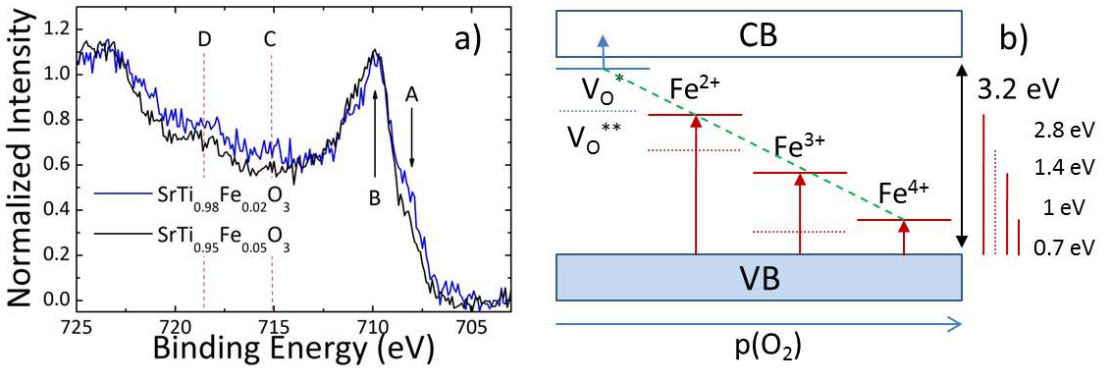

Figure 5.15: a): Fe 2p core level spectra recorded at 5500 eV excitation energy for $SrTi_{0.98}Fe_{0.02}O_3$ (blue line) and $SrTi_{0.95}Fe_{0.05}O_3$ (black line). See text. b): Schematic representation of the Fe- and V_O- related defect levels in the band gap of $SrTiO_3$. The green line indicates the position of the Fermi level in dependence of the oxygen partial pressure as given by defect chemistry.

$V_O^x \rightarrow V_O^\bullet + e^-$ has been given as 3 meV (indicated by the solid blue line), and the second as ∼0.3 eV (dotted blue line), measured from the bottom of the conduction band. In essence, this means that oxygen vacancies are singly ionized down to cryogenic temperatures. It should be mentioned that the spread of the precise energy levels related to Fe reported in literature is significant, and the values given here are representative but not should not be considered accurate. Especially the position of the Fe^{2+} level is uncertain since there is no unambiguous identification of this center experimentally, and it lies very close in energy to the $V_O^{\bullet\bullet}$ level. The position that the Fermi level would be located at if the respective dopant was the dominant one, is sketched with a dashed green line, indicating the E_F- dependence on $p(O_2)$ as predicted by defect chemistry and the fact that E_F will be pinned at the level of the dominant defect type in a semiconductor.
The Fe 2p spectra shown in figure 5.15 a) yield some insight into the situation in the $SrTi_{1-x}Fe_xO_3$ films. A detailed analysis of the Fe 2p multiplet structure has been attempted by various authors, however, it remains less well understood than the Ti 2p emission lines due its complicated structure [96, 97]. In the case of monovalent compounds, the Fe 2p lines already show a complicated structure due to the configuration-interaction of the final states (see chapter 3.4), and the situation is complicated by the influence of oxygen on the magnetic structure and spin-state of the Fe - ions and ligand-to-metal charge-transfer. These factors result in emission lines that consist of several spectral features for a monovalent ion, and for aliovalent ions like Fe in $SrTiO_3$, the emission lines will be accordingly more complex. On the example of Fe_3O_4 containing two sublattices of Fe^{3+} and Fe^{4+}, Grosvenor *et al.* use no less than 9 spectral components to fit the structure of the Fe $2p_{3/2}$ line, resulting in a good fit but very little real information regarding the

multiplet structure [97].
However, some spectral features can be identified that act as fingerprints to a certain valence state, indicated by A - D in figure 5.15. In general, the spectral weight at lower binding energies is attributed to Fe states with lower valence, since the additional valence electron will increase the screening of the core-potential felt by the core-level electrons. We can therefore attribute spectral weight in the region marked "A" on the left-hand side of figure 5.15 to a contribution from Fe in a lower valence state, and "B" to that from a higher valence state. Keeping in mind the results obtained by XAFS (see 5.2.1) show that Fe^{4+} is absent from the bulk of the film, features "A" and "B" can be assumed to derive mainly from Fe^{2+} and Fe^{3+}, respectively. A corresponding interpretation has been concluded from a comparative study by McIntyre *et al.*[96].
In addition, the CT-satellites (marked "C" and "D") for both valence states are observed at different positions, with the lower binding energy satellite "C" weakly observed at 715 eV and the stronger satellite "D" at 718 eV. The position of satellite "C" corresponds to that found in FeO, with a distance from the main peak of 6 eV (peak "A"), while satellite "D" is located 8 eV above peak "B" and corresponds to that found in Fe_2O_3 [96].
To compare the Fe 2p spectra of $SrTi_{1-x}Fe_xO_3$ with 2% and 5% Fe, a linear background function, extrapolated from the pre-peak intensity, was subtracted, and the post-peak intensity normalized in such a manner that both Fe $2p_{3/2}$ (E_{bind} = 710 eV) and Fe $2p_{1/2}$ (E_{bind} = 724 eV) are equal in intensity. As can be seen in figure 5.15, the intensity ratio of feature "B" to feature "A", I_B/I_A, is larger for $SrTi_{0.95}Fe_{0.05}O_3$ than for $SrTi_{0.98}Fe_{0.02}O_3$, implying a slightly higher content of Fe^{3+} for the higher Fe-concentration. Correspondingly, satellite "D" is stronger for $SrTi_{0.95}Fe_{0.05}O_3$, while $SrTi_{0.98}Fe_{0.02}O_3$ shows increased intensity in the position of satellite "C", which is in agreement with the conclusion from I_B/I_A. The intensity ratios of the peaks and the satellites suggest that the fraction of $[Fe^{3+}]/[Fe_{tot}]$ is higher in the $SrTi_{0.95}Fe_{0.05}O_3$ film than in the $SrTi_{0.98}Fe_{0.02}O_3$ film, and consequently the Fe^{2+} content in the $SrTi_{0.98}Fe_{0.02}O_3$ film is larger. Considering the energy levels of Fe^{2+} and Fe^{3+} as depicted in figure 5.15 b), the position of the Fermi level in the band gap should decrease with increasing valence state of Fe, as would be expected for acceptor doping. Recalling figure 5.11, the position of E_F is decreasing with increasing Fe-content, starting with just below the conduction band in the case of $SrTiO_3$ and succesively shifting by $\sim$ 100 meV each when going to $SrTi_{0.98}Fe_{0.02}O_3$ and $SrTi_{0.95}Fe_{0.05}O_3$. The trend that is observable in the position of E_F is in agreement with the finding that $SrTi_{0.95}Fe_{0.05}O_3$ has a larger fraction of Fe^{3+} than $SrTi_{0.98}Fe_{0.02}O_3$.
It can therefore be assumed that the concentration of Fe influences the position of E_F, as would indeed be expected for an acceptor. As mentioned before, a systematic decrease of oxygen vacancies with increasing Fe content due to the PLD process cannot be excluded [66].

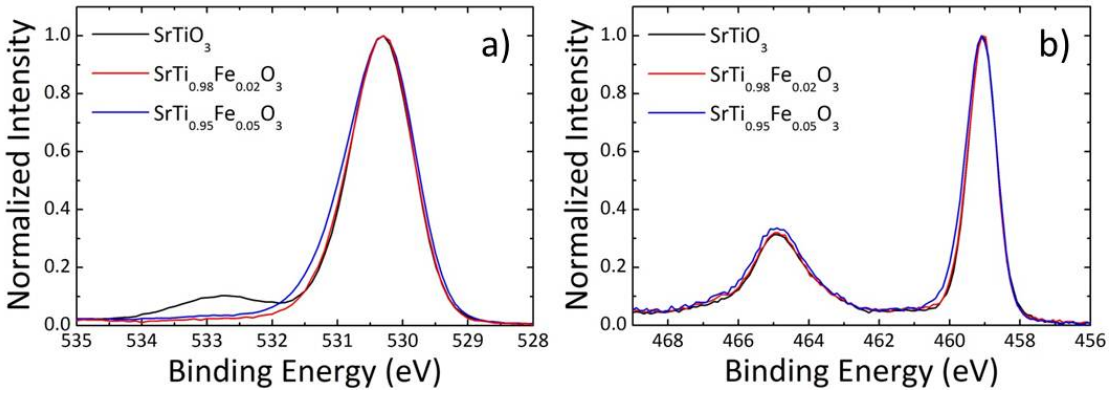

Figure 5.16: O 1s (a) and Ti 2p (b) emission spectra of $SrTiO_3$, $SrTi_{0.98}Fe_{0.02}O_3$ and $SrTi_{0.95}Fe_{0.05}O_3$ (black, red and blue, respectively) recorded at 5500 eV excitation energy.

To provide a complete picture, figure 5.16 shows the O 1s (a) and Ti 2p (b) emission lines, recorded at 5500 eV excitation energy on the same set of samples. The main O 1s line at E_{bind} = 530.3 eV corresponds to lattice oxygen of $SrTiO_3$ while the smaller peak at 532.8 eV is related to adsorbates on the sample surface (the intensity of the C 1s line confirms that the surface of the $SrTiO_3$ film is considerably more contaminted). A contribution from the SrO that was found in the Sr 3d doublet is also possible, but cannot be isolated. The Ti 2p doublet corresponds to that of undoped $SrTiO_3$, and no lower oxidation states are visible in the spectra. However, a small but significant asymmetric broadening of both Ti $2p_{3/2}$ and O 1s lines at the higher binding energy side can be observed in the case $SrTi_{0.95}Fe_{0.05}O_3$ compared to the other two films. This asymmetric broadening is reminiscent of the line shape of Ti 2p in $FeTiO_3$ [86, 98], and is likely connected to charge-transfer processes in the cation-sublattice (Fe^{2+} + Ti^{4+} → Fe^{3+} + Ti^{3+}) or a product of increasing influence of Fe on the electronic structure of $SrTi_{1-x}Fe_xO_3$ and a corresponding change in the transition matrix elements for photoemission, or both.

Knowing the relative position of E_F and VBM, we can calculate the energy difference E_C - E_F = E_{VBM} - E_F + 3.2 eV. For non-degenerate semiconductors (E_C - E_F > 3 kT), this energy difference can be evaluated to estimate the charge carrier concentration n_0:

$$E_F - E_C = kTln\frac{n_0}{N_C} \tag{5.4}$$

where N_C is the effective density of states in the conduction band, which has been calculated to [99]:

$$N_C(T) = 4.1 * 10^{16} cm^{-3}(T/K)^{3/2} \tag{5.5}$$

At 300 K, this yieds a value of N_C = 2.13 * 10^{20} cm^{-3}. Using equation 5.4, we can calculate n_0 from the E_C - E_F. The results are tabulated in table 5.2.

Table 5.2: Calculated values for the charge carrier concentration in $SrTi_{1-x}Fe_xO_3$ thin films.

% Fe	E_C - E_F [meV]	n_0 [cm^{-3}]
0	101	3.7 * 10^{18}
2	212	4.4 * 10^{16}
5	313	7.8 * 10^{14}

5.4 Conclusions

The combined results of the spectroscopical techniques indicate that Fe enters the $SrTiO_3$ lattice as a B-site substituent with mainly the oxidation state +3. The intensity of the pre-edge feature characteristic of Fe-$V_O^{\bullet\bullet}$ indicates a high degree of association similar to the anodic region of an electrocolored single crystal (where the estimation is 30%), and a dependence of the degree of association on Fe concentration. The high electron concentration ($> 10^{18}$ cm^{-3}) of the undoped $SrTiO_3$ films determined by photoemission is an indication that the oxygen vacancy concentration is strongly influenced by the growth processes during thin film deposition, since the oxygen partial pressure of 0.25 mbar would provide an oxidizing environment under equilibrium conditions.
The successive lowering of the Fermi level with increasing Fe-content indicates that Fe is electronically active in the $SrTiO_3$ lattice, or that Fe influences the deposition in such a way that less $V_O^{\bullet\bullet}$ are incorporated into the film. The lowering of the electron concentration n_0 indicates that Fe acts as an electron trap that compensates the excess electrons induced by the non-equilibrium amount of $V_O^{\bullet\bullet}$ since the thin film is already highly oxygen deficient (as can be seen on the highly *n*-doped $SrTiO_3$ film). Whereas the 'negative' dopant Fe is compensated by positively charged oxygen vacancies under moderate oxygen partial pressure (intrinsic regime) in equilibrium, in the thin film it is compensated by a hole in the *conduction* band (i.e., Fe removes electrons from the conduction band).
The lower charge carrier concentration for high Fe content can also be seen in the height of the interfacial Schottky-type barrier that is formed at the $SrTi_{1-x}Fe_xO_3$ / Pt interface (see chapter 6). There is no indication of Fe on the A-site of the perovskite lattice or Fe-segregation into separate phases. Surface-sensitive photoemission techniques indicate the presence of Fe^{2+} near the surface (compare also [86]).
However, XAFS data indicate the existence of two non-equivalent types of Fe-centers. One explanation can be Fe^{3+} and its oxygen vacancy complex, but another explanation could be that there are structurally inequivalent regions in the thin films. GISAXS data suggests that $SrTi_{0.99}Fe_{0.01}O_3$ films are reduced along filamentary pathways when brought into contact with metallic Ti [11], which could

be due to the existence of defect-rich regions where the reduction enthalpy of oxygen is lowered [100]. Even assuming perfect dispersion of Fe in the $SrTiO_3$ lattice, the existence of such structurally inequivalent regions would cause the appearance of two types of Fe in slightly different structural environments. Since these regions are assumed to have dimensions of a few tens of nm, they are extremely difficult to separate since most techniques are averaging over large areas.

Chapter 6

Resistive Switching of Fe-doped $SrTiO_3$ thin films

The first part of this chapter will discuss the resistive switching effect in thin films of $SrTi_{1-x}Fe_xO_3$ with a thickness of 100 nm or more, which will be termed 'thick films' in the following. These films usually require a dedicated DC-treatment for a prolonged period of time (called hard-forming) prior to switching, and part of this chapter will focus on the exceptions from that rule.
The second part of this chapter deals with film thicknesses of 20 nm or less, which will be called 'thin films' to distinguish the two thickness regimes. No hard-forming is required for these films, and only the homogeneous switching polarity can be observed in this thickness regime.
The sign of the voltage is always in reference to the top electrode, meaning a positive voltage is biased positively at the top electrode and vice versa.

6.1 Thick Films ($\geq$100 nm)

For most MIM-cells consisting of two metal electrodes and an insulating layer, the initial resistance of the MIM-cell is very high and needs to be permanently lowered in order to enable resistive switching. The simplest way to achieve this is to apply a DC-voltage to the MIM-cell and monitor the current until there is a sharp increase. This breakdown of the resistance is called electroforming and needs to be carefully controlled in such a way that the MIM-cell is not destroyed. The main problem with electroforming is that the required voltage and time are seemingly random even for MIM-cells made on the same sample. In the most extreme cases, forming times of below 1 second are observed for a given voltage, while the next electrode might not show any irreversible lowering of the resistance with time. Another possibility is that one electrode requires a dedicated forming step, while the one right next to it does not and exhibits resistance switching instantly.
An example for this behavior is given in figure 6.1 a), which shows the switching characteristics of two electrode pads on a 30 nm Pt/ 400 nm $SrTi_{0.99}Fe_{0.01}O_3$ Nb:STO sample. The I(V)-curve shown in black was measured after DC-forming using a +7 V bias at the Pt top electrode to break down the high initial resistance, while the other pad (red line) was not subjected to a dedicated forming step. The most striking difference between the two is the switching polarity: the resistance of the DC-formed pad is lowered upon applying a negative voltage, and increased with a positive voltage. This switching polarity has been called "couter-eightwise"

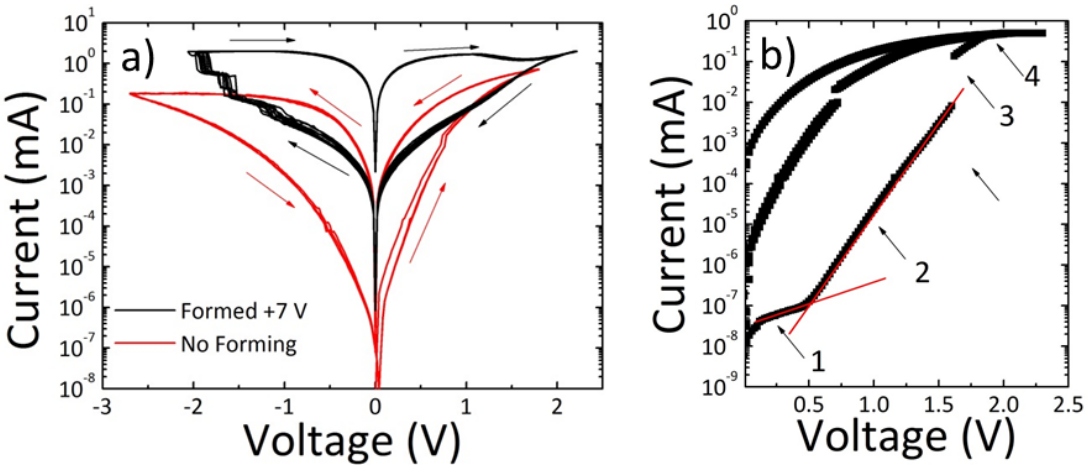

Figure 6.1: a): Current - voltage characteristics of two MIM-pads on the same 400 nm $SrTi_{0.99}Fe_{0.01}O_3$ film, one after DC-forming at +7 V and the other without a dedicated forming step. The switching polarity is indicated by the black and red arrows. b): First voltage sweep showing soft-forming. Four different slopes of the I(V)-curve can be marked, indicating four different conduction regimes.

or filamentary, while the polarity exhibited by the other pad (SET-voltage positive, RESET-voltage negative) is called "eightwise" or homogeneous [32].

There are a few differences between the two switching polarities that can generally be observed and will be discussed in exemplary form on figure 6.1 a). The resistance range accessible by the filamentary polarity is generally lower than the one accessible by the homogeneous polarity, a fact that is observed for samples showing both polarities. Another important point is that the current shows a series of discontinuities in the "SET"-sweep of the filamentary pad, which is always observed for this polarity. The important consequence is that for the filamentary polarity, only fixed resistance levels can be written, in contrast to the homogeneous polarity, as will be shown in 6.2.4. For the filamentary polarity, a fine control over the switching voltage-window is extremely important since the "SET"-voltage, at which the current-discontinuities are seen, are prone to drift if an equilibrium is not established. This drift can be seen in figure 6.1 a), where the "SET"-voltage drifts from approx. -1.8 V to -1.95 V within a few switching cycles, which is a good indication that the "RESET"-voltage is too large. While a resistance drift can also be observed for unsuitable voltages in the homogeneous polarity, it is generally much less prone to perturbation since the current shows a continuous behavior without any current jumps.

While the pad showing the filamentary polarity (black line in figure 6.1 a)) was highly insulating initially ($R > 10^{12}\Omega$) and the resistance was not perturbed with voltages up to $\pm$ 2V, the pad showing the homogeneous polarity (red line) shows a different behavior in the virgin state. The first I(V) -sweep recorded on the virgin

pad is shown in figure 6.1 b). The initial resistance is also high (region 1), but the current starts to increase exponentially above a voltage of 0.5 V (region 2). This first I(V)-sweep shows an abrupt increase in the current of ~ 1 order of magnitude around 1.6 V, which corresponds to a forming process (3). This behavior where the forming voltage is equal to or smaller than the switching voltages applied is called "soft-forming". After the current jump, a steep continuous increase is observed (4) up to a point where the current slope changes again. After this point, the current is identical on the "up"-sweep and the "down"-sweep, indicating that the "SET"-state is reached and no further change in resistance takes place. It is readily apparent that for a description of the virgin sweep displayed in figure 6.1 b), 4 different mechanisms would be required in the low, intermediate and high voltage regime and the current jump to describe the current from 0 V to the SET-voltage. Therefore, the conduction mechanism in the MIM-structures is not easily inferred from the I(V)-characteristics. Menke has shown that for films thicker than 200 nm, two contributions to the complex impedance can be separated and assigned to an "interface"-contribution deriving from the contact of Pt and $SrTi_{1-x}Fe_xO_3$, as well as a bulk contribution from the insulator [33]. Both contributions are voltage dependent and at least one, if not both, show memristic behavior and change under an electrical stimulus. While it has been shown that both switching polarities co-exist under one formed electrode pad and can be accessed via a careful voltage control [32], the fact that thick $SrTi_{1-x}Fe_xO_3$ films show softforming is not explained yet and will be examined here.

6.1.1 Voltage-Time Relation

A systematic study of the electroforming is complicated by the large inherent spread of forming times and resistance values after forming. Menke observed a variation of 5 order of magnitude in forming time for a given voltage and film thickness [101]. However, there is a correlation between the forming voltage and the forming time, as can be seen in figure 6.2 a). For this study, a film of 100 nm $SrTi_{0.95}Fe_{0.05}O_3$ was grown on Nb:STO and a 30 nm Pt layer was patterned into 200 x 200 μm^2 electrodes. The average forming time (time until the current compliance is reached) is significantly shorter for a forming voltage of +10 V than for +8 V, which is intuitively understood since the electroforming is commonly ascribed to oxygen vacancy movement, and the driving force for this movement increases with increasing potential drop over the MIM-cell. It is clear from the large standard deviation δ observed that a systematic study of the voltage-time relation is not accurately described by a Gaussian distribution, which will be discussed in detail in section 6.1.4 along with the difficulty to obtain comparable populations. It should be noted that this voltage-time relation is not readily observed in all samples. The forming processes shown in figure 6.2 were performed with a 10 kΩ

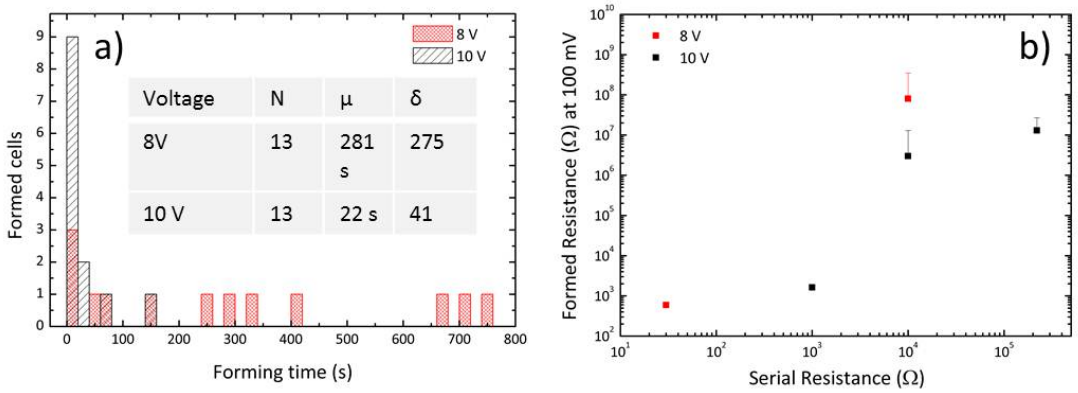

Figure 6.2: a): Histogram showing the number of formed pads vs. forming time, at a forming voltage of +8V (red) and +10V (black). Both experimental SETups use a 10 kΩ resistor in parallel. N: total number; μ: mean value; δ: standard deviation. b): Resistance after electroforming plotted vs. the serial resistance used during forming. Forming voltages are +8V (red) and + 10V (black).

resistor in parallel to avoid sample damage.

6.1.2 Current Control

One inherent difficulty associated with electroforming is the dichotomy between forming voltage and time. Low forming voltages are beneficial since they lower the risk of irreversible dielectric breakdown that increases strongly with higher forming voltage, but the times needed to form the MIM-cells can be unrealistically long for application (> several hours in extreme cases). An elegant way to solve this problem is to use ohmic resistors in series with the MIM-cell, since the resistor does not only act as an instantaneous current compliance, but can also be used to define the formed resistance of the MIM-structure. Figure 6.2 b) can be seen as a proof of principle: the resistance of the MIM-cell after the forming procedure R_{formed} is plotted for different serial resistors for + 8V and + 10V. Note that the data point at 30 Ω approximates the resistance of the measurement setup and does not use a dedicated resistor. Without a resistor in series, R_{formed} is, in this case, too low for resistance switching and can be considered as a dielectric breakdown, while a clear increase of R_{formed} is observed when a large serial resistance is employed during forming. The formed resistance decreases for increasing voltage but increases with the resistance in series. Since this setup acts as a voltage divider, the total resistance is the sum of both contributions $R_{total} = R_{MIM} + R_{serial}$. Before forming takes place, the high initial value of R_{MIM} means that $R_{total} = R_{MIM}$, which means that the resistor has no significant effect on the electric field gradient in the MIM cell. After forming, the highly non-linear character of $R_{MIM}(V)$ ensure that

R_{total} will be dominated by the R_{serial} at high voltages, while R_{MIM} dominates for low voltages.

6.1.3 Influence of Screw Dislocations

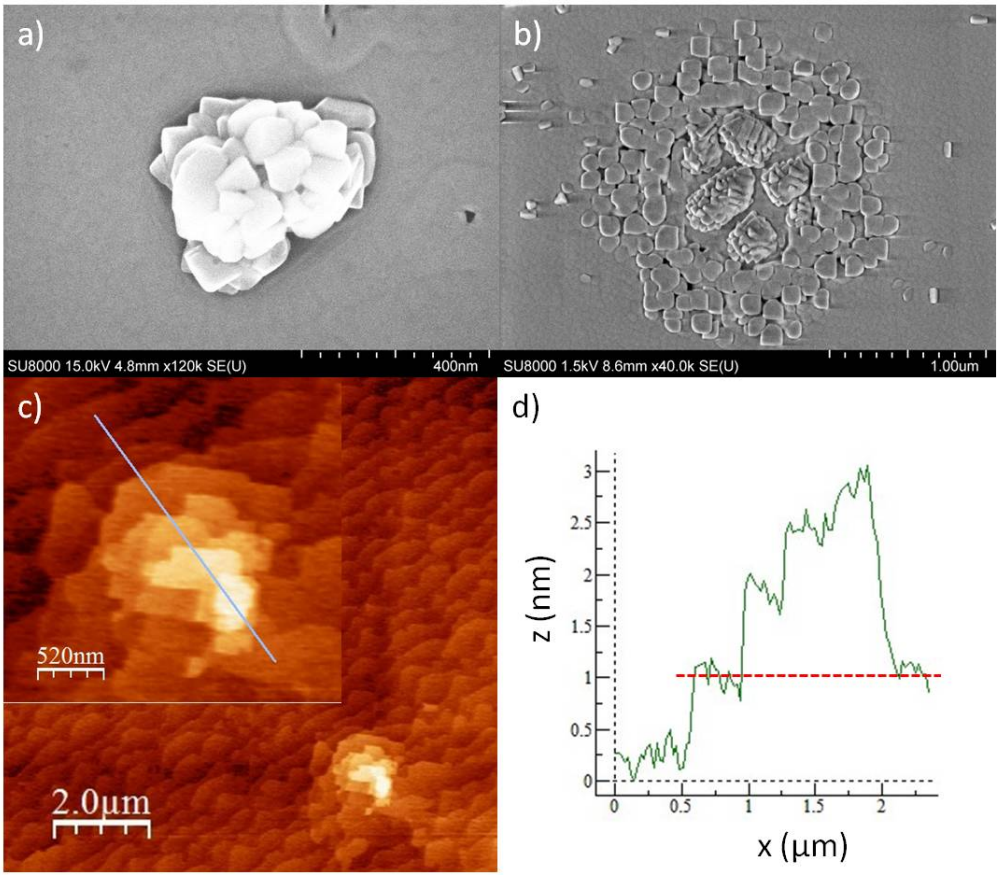

Figure 6.3: a) and b): SEM images of defective regions on an as-deposited $SrTi_{0.95}Fe_{0.05}O_3$ thin film. c) and d): AFM scan of a screw dislocation exit on a recrystallized (001)-surface on a Nb:STO crystal (magnification in inset), and a line scan of the exit, respectively. The dashed red line indicates the level of the crystal surface.

As discussed in 6.1.1, the forming voltage and time are interrelated; however, an unreasonably large standard deviation is observed for the forming-time when a Gaussian distribution is assumed. Together with the simultaneous appearance of hard- and softforming on the same sample as discussed above, this is strong circumstantial evidence for the presence of another factor influencing the electroforming process that is not accounted for. Considering the apparent random character of the forming time and of whether or not a DC-voltage treatment is necessary, the

most likely reason for this behavior are defects that are statistically distributed in the sample.
An examination of the surface of a 100 nm $SrTi_{0.95}Fe_{0.05}O_3$ film after growth by high-resolution scanning electron microscopy (SEM) reveals defective areas varying in size between several μm and a few tens of nm. Two representative examples are depicted in figure 6.3, others can be found in the appendix (section 9.4). A comparison of the defect shown in figure 6.3 a) with the AFM-picture in c), which shows the exit of a screw-dislocation on an annealed Nb:STO (001)-surface, demonstrates that the size-regime of the crystal surface that is affected by the dislocation's strain-field is comparable to that of the defective region on the grown film. From the line scan shown in figure 6.3 d), it is possible to estimate the size of this area to ~ 1 μm. For a screw dislocation, the Burger's vector is parallel to the dislocation line, which means that the lattice around the dislocation line is distorted into a spiral that advances one Burger's vector for every revolution around the dislocation core. When a screw dislocation intersects a crystal surface, the area around the core is consequently sheared parallel to the dislocation line. During surface recrystallization or thin film growth, adatoms diffusing over the surface are preferentially trapped at the screw dislocation because of the higher density of sites with coordination number > 1 [102]. On a recrystallized surface such as shown in figure 6.3 c), the concentration of step-sites is locally much higher than around it due to the pyramidal shape of the dislocation exit, implying preferred growth at this location.

The nature of the defective regions on the as-deposited thin film can be elucidated by the high-magnification image shown in figure 6.4. The circumference of the defect is circular, with a diameter of $\sim$ 300 nm. The surface-sensitive secondary electron (SE) image - obtained using a low acceleration voltage of 1.5 kV - in figure 6.4 enables the visual evaluation of the structural blocks that form the surface-defect. The single building-blocks of the defect structure are intergrown nano-crystallites of 60 - 80 nm size, growing mainly in a cubic habitus as indicated by the dashed red lines and favoring low-index crystal faces {100} and {111}. Since these are crystal faces that exhibit the highest packing density and therefore the lowest surface free energy, the shape of the crystallites suggests that they are grown under a thermodynamic driving force, rather than ablated from the target in this manner. The nano-crystallites are intergrown in a roughly hemispherical manner, indicating a single core or seed in the center of the hemisphere under isotropic growth conditions. A likely cause for the appearance of these growth defects is the presence of a screw dislocation exit in the crystal surface of the substrate, where the film grows much faster due to the high amount of step-sites around the core.
Another indication that these defect structures are formed during growth, rather than ablated particles on the surface, is the mechanical strain field visible around the larger defect structures. Comparing figure 6.3 a) and b), the former defect - which gives the impression of being composed of two 'cores' - does not cause

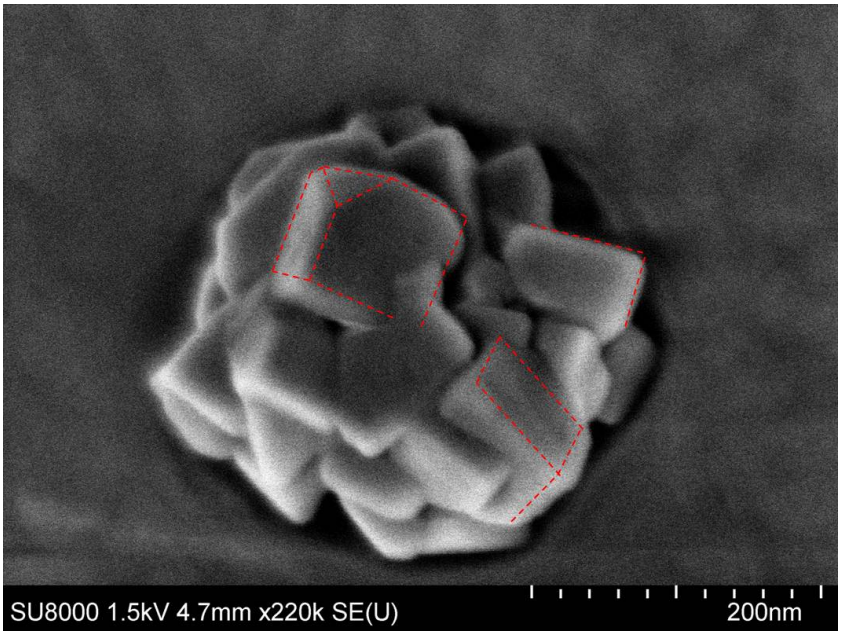

Figure 6.4: SEM image of a structural defect on a 100 nm $SrTi_{0.95}Fe_{0.05}O_3$ thin film. Note the cube on top showing {100} (square) and {111} (triangle) crystal faces.

significant changes in the film around it, while the latter defect induces enough stress to crack the thin film around it. This defect is significantly larger than the former, and seems to be composed an agglomeration of 4-5 single defects, and the combined stress is large enough to induce strain relaxation in the thin film, causing it to grow in square platelets rather than a closed film. These strain fields can again be attributed to the presence of dislocations. In a single crystal, the strain fields around dislocations repulse other dislocations and preserve the crystal lattice. Due to the circular arrangement of these defect features, it seems likely that they originate from the same seed on the substrate, but grow into several dislocations during the fast and non-equilibrium deposition process. For the largest defect agglomerates observed, the area affected by the radial strain field around the defect is approximately 5 μm in size (see figure 9.4 in the appendix).

The influence of the dislocation agglomerates on the electroforming of the 100 nm $SrTi_{0.95}Fe_{0.05}O_3$ film was investigated by selectively depositing electrodes on top of defective areas. To achieve this, a Pt marker structure was deposited via electron-beam lithography, using a positive process on a double PMMA layer. For direct comparison, 30 nm Pt electrode pads of 10x10 μm^2, 5x5 μm^2 and 3x3 μm^2 were sputter-deposited on surface defects and on areas without any visible defects via e-beam lithography. Electrical characterization of these pads was carried out using a 'whisker'-needle with a tip radius of 7 μm.

Figure 6.5 summarizes the characteristics of pads with and without defects on two representative examples: a) shows a SEM image of a large defect after mask-

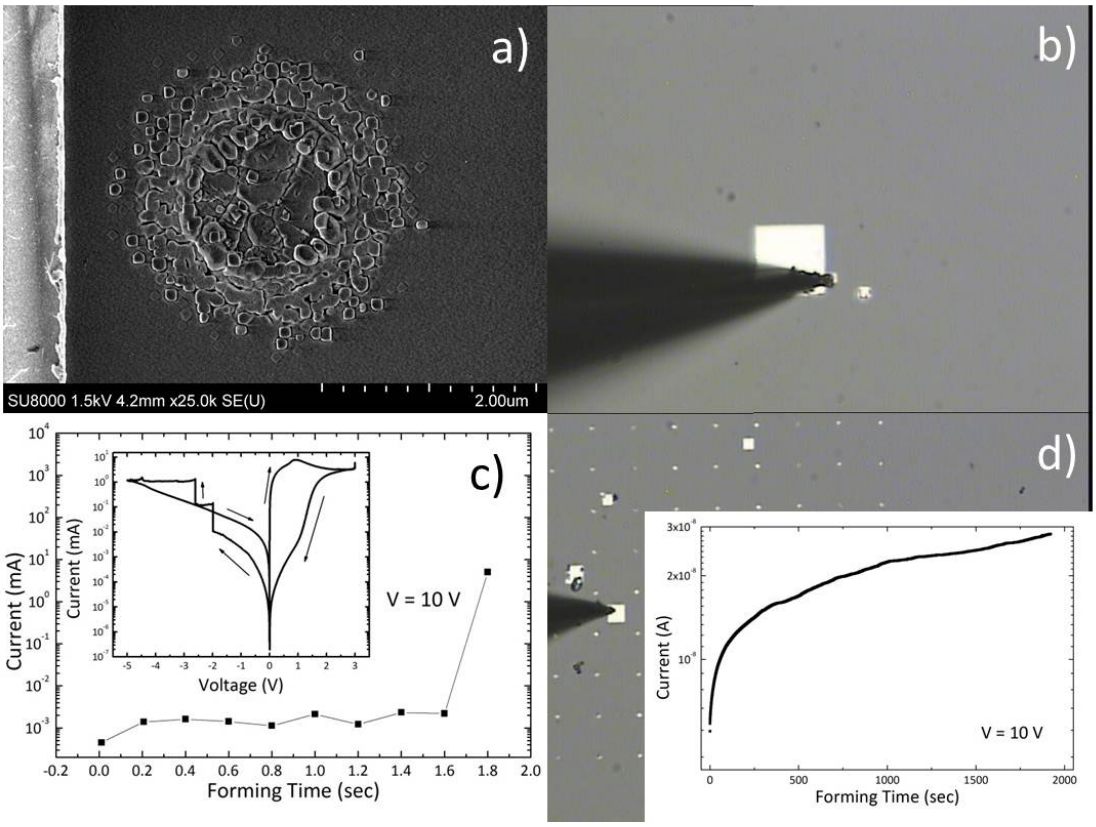

Figure 6.5: a) SEM image of a defect on a 100 nm $SrTi_{0.95}Fe_{0.05}O_3$ film prior to electrode deposition, b) the same defect in an optical microscope, covered with a Pt electrode and contacted with a needle, c) forming current vs. time and current-voltage characteristics (inset), and d) an electrode pad deposited on a defect-free region of the same film, with the current response to a +10V voltage applied for 2000 seconds.

deposition, with the Pt-marker visible on the left fringe of the image, and b) shows an optical microscope image of the same defect after deposition of a 5x5 μm^2 top electrode, contacted with a needle. Figure 6.5 c) shows the electroforming current of this pad, and the I(V)-characteristics after forming in the inset. At a forming voltage of +10 V, the forming current of the defective pad has reached 5 mA after only 1.8 seconds. The I(V)-characteristics of the formed pad is complex in that it exhibits both switching polarities. This can be seen in the "SET"-sweep, where the discontinuous current increases associated with the filamentary "SET"-process are superimposed with voltage regions showing negative differential resistance (constant current between the jumps), which is the hallmark of the homogeneous "RESET"-process. This is the reason why the I(V)-curve crosses itself after a sweep to -5 V, meaning that one polarity could be selected by an appropriate voltage window.

In contrast, a 10x10 μm^2 electrode pad deposited on a defect-free region of the thin film does not show any irreversible resistance lowering after the application of +10 V for over 30 minutes (figure 6.5 d)). In fact, the same electrode pad withstood a voltage of +20 V for 300 seconds before the whole area disintegrated in a large-scale dielectric breakdown. These two exemplary findings are corroborated by several other pads, showing even shorter forming times for electrode pads deposited on defects and no electroforming observable on pads without defects. It is noteworthy that in an unrelated investigation on 200 nm $SrTi_{0.98}Fe_{0.02}O_3$ films, it was impossible to electroform 3x3 and 4x4 μm^2 pads, while 25x25 and 50x50 μm^2 pads were formable with +7 V. It seems that large electrode pads (> 25 μm side length) stand a higher chance of electroforming without the presence of a structural defect. At the same time, larger pads have a higher change of covering a defect, but this case is easily recognized since the forming time is very short.
The conclusions from these investigations are twofold: i) pre-existing structural defects (such as screw dislocations) play a key role for the electroforming process, and the fact that the I(V)-characteristics of the defect-pad is similar to that of "normal" MIM-pads implies that electroforming on a defect-free pad can be interpreted as the creation of a defect-rich region, and ii) that any statistical analysis of the electroforming parameters needs to be corrected for the presence of these defects.

6.1.4 Correlation of Forming Parameters

In order to investigate the systematic influence of the forming voltage on forming probability, time and resistance, rows of 200x200 μm^2 electrodes were patterned from a 30 nm Pt-layer onto a 100 nm $SrTi_{0.95}Fe_{0.05}O_3$ film via optical lithography. Forming experiments were executed in a fully automated prober setup, using a movable sample stage to adjust the sample position under the probeheads. An *Agilent B 1500A* semiconductor analyzer was used for the electrical measurements. The measurement routine was set to apply a defined voltage to the top electrode and hold for 500 seconds or until a current of 5 mA was reached. The resistance of the cell prior to and after the forming was read by a 100 mV I(V) sweep. For the voltages of 8, 8.2, 8.4, 8.5, 9, 10, 10.5 and 11 V, at least 36 pads each were subjected to the voltage bias, and the forming probability was calculated from the number of pads that showed successful electroforming, divided by the total number of biased pads.
As mentioned above, the influence of structural defects has to be accounted for in order to obtain a meaningful correlation between the forming parameters. A detailed analysis of the forming data showed a number of pads in each batch with a low initial resistance, which can be interpreted as related to the presence of large defects under the electrode. These pads were removed from the statistical analysis,

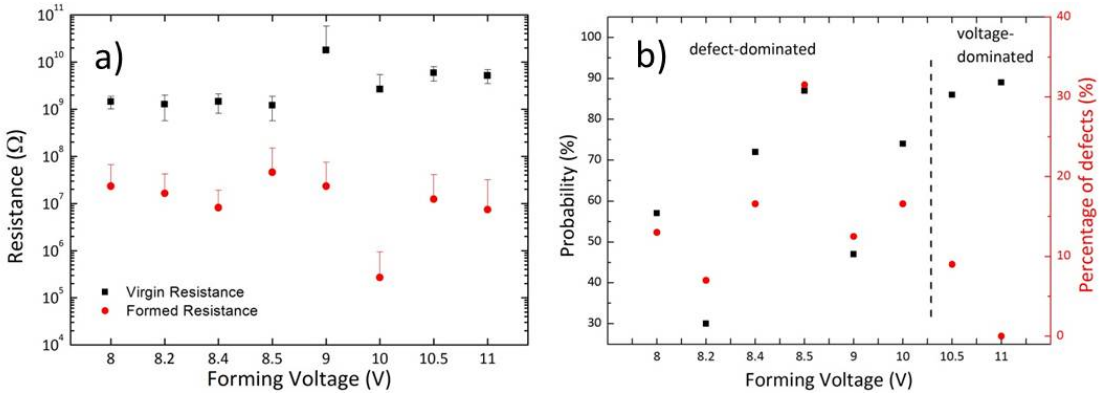

Figure 6.6: a): Average resistances of each MIM-cell array before and after electroforming at the indicated voltage, with a current compliance of 5 mA. b): Probability for electroforming in 500 seconds vs. forming voltage, correlated to the number of defective pads ($R_{virgin} < 1$ MΩ) that were *removed* from the population of the analysis.

and furthermore can be used as an approximation of the probability of encountering a defect under each electrode. The formed resistance shows no systematic variation with the applied forming voltage (figure 6.6 a)) and is comparable for each voltage, implying that the forming current is the decisive factor that determines the resistance after forming. However, the resistance of the MIM-cells was invariably lowered by 1-2 orders of magnitude by the DC-voltage. Figure 6.6 b) shows the forming probability after 500 seconds $P_{form}(500\ s)$ plotted against the applied voltage. It is striking that no systematic variation can be observed, and in fact the forming probability at 8.5 V is much higher than at 9 V, which is counterintuitive. The seemingly random variation of $P_{form}(500\ s)$, however, is correlated to the percentage of pads that were removed from the analysis due to low virgin resistance. To clarify this point, $P_{form}(500\ s)$ was calculated *after* the defective pads were removed from the population of the analysis, therefore the observed correlation is not introduced by the evaluation method. This correlation can be observed for voltages up to 10 V, while higher voltages invariably show a high forming probability irrespective of the defect concentration. In fact, a forming voltage of 11 V yields a probability of 89% even though all investigated pads were found to have high virgin resistance, i.e. the defect concentration is 0.
One interpretation of this correlation is that the amount of electrode pads with low virgin resistance is a measure for the defect concentration on the sample in the area where the measured pads are located. Since all investigated electrodes were close together, the area-concentration of defects is the decisive parameter for the forming probability, at least up to a certain voltage. In other words, the electroforming at voltages below 10 V is probably mediated via pre-existing defects and is therefore a *extrinsic* process, whereas the *intrinsic* forming (i.e. without

pre-existing defects) dominates for voltages above 10 V. One important factor for this is that a low initial resistance of the MIM-pad is only measured when a certain concentration (or size) of defects is reached underneath the electrode, while it is possible for defects to be present without lowering the virgin resistance. Since the virgin resistance is measured by a low-voltage readout sweep, the presence of structural defects could go undetected at 100 mV but decisively influence the pad resistance at applied voltages greater than 8 V.
It should be noted that no appreciable difference was observed in the switching characteristics of *intrinsically* and *extrinsically* formed electrodes. Furthermore, no conceivable distribution of growth defects can logically explain the observed behavior, therefore further studies on the specific influence and distribution of growth defects are necessary.

6.1.5 Summary

The electroforming of thick $SrTi_{1-x}Fe_xO_3$ films is strongly influenced by the presence of **defective regions** in the thin film that grows around **screw dislocation** exits in the substrate during the deposition process. Electrodes deposited on these defects showed forming times of a few seconds or less, whereas electrodes of the same size deposited on the defect-free film could not be electroformed in 2000 s. The low initial resistance of the 'defect-electrodes' enables the homogeneous switching polarity to be observed without a DC forming step.
The **probability** of forming in a certain time can be correlated to the presence of **extrinsic** defects under the electrode pads for voltages below a certain value, which is ∼10 V for a 100 nm $SrTi_{0.95}Fe_{0.05}O_3$ film. The applicability of thick $SrTi_{1-x}Fe_xO_3$ films for memory devices is significantly hindered by the large spread in forming times and the influence of statistically distributed defects.

6.2 Thin Films (≤20 nm)

One of the major criteria for a logical memory is reproducibility - the statistical spread of switching parameters across a sample. Since this is also a very important issue for characterization techniques that require large arrays of switched electrodes, the following paragraph describes a way to improve the reproducibility by reducing the film thickness. The forming voltage is generally lower than the SET-voltage, which reduces the influence of defects since the electrodes are formed during the first I(V)-sweep and no DC treatment is required. In addition, the multi-level capability of thin films is discussed.

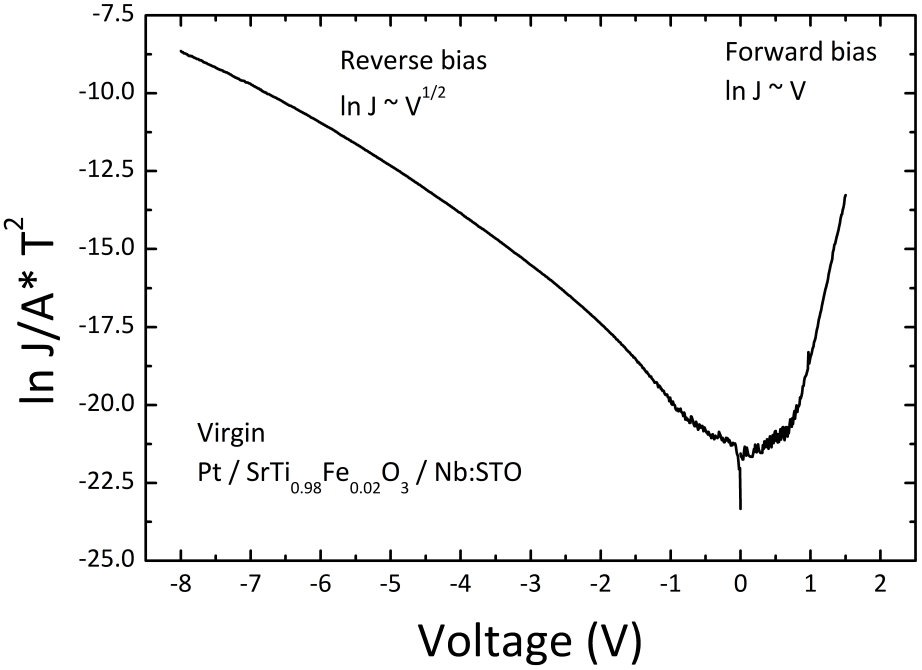

Figure 6.7: Virgin I(V) characteristics of a 10 nm Pt / 20 nm $SrTi_{0.98}Fe_{0.02}O_3$/ Nb:STO MIM cell with dimension 200 x 200 μm^2. Evaluation of the barrier height in foward and reverse direction yields $\phi_b \simeq 0.7$ eV, a depletion layer width of 10.4 nm and an ideality factor of 4.7.

6.2.1 Virgin Cells

The as-deposited cells are often called "virgin" with respect to their electrical properties. The electrical properties of a virgin MIM-cell can be most accurately described by thermionic field-emission across an interface barrier caused by a Schottky contact (see figure 6.7). The forward current can be described by the Schockley equation (see eq. 6.2), while the reverse current includes an image force lowering of the barrier height called the Schottky-effect (see eq. 6.3). The rectifiying properties of the Schottky junction are caused by the difference in work-function of the noble metal electrode and the insulator, and the barrier height can be estimated by the Mott-Schottky relation to Φ_{Pt} - χ_{STO} = 5.65 eV - 4.1 eV = 1.55 eV for $Pt/SrTiO_3$ junctions. This idealized case neglects effect commonly found in practice, such as interface states and traps in the space-charge region. Upon contact, the Fermi-level equilibrates throughout the system, causing electrons to flow from the insulator into the metal and forming a space-charge zone (SCZ) devoid of mobile charge carriers in the insulator. The extension of the SCZ depends on the charge carrier concentration and the static dielectric constant of the material. A

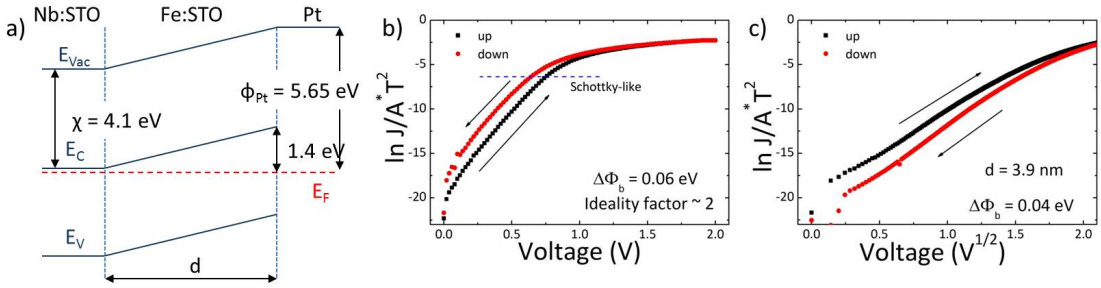

Figure 6.8: a): Schematic energy-band scheme of a $SrTi_{1-x}Fe_xO_3$film of thickness $d << L_D$. The Fermi level is pinned at the top and bottom interface by the electrode materials, respectively. b): Forward current through a Nb:STO/ 4 nm $SrTi_{0.98}Fe_{0.02}O_3$Pt junction. I(V) characteristics follow Schottky-behavior up to $\sim +0.75$ V. c): Reverse current through the same junction.

good measure for the minimum extension of the SCZ is the Debye length:

$$L_D = \sqrt{\epsilon_0 \epsilon_r kT/2e^2 n_0} \tag{6.1}$$

where n_0 is the charge carrier concentration, ϵ_0 and ϵ_r are the permittivity of vacuum and the static dielectric constant of the material, respectively. Using the charge carrier densities calculated by the position of the Fermi energy in the band-gap (see table 5.2), it is possible to estimate the Debye-length based on equation 6.1 as 7.5 nm for a $SrTiO_3$ film, assuming $\epsilon_r = 300$ and $n_0 = 3.7 * 10^{-18}\text{cm}^{-3}$.
Since the Debye-length is a measure for the screening length of electric fields in the solid, we can assume L_D to be a lower boundary of the extension of the SCZ. In reality, the extension of the SCZ is estimated as about 8-10 L_D [103]. From this estimation, it is clear that $SrTiO_3$ films with 20 nm thickness are below 8-10 L_D, and accordingly the system cannot be treated as an ideal Pt/$SrTiO_3$ Schottky-junction since the film thickness is smaller than the minimal value that can be expected for the extension of the SCZ.
Since the $SrTi_{1-x}Fe_xO_3$ film is sandwiched between two materials with a high electron density in the conduction band, the Fermi level in the film can be regarded as "pinned" at both the top and bottom electrode interfaces. In the simplest case, the slope of the energy bands is linear between the two interfaces. This assumption can be made for the case that the film thickness is much smaller than L_D since there is insufficient semiconductor materials to completely shield the electrical field. The $SrTi_{1-x}Fe_xO_3$ film can then be regarded as a triangular barrier for electrons injected at the cathode. This scenario is sketched in figure 6.8 with the example of a 4 nm thin $SrTi_{0.98}Fe_{0.02}O_3$ film grown on Nb:STO and contacted with Pt.
Even though quasi-static current-voltage behavior is not an ideal way to establish the conduction mechanism of a system, if can yield a first starting point to get an idea about the response of the system to voltage stimuli. Figure 6.8 b) and c) shows the up- and down-sweep for forward and reverse bias, respectively. While the

low-voltage regime of the forward current shows $ln(I) \propto V$ behavior, the reverse current shows $ln(I) \propto \sqrt{V}$ over an extended voltage regime. This current-voltage behavior is often ascribed to thermionic-field emission over a Schottky-barrier, reading for the forward direction of transport [103]:

$$J = J_s exp\frac{-eV}{nkT} \qquad J_s = A^*T^2 exp\frac{-e\Phi_B}{kT} \tag{6.2}$$

where J_s is the saturation current, A^* is the effective Richardson constant, e is the elemental charge, k is the Boltzmann constant, T is the absolute temperature in K, Φ_B is the Schottky barrier height and n is the ideality factor of the junction. The reverse current can be described by:

$$J(V) = A^*T^2 exp(-e/kT(\Phi_B + (eE^{00}/4\pi\epsilon_0\epsilon_r)^{\frac{1}{2}}) \tag{6.3}$$

Equation 6.2 can be evaluated for the I(V) behavior shown in figure 6.8 b), and yields a barrier height of 0.49 eV and 0.43 eV and an ideality factor of 2.19 and 2.22 for the up- and down-sweep, respectively. The deviation of n from 1 demonstrates that the junction is not perfectly described by the thermionic-field emission theory. Rather, $n = 2$ is expected for a p-n junction where recombination of carriers in the space charge zone dominates the observed current.
We can assume that recombination is strongly enhanced in the acceptor-doped $SrTi_{1-x}Fe_xO_3$ film, which is depleted of electrons and contains ionized acceptors (Fe^{3+}) and empty electron traps (e.g. $V_O^{\bullet\bullet}$). The evaluation of the barrier height implies that Φ_b is lowered during the "SET"-sweep. Using equation 6.3, the barrier height can be evaluated for the "RESET"-sweep to 0.51 eV and 0.55 eV for the up- and down-sweep, respectively. This is unexpected since the barrier height in reverse direction is lowered due to the image force effect [103], but the difference in barrier heights implies a regeneration of the barrier during "RESET". The slope of the I(V)-curves yields a first approximation of the depletion layer width of the junction through:

$$\ln(\frac{J}{A^*T^2}) = \frac{-e\Phi_b}{kT} + \frac{e}{kT}\sqrt{\frac{e}{4\pi\epsilon_0\epsilon_r d}}\, V^{\frac{1}{2}} \tag{6.4}$$

It has been argued that for thermionic field-emission, the electron passes through the barrier sufficiently fast that the lattice is not polarized by the electric field of the electron, and the optical dielectric constant $\epsilon_\infty = 5.6$ should be used instead of the static dielectric constant ϵ_r [104]. Evaluating equation 6.4 with either value, we find a depletion layer width of 73 pm for $\epsilon = 300$ and of 3.9 nm for $\epsilon = 5.6$, which is in agreement with the assumption made by Dietz *et.* al since the film thickness is ~ 4 nm in this case and a value of 73 pm is shorter than a Ti-O bond. The above considerations yield two important conclusions: i) the barrier height in these junctions is much smaller than it would be expected from the Mott-Schottky

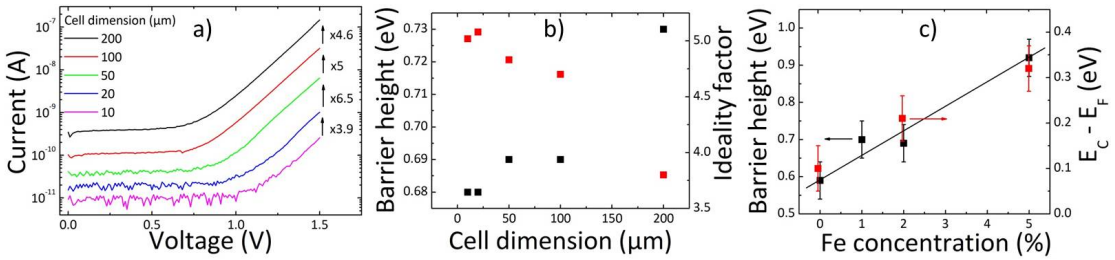

Figure 6.9: Left: Area dependence of the forward current of $Pt/SrTi_{0.99}Fe_{0.01}O_3/Nb{:}STO$ junctions with side-length given in the legend. Center: variation of barrier height ϕ_b and ideality factor n with electrode area. Right: Variation of barrier height ϕ_b with Fe site-fraction, correlated to the position of the Fermi level $E_C - E_F$ in reference samples.

relation Φ_{Pt} - χ_{STO} = 5.65 eV - 4.1 eV = 1.55 eV, and ii) the ideality factor n indicates a significant deviation from the ideal case of thermionic field-emission over a Schottky-barrier.

Increased values of n can be an indication of strong contributions from tunneling currents in the system [103]. The reduced barrier height (compared to the ideal case of 1.55 eV) is likely a consequence of positively charged defects in the $SrTi_{0.98}Fe_{0.02}O_3$ film (e.g. V_O), since a high density of positively charged defects would electrostatically reduce the effective barrier height in the system. Above a voltage of $\sim$ + 0.9 V, the current response to the applied bias is linear, implying that the interface barrier is flattened through the external voltage and charge carriers can flow unhindered through the structure.

The systematic variation of the current with junction area is depicted in figure 6.9 a) for a 10 nm Pt/ 20 nm $SrTi_{0.99}Fe_{0.01}O_3$ /Nb:STO sample. The area dependence confirms that in the virgin state, the whole junction area is active. The correlation between current and electrode area is very good, and deviations between the current and the geometric factors relating the different electrode sizes can be understood by simultaneous variations in the parameters ϕ_b and n (as shown in figure 6.9 b)). The increase of the ideality factor and slight decrease of barrier height with decreasing junction area could be a consequence of an increased circumference / area ratio, and a corresponding increase of electrode edge-effects. The electrode edge causes a locally higher electric field due to the curvature of the field lines [101], and a higher contribution of tunneling currents could be the consequence. It is clear, however, that the calculated values for ϕ_b are higher than for the 4 nm $SrTi_{1-x}Fe_xO_3$ film, although they are still smaller than the value that Menke calculated for Pt/ 500 nm $SrTi_{0.99}Fe_{0.01}O_3$ structures of 1.06 eV [101].

Interestingly, the barrier height for Pt/20 nm $SrTi_{1-x}Fe_xO_3$ junctions varies as a function of Fe site-fraction, as can be seen in figure 6.9 c). This variation is correlated to the position of the Fermi level in the band-gap, which is a function of Fe content (see section 5). The relative differences in ϕ_b and $E_C - E_F$ between the

different Fe-concentrations are identical within the measurement error. Increased values for ϕ_b can be understood as a consequence of a lower charge carrier concentration n_0, which increases the screening length in the material ($L_D \propto 1/\sqrt{n_0}$). The voltage region that can be described by equations 6.2 and 6.3 also depends on the electrode area: while large electrodes with 200x200 μm^2 already shows resistive "SET" behavior at +2V, the 10x10 μm^2 electrodes require voltages of up to +4 V to switch on (for $SrTi_{0.99}Fe_{0.01}O_3$). This relation is not easily quantified since the first switching can be a stochastic process, but the tendency is also observed in 20x20 μm^2 Pt/Ti electrodes and 10x10 μm^2 Rh and Au electrodes (see chapter 8). The latter require voltages exceeding +6 V for the initial SET process ($SrTi_{0.95}Fe_{0.05}O_3$).

6.2.2 Resistive Switching - Thickness Dependence

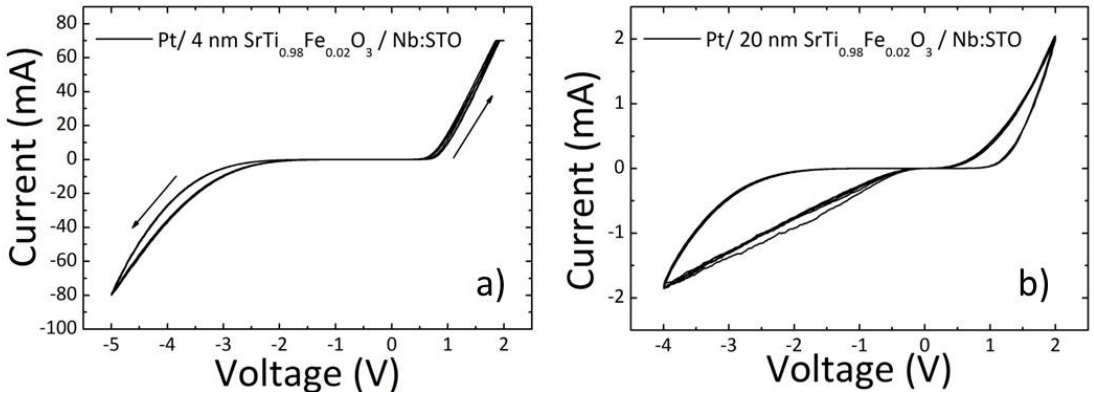

Figure 6.10: I(V)- characteristics for 4 (a) and 20 (b) nm $SrTi_{1-x}Fe_xO_3$ films with Pt top- and Nb:STO bottom electrodes, respectively. The leakage current through the MIM-cell decreases by a factor of 35 when increasing the dielectric thickness 5 times.

In a first step, a 4 nm $SrTi_{0.98}Fe_{0.02}O_3$ film was grown on a Nb:STO substrate and structured with 50 nm Pt electrodes ($\sim$ 200 μm diameter) sputtered through a shadow mask. Figure 6.10 a) shows the I(V)-characteristics of this structure. The current hysteresis turns with the 'homogeneous' polarity, switching the junction to the SET-state with a positive voltage sweep and RESET with a negative voltage. The "SET"- and "RESET"-resistances for the chosen voltages are $2*10^6\Omega$ and $2*10^7\Omega$, respectively, yielding a resistance ratio of 10. Above a voltage of $\sim$ +0.9 V, the current response of the junction is perfectly ohmic with resistance around 30 Ω, which is the line resistance of the setup. The actual junction resistance is therefore smaller, and it can be assumed that electrons tunnel directly from the Nb:STO to the Pt electrode. In reverse bias, the current shows an exponential

dependence on the voltage. The asymmetry of the I(V)-curve is reminiscent of a diode, showing a pronounced forward direction with positive bias. However, the rectification is not very large and significant current is transported under reverse bias, which is likely related to the fact that $SrTi_{1-x}Fe_xO_3$ is not a perfect insulator, but shows some finite conductivity. The I(V)-curves can be qualitatively described by the thermionic field-emission theory with a low interface barrier, as described above.
The comparison to a 8 nm Pt/ 20 nm $SrTi_{0.98}Fe_{0.02}O_3$ Nb:STO film (figure 6.10 b)) shows the influence of the dielectric layer-thickness on the switching characteristics of the junction, the main difference being a much reduced leakage current. The onset of ohmic conductivity in the forward direction can be extrapolated to $\sim +1.3$ V from the intersection with the voltage axis. The current in reverse direction shows ohmic behavior for the up-sweep, albeit with higher resistance than the "SET"-direction. The resistance values for the "SET"- and "RESET"- states with the chosen voltages are $7*10^4\Omega$ and $3*10^7\Omega$, respectively, where the ratio is nearly two orders of magnitude larger than for the 4 nm film.
This simple consideration shows that the thickness of the $SrTi_{1-x}Fe_xO_3$ film is important for the switching properties of the MIM-cell, and points to two possible scenarios: i) the switching process does not occur at the Pt/$SrTi_{1-x}Fe_xO_3$ interface alone, but also in the bulk of the film, or ii) the Pt/$SrTi_{1-x}Fe_xO_3$ "interface" extends well into the film, via e.g. a space-charge region from the Schottky-type contact. Interestingly, the ohmic resistance of the 20 nm device is never smaller than 1000 Ω and therefore larger than the line resistance of the setup, demonstrating that the ohmic behavior is indeed related to the current transport in the MIM-structure.
The leakage current at +2 V in the 4 nm and the 20 nm device is 70 mA and 2 mA, respectively, yielding a ratio of 35. It is clear from this thickness dependence of the leakage current that tunneling currents, specifically charge carrier transport by Fowler-Nordheim tunneling, play an important role, since a ratio of 20 nm / 4 nm = 5 could be expected for ohmic band transport. This is not surprising since at an external voltage of +0.9 V, the nominal electric field strength across the 4 nm MIM-cell is 2250 kV/cm assuming a linear voltage drop across the insulator and Fowler-Nordheim tunneling depends exponentially on the applied voltage. Additionally, the strongly increased resistance ratio points to the fact that the switching process does not happen within a few monolayers of the Pt/$SrTi_{1-x}Fe_xO_3$ interface, but includes the "bulk" of the film as well.
However, the observed current-voltage characteristics during switching cannot be adequately described by the thermionic field-emission theory alone for 20 nm $SrTi_{1-x}Fe_xO_3$ films. Even if an analysis of the exponential current-voltage relation was attempted, one large uncertainty for the evaluation of ϕ_b is the calculation of the current density. There is ample evidence that the switching process is locally confined to an area that can be anything from a few hundred nm to a few μm in

diameter [6, 32]. It would therefore be necessary to control the size of the switching filament for each MIM-cell, which is difficult to attempt $in-situ$. Without precise knowledge of the current density, however, a quantitative evaluation is not possible.

6.2.3 Resistive Switching - Reliability Improvement

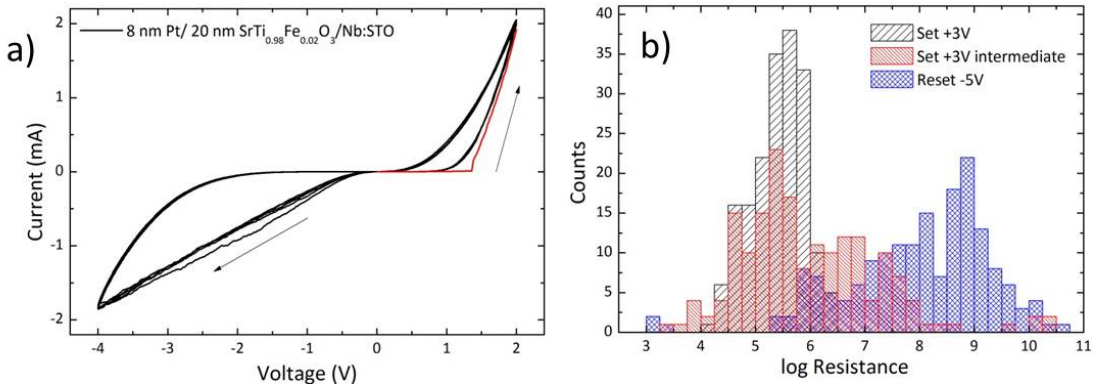

Figure 6.11: a): Representative I(V)-response to a quasistatic voltage sweep between +2V and -4V. b): The logarithm of the resistance after each write-pulse plotted in a histogram.

One major issue with regard to technological application is the reliability of a memory device. For thick films where an electroforming step is necessary, the inherent spread of forming parameters (refer to section 6.1) complicates the use of $SrTi_{1-x}Fe_xO_3$ as a memory-material. However, MIM devices with a 20 nm dielectric layer show much higher reliability as well as only a single switching polarity. Figure 6.11 a) depicts the switching cycle of a 8 nm Pt/ 20 nm $SrTi_{0.98}Fe_{0.02}O_3$ Nb:STO stack, with the first softforming sweep highlighted in red. The I(V)-curve is steady and shows no current jumps except in the first cycle, with a transition to the ohmic regime for high positive voltages, as discussed in section 6.2.2.
To investigate the reliability, an automated switching setup with fixed switching parameters was used. The sample was mounted on an automated stage and translated under the fixed needles, which adressed each 200 x 200 μm^2 pads with the same voltage pattern. For the "SET"-process, a voltage of +3 V was applied for 3 seconds to the Pt top electrode, and the resistance was subsequently read with a 100 mV low-voltage readout. For the "RESET"-process, pads were first written into the "SET"-state by the above procedure, and subsequently written into the "RESET"-state by a -5V voltage applied to the top electrode for 3 seconds. The statistical evaluation of the resistances that were read after each 3s-pulse is shown in figure 6.11 b) in form of a histogram, plotting the number of pads in a given

resistance interval against the logarithm of the resistance. Each histogram is based on a population of 180, the resistance value are shown in table 6.1. Considering the quasistatic I(V)-response of the virgin MIM-cell, it is clear that a softforming process happens at a voltage of $\sim +1.4$ V in the first voltage sweep. As a consequence, a voltage pulse of +3 V can be considered reliable to set the cell into the LRS, improving the device yield up to 100%. This is not only important for applications, but for many characterization techniques as well when larger arrays are needed. This improvement of the reliability is not limited to Pt electrodes, but can be observed for other materials as well, such as Rh, Au or Ti/Pt stacks.

Table 6.1: Root-mean-square (RMS) resistance values calculated from the data shown in figure 6.11. σ: standard deviation, N: population.

	SET (+3V)	RESET - intermediate (+3V)	RESET (-5V)
RMS	5.36	5.99	7.97
σ	0.76	1.26	1.32
N	183	176	176

6.2.4 Multilevel Capability

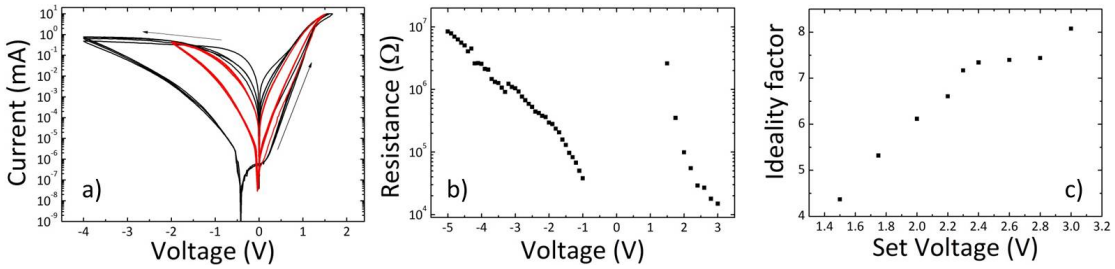

Figure 6.12: a): I(V)-curves recorded different voltages (see text). b): Dependence of the resistance on the SET- and RESET-voltage. c): Ideality factors evaluated from the slope of $ln(I)$ vs V for different SET-voltages.

From a technological point of view, the possibility to control the resistance value in a continuous manner is highly attractive since it opens the possibility to program several bits into the same cell. This multi-level capability is also interesting from a physical point of view since the continuous change of resistance does not agree with the physical model of the discontinuous formation and rupture of a conductive filament. The current-voltage characteristics for two different sweep amplitudes of a 200 nm Pt/ 21.5 nm $SrTi_{0.95}Fe_{0.05}O_3$ Nb:STO sample are shown in figure 6.12 a). The I(V)-curve shows the characteristic asymmetry of a thin film device, with a very pronounced NDR-region on the upsweep for a negative voltage polarity. One remarkable feature of the I(V)-curve is the absence of any

discontinuity or current jump. This implies that the state-variable of the memristive device changes continuously with the applied voltage amplitude, instead of abruptly at a threshold voltage. This is shown in figure 6.12 b), which plots the resistance values (read at +100 mV) after each SET and RESET process against the respective SET- or RESET-voltage. The written resistance shows a roughly exponential dependence on the voltage amplitude of the write sweep, which implies that the state variable of the memristive device is exponentially connected to the voltage amplitude. With voltage amplitudes between + 3V and - 5V, the resistance can be varied by about 3 orders of magnitude.

6.2.5 Temperature Dependence

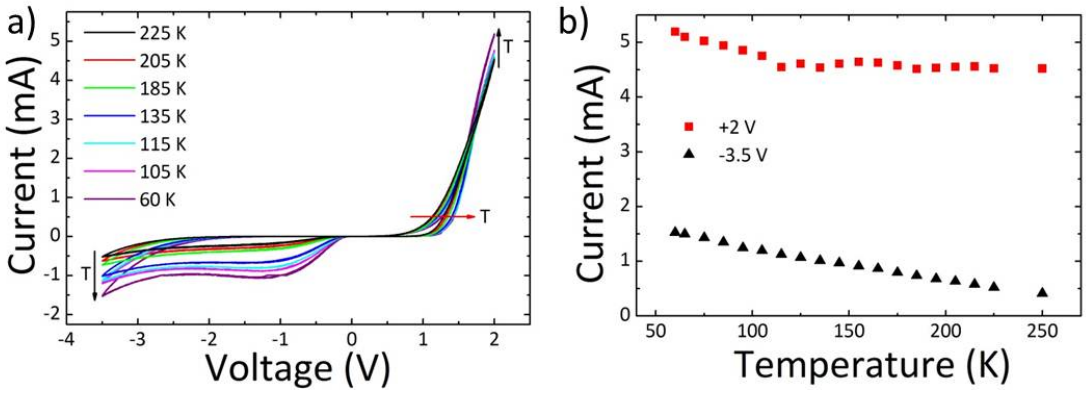

Figure 6.13: a): I(V) curves measured at temperatures between 225 K and 60 K. The tendencies of SET and RESET current as well as the threshold voltage are marked with arrows. b): SET (red squares) and RESET (black triangles) current as a function of temperature, as determined from the I(V) curves. The temperature behavior implies metallic conductivity in the high voltage regime for both polarities.

The same sample (200 nm Pt/ 21.5 nm $SrTi_{0.95}Fe_{0.05}O_3$/ Nb:STO) was cooled down to 50 K in a He cryostat equipped with electrical probes, and I(V) sweeps were taken at 10 K intervals. At each temperature, the system was equilibrated for 5 minutes prior to the measurement. The SET and RESET voltages of each sweep were +2 V and -3.5 V, respectively. The evolution of the I(V) curves with temperature is shown in figure 6.13 a), restricted to selected temperatures for the sake of clarity. Each I(V) sweep was executed several times to establish a stable hysteresis loop and eliminate possible drifts of the resistance.
The SET and RESET currents increase with decreasing temperature, indicated by the black arrows in figure 6.13 a) and quantified in figure 6.13 b). The temperature behavior and the weak temperature dependence enforce the impression that

at both SET and RESET voltages, charge carrier transport is 'metallic'. This corresponds to a situation where internal electric fields in the junction are negligible in comparison to the externally applied voltage, and charge carrier transport is mainly limited through scattering at defects.
More information can be gained from the voltage dependence of the current under both polarities. The exponential current-voltage relation at low positive voltages fits well to either a *pn*- contact or a Schottky-type barrier, and the linear 'high voltage' regime can also be expected for both scenarios. The reverse current of the switched junction is markedly different from that of the Schottky-type barrier that is observed in the Virgin state (see section 6.2.1), and is reminiscent of the reverse current direction in a *pn*-contact. In an ideal *pn*-diode, the reverse current saturates at a given value J_0, which is dependend only on the material properties of the carriers in the junction [103]. The saturation current is (ideally) voltage independent and therefore shows a pronounced NDR behavior, similar to the switched samples.
As mentioned before, the SET sweep shows a transition from an insulating behavior at low voltage to a highly conductive, linear behavior at high positive voltages. The forward voltage V_F at which this transition occurs increases as a function of temperature, as indicated by the red arrow in figure 6.13 a). Selected values of V_F are displayed as red dots in figure 6.15 a), showing a clear decrease with increasing temperature. The values are determined by a linear extrapolation of the high-voltage regime to the voltage axis (see figure 6.14). Similarly, the voltage values where measurable conduction occurs under reverse bias V_R are drawn as

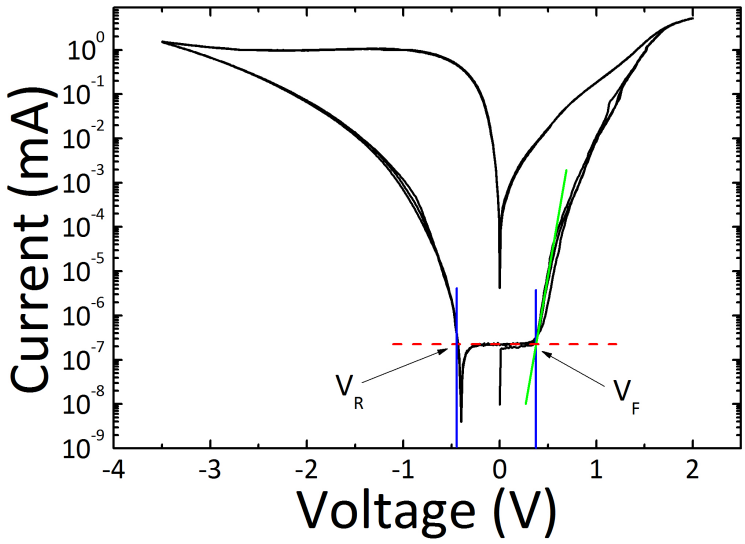

Figure 6.14: I(V) - characteristics of a 200 nm Pt/ 21.5 nm $SrTi_{0.95}Fe_{0.05}O_3$ Nb:STO device at 60 K. The values for V_F and V_R are marked by arrows and blue lines.

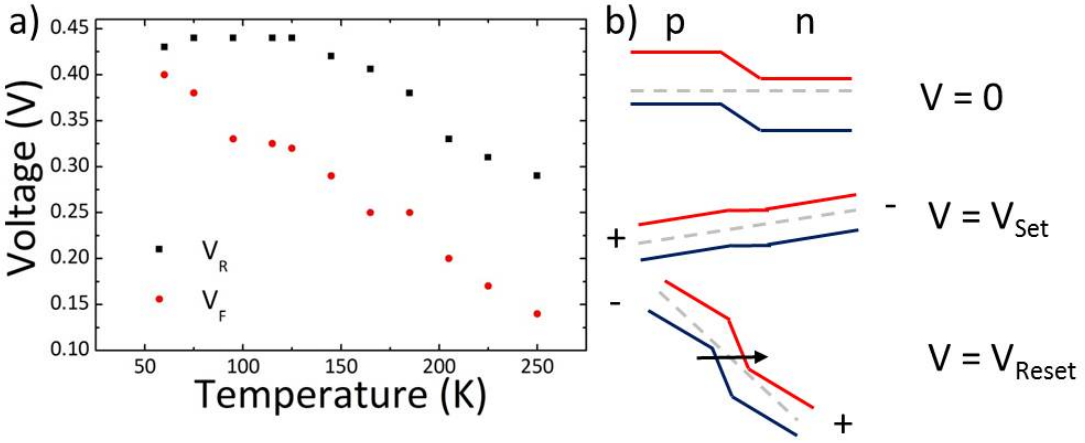

Figure 6.15: a): Forward (V_F) and Reverse (V_R) voltage as a function of temperature. V_F values are extrapolations of the linear region in the I(V)-curve to the voltage axis. b): Band schemes for the unbiased junction (V = 0), forward bias (V = V_{SET}) and reverse bias (V = V_{RESET}).

black squares in figure 6.15 a), showing a very similar temperature behavior as V_F. Both voltage values increase with decreasing temperature and therefore exhibit a negative temperature coefficient (NTC) of the conductivity.
The negative temperature coefficients (NTC) of the breakdown voltage in Si-diodes is a sign of tunneling currents that occur for $V \leq 4E_G/q$ [103]. In the model of a *pn*-junction, the temperature and voltage dependence of the forward and reverse currents in the $Pt/SrTi_{0.95}Fe_{0.05}O_3$ / Nb:STO junction can be schematically depicted as shown in figure 6.15 b): without external bias (V = 0), the *p*-type and *n*-type regions are separated by a depleted SCZ. Under large forward bias in the conductive regime (V = V_{SET}), the slope of the energy bands is dominated by the external voltage and the voltage drop over the *pn*-region is comparatively small. This is a consequence of the strong electron injection from the cathode and is known as high-injection [103]. Under reverse bias, the applied voltage distorts the *pn*-region in such a way that tunneling currents become dominant. The width of the tunneling barrier is the spatial separation of the *p*- and *n*-region, which depends on the reverse bias, and the tunneling barrier height corresponds to the band-gap.

An analytical description of the memristive system is significantly complicated by the fact that in contrast to Si, acceptor doping in $SrTiO_3$ does not induce holes in the valence band as long as the acceptors are compensated by oxygen vacancies. The Fe concentration in the $SrTi_{0.95}Fe_{0.05}O_3$ film corresponds to 8.4 * 10^{20} cm^{-3}, and we can assume that Fe contributes significantly to the electronic structure at this level [36]. It is very likely that a *pn*-type contact evolves in the film between

regions that are heavily doped with either Fe or oxygen vacancies, and correspondingly the energy difference between 'conduction' band and 'valence' band are not given by $SrTiO_3$ but by the difference in doping energy levels. This might explain why V_F and V_R have small values, which would not be expected for $SrTiO_3$ with a band gap of 3.2 eV.

6.2.6 Switching Model

A simple model for memristive behavior in oxidic MIM-structures is the presence of a conducting and an insulating region in the oxide, which are connected in series. Changing the respective amount of these phases by the movement of oxygen vacancies changes the resistance of the system [105]. This idea is conceptually similar to the *pn*-junction discussed above and is reflected in figure 6.16, showing an idealized Pt/ $SrTi_{1-x}Fe_xO_3$ / Nb:STO cell in possible configurations for Virgin, SET and RESET.

As discussed in section 6.2.1, the Virgin cell is characterized by a Schottky-like rectifying behavior. The interfacial barrier height (0.6 eV to 0.9 eV, depending on the Fe doping) indicates a moderate amount of oxygen vacancies in the thin film, which is confirmed by spectroscopic methods in section 5.3.1. The film can be assumed to be depleted of charge carriers since the film thickness is smaller than the expected extension of the SCZ (8-10 L_D). This situation is sketched figure 6.16 a), and the corresponding scheme of a band energy diagram reflects the pinning of the Fermi level at both top and bottom electrode interfaces.

The cell is switched into the SET state by applying a positive voltage to the top electrode, repulsing the positively charged oxygen vacancies from the top interface and creating a thin, vacancy-depleted (oxidized) region under the top electrode. The internal redistribution of oxygen vacancies creates a *pn*-type contact inside of the MIM-structure, which is schematically shown in the band diagram. The concentration of oxygen vacancies is correspondingly increased, creating a strong *n*-doping (and of course, the bottom electrode itself is degenerately *n*-doped $SrTiO_3$), whereas the vacancy depleted region near the top interface is '*p*-type'. The junction is too confined for a full SCZ to develop - SCZ extensions of several hundred nm can be expected for Nb:STO / Fe:STO *pn*-junctions [106].

For small voltages, it is more appropriate to describe the junction with a tunneling gap *d*. The electrical transport through the MIM structure at low voltages is dominated by tunneling currents between the *n*-doped side and the top electrode, and the size of *d* determines the resistance that is read with low voltage signals. In this scenario, the tunneling barrier *d* corresponds to the width of the vacancy depleted, *p*-type region. The strong electron tunneling is reflected in the increasing ideality factor *n* with increasing SET voltage (see figure 6.12 c)), which can be interpreted as a decrease of *d*. After a high voltage SET process, the junction is reminiscent

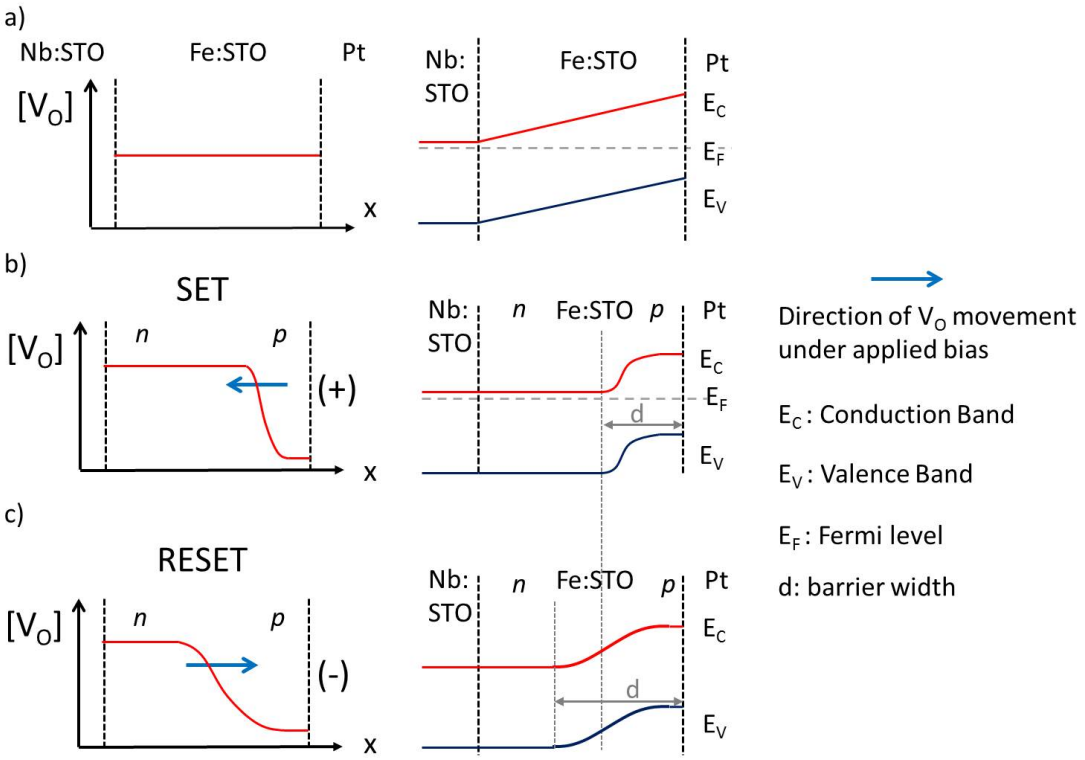

Figure 6.16: Schematic model of the homogeneous switching mechanism in thin $Pt/SrTi_{1-x}Fe_xO_3$ /Nb:STO junctions. a): Virgin state in full depletion approximation. b) The SET process creates an oxygen vacancy depleted, *p*-type region close to the top interface, resulting in an internal *pn*-junction in the material. Charge carrier transport at low voltages (read currents) are dominated by tunneling through the gap d. c): resetting the junction via a negative voltage broadens the gap d and decreases the low voltage tunneling currents.

of a Zener diode with two heavily doped regions and a correspondingly small SCZ. Sweeping the voltage to negative values then produces the NDR region, which can be interpreted as the reverse current of a *pn*-junction. At the same time, oxygen vacancies drift under the applied voltage toward the negatively biased top electrode. This can be interpreted as a broadening of the tunneling gap d since the effective doping level in the middle of the film (where n and p-type regions meet) is reduced through mutual compensation. In other words, the positively charged oxygen vacancies are compensated by the negatively charged acceptors, locally reducing the effective doping concentration. The 'full RESET'-situation would be the restoration of the Virgin state with homogeneously distributed oxygen vacancies and a Schottky barrier at the top interface. The actual decrease of the current during the RESET sweep can be seen as a product of the $V_O^{\bullet\bullet}$ drift, which reduces the slope of the energy bands and increases d.

The continuously tunable resistance can be interpreted as a tuning of the tunneling gap d between the top electrode and n-type regions by varying the applied voltage and correspondingly the electric field gradient in the cell that causes the oxygen vacancies to move. Low voltage readout currents are dominantly tunneling currents, whereas charge-carrier transport under the high voltages can only be described by taking into account the distortion of the energy band structure by the external voltage (Fowler-Nordheim tunneling and thermionic field-emission). Note that due to the same phenomenological description of pn-junctions and Schottky barriers by the Shockley equation, forward currents for both types may be very similar and occur simultaneously. The same situation would arise for undoped $SrTiO_3$ where an intrinsic region would be created instead of a p-type region, therefore this description is not limited to $SrTi_{1-x}Fe_xO_3$ films.
This model is supported by preliminary electron holography investigations, another promising technique for the characterization of MIM-cells. This technique is

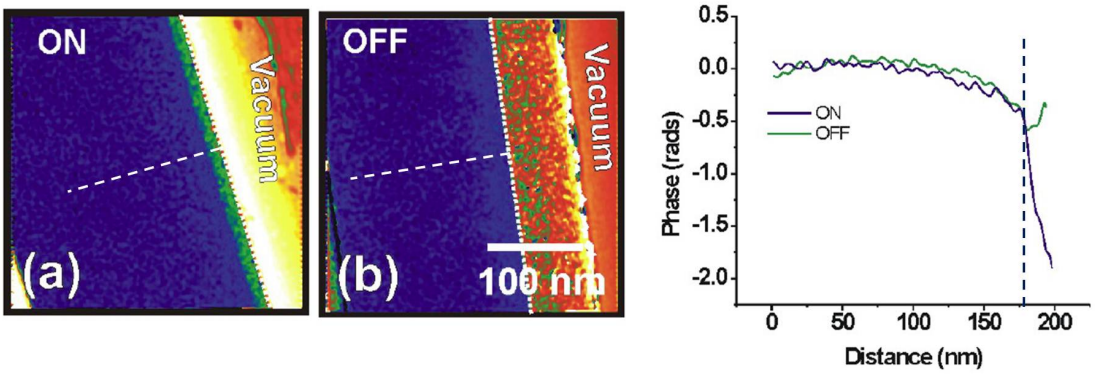

Figure 6.17: (a) and (b): electron holography phase images recorded on a Nb:STO/$SrTi_{0.99}Fe_{0.01}O_3$ /Pt sample in the SET (On) and RESET (Off) state, respectively. The phase along the dashed white lines is shown in the diagram, showing a change corresponding to 0.8 V in the SET (On-) sample whereas the potential is almost flat in the RESET (Off) case. Measurements performed by D. Cooper at CEA LETI.

sensitive to local electric fields in the solid, and can yield quantitative information about the energy bands in switched samples. The phase shift of an electron passing through the sample is compared to a reference beam, and can be evaluated in terms of a local potential. Figure 9.2 shows electron holography phase images (recorded by D. Cooper at CEA LETI, Grenoble) of two Nb:STO/$SrTi_{0.99}Fe_{0.01}O_3$ /Pt stacks in the SET (On-) state (a) and RESET (Off-) state (b). The false color plots correspond to the phase shift measured in both samples. The green region close to the interface in (a) corresponds to the $SrTi_{0.99}Fe_{0.01}O_3$ film, which is not visible in the phase image of the RESET sample (b). The two phase shifts along a line perpendicular (sketched in white) to the interface are shown in the diagram

next to the images.
The phase is approximately constant across the Nb:STO substrate, and shows a sharp decrease in the $SrTi_{0.99}Fe_{0.01}O_3$ of the On-sample (onset of $SrTi_{0.99}Fe_{0.01}O_3$ is marked with dashed blue line). This shift corresponds to acceptor doping and was evaluated to 0.8 V, which is in agreement with the presence of a region that is strongly depleted of oxygen vacancies in the SET sample. It should be mentioned that the spatial resolution is 3 nm and the region close to the interface to Pt is difficult to analyze. The polycrystalline nature of the Pt electrode make it impossible to utilize this technique in the region where Pt is found. However, the possibility to access changes in the crystal potential is a very powerful tool, especially for *pn*-type contacts and band bending at interfaces.
The considerations given here do not specify the junction area that is active during the switching. Investigations by Muenstermann *et* al. suggest an area scaling of this polarity [32]. However, a scaling of the R_{RESET}/R_{SET} ratio or at least the absolute resistance values would be expected if the whole junction area was active. This can be shown for the Virgin state, but not for the switched states, implying that not the whole electrode area is active during the switching process. The resistance tunability is unlikely to be a product of active junction area only since the area scaling of the resistance is linear and would therefore be observable with different electrode sizes. No indication of this was found.

6.3 Switching Polarity - Thickness Dependence

The observation of two switching polarities on $SrTi_{1-x}Fe_xO_3$ films of 50 and 500 nm thickness indicates that two processes co-exist underneath the same electrode [32]. It can be possbile to 'select' one polarity by the amplitude of the negative bias sweep. However, the filamentary (or eight-wise) switching polarity cannot be observed in Pt/ $SrTi_{1-x}Fe_xO_3$ /Nb:STO junction where the thickness of the insulator is $\leq$ 20 nm. This is shown in figure 6.18 a), where a thin 20 nm (red) and a thick 400 nm (black) film are compared. The I(V) curve recorded for the 20 nm film is completely continuous and no current jumps occur for either polarity, which is a hallmark of the homogeneous (counter-eightwise) polarity as well as the pronounced NDR regime. In contrast, a thick insulating layer (e.g. 400 nm) that requires a dedicated electroforming step displays very stable filamentary switching (black line). The negative voltage sweep for this polarity always shows at least one discontinuity in the I(V) curve, corresponding to an abrupt SET process that is faster than the delay time of the voltage sweep. These 'current jumps' are a hallmark of the filamentary polarity.
$SrTi_{1-x}Fe_xO_3$ films with intermediate thicknesses show both switching polarities in a pronounced way, as can be seen in figure 6.18 b). Here, a 100 nm film shows

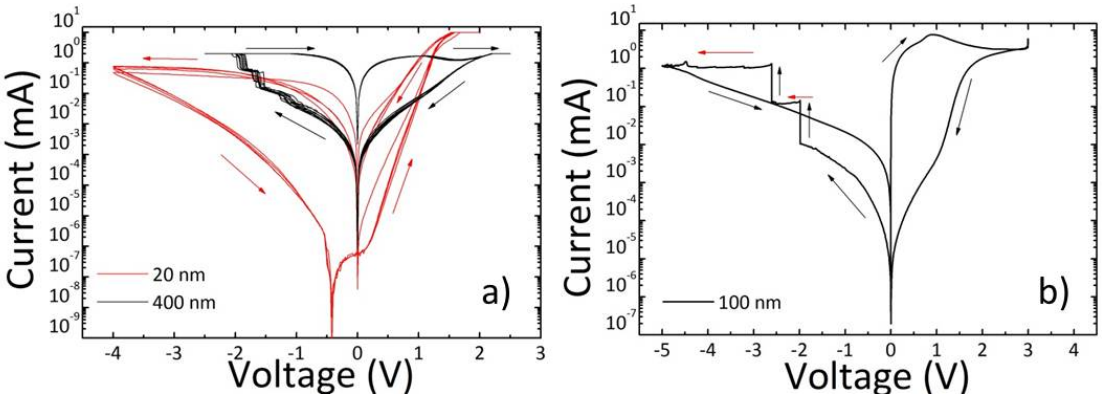

Figure 6.18: a): I(V) characteristis of Pt/ $SrTi_{1-x}Fe_xO_3$ /Nb:STO MIM structures with 20 nm (red) and 400 nm (black) thickness, showing the homogeneous and the filamentary switching polarity, respectively. b): I(V) characteristic of a 100 nm $SrTi_{1-x}Fe_xO_3$ film. The intermediate thickness shows both polarities in a pronounced way, which is the reason for the self-crossing curves.

both polarities in the negative voltage branch. Going from a HRS to negative voltages, the current increases abruptly around -2 V by one order of magnitude. This jump is immediately followed by a NDR regime until the next jump occurs around -2.8 V. Sweeping all the way to -5 V, a pronounced NDR region can be observed that increases the resistance, which results in a self-crossing I(V) curve. The homogeneous contributions to the I(V) curve have been marked with a red arrow, the filamentary contributions with a black arrow. In this case, the filamentary SET has more weight than the homogeneous RESET, and the overall resistance is decreased during the voltage sweep.
Samples using different insulator thicknesses are difficult to compare since the forming process is more or less unique to each pad. However, a tendency of thick films to stabilize the filamentary polarity was observed throughout this thesis. The tendency seems to be that thick films stabilize the filamentary polarity, whereas thin films stabilize the homogeneous polarity.

6.4 Forming-free Thin Film Devices

One very important consideration for MIM-cells using thin $SrTiO_3$ films is that the growth of an oxidizable electrode can change the oxygen content of the oxide thin film. Titanium has the highest oxygen affinity and metal-oxygen bond enthalpy of the $3d$ transition metals [34], which means that it is able to reduce the $SrTiO_3$ interface. In the case of $SrTiO_3$, changes in the oxygen stoichiometry can easily be demonstrated by changes in the electrical conductivity. Figure 6.19 illustrates

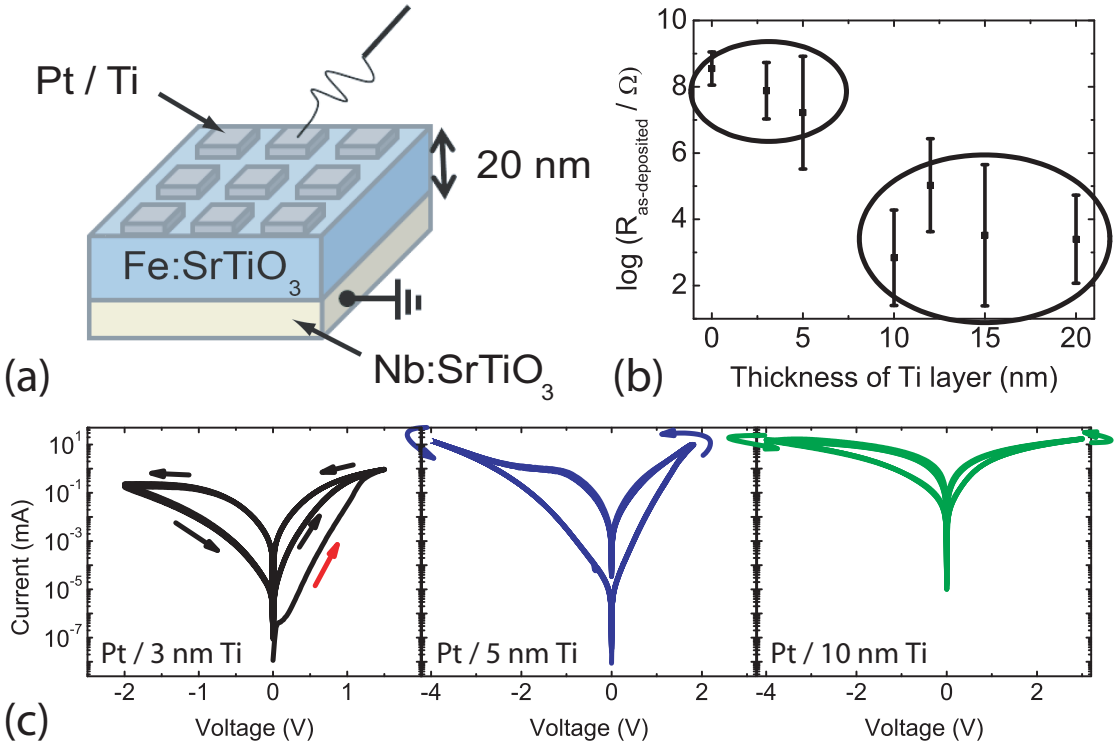

Figure 6.19: (a) Sketch of the sample geometry. (b) Initial resistance of Pt/Ti/Fe:STO/Nb:STO MIM structures vs. thickness of Ti layer determined at ± 100 mV. (c) Representative $I(V)$-curves of samples with different Ti thicknesses. Depending on the Ti thickness and the resulting initial resistivity, samples with Pt/Ti electrodes are forming-free. (adapted from [11])

this fact on the example of MIM-cells from 20 nm $SrTi_{0.99}Fe_{0.01}O_3$ layers with Ti electrodes of different thickness. A systematic study of the initial resistance R_i in dependence of the Ti thickness shows that above a certain critical layer thickness, the R_i of the MIM-stack is drastically decreased (figure 6.19 b)). The initial resistance is decisive in whether or not a softforming step is observed in the first I(V)-sweep. As can be seen in figure 6.19 c), a softforming step is necessary for high R_i, which is typically observed below 5 nm Ti thickness in this particular system, and is not necessary for MIM-stacks with a lower initial resistance. Increasing the Ti thickness further reduces R_i, which is unfavorable for application as resistive switches since the resistance of the "RESET"-state corresponds to the initial resistance, and thus the resistance ratio obtainable by switching is smaller for reduced R_i. However, for suitable combinations of $SrTi_{1-x}Fe_xO_3$ and Ti, the need for a electroforming can be eliminated.

Furthermore, it can be demonstrated that the thickness ratio $Ti/SrTi_{1-x}Fe_xO_3$ is the factor that determines the initial resistance of the MIM-stack. Figure 6.20 shows three low-voltage readout sweeps from two samples with the structure 25 nm

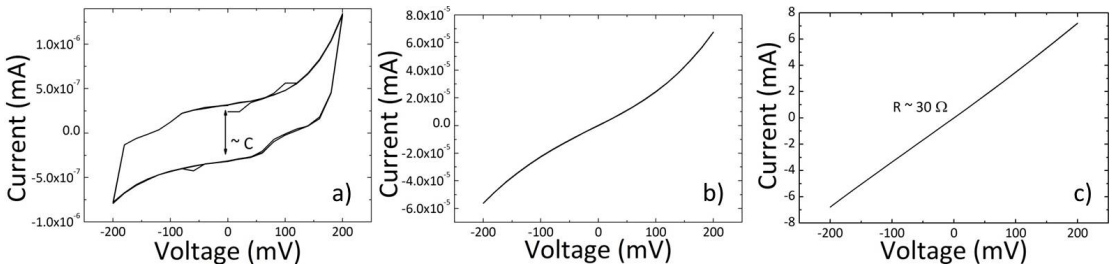

[h]

Figure 6.20: Low voltage readouts of 25 nm Pt/ 5 nm Ti electrodes on 20 nm $SrTi_{0.98}Fe_{0.02}O_3$ (a) + b)) and on 10 nm $SrTi_{0.98}Fe_{0.02}O_3$ (c)).

Pt/ 5 nm Ti/ x nm $SrTi_{0.98}Fe_{0.02}O_3$ Nb:STO with $x = 10$ and 20 nm, respectively. Both figure 6.20 a) and b) show readout sweeps from the sample with the thicker $SrTi_{1-x}Fe_xO_3$ film, the former from a pad with high R_i (10^{11} Ω) and the latter from a pad with intermediate resistance ($\sim 10^6$ Ω). The fact that both resistance states can be observed on the same sample illustrates the sensitivity of the resistance to local thickness variations and sample inhomogeneities, such as defects. In stark contrast, the same 25 nm Pt/ 5 nm Ti electrode deposited on a 10 nm $SrTi_{0.98}Fe_{0.02}O_3$ film yields exclusively MIM-cells with initial resistances ranging from 30 Ω to 120 Ω. These pads can be considered as shortened and cannot be resistively switched.

Again, it can be seen in figure 6.21 a) that initial resistance determines whether or not forming is necessary and the resistance ratio achievable by a given voltage. The I(V)-curve marked with the black line was measured on the MIM-cell with high R_i, while the blue line shows the I(V)-characteristics of the MIM-cell with R_i $\sim 10^6$ Ω. Interestingly, the current at high voltages is independent of the initial resistance, which points to a charge transport mechanism that is correlated to the thickness of the $SrTi_{1-x}Fe_xO_3$ layer. In addition, figure 6.21 b) shows that low initial resistance achieved through Ti deposition is not always irreversible. The depicted I(V)-curve was measured on a MIM-cell with an initial resistance of 200 Ω, which could also be found on the same sample. In contrast to the "conventional" softforming, a voltage sweep to negative values could be used to set the device into the "RESET"-state (the 1st sweep is marked by a red line), after which normal resistance switching occurred. Note that in this case, the switching current is higher than for conventionally formed pads, which means that this so-called "reverse-forming" does not end in the same state as softforming. Note also that this behavior is rarely observed, since the voltage drop in the sample needs to be high enough to induce oxygen-vacancy movement. The low-resistance pads on the 10 nm $SrTi_{0.98}Fe_{0.02}O_3$ film, for example, could not be transferred into a higher resistance state in this way.

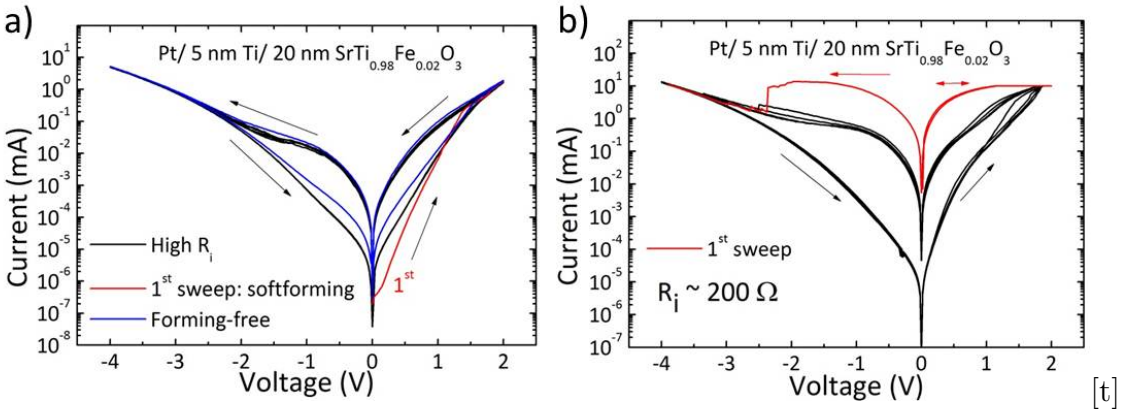

[t]

Figure 6.21: a): I(V)-characteristics of a MIM-cell were softforming is necessary (black line, with the forming sweep highlighted in red) and a forming-free cell (blue). b): MIM-cell showing low resistance after electrode deposition and "reverse-forming".

Chapter 7

Bulk-Sensitive Spectroscopy on MIM Cells: Thick Films

This chapter deals with the investigation of resistive switching samples by means of spectroscopy to gain information about the structural and chemical changes that take place during switching. Since the resistive switching effect in $SrTiO_3$ is non-volatile, all resistive states were written prior to the spectroscopy measurements.
In the first part of this chapter, the application of hard X-ray absorption spectroscopy using focused synchrotron radiation will be discussed. The investigations were done in fluorescence mode and therefore yield bulk-sensitive information. This part of the chapter was published in the Journal of Applied Physics.[6]
Techniques that make use of photo- and secondary electrons are more surface sensitive and discussed in the second part of this chapter. Imaging with secondary electrons at resonant energies can be done by photoemission electron microscopy (PEEM), yielding chemical and spatial information. Hard x-ray photoelectron spectroscopy (HAXPES) is performed with neither imaging nor focused radiation and therefore yields information about large arrays of electrodes that have been switched by identical electrical treatment.

7.1 μ - X-ray Absorption Fine Structure - μXAFS

Memristive devices were fabricated from $SrTi_{0.95}Fe_{0.05}O_3$ thin films with a thickness of 200 nm, grown by pulsed laser deposition (PLD) on a conducting Nb-doped $SrTiO_3$ single crystal. A 30 nm Pt layer was sputtered onto the insulating layer and structured via UV-lithography and reactive ion beam etching (RIBE). These films correspond to the 'thick' films discussed in chapter 6 without defects.
After the initially insulating devices are electroformed with a DC voltage of +7 V (voltage bias applied to the Pt top-electrode), the MIM-structures are switching in a "counter-eightwise" polarity[32] as depicted in Fig. 7.1. The low resistance "SET"-state is reached by applying a negative bias to the top electrode and shows linear I(V)-characteristic in the low voltage readout sweep, whereas the high resistance "RESET"- state is reached with a positive voltage bias and shows a distinctly non-linear I(V)-characteristics.

Iron K-edge XANES experiments were performed at the ID03 beamline at the European Synchrotron Radiation Facility (ESRF), equipped with a monolithic channel-cut Si(111) monochromator and a KB-mirror focusing optics to obtain

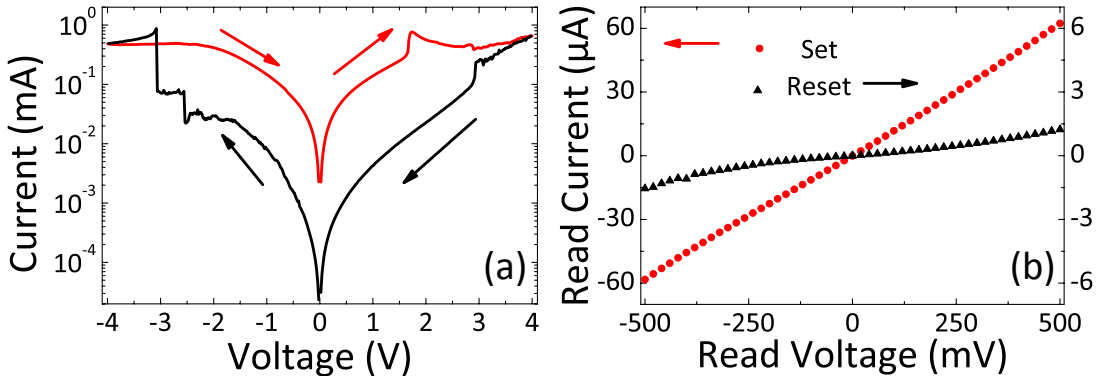

Figure 7.1: (a): Current-voltage characteristics of the Pt/200 nm $SrTi_{0.95}Fe_{0.05}O_3$/Nb:STO memristive device. The switching polarity is indicated by the arrows. (b) Current response to a low read-out voltage, highlighting the change of the conduction mechanism between "SET"- and "RESET"-state (red and black symbols, respectively).

a beam diameter of 7 μm. The Fe K-edge XANES was measured in fluorescence mode by placing the sample and a silicon drift detector (SDD) perpendicular to the incoming x-ray beam (90°-geometry). While the Fe Kα fluorescence derives from the thin film only, the Ti Kα fluorescence, which was measured simultaneously as a reference, has an escape depths of several μm and originates mainly from the substrate.

Iron acts as a B-site acceptor dopant in $SrTiO_3$ and can be used as a tracer to track the valence change and presence of oxygen vacancy associates in the material.[76] As a reference, we will use a Fe-doped $SrTiO_3$ single crystal that has been subjected to a long-term dc voltage at moderately elevated temperature. Such treatment induces an ion concentration polarization and a corresponding oxidation and reduction near the anode and cathode, respectively, which leads to pronounced coloration at the anode (called *electrocoloration*) because of the Fe-doping. Fig. 7.2 shows the Fe K-edge XANES of an as-deposited thin film, compared with two spectra recorded at cathode and anode of the electrocolored single crystal that contains predominantly Fe^{3+} with a significant amount of Fe–$V_O^{\bullet\bullet}$ (cathode), as well as one that contains mostly Fe^{4+} and no Fe–$V_O^{\bullet\bullet}$ (anode; for details, see section 5.1) The spectral difference visible at the strongly reduced cathode (see shoulder S) is caused by the presence of Fe–$V_O^{\bullet\bullet}$ complexes, and the resemblance of the XANES indicates a very similar degree of association of Fe–$V_O^{\bullet\bullet}$ in the as-deposited film and the cathode. However, the MIM-cells remain insulating ($R > 10^{11}$ Ω) because the charge carriers introduced by the oxygen vacancies are partially compensated by the high acceptor doping. Considering Fig. 7.2, it is obvious that the resistance change in the thin film does not rely on the Fe^{3+}/Fe^{4+} redox-pair for resistance change as the film does not contain Fe^{4+}.

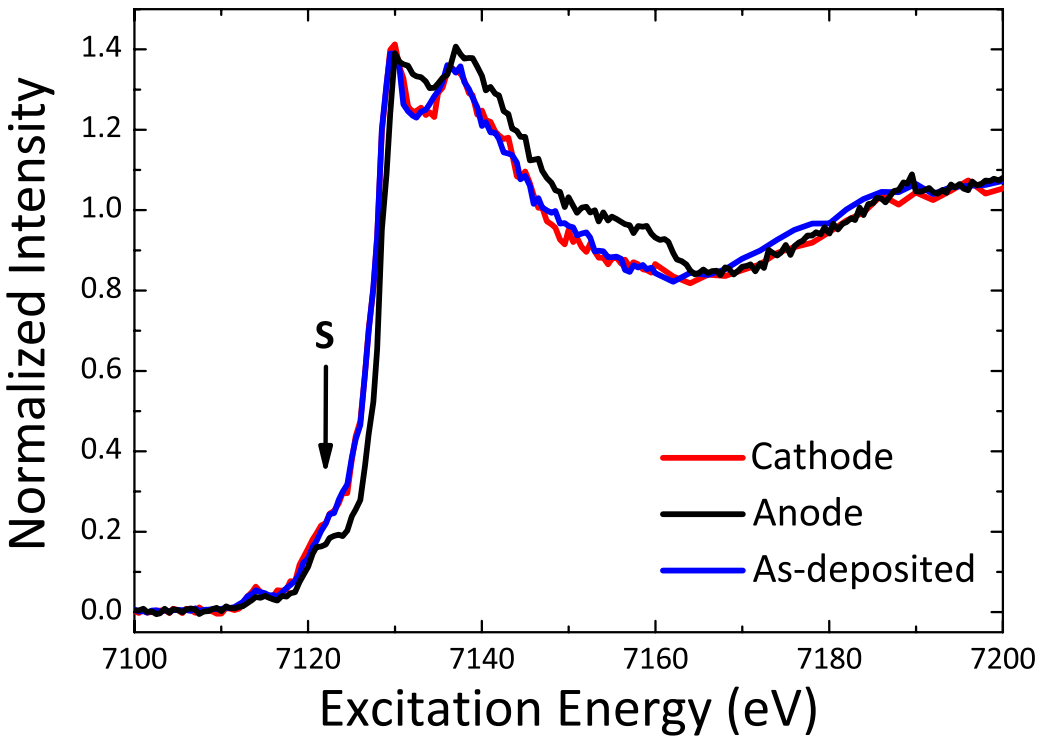

Figure 7.2: Fe K-edge XANES of the as-deposited thin film (blue), as well as the cathode (red) and anode (black) regions of an electrocolored Fe-doped $SrTiO_3$ single crystal.

A micro-focused x-ray beam was used to record XY-maps (Fig. 7.3(a)) of the oxygen vacancy concentration on a MIM structure in the low-resistance "SET"-state by measuring the Fe Kα fluorescence intensity at the excitation energy 7122 eV, i.e. at the maximum contrast in the pre-edge region caused by vacancies and indicated by the shoulder S (Fig. 7.3(b)). The XY-scanning was performed with a step size 2 μm, and an x-ray beam diameter of 7 μm. The mapping reveals a single location with a large fluorescence intensity increase compared to the surrounding electrode (see dashed, red box in Fig. 7.3(a)), which can be attributed to the location of the conducting filament. We note that outside of the electrode area, the apparent increase of S is an artifact caused by a higher total fluorescene intensity since the radiation is not attenuated by the electrode material. The Fe K-edge XANES measured at several locations on the electrode pad (Fig. 7.3(b), blue) and at the filament location (red) confirms that the intensity of S is increased homogeneously over the whole electrode area as compared to the as-deposited film (black). A non-resonant Ti Kα map recorded simultaneously shows the top electrode to be free of holes or structural artifacts that could lead to the observed Fe Kα intensity increase (data not shown here). The Fe K-edge XANES was also

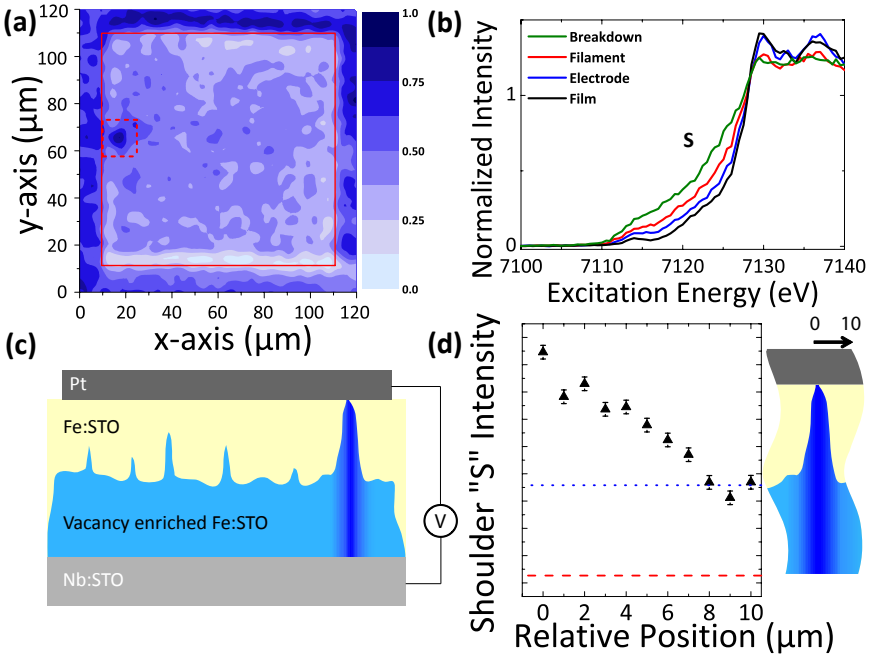

Figure 7.3: (a) XY-map of the Fe Kα fluorescence intensity recorded on a 100×100 μm^2 MIM structure at 7122 eV excitation energy. The solid red line is a guide to the eye indicating the electrode area. (b) Fe K-edge XANES at the filament (red) and several different (blue) locations on the electrode area, the as-deposited thin film (black), and a different electrode pad after "hard" dielectric breakdown (green). (c) Schematic model of the oxygen vacancy distribution in the switched memristive device. (d) Variation of the Fe Kα fluorescence intensity, excited at 7122 eV, from the center to the border of the conducting filament location.

measured on a different electrode pad that had been subjected to an irreversible, "hard" dielectric breakdown (green), after which the overall MIM resistance was ∼200 Ω. The similarity of the two filaments suggests that the physical mechanism leading to "hard" and "soft" breakdown is identical, and that only the magnitude of this effect is relevant for the resistive state. Local conductivity investigations on Fe-doped $SrTiO_3$ MIM-structures show an increase of conductivity localized to ∼1 μm, while the remaining area under the electrode remains highly insulating.[32] The presented μXANES study demonstrates that during electroforming, the field-induced migration of oxygen vacancies is initially homogeneous over most of the electrode area, until electrical breakdown is achieved at a single point under the electrode. Fig. 7.3(c) combines the conclusions of both experiments in a schematic sketch of the oxygen vacancy distribution in the memristive device. The darker color highlights that the filament is structurally different from the surrounding material, as will be discussed later. It is readily apparent from the profile scan shown in Fig. 7.3(d) that the observed intensity drop is correlated to the beam

size on the sample, since the intensity of S has dropped to the level observed on the whole electrode area (indicated by the dotted blue line) when the position of the beam is 7 μm away from the maximum of S (position "0"). Since the filament itself contributes no discernible broadening of the intensity decay, it follows that the diameter is much smaller than the beam size and likely <1 μm. For comparison, the intensity of S observed on the as-deposited film is marked by the dashed red line. Close examination shows that the Fe K-edge XANES measured at the

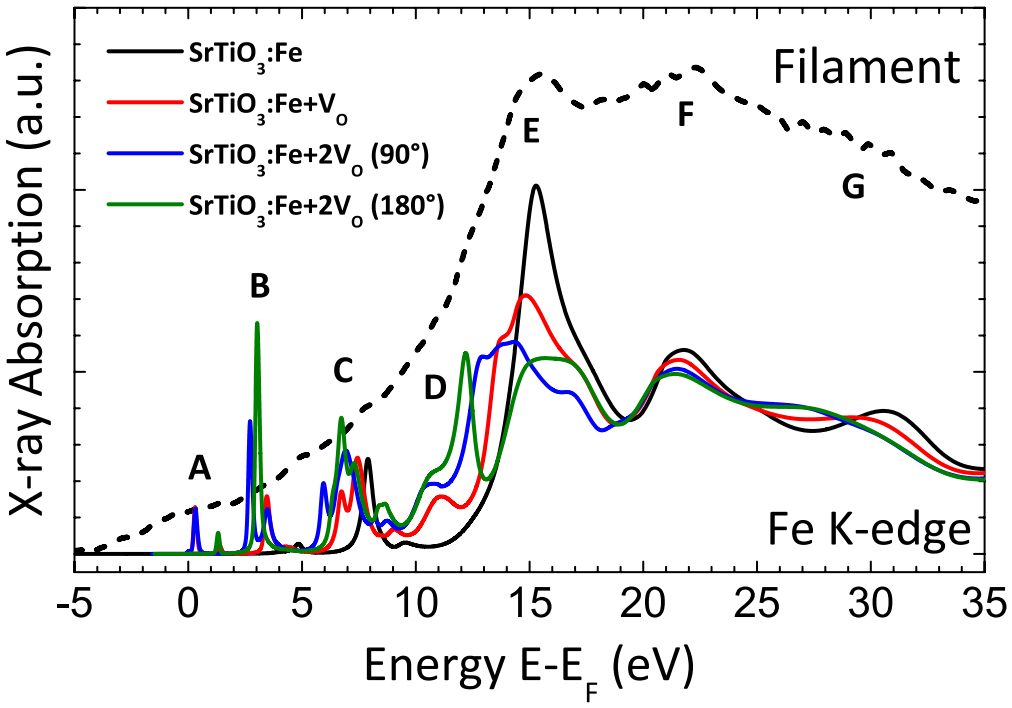

Figure 7.4: (FMS XANES calculations of the Fe K-edge XANES for undistorted $SrTiO_3$ (black), one vacancy (red) and two vacancies (in 90° (blue) and 180° (green) $V_O^{\bullet\bullet}$–Fe–$V_O^{\bullet\bullet}$ configurations) in the first shell.

filament location deviates significantly from that of the surrounding electrode area, with a much stronger increase in intensity of the shoulder S and a decrease of the white line intensity at 7130 eV (Fig. 7.3(b)). While the homogeneous reduction of the electrode can be interpreted as a simple increase of the Fe–$V_O^{\bullet\bullet}$-concentration, the spectral changes at the location of the filament are further examined through self-consistent, real-space full-multiple-scattering (FMS) XANES calculations [76] by the FDMNES code,[60] performed within the quadrupole and non-muffin-tin approximation using the finite difference method (FDM). Fig. 7.4 elucidates the influence of oxygen vacancies on the shape of the Fe K-edge XANES, demonstrating that the decrease of the white line intensity (peak E) and an increase of the shoulder S intensity (corresponding to the peaks C and D in the calculated XANES), as observed at the location of the filament, can be explained by the presence of an ad-

ditional oxygen vacancy in the first coordination shell of the Fe atoms. Moreover, a comparison of our XANES calculations with the experiment suggests that the two oxygen vacancies will most likely occupy nearest sites, forming a 90° $V_O^{\bullet\bullet}$–Fe–$V_O^{\bullet\bullet}$ configuration. It is important to note that the FMS simulations are very sensitive to the coordination geometry of Fe, but do not yield any information about the valence state. In the case of a $V_O^{\bullet\bullet}$–Fe–$V_O^{\bullet\bullet}$ complex, the presence of Fe^{2+} cannot be excluded.

In summary, we have shown PLD-grown $SrTi_{0.95}Fe_{0.05}O_3$ thin films to contain Fe^{3+} and a high degree of Fe^{3+}–$V_O^{\bullet\bullet}$ associates in the as-deposited state. We demonstrate through micro-focused XANES on a resistively switched MIM-structure that electroforming increases the Fe–$V_O^{\bullet\bullet}$ concentration homogeneously over the whole electrode area until local breakdown is achieved. FMS XANES calculations suggest that the observed XANES in the region of the conducting filament can be interpreted by the association of two oxygen vacancies to the probed Fe in the filament region.

Chapter 8

Surface-Sensitive Spectroscopy on MIM Cells: Thin Films

Top Electrode Materials

As an introductory note, a short discussion of the different top electrode materials used for the MIM cells is in order. The standard electrode material is Pt, which was used for most of the I(V)-characterization in chapter 6, which is sputtered $ex-situ$ and is used for HAXPES. However, the Pt 4s emission line is coincident in energy with the Fe2p doublet, which therefore cannot be analysed with photoemission spectroscopy through Pt electrodes. To circumvent this problem, the chemically similar metal Rh was used for the top electrodes. An added benefit is that absorption of photoelectrons in Rh (atomic number: 45) is significantly weaker than in Pt (atomic number: 78), which means a thicker electrode layer can be used for HAXPES. This is beneficial for the switching properties, as will be shown in section 8.2.1.
In contrast to Pt, Au can be sputtered $in-situ$ in the PLD chamber, which can be expected to result in a cleaner interface between metal and insulator. Due to the tendency of Au electrodes to expose the thermally stressed switching craters, samples with Au electrodes are analyzed with PEEM.
Since oxidizable electrodes change the chemistry of the as-deposited cells and offer advantages for the switching behavior (see chapter 6), the electrode system Ti/Pt is analyzed using HAXPES to investigate the chemical state of both Ti electrode and $SrTi_{1-x}Fe_xO_3$ film.

8.1 Photoemission Electron Microscopy - PEEM

8.1.1 Sample Preparation

Photoemission electron microscopy (PEEM) was performed by Marten Patt at the NanoEsca endstation in Trieste, using an Elmitec PEEM. Epitaxial $SrTi_{0.95}Fe_{0.05}O_3$ films of 20 nm thickness were grown on Nb:STO substrates via PLD and covered with a 7 nm Au layer $in-situ$ by sputtering. The Au layer was structured into 10x10 μm^2 pads with a marker structure to enable the identification of specific pads. Here, we will focus on one pad that was treated in a special way: In the first step, a tungsten whisker-needle with a small tip radius was used to contact the pad, and a positive voltage sweep 0 V $\rightarrow$ +7 V was applied to switch the pad

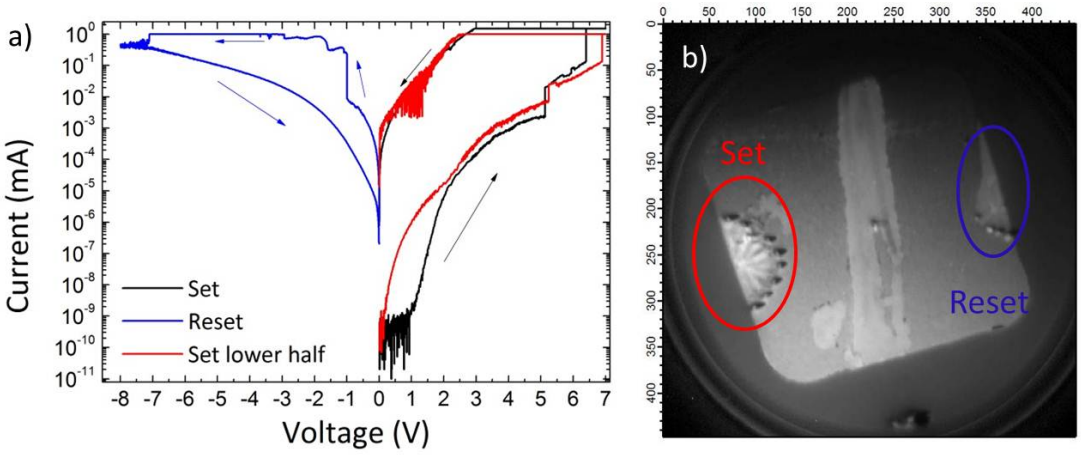

Figure 8.1: a): I(V)-curves recorded on the virgin pad: first SET (black), RESET (blue), and second SET (red) after separation from the first crater. b): Secondary electron image recorded at the Ti L-edge, highlighting the regions were the Au-electrode was removed due to electrical treatment (blue and red oval marking the RESET and SET crater, respectively) and the scratch from the W-needle bisecting the pad.

into the SET state (black line in figure 8.1 a)), while the current was limited internally to 1.5 mA. The current shows two jumps at 5.1 V and 6.4 V. The cell was subsequently switched into the RESET state by a 0 V $\rightarrow$ -8 V sweep (blue line), with the current being restricted to -1 mA for most of the sweep. The RESET-resistance was determined via a low voltage readout sweep of 100 mV to 21 MΩ. During the initial SET-sweep, the electrode was damaged in the area marked with the blue oval in the secondary electron image of figure 8.1 b). This is an indication for local heating: the Au film has very poor adhesion to the oxide since the metal-metal interaction is much stronger than the metal-oxide interaction and consequently, the metal will be driven to minimize the free energy by reducing surface area and increasing volume. The dark spot visible around the damaged areas (hereafter called craters) are Au particles that show the film "rolling" back, which is kinetically possible since the electrode is heated by the Joule heating of the localized current transport.
Following the initial voltage treatment, the W-needle was used to scratch through the center of the pad to electrically disconnect the two halfs. A read-out sweep confirmed that the half of the electrode that did not contain the switching crater was still highly insulating. A 0 V $\rightarrow$ +7 V sweep set the remaining half into the SET state (red line), but the compliance current was chosen slightly smaller (1 mA) to avoid hard breakdown. Interestingly, the "soft-forming" feature that is visible in the initial voltage sweep on the undamaged pad (black line) is not observed in the sweep on the bisected pad (blue line), indicating that the initial forming process that causes the first sweep to deviate from the following ones takes

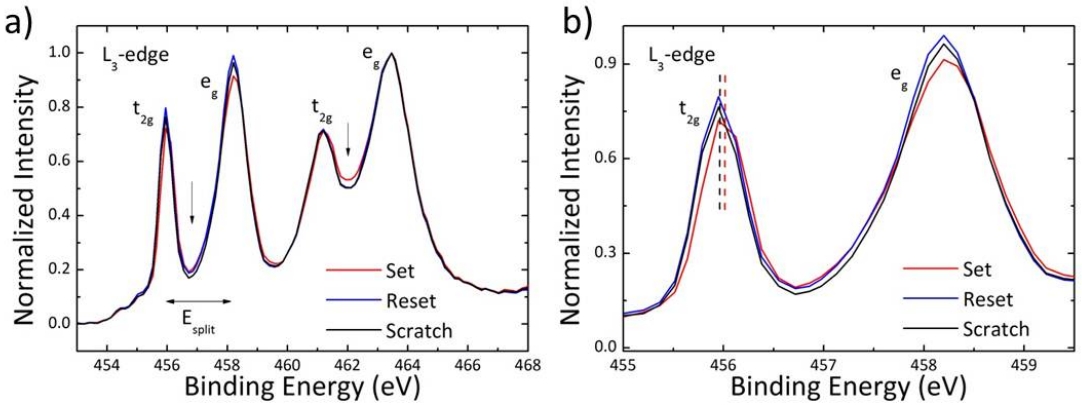

Figure 8.2: a): Ti L-edge absorption spectra recorded in the SET (red) and RESET (blue) crater and the scratch (black). b): Magnification of the L_3 edge showing the reduced splitting of the L_3 edge recorded in the SET crater.

place homogeneously under the whole electrode. This is comparable to the observations made by μXANES on thicker films during hard-forming (see section 7.1). Like the initial sweep, the SET-sweep on this half of the pad shows two current jumps at +5.2 V and +6.9 V, and the SET-resistance was read out to 28 kΩ at 100 mV. During this SET-sweep, a second crater (indicated by the red oval in b)) appeared. Presumably, these craters form around the regions with the highest temperature evolution during the switching, and therefore contain the conductive regions created during switching.

8.1.2 X-ray Absoprtion Spectroscopy - XAS

This electrode was investigated with PEEM in x-ray absorption mode, using secondary electrons as a measure for the absorption while the energy of the exciting x-ray beam is continuously varied over an absorption edge. An image is recorded for each energy, which allows the extraction of an absorption spectrum anywhere in the image area. The advantage is that multiple regions are measured simultaneously. For this pad, XAS was recorded for Ti $L_{2,3}$, Fe $L_{2,3}$ and O K-edge, as well as Sr $M_{2,3}$.

Ti L-edge

The Ti absorption spectrum extracted from the two craters and the scratch are shown in figure 8.2 a) and b). All measured spectra correspond to a Ti ion in octahedral oxygen coordination [107], but whereas the spectra for the RESET-crater and the scratch are virtually identical, the spectrum from the SET-crater

shows slight deviations. A magnification of the L_3 edge (figure 8.2 b)) shows that the energy position of the L_3 e_g peak is constant, while the t_{2g} peak is shifted slightly toward the e_g peak for the SET spectrum. This reflects a decrease of the crystal-field energy that splits the e_g and t_{2g} peaks [107], indicating a smaller overlap of Ti 2p and O 1s orbitals. Such effects can be caused by an increase in Ti-O distance [108] or a decrease of the coordination number, both a which are indicative of a change of the atomic environment around the Ti atoms. This is complemented by an increase of the width of both e_g lines, which results in the impression of increased intensity in-between the two peaks of each edge. The respective absorption spectra were fitted with Voigt-peaks to monitor changes in the peak parameters, and the results can be seen table 8.1.

Table 8.1: Peak parameters evaluated by fitting Voigt-profiles to the Ti L-edge XAS for SET, RESET and scratch. All numbers are in [eV]

		SET		RESET		scratch	
		center	FWHM	center	FWHM	center	FWHM
L3	t_{2g}	456	0.563	455.96	0.564	455.96	0.56
	e_g	458.2	1.21	458.18	1.1	458.19	1.098
L2	t_{2g}	461.14	1.27	461.1	1.253	461.1	1.26
	e_g	463.39	2.19	463.38	2.11	463.41	2.11

The fitted values support the visual impression that the energy separation between the SET - L_3 t_{2g} and e_g peaks is smaller than for the RESET- and scratch- spectra, although the effect is very small ($\sim$50 meV). At the same time, the FWHM of the e_g peak increases, which is the cause for the increased intensity between the two peaks. All these effects are an indication of a perturbation of the cubic site symmetry of the Ti ions and a (corresponding) change in the Ti-O distance, since a broadening of the L_3 e_g peak can be caused by additional contributions to the absorption lines, such as non-degenerate absorption channels due to inequivalent Ti-O bonds. A good reference for this fact is the XAS L-edge of rutile, that has strongly "broadened" lines due to the decreased site symmetry [107].

O K-edge

Additional information can be obtained from the O K-edge measured in the three regions. Since the oxygen K-edge has a singlet ground state with a wavefunction of *s*-character, the structure at higher energies can be interpreted as a direct consequence of the chemical environment of oxygen. Brydson et. *al* argue that the spectrum can be divided into two parts, a low energy part involving the first two

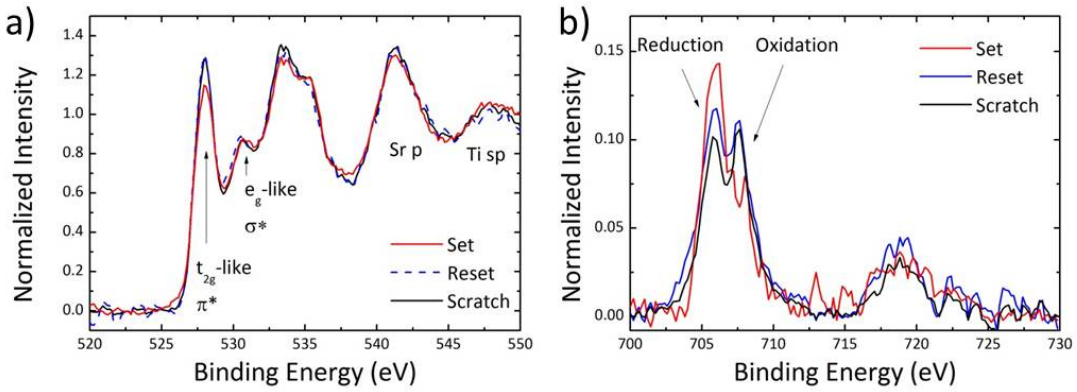

Figure 8.3: Left: Oxygen K-edge (right) and Fe L-edge (left) absorption spectra recorded on the three regions.

peaks and a high energy part starting beyond the second peak [109]. The first two peaks are a consequence of the Ti - O interaction and mainly derive from transition from the O 1s orbital to antibonding states with Ti 3d t_{2g} and e_g character for the first and second peak, respectively. In the binary oxide TiO_2 these peaks have very similar intensities, whereas the intensity of the e_g peak (σ^*) is strongly reduced in cubic perovskites such as $SrTiO_3$. Brydson et. *al* interpret this reduction as a hallmark of linear Ti - O - Ti chains in the crystal structure, and furthermore mention that the relative intensities of the t_{2g} and e_g peaks depend on the electron population of the respective bands in a non-trivial manner. However, a relative decrease of the t_{2g} line with respect to the e_g line is visible when going from TiO_2 to Ti_2O_3, which de Groot et. *al* attribute to a reduced number of unoccupied states in Ti_2O_3 conduction band that is comprised of hybridized states with Ti $3d$ (e_g) and O $2p$ character [110].
A similar decrease can be observed in the O K-edge spectrum recorded in the SET crater (figure 8.3 a)). While the high-energy part of the spectrum (E - E_F > 6 eV) is virtually unchanged for all the spectra, the ratio of t_{2g}/e_g contributions in the absorption edge (branching ratio) decreases for the SET- spectrum, while the RESET- and scratch spectra are virtually coincident. This indicates an increased occupancy of conduction band states with t_{2g} character, which form the bottom of the conduction band. The additional electrons in the conduction band are most likely introduced by oxygen vacancies, suggesting that the material in the SET-crater is chemically reduced.

Fe L-edge

The interpretation of the Fe L-edge in oxides, especially in substituted $SrTiO_3$, is non-trivial. One interpretation is that the L_3 edge consists of a crystal-field split

doublet of approximately equal intensity, depending on the crystal field strength. Another interpretation is that the split edge is a product of multiple valence states, Fe^{2+} and Fe^{3+}, that are present in the material. However, even Fe^{3+} compounds like $LaFeO_3$ show a split L_3 edge. At the same time, FeO shows only a single peak in the L_3 edge, with a broad shoulder at the higher binding energy side. These considerations point out that the oxygen coordination and distance are crucial for the interpretation of the Fe L_3 edge, which are not well known for Fe^{2+} in $SrTiO_3$. However, a clear correlation between heat treatment in UHV and the increase of the t_{2g}/e_g branching ratio has been found, such that after 630°C annealing in UHV the ratio was much higher than in the as-deposited state [86]. We can therefore consider the branching ratio as an indication of the oxidation-state of the $SrTi_{0.95}Fe_{0.05}O_3$.
The Fe L-edge spectrum recorded on the scratch is very similar to that found on a $SrTi_{0.95}Fe_{0.05}O_3$ film after annealing at 300°C in UHV (see figure 8.3 b)). The Fe L-edge of the RESET- crater is very similar to the scratch- spectrum, with a slightly larger branching ratio, while the branching ratio for the SET- spectrum shows a significant increase. This is clear evidence that the SET- crater contains reduced Fe-species, which corroborates the conclusion from the O K-edge that the SET crater is chemically reduced. Since the Fe-O bond strength is smaller than Ti-O, the removal of oxygen occurs predominantly at the Fe-site, which is why there are only small changes visible in the Ti absorption spectrum [34].

8.1.3 Structural Considerations

Scanning electron microscopy (SEM)

To complement the chemical analysis of the switched regions with PEEM, scanning electron microscopy is convenient since it offers a much improved spatial resolution and image quality, at the cost of the chemical sensitivity. To investigate the topographical changes taking place during the switching process, SEM images of 7 nm Au/ $SrTi_{0.95}Fe_{0.05}O_3$ / Nb:STO MIM-cells are presented in figure 8.4. The two images show two different electrode pads at different magnifications after an I(V)-sweep to positive voltages that switched both devices into the SET- state. In figure 8.4 a), the contact point of the probe (dotted circle) is clearly separated from the circular hole in the electrode that was created during the SET- process. Since the interaction between Au and $SrTiO_3$ is very weak, physical contact between the electrode surface and the probe tip is sufficient to remove some Au, which sticks much better to the tungsten tip than to the oxide. However, this image clearly shows that the location of the SET- crater (dashed circle) is not necessarily the same as that of the probe contact point, and also that while the crater often appears at the edge of the electrode, this is also not necessarily the case.

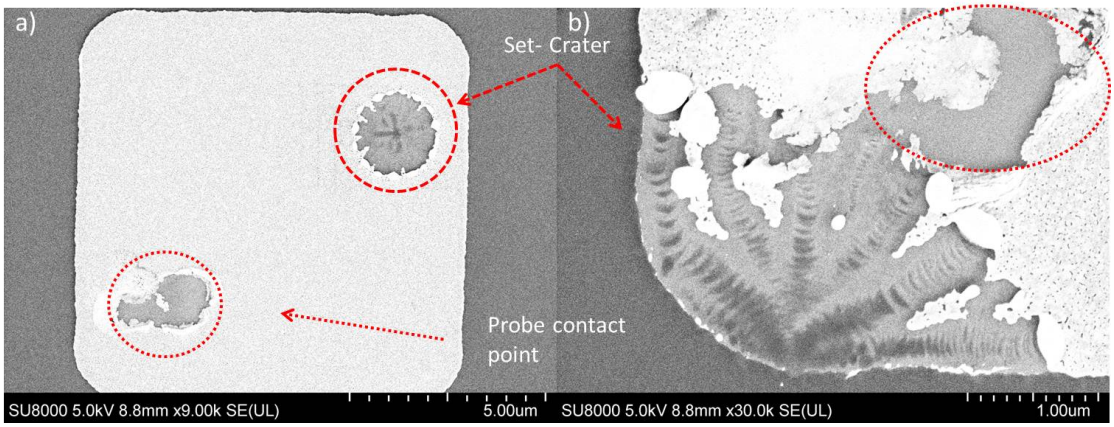

Figure 8.4: Two MIM-pads of a 7 nm Au/ 20 nm $SrTi_{0.95}Fe_{0.05}O_3$ / Nb:STO sample after application of a positive voltage into a SET-state. a): The contact point of the probe is not necessarily correlated to the switching location. b): The switched region shows a fine structure of light and dark areas, corresponding to different SE-yields. Some possible causes are differences in topography, conductivity or average atomic weight.

Figure 8.4 b) shows a high-magnification image of another electrode on the same sample. On this pad, the probe contact point (dotted circle) is close enough to the SET- crater (dashed circle) that they appear coincident under an optical microscope, but the SEM image reveals them to be separated. On both pads, the scratches caused by the needle show a homogeneous film underneath the electrode, while the material in the craters has clearly been altered. The high-magnification image (figure 8.4 b)) shows a quarter-circle where the Au electrode has been partially removed, with the center of the circle located in the lower-left corner of the electrode. Radiating out from the center in a star-like pattern are areas where the secondary electron-yield is smaller than in the surrounding area, as shown by the darker color. These 'rays' seem to consist of stacked, crescent shapes that are further apart the farther they are located from the center of the crater. A complementary feature are the remains of the Au electrode, which appear in an interlocking pattern with the dark area radiating out from the center of the crater. At the end of each 'ray', a small and completely 'white' area is located in the SE-image, which can be interpreted as spherical agglomerations of Au that enhance the topographical contrast in the SE-image.
The role of Joule heating for the local acceleration of oxygen diffusion in resistive switching transition metal oxides has been discussed in the literature [7, 22]. The appearance of the SET-crater in the devices discussed above shows definite signs of a local temperature increase, most prominently the spherical Au agglomerations at the end of each of the 'rays'. These features are consistently observed in the $Au/SrTi_{1-x}Fe_xO_3$ system after SET. Similar effects can be found in MIM-cells

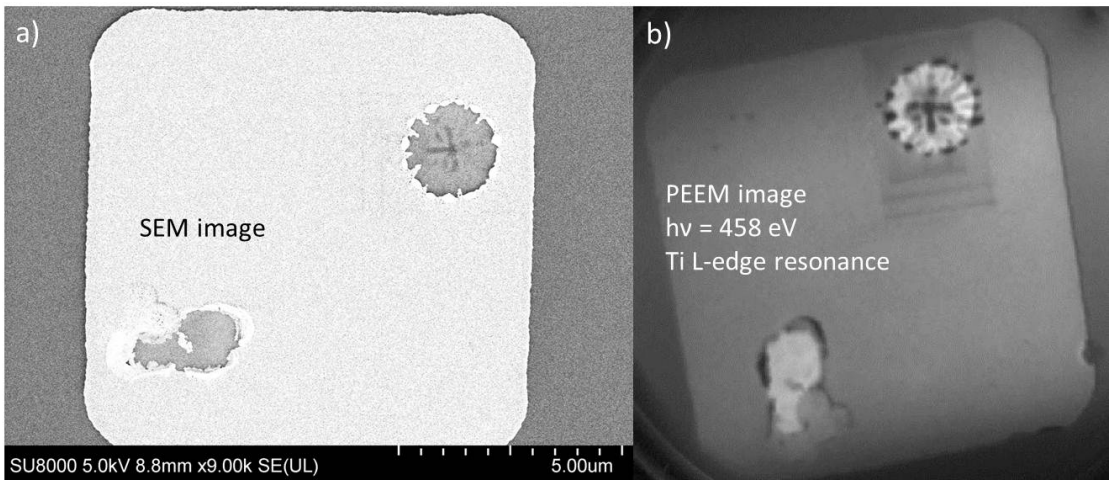

Figure 8.5: SEM image (a)) and PEEM image recorded at $h\nu = 458$ eV (b)) of the same 7 nm Au/ 20 nm $SrTi_{0.95}Fe_{0.05}O_3$/ Nb:STO pad. PEEM shows that the structure in the crater that can be observed in the SE image is correlated to an increase in Ti L-edge absorption., corresponding to a lateral concentration gradient of Ti.

using other noble metals, e.g. Rh (see figure 9.8 in the appendix). However, the observable structure of the craters of the $Au/SrTi_{0.95}Fe_{0.05}O_3$ samples implies a radial temperature distribution, with a 'hot spot' in the center of the crater (which equals the main conduction path). The Au electrode retracts from the center along discrete paths ('rays'). Since the volume free energy $-\Delta G_{Vol}$ is much more negative than the free energy of the metal/oxide interface $-\Delta G_{int}$ for noble metals, the metal will try to agglomerate into metal particles with a maximal surface/volume ratio, which is the reason for the spherical Au particles at the tip of each 'hot ray'.

Comparison of PEEM and SEM

The structural changes observable by SEM can be directly compared to chemically sensitive imaging by PEEM. Figure 8.5 compares two images of the same electrode pad, image a) a SEM image taken at an acceleration voltage of 5 kV, and image b) a chemically sensitive PEEM image taken at a photon-energy of $h\nu = 458$ eV, corresponding to the Ti L_3 e_g line. Note that the PEEM image is mirrored due to the microscopy optics, and rotated by 90°. The inhomogeneities in the SET-crater are more pronounced at Ti resonance, with light and dark areas indicating a lateral concentration profile of Ti. A shift in the Ti L-edge in both regions can be excluded since in this case, the area that is dark in the image should light up at a different photon energy. However, it is consistently dark while the light area in the image lights up at all four Ti L-edge absorption features. At the same time,

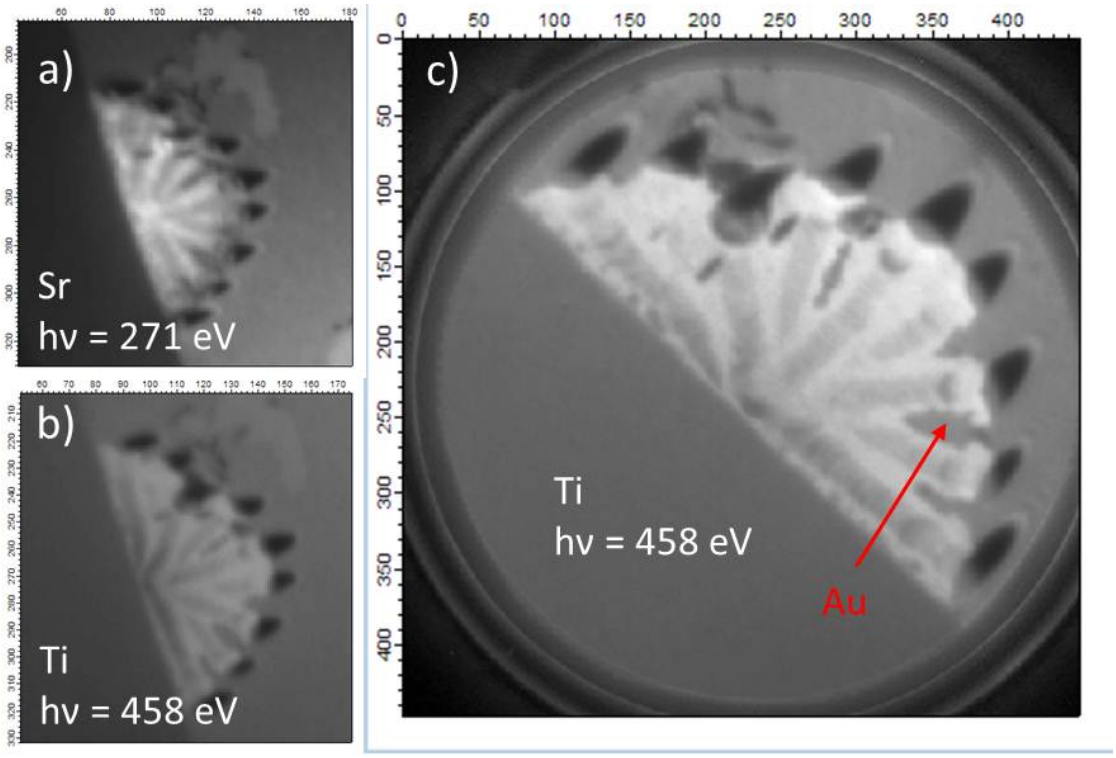

Figure 8.6: PEEM images of the SET-crater on a 7 nm Au/ 20 nm $SrTi_{0.95}Fe_{0.05}O_3$/ Nb:STO MIM-cell. c): High-resolution image of the crater at $h\nu = 458$ eV (Ti L_3 e_g edge). a): digital zoom on the crater of a larger image recorded at $h\nu = 271$ eV (Sr M_5 edge). b): The same image recorded at 458 eV. Note the inversion of the dark-light contrast for the Sr- and Ti-resonance images.

the scratch induced by the probe contact remains homogeneous in brightness at all four absorption lines of the Ti L-edge, which is proof that the inhomogeneities are induced by the electrical treatment. The area around the electrode pad remains darker due to the RIBE etchdown that was used to structure the sample.
The area that remains consistently dark during the energy scan over the Ti L-edge corresponds to the dark areas radiating of the 'hot spot' at the center of the crater. The same contrast is found at the O K-edge. This contrast is inverted as the excitation energy is scanned over the Sr M_5 edge at 271 eV, as shown in figure 8.6 a)-c). The large image (c) is a close-up of the SET-crater taken on the sample discussed in the section above, 8.1, while the two smaller images are digital magnifications cut out from a large-area scan on the same pad. The pattern appears in the close-up image of the crater recorded at the Ti L-edge at 458 eV excitation energy (figure 8.6 c)): the Ti absorption is less pronounced in the dark 'rays' going out radially from the dark 'hot spot', whereas the areas in between those 'rays' shows enhanced Ti absorption. At the end of each 'ray', a small sphere of Au is visible, whereas there is actually Au left on the surface of the light, Ti-rich

areas (marked with a red arrow). The crescent-shaped nano-structure visible in SEM (figure 8.5) is hinted at by the contrast of the image. Image b) is identical, only less well resolved and serves the purpose of a reference for the Sr image a). This image is recorded at an excitation energy of $h\nu = 271$ eV and shows a light-dark contrast that is inverted from the Ti L-edge: the 'rays' pointing at the Au spheres are light, whereas the area in between is dark. This indicates a Sr enrichment in the 'rays' and a corresponding lateral gradient of the Sr/Ti ratio in the surface of the SET-crater.

8.1.4 Consequences for the Switching Mechanism

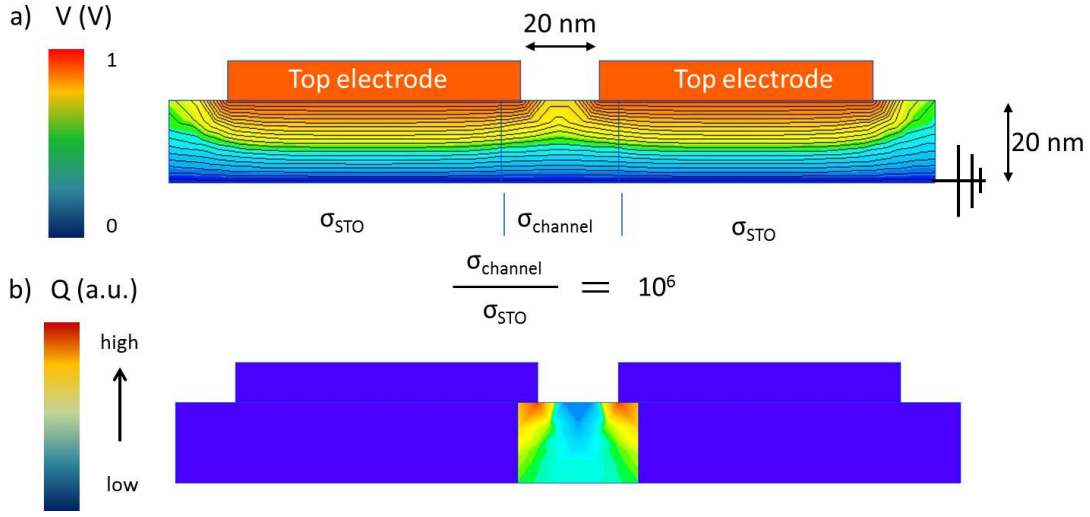

Figure 8.7: FEA simulations of a 20 nm thick $SrTiO_3$ film with a damaged top electrode. a): Potential distribution V for a bias of +1 V applied to the top electrode. Black lines are lines of equal potential. b): Distribution of Joule heating Q in the conducting channel.

A discussion of the possible origin for the homogeneous switching polarity has been given in section 6 on the basis of oxygen vacancy movement and the formation of local *pn*-type junctions. This model neglects spatial inhomogeneities in the switched sample, in favor of simplicity. Here, additional features can be added from the PEEM investigation presented above. A summary of the most important points:

• I(V) characteristics: Bisecting the electrode after the inital SET shows that the switching process takes place very close to the crater that is formed during SET. Assuming that the crater itself is disconnected electrically since the electrode does not cover it, we can assume the switching to take place very close to the crater in the area that is still covered by the electrode.

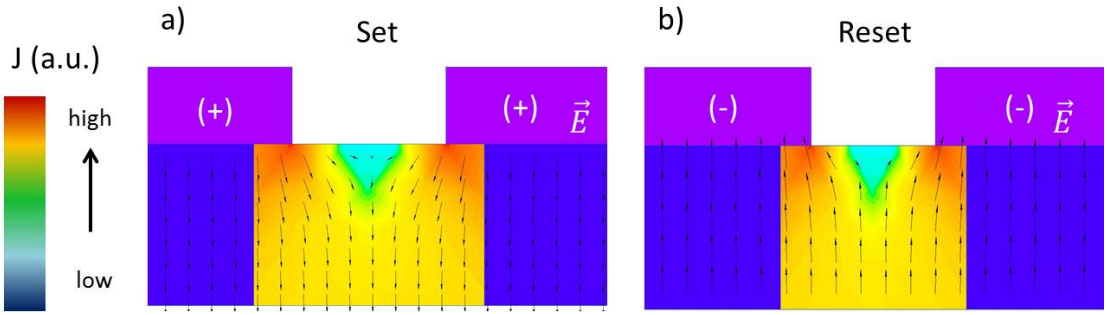

Figure 8.8: FEA simulation of the current density in the damaged MIM structure under a) positive bias and b) negative bias applied to the top electrode. Black lines indicate the direction of $\vec{E}$ and correspondingly the oxygen vacancy movement.

• Spectroscopy of the switched craters shows that the SET crater is chemically reduced, while the RESET crater is (re-)oxidized. This is not intuitive since they are no longer electrically connected to the electrode.
• High-resolution imaging reveals a nanoscale fine-structure in the SET crater that consists of areas with different secondary electron yields. PEEM imaging implies a separation into a Sr-rich and a Ti-rich phase on the surface. The length scale of demixing can be estimated from the size of the nanoscaled regions to $\sim$ 20 nm.

To consider the change in the electric field induced by the electrode damage, figure 8.7 shows Finite Element Analysis (FEA) simulations of a 2-dimensional cut through a MIM-stack where the top electrode has been damaged. The basic model for the FEA assumes that during soft-forming, a conducting channel is created in the $SrTiO_3$. Due to increased local Joule heating, a hole opens in the electrode on top of the channel. The simulation models a 20 nm wide hole in a 8 nm thick electrode, on top of a 20 nm thick $SrTiO_3$ film. The parameter that distinguishes the respective regions is the DC-conductivity, which for the sake of simplicity has been assumed to be a factor of 10^6 greater in the channel than in the $SrTiO_3$.

Figure 8.7 a) shows the potential distribution in the cell when a bias of +1 V is applied to the top electrode. Assuming the potential drops across the insulator exclusively, we observe curving lines of equal potential around the edges of the electrode. These curving lines induce a lateral component into the electric field close to the surface (the electric field vector is perpendicular to the lines of equal potential). Figure 8.7 b) shows a calculation of the Joule heating in the structure under applied bias. Since the conductivity of the channel is much greater than that of the $SrTiO_3$ film, the current is flowing almost exclusively through the channel. The hole in the electrode, however, means that the maximum Joule heating is localized right under the edge of the electrode. The highest temperature - and therefore the highest mobility of oxygen vacancies - is reached at the out-

side of the channel, implying that a anion-migration mediated switching process will preferentially happen here. This agrees with the finding of Muenstermann *et.* al that the homogeneous polarity appears in a 'halo' around the area of highest conductance [32].
The influence of the 'hole' on the electric field $\vec{E}$ in the insulator is shown in figure 8.8 a) and b) for SET and RESET bias, respectively. The black arrows indicate the electric field vectors that are perpendicular to the lines of equal potential, whereas the color scale shows the current density J through the cell. Since oxygen vacancies are positively charged defects, the drift direction under an applied field is parallel to $\vec{E}$. Close to the surface there is an appreciable lateral component in the electric field, which is induced by the curving lines of equal potential around the electrode edges. Further into the film, this lateral component vanishes almost completely. The mobility of oxygen vacancies is a function of the local temperature, and will be highest at the regions of highest Joule heating, which is roughly proportional to the current density.
Under SET bias, the lateral component of $\vec{E}$ induces oxygen vacancy migration toward the center of the channel, which fits to the observation by spectroscopy that the SET crater is chemically reduced. Under RESET bias, the direction of movement is reversed and oxygen vacancies will move away from the center of the channel, and correspondingly the center of the RESET crater appears oxidized by spectroscopy. These considerations are therefore in qualitative agreement with experimental observations. It needs to be stressed that the observed redox-process is not the origin of the resistance change in this model, but a consequence of it.
Two issues need to be addressed, however: the first is that the simulations assume a hole in the electrode of 20 nm, whereas the holes observed experimentally are on the order of 1 μm. However, this does not change the character of the curved lines at the electrode edges. Furthermore, the simulation assumes a single electrode edge, whereas the experimentally observed craters usually show frayed edges, where some electrode material still protrudes into the crater region. A simluation with more realistic dimensions is difficult because of the high aspect ratio of the problem.
The second issue is that of the diffusion length: it is unrealistic to assume that the in-plane oxygen vacancy diffusion over μm-distances plays a role in comparison to the out-of-plane diffusion, which is restricted to the film thickness of 20 nm. If the surface in the crater region shows demixing into Sr-rich and Ti-rich phases, then one possibility is the formation of conductive oxide phases on the surface of the crater. The length scale of this segregation can be estimated from SEM to a few ten nm. A possibility then is that while the conductive surface phase is still electrically connected to the electrode, that edge effects as described above play a role in-plane on the scale of 20 nm. However, this is theory needs strong experimental verification and should be regarded as a possibility only.

In summary, the FEA modeling shows that the observed reduction/re-oxidation of the switching craters are in agreement with the switching mechanism discussed in 6, and are probably mediated by the change in electrode geometry. It is noteworthy that while LC-AFM investigations found that the whole electrode area was switchable after electrode removal, only the 'halo' region close to the crater was actually changed after switching the MIM-structure [111]. This is also in agreement with the theory that homogeneous switching takes place mainly close to the crater and is mediated by electrode edge effects.

8.2 Hard X-ray Photoelectron Spectroscopy

8.2.1 Sample preparation

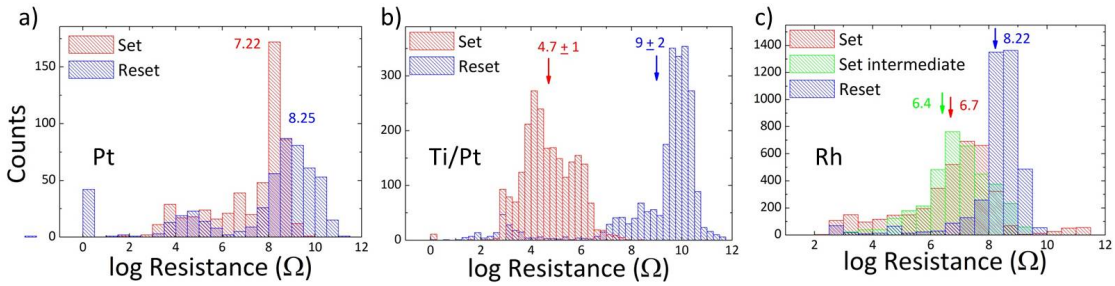

Figure 8.9: Resistance histograms for three different top electrode combinations: a): Pt , b:) Ti/Pt and c:) Rh. Switching voltages for SET were +4.25 V for Pt, +10 V for Ti/Pt and +6 V for Rh. RESET voltages were -5.5 V for Pt, -7 B for Ti/Pt and -7 V for Rh.

Hard X-ray Photoelectron Spectroscopy (HAXPES) was performed at beamline P09 (PETRA III, Hasylab, Hamburg). Since the beam size on the sample at P09 is approximately 200 x 500 μm^2 normal to the beam, it is not possible to investigate single electrodes and therefore large arrays of MIM-cells have to be fabricated. The first necessity for this experiment is to improve the reliability of the investigated sample in such a way that all electrodes can be treated in the same way electrically and show a similar response. As we have seen in chapter 6, this condition is given only for thin films with thickness < 20 nm, which is also ideal to avoid unwanted spectral intensity from the substrate.
$SrTi_{0.95}Fe_{0.05}O_3$ films were grown by PLD onto conducting, Nb-doped $SrTiO_3$ single crystals with (001) orientation. Three different top electrode materials were investigated: Pt, Ti/Pt and Rh. Initial experiments using 100 x 100 μm^2 Pt-electrodes underlined the fact that Pt is a very strong absorber for photoelectrons, and an electrode thickness of 2 nm should not be exceeded. Samples with Ti/Pt

top electrodes were fabricated into arrays with 20 x 20 μm^2 electrodes from 4 nm Ti/ 2 nm Pt stacks, while a 5 nm Rh film was used to fabricate arrays of 10 x 10 μm^2 electrodes. The switching voltage and the current compliance had to be adjusted for each individual sample to achieve a maximized resistance ratio, and they are given in the caption of figure 8.9. The resistance histograms after switching are shown in figure 8.9 for all three electrodes types: 2 nm Pt, 4 nm Ti/ 2 nm Pt and 5 nm Rh.
We see that a 2 nm Pt electrode does not yield favorable results for resistive switching. A Ti adhesion layer improves the switching characteristics significantly, as can be seen by the increased R_{RESET}/R_{SET} ratio. It should be mentioned that for this sample, the SET-voltage was chosen to +10 V to ensure reliable switching, and that the initial SET-switch for the RESET-array was chosen to +9 V. Therefore, the distribution slightly overstates the resistance ratio since the SET process was slightly different from the RESET process, but this was necessary to achieve reliable RESET-switching. The Rh electrode displays much more favorable switching characteristics than the thin Pt layer, despite the chemical similarity between the two materials.

8.2.2 Interfacial Band Line-Up

Photoemission spectroscopy is a popular tool to investigate surface band bending and line-up, since the information about the position of core level emission lines relative to the reference level (Fermi level) can be directly evaluated as a band bending in the absence of chemical changes (changes in line-shape or chemical shifts). Furthermore, the band line-up at the interface can be evaluated by comparison with suitable reference samples.
The procedure is outlined in figure 8.10 in three steps: The reference energy positions of the two interfacing materials need to be established on samples where

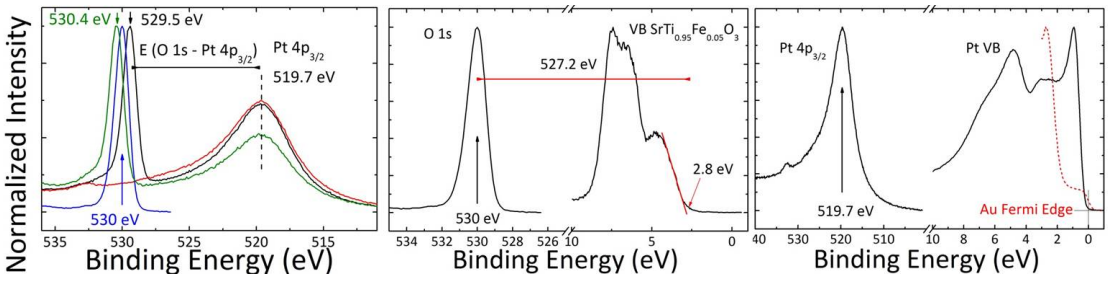

Figure 8.10: Photoemission spectra taken at 4.2 keV excitation energy of O 1s and Pt $4p_{3/2}$ core levels, as well as the $SrTi_{0.95}Fe_{0.05}O_3$ and Pt valence bands. The relative separations in energy can by used to determine the interfacial band offset.

band bending or chemical shifts are absent. For the $Pt/SrTi_{0.95}Fe_{0.05}O_3$ interface, we use a 40 nm Pt layer sputtered onto a Nb:STO crystal as a reference for the energy position of the Pt $4p_{3/2}$ line with respect to the Fermi edge (top of the Pt valence band), and the distance of the O 1s emission line to the valence band maximum is measured on an as-deposited 20 nm $SrTi_{0.95}Fe_{0.05}O_3$ film. The position of the valence band maximum (VBM) is determined by linear extrapolation of the leading edge to the energy axis [112]. During the determination of the reference energy positions, the photon energy was frequently calibrated at the Au Fermi edge of a Au strip in electrical contact with the samples. The relative distance between these emission lines can be evaluated to determine the valence band-offset (VBO) at the interface:

$$VBO = (E_{O1s} - E_{Pt4p_{3/2}}) + (E_{Pt4p_{3/2}} - E_F)_{Pt} - (E_{O1s} - E_{VBM})_{STO} \tag{8.1}$$

or since the Pt core level is referenced to the Fermi level

$$VBO = E_{O1s,sample} - (E_{O1s} - E_{VBM})_{STO} \tag{8.2}$$

To certify that the observed effect is due to a band offset, the observed shift has to be visible in all core-levels. While the quantification according to equation (8.2) can be executed for any given core-level, the O 1s line improves the reliability of the method since the difference $E_{O1s} - E_{Pt4p_{3/2}}$ can be taken in the same spectrum, excluding artifacts from photon energy fluctuations. Deviations between the electrically and spectroscopically determined values can potentially be caused by the sampling depth of the HAXPES experiment, which can induce peak shift of around 100 meV.
The values displayed in figure 8.10 yield a valence band-offset of 2.3 eV for the 2 nm $Pt/SrTi_{0.95}Fe_{0.05}O_3$ structure, which corresponds to a conduction band offset (CBO) of 0.9 eV when assuming a band-gap of 3.2 eV. This value is lower than value expected from bulk work-functions, but corresponds closely to the Schottky-barrier height of 0.9 eV calculated from I(V)-behavior for $Pt/SrTi_{0.95}Fe_{0.05}O_3$ (see chapter 6).
An interesting observation is made for the sample with 4 nm Ti/ 2 nm Pt top electrodes, since the O 1s line (green line in figure 8.10) is shifted to higher binding energies (530.4 eV) with respect to the reference film. The VBO according to equation (8.2) is 3.2 eV for this case, and as a consequence the Fermi level can be assumed to be positioned close to the bottom of the conduction band. From electrical data, it is known that these MIM-structures are insulating in the virgin state, therefore E_F is more than $3kT$ under the conduction band minimum (CBM). However, low electrical resistance in the virgin state has been found for Ti layer thicker than 5 nm (in the case of 20 nm $SrTi_{1-x}Fe_xO_3$ films), and indeed an additional peak shift by about 100 meV to higher binding energies is observed for thicker Ti layers when comparing uncapped Ti layers on 20 nm $SrTi_{0.95}Fe_{0.05}O_3$

films (see figure 8.11 c)). This confirms that the Fermi level is indeed located closer than $3kT$ to the conduction band for thicker Ti layers, which can be considered as the onset of degeneracy in a semiconductor. The accuracy of this method is on the order of 100 meV, but it confirms that the onset of conductivity can be examined via HAXPES.

A corresponding shift that coincides with that found at the O 1s line can be seen at the Sr 3p doublet (see figure 9.6 in the appendix), demonstrating that the shift in the O 1s line is not due to a different chemical species of oxygen in the oxidized Ti layer. The chemical shift induced by the slightly different chemical environments is likely much smaller than the shift in the Fermi level with respect to insulating $SrTi_{0.95}Fe_{0.05}O_3$.

Figure 8.11 a) and b) show schematic band energy diagrams for both Pt and Ti/Pt top electrodes, respectively, as evaluated by HAXPES. For Pt electrodes, the assumption of full depletion is made. Note that the band alignment at the interface is clearly defined by the core-level shifts, regardless of the slope of the energy bands. It is clear from the values determined for the VBO and CBO that a Schottky-type barrier with a barrier height of $\Phi = \phi_{Pt}$ - χ_{STO} = 5.65 eV - 4.1 eV = 1.55 eV does not adequately describe the $PtSrTi_{0.95}Fe_{0.05}O_3$ interface.

It is likely that the barrier is modified by positively charged traps at the interface that decrease the effective barrier height. It has indeed been found by XPS that the valence of the Fe dopants is lower at the surface of $SrTi_{0.95}Fe_{0.05}O_3$ films, which points to an increased amount of oxygen vacancies at the surface [86]. In the case of a depleted film, the oxygen vacancies are doubly ionized and can thus act as positive charges located at the interface.

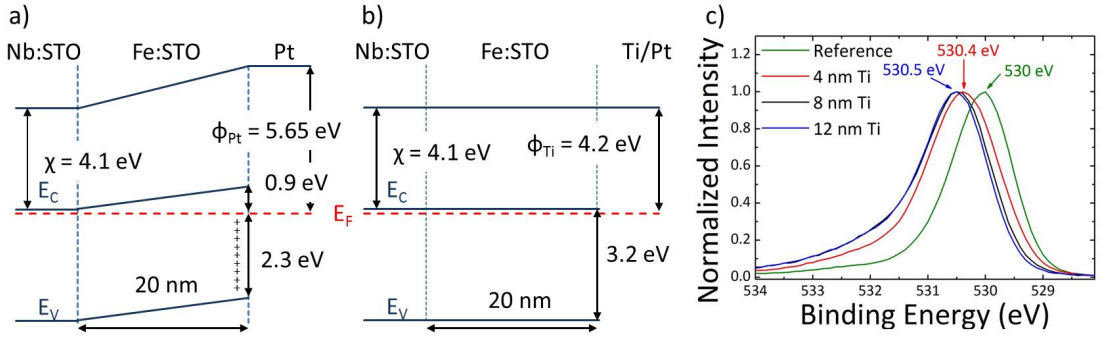

Figure 8.11: a) and b): simplified band energy schemes in $SrTi_{1-x}Fe_xO_3$ with Pt and Ti/Pt electrodes, respectively. The respective values of the band offsets have been determined by HAXPES. c): Energy shift of the O 1s line with increasing Ti thickness on a $SrTi_{0.95}Fe_{0.05}O_3$ film. A comparable shift is found in the Sr 3p lines (figure 9.6 in the appendix), excluding a chemical shift of the O 1s line as the source.

8.2.3 Ti Electrodes

A redox-active adhesion-layer between the oxide and the Pt layer can provide distinct advantages for resistive switching, as described in section 6.4. A 20 nm $SrTi_{0.95}Fe_{0.05}O_3$ film was deposited via PLD onto a conduction Nb:STO substrate, and a 4 nm Ti/ 2 nm Pt layer was structured via photolithography into 20 x 20 μm^2 electrode pads with 1 μm separation. To investigate the chemical state of the Ti/$SrTi_{0.95}Fe_{0.05}O_3$ interface and the dependence of the initial resistance on the Ti/$SrTi_{1-x}Fe_xO_3$ thickness ratio, hard X-ray photoemission (HAXPES) experiments were performed at beamline P09 (HASYLAB, Hamburg). The energy resolution of the experiment was 500 meV as determined by the width of the Au Fermi-edge at a photon energy of E_{photon} = 4200 eV. For the spectra presented here, take-off angles close to the surface normal were chosen to maximize the information depth. The electron attenuation length (EAL) in Pt and TiO_x is 22 Å and 53 Å under these conditions, respectively (see figure 9.7 in the appendix).
Figure 8.12 a) shows the Ti 2p photoemission spectra recorded on a 2 nm Pt/ 4 nm Ti/ 10 nm $SrTi_{0.95}Fe_{0.05}O_3$ stack (bottom) and a 2 nm Pt/ 4 nm Ti/ 20 nm $SrTi_{0.95}Fe_{0.05}O_3$ stack (middle), as well as a 2 nm Pt/ 20 nm $SrTi_{0.95}Fe_{0.05}O_3$ (top) as a reference for the as-deposited Fe:STO. We confirmed that the 2 nm Pt layer is closed by means of AFM and SEM (see appendix, 9.5). Only a single spin-orbit split doublet with the Ti $2p_{3/2}$ line at E_{bind} = 458.9 eV is observable for the Pt-covered Fe:STO, corresponding to Ti^{4+} and labeled as component A. The 2 nm Pt/ 4 nm Ti/ 20 nm $SrTi_{0.95}Fe_{0.05}O_3$ stack shows a broad shoulder at the lower binding energy side of the Ti 2p doublet, while in the case of the 10 nm $SrTi_{0.95}Fe_{0.05}O_3$ film the shoulder is much more pronounced and shows distinct structure.
The envelopes are analyzed with a peak-fitting procedure assuming spectral components of Lorentzian lineshape with a FWHM of 1.5 eV for components B - D, although some gaussian broadening of the peaks was permitted where it improved the fit. The envelope of the Ti 2p spectrum cannot be reproduced with less than four spectral components. According to their binding energy, component B (457.4 eV) and component D (455.1 eV) can be attributed to Ti_2O_3 and TiO, respectively [113]. The intermediate energy position of component C cannot be assigned to a specific oxidation state of Ti in a straightforward manner, and likely corresponds to non-stoichiometric suboxides between TiO and Ti_2O_3, while metallic Ti is notably absent.
The effect of an applied positive voltage on the oxidation state of the top electrode can be seen in figure 8.12 b). Large arrays of 20 x 20 μm^2 electrodes of 2 nm Pt/ 4 nm Ti on a 20 nm $SrTi_{0.95}Fe_{0.05}O_3$ film were subjected to a positive voltage to lower the stack resistance (for details, refer to chapter 8). The comparison of a virgin array with arrays both in the "SET" and "RESET"-state shows a decrease of

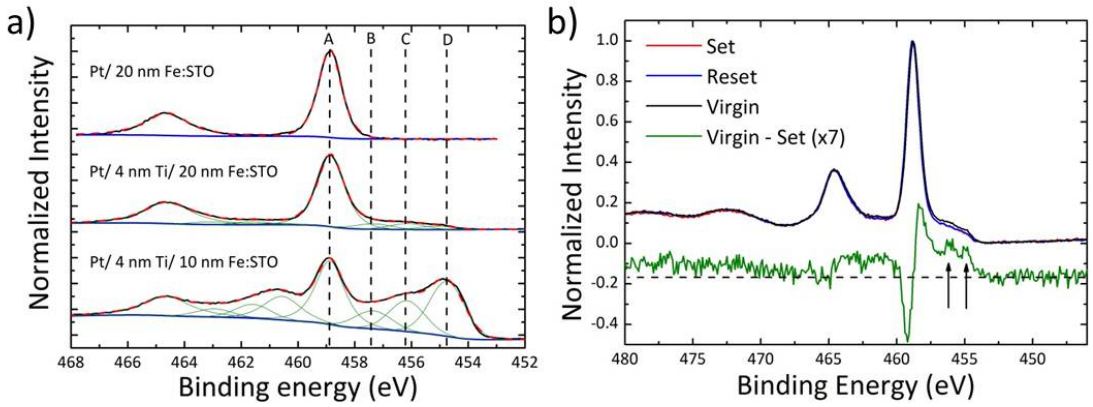

[h]

Figure 8.12: a): HAXPES spectra taken on three $SrTi_{1-x}Fe_xO_3$ films with different electrodes and thickness. b): Ti 2p spectra from arrays in different resistive states. The difference spectrum (green line) has been shifted for clarity and multiplied by 7 to show the fine structure.

the intensity of the low binding energy shoulder of the Ti $2p_{3/2}$ line, corresponding to a decrease of Ti suboxides. The difference spectrum of the "Virgin" (black line) and "SET"-spectra (red line) shows some structure that can be related to the Ti oxidation states discussed above, and a sharp oscillation that is due to slight differences in peak-shape and energy position of the Ti^{4+} component. This is direct evidence of oxygen movement in the MIM-structure under an applied bias, transferring O^{2-} ions from the $SrTi_{0.95}Fe_{0.05}O_3$ film to the Ti electrode. The additional oxidation transfers TiO_x to TiO_2 in the electrode and reduces the $SrTi_{0.95}Fe_{0.05}O_3$ thin film. The fact that "SET"- and "RESET"- state (blue line) show identical structure means that the observed change is due to the softforming process only. In summary, increasing the ratio of $Ti/SrTi_{1-x}Fe_xO_3$ thickness leads to a decrease of the initial resistance of the MIM-stack through a transfer of oxygen from the insulator to the electrode, which increases the conductivity of the insulator by oxygen vacancy doping. HAXPES experiments demonstrate that the amount of oxidation taking place at the $Ti/SrTi_{1-x}Fe_xO_3$ interface depends on the thickness ratio, and that a transfer of oxygen can also be achieved by an electrical stimulus. The conclusion is that the Ti-oxidation is mainly induced by the redox-reaction

$$Ti + SrTiO_3 \rightleftharpoons TiO_x + SrTiO_{3-x} \tag{8.3}$$

of the Ti layer with the underlying $SrTi_{0.95}Fe_{0.05}O_3$ thin film. The resistance of the top electrode R_{TiO_x} remains low due to the presence of conductive Ti-suboxides, therefore $R_i = R_{TiO_x} + R_{STO}$ is high until a critical degree of reduction is reached in the STO film. The reduction enthalpy of the $SrTi_{1-x}Fe_xO_3$ is given by

$$-\Delta G_{STFO} = -\Delta\bar{\mu} - zF\Delta\phi \tag{8.4}$$

therefore the redox-reaction can be shifted toward TiO_x + $SrTiO_{3-x}$ by either an applied voltage ($V = \Delta\phi$) or a strong gradient in the chemical potential $\bar{\mu}$ (metal/oxide interface). In equation (8.4), z is the particle charge and F is the Faraday constant.
However, there was no visible change in the lineshapes of the Ti, Sr and O core-levels when comparing the electrode arrays in different resistive states. Presumably, the switched area is still too small to be detectable for 20 x 20 μm^2 electrodes.

8.2.4 Pt Electrodes

Large arrays of 100 x 100 μm^2 electrodes fabricated from a 2 nm Pt film were investigated by HAXPES with an excitation energy of 4200 eV, using a Si (111) monochromator crystal. The total energy resolution of the experiment was $\sim$ 500 meV. To ascertain that the Pt grows in a closed layer, the surface of the electrodes was investigated with SEM and AFM to check for pinholes, cracks or clusters. The electrode was found to form a closed layer (see figure 9.5 in the appendix).
Core levels of all three major constituents were measured under take-off angles (TOA) of 45° and 90° (normal emission). As a representative example, the spectra taken under both angles are shown in figure 8.13 for the electrically unmodified virgin electrodes. The only consistently observable difference between the two TOA is a slight broadening observable for all three core levels (Sr 3d, Ti 2p, O1s) for the spectra taken under TOA of 45°. The most likely explanation for the peak broadening are slightly different atomistic environments within the probed volume, which can be caused by band-bending at the interface due to a surface dipole or a Schottky-type barrier. Another interpretation is kinetical demixing during the sputtering process, causing the appearance of additional spectral components around the main Ti^{4+} lines [114]. However, this effect is predicted to segregate Sr toward the surface and Ti into sub-surface regions (2-3 nm), which does not agree with the experimental data presented here since the peak broadening shows the same tendency in both Sr 3d and Ti 2p. Furthermore, the shape of the O1s line does not change significantly between the two TOA, and a contribution from Ti_2O_3 as in Ref. [114] is not apparent. This observation is facilitated by the very low spectral contribution of oxygen from physisorbants on the Pt surface due to the high information depth in HAXPES.

Such peak broadening could also be an artifact of increased surface scattering, but was not observed for the Ti/Pt electrodes and therefore seems unlikely.
The spectra depicted in figure 8.13 were shifted in energy to coincide and facilitate the observation of the peak broadening. In the unshifted data, an energy shift of $\sim$ 300 meV can be observed between the two TOA, with the spectrum measured

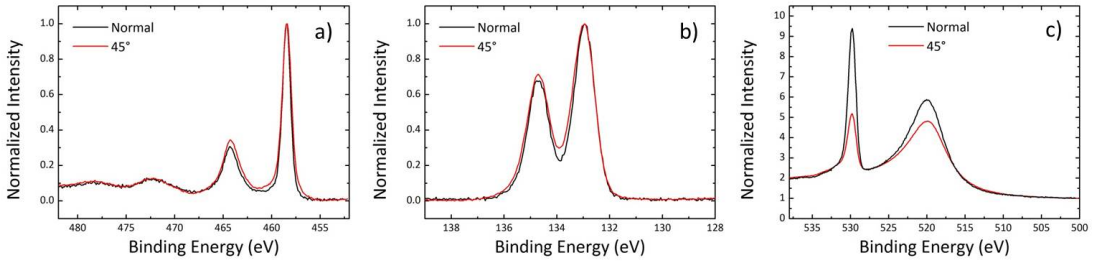

Figure 8.13: Angular resolved photoemission spectra of Ti 2p (a), Sr 3d (b) and O1s / Pt $4p_{3/2}$ (c) recorded on a 2 nm Pt/ 20 nm $SrTi_{0.95}Fe_{0.05}O_3$structure in the virgin state. The spectra were shifted in energy to coincide.

under 45° shifted to higher binding energy. This energy shift is observable for all measured spectra, including the Pt $4p_{3/2}$ peak. Such behavior cannot be explained by an escape-depth dependent shift of the quasi Fermi-level as it is caused by band bending, since in this case the Pt emission line would not be expected to shift. Rather, such behavior is indicative for a surface photo-voltage (SPV) as has been observed for several metal/semiconductor interfaces [115].
The SPV is a consequence of the interfacial band bending at a metal/semiconductor interface: photo-ionization by the incident X-rays creates electron-hole pairs in the sample, which move in different directions under an applied electric field (or a gradient in the energy bands). While the excited electrons move deeper into the film, the holes are drawn toward the metal and accumulate at the interface, reducing the effective barrier height. The observable effect on the binding energy is akin to sample charging in that for n-type semiconductors, the binding energy shift has the same sign as charging. A charging effect is the result of insufficient conductivity in the sample to compensate the loss of the photoelectrons through the surface, and correspondingly the sample appears positively charged. However, charging effects have generally not been observed on 20 nm $SrTi_{1-x}Fe_xO_3$ films on Nb:STO even in soft x-ray photoemission spectroscopy, and charging effects are typically larger in magnitude than 300 meV. However, charging cannot be excluded completely.
According to Alonso *et* al., the magnitude of SPV depends exponentially on the band gap of the semiconductor and also on the recombination rate in the space-charge zone. While Si (E_G = 1.1 eV) needs to be cooled to cryogenic temperatures to suppress charge-carrier recombination in order to observe SPV, it is readily observable in GaP (E_G = 2.25 eV) at room temperature. Accordingly, the effect can be expected to be larger still in $SrTiO_3$ (E_G = 3.2 eV).
SPV has been observed for metal thickness up to 11 nm (in the case of Ag), and Alonso *et* al. explicitly mention that the presence of SPV has to be accounted for when investigating electrode layer 10 - 20 Å thick. However, this thickness dependence has been attributed to absorption in the metal layer, since the study presented in [115] uses a photon energy of 55 eV. For HAXPES, such restrictions

are unlikely since the hard X-rays have much larger penetration depth in matter. An angular dependence of SPV as mentioned by Alonso *et* al. can also be observed for the presented experiments. Notably, the spectra recorded under a 45° angle are shifted by 300 meV with respect to the spectra recorded under normal emission. It is important to consider that during these measurements, the angle between the incident beam and the photoelectron analyzer was 45°, therefore spectra taken under normal emission have an angle of incidence of 45°. This means that the effective path length of the photons through the $SrTi_{0.95}Fe_{0.05}O_3$ film is 20 nm/sin 45° = 28.3 nm, while the 45°-emission spectra were recorded under a grazing incidence angle. Assuming 5° as angle of incidence, the effective path increases to 20 nm/sin 5° = 230 nm, which increases the effective absorption by a factor of ~ 5 if an absorption length of 5.4 μm is assumed [45]. A corresponding increase in photoionization explains the shift of the 45° spectra to higher binding energies, since the quasi Fermi-level at the surface is decreased with respect to the reference Fermi level. Without an explicit definition of the reference Fermi level, e.g. measured on a Au reference, this shift cannot be quantitatively evaluated.
However, the important point for the $Pt/SrTi_{1-x}Fe_xO_3$ system is that SPV is only observed in the presence of an interface band-bending. The direction of the SPV shift is compatible with an n-doped semiconductor forming a Schottky-type depletion layer at the interface.
The observed peak-broadening, however, is not compatible with a spread of binding energie s perpendicular to the surface, since the smaller escape depth at 45° should yield less broad peaks in this case. The broadening can be understood when considering lateral inhomogeneities close to the $Pt/SrTi_{0.95}Fe_{0.05}O_3$ interface, which derive from regions of slightly different chemical states parallel to the electrode interface. This has been shown for as-grown films by LC-AFM in terms of an inhomogeneous distribution of in-plane conductivity [31], and for chemically reduced $SrTi_{0.99}Fe_{0.01}O_3$ films with Ti electrodes showing filamentary structures with modified electron density [11]. There are no spectral differences visible in the lineshape of Sr and Ti core levels between switched (SET, RESET) and the virgin regions. With respect to a spectroscopic signature of the switching itself, it is very likely that there are no observable traces since the switched area is much too small. Considering that spatially resolved experiments have consistently shown the switched area in $SrTi_{1-x}Fe_xO_3$ MIM-cells to be on the order of 1 μm^2, the percentage of switched area on the 100 x 100 μm^2 electrodes is approximately 0.01%, which will not be observable by XPS. The lesson here is to reduce the size of the electrodes and in this way increase the density of switched material in the investigated area.

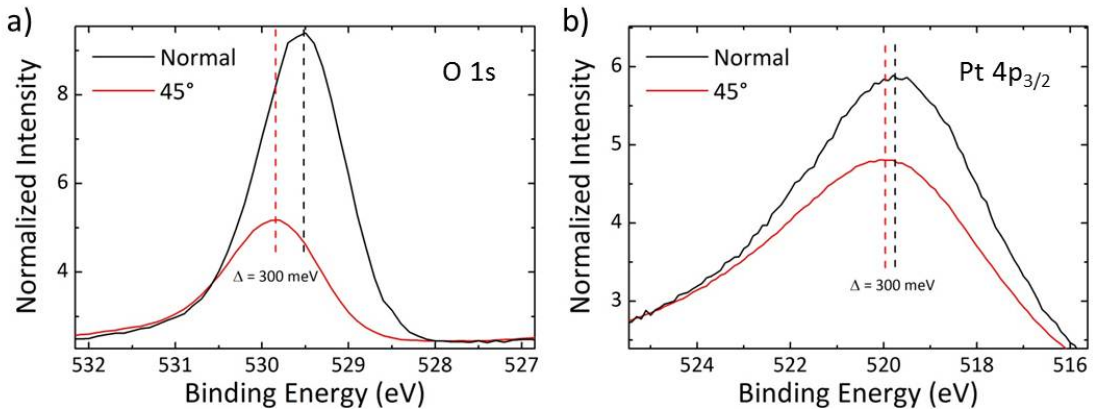

Figure 8.14: Core-level energy shifts in O 1s (a) and Pt $4p_{3/2}$ (b) under two different take-off angles, which are related to the presence of a surface photovoltage (SPV) under photon irradiation.

8.2.5 Rh electrodes

Sample Preparation and Experiment

A 5 nm thin Rh film was deposited on 20 nm $SrTi_{0.95}Fe_{0.05}O_3$ by molecular beam epitaxy (MBE) and fabricated into electrode arrays consisting of 10 x 10 μm^2 electrodes separated by 1-2 μm. Using an automated switching setup, two arrays were set into a SET and a RESET state while another array served as a Virgin-state reference. The electrode array that was set into the SET-state has a nominal distance between electrodes of 2 μm, while the RESET-array nominally has 1 μm distance and the virgin arrays 1.5 μm distance. This is important when considering the signal that derives from the area between the electrodes. HAXPES experiments were performed at P09 at an excitation energy of 5.5 keV, using a Si 311 monochromator and an analyzer pass-energy of 40 eV, resulting in an overall energy resolution of $\sim$ 350 meV as determined by the width of the Au Fermi edge. The energy calibration of the beamline was periodically checked before and after each sample using a Au foil that was in electrical contact with the samples, determining the reference level for photoemission (E_F). Every spectrum has been shifted in energy according to this energy calibration. All spectra have been recorded under a take-off angle close to the surface normal, unless specified otherwise. It is important to note that for any difference spectra shown, no background correction was performed since this is a certain way to introduce artifacts into the difference spectra.

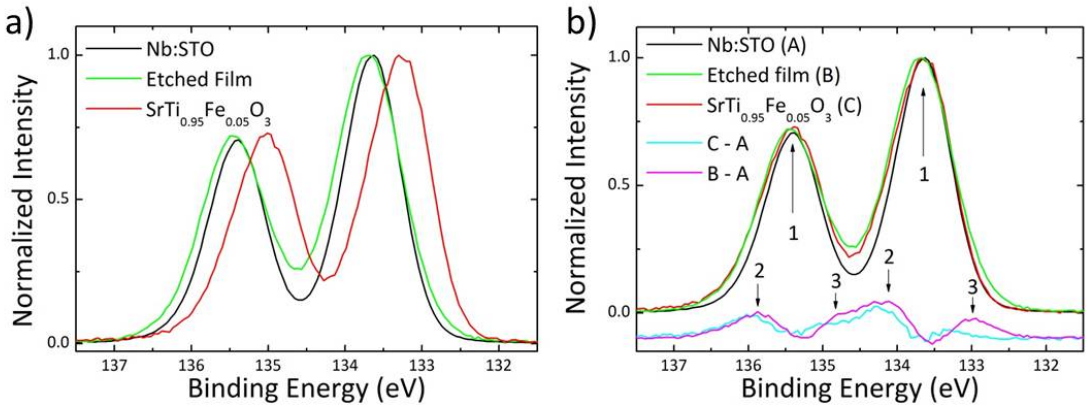

Figure 8.15: a): Sr 3d emission lines of a Nb-doped $SrTiO_3$ single crystal (black), a $SrTi_{0.95}Fe_{0.05}O_3$ thin film and a $SrTi_{0.95}Fe_{0.05}O_3$ thin film after etching in an Ar-plasma (green). The energy shifts are electronic shifts caused by the position of the Fermi level in the band-gap. b): Difference spectra: $SrTi_{0.95}Fe_{0.05}O_3$ - Nb:STO (C - A, cyan) and etched $SrTi_{0.95}Fe_{0.05}O_3$ - Nb:STO (B - A, magenta) show that next to the main $SrTiO_3$ component (1), component (2) can be found in $SrTi_{0.95}Fe_{0.05}O_3$ films, while component (3) appears after Ar-ion etching. Note that the $SrTi_{0.95}Fe_{0.05}O_3$ spectrum has been shifted in energy to coincide with the Nb:STO, and the difference spectra have been offset for clarity.

Virgin state

In the analysis of the as-deposited films (chapter 5), additional spectral components were found especially in the Sr3d doublet that can be interpreted as defective or non-stoichiometric surface phases. In the analysis of the photoemission data from MIM-structures, the main argument will be the energy position of spectral components that appear or disappear in correlation with resistive switching. There are two possible mechanisms that can cause shifts of core-level photoemission lines (refer also to chapter 3): *chemical* shifts that are related to a change of the chemical composition of the probed volume, and *electronic* shifts that are related to a shift of the Fermi level in the sample, for example by doping. Both shifts are illustrated in figure 8.15: a) shows three Sr 3d emission doublets from a Nb-doped $SrTiO_3$ single crystal, and $SrTi_{0.95}Fe_{0.05}O_3$ films after deposition and after Ar-ion etching (during RIBE etchdown). The energy shift observable between the Nb:STO single crystal and the $SrTi_{0.95}Fe_{0.05}O_3$ film is due to the position of the Fermi level in the band-gap (see chapter 5), which is a consequence of the Nb-doping in the single crystal. The energy position of the etched film is almost coincident with that of the conductive single crystal since the Ar etching reduces the surface of the film [116]. Figure 8.15 b) shows the difference spectra between these three Sr 3d emission lines, revealing the presence of Sr components that are shifted in energy due to chemical changes. Component 2 is observable in the as-deposited $SrTi_{0.95}Fe_{0.05}O_3$

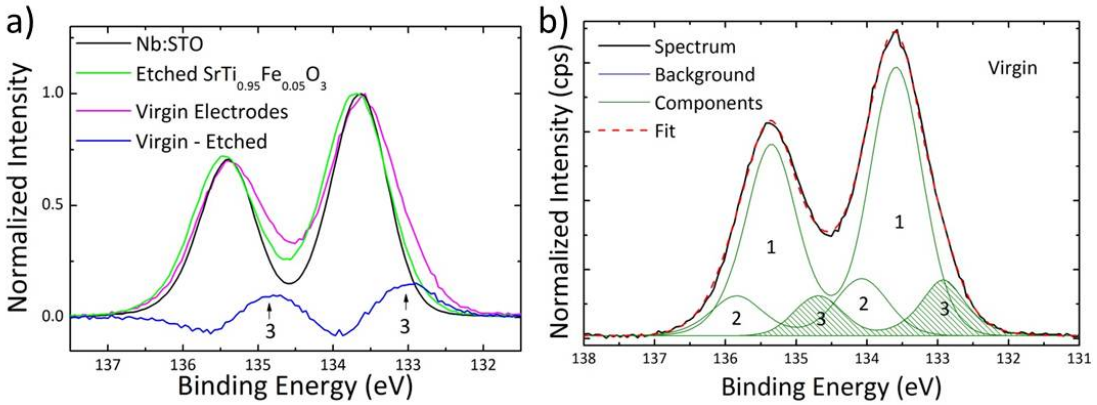

Figure 8.16: a): Comparison of the Sr 3d spectrum recorded on the Nb:STO single crystal (black), the etched $SrTi_{0.95}Fe_{0.05}O_3$ film (green) and the Virgin electrode array (magenta). The difference spectrum of Virgin and the etched film is shown in blue and consists mainly of contribution 3, which is shifted to lower E_b. b): The peak-fitting analysis reproduces all three components, but gives a more accurate picture of the intensities of the respective contributions.

films and is attributed to a Sr-rich surface phase, while an additional component (3) appears after Ar etching. The envelope of the Sr 3d emission line of the etched $SrTi_{0.95}Fe_{0.05}O_3$ film is composed of all three components, which are *chemically* shifted with respect to each other. Both effects need to be considered when examining peak shifts.

Figure 8.16 a) shows the Sr 3d emission doublet measured on the electrically untreated Virgin-array (magenta), compared to the Nb:STO single crystal (black) and the etched $SrTi_{0.95}Fe_{0.05}O_3$ film (green). The difference spectrum of the Virgin electrodes and the etched film is shown in blue, and consists mainly of contribution 3. All three contributions are needed to reproduce the spectral envelope of the Virgin electrode. A key challenge in the interpretation of the energy positions is the fact that small uncertainties in the total energy calibration can influence the fine structure contained in the envelope in a drastic way. Peak-fitting is more reliable in this way than difference spectra since the relative intensity of the spectral contributions is not artificially influenced by an energy shift between two spectra. For the presented fit in figure 8.16 b), the peak-shape and width for components 1 and 2 was fixed to the values obtained for the Nb:STO single crystal, while component three was allowed to vary. Both the spectral comparison and the peak-fitting reveal an increase in spectral intensity on the low binding energy side of the Sr 3d doublet for the Virgin electrodes, which can be described by an additional spectral contribution (component 3) that is energy-shifted by 0.6 eV to lower binding energy with respect to component 1.

It is clear from the comparison of the etched film and the Virgin array that com-

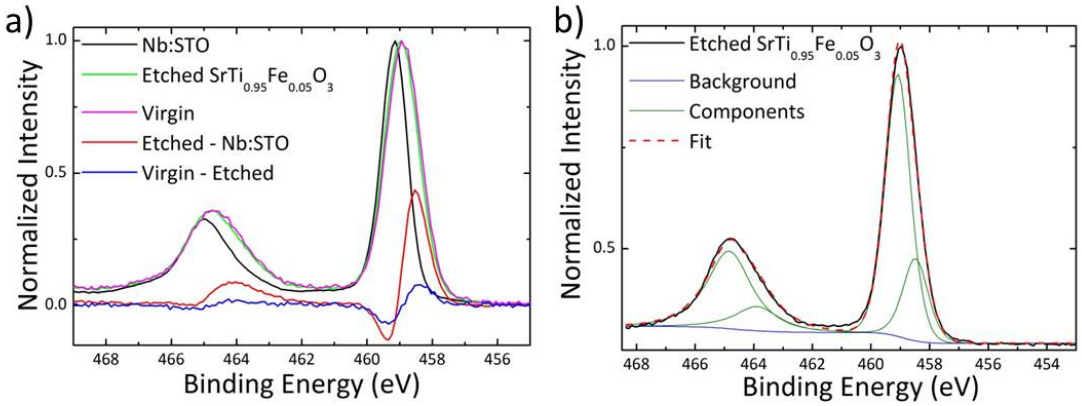

Figure 8.17: a): Ti 2p photoemission spectra from a Nb:STO single crystal (black), an Ar etched $SrTi_{0.95}Fe_{0.05}O_3$ film (green) and the virgin electrode array (magenta). The difference spectrum highlighting the additional contribution in the $SrTi_{0.95}Fe_{0.05}O_3$ spectrum is shown in red, and the small difference between Virgin and the etched $SrTi_{0.95}Fe_{0.05}O_3$ film is shown in red. b): Peak-fit analysis of the etched $SrTi_{0.95}Fe_{0.05}O_3$ doublet, using two sets of lines with identical parameters (LG-mix, FWHM) that are shifted by 0.6 eV with respect to each other.

ponent 3 is strongly enhanced in the latter, while component 2 might be stronger in the etched film. However, the direct comparison of the high energy flank of the Sr 3d envelope depends very strongly on the energy calibration since the shape of the flank is very similar. A shift of only 50 meV, which is on the order of photon energy fluctuations, can change the shape of the difference spectrum on this side. The low energy side of the doublet exhibits a clearly different slope, and is more reliable for interpretation since the spectral difference is not changed by such small energy variations.

The spectral shape of the Ti 2p doublet is less straightforward to interpret due to the larger inherent line-width. Figure 8.17 a) depicts the Ti 2p emission spectrum of a Nb:STO single crystal and the $SrTi_{0.95}Fe_{0.05}O_3$ film after Ar etching. The discussion will be focused on the Ti $2p_{3/2}$ line rather than the Ti $2p_{1/2}$ line due to the much smaller inherent line-width of the former. The Nb:STO reference exhibits a narrow emission line corresponding to Ti^{4+}, and the contribution from Ti^{3+} due to the Nb^{5+} doping induces only a very small change in the slope of the low-energy side of the line. The presence of Ti^{3+} is not directly obvious from the spectrum despite the fact that the crystal shows metallic conductivity and has about 1 at-% donor doping, which is a useful consideration when looking for changes in the emission line induced by resistive switching. In comparison, the Ti $2p_{3/2}$ line of the etched film is significantly broader and the center is shifted toward lower binding energy. Analytically, both line broadening and shift can be described by an additional contribution to the emission line, as can be seen from

the difference spectrum (red line).
A more accurate analysis is again provided by a peak-fitting procedure shown in figure 8.17 b) that reproduces the two contributions to the spectrum. Both doublets have been fitted with identical spectral shape (LG-mix, FWHM) and are shifted in energy by 0.6 eV. The main component can be ascribed to Ti^{4+}, which can be assumed to be the prevalent valence state despite the Ar etching, while the lower energy component is induced by the etching and corresponds to Ti in lower oxidations states or chemically different environments. However, a contribution from Ti^{3+} would be expected at E_b = 457.4 eV and cannot be clearly resolved. The shifted Ti line is more likely to correspond to non-stoichiometric $SrTiO_3$ since oxygen is preferentially removed from the surface region by Ar sputtering [116]. The sputter treatment induces electronic states in the band-gap up to the Fermi level, resulting in a finite electronic conductivity (see figure 9.9 in the appendix). Since the top of the valence band is mainly composed of Ti 3d orbitals that are hybridized with O 2p orbitals, the in-gap states likely result from Ti ions with a higher electron density (lower oxidation state) than Ti^{4+} which are created by the selective removal of oxygen and the perturbation of the perovskite lattice. The fingerprint for these states seems to be an additional contribution at the lower binding energy side of the Ti 2p doublet. The Ti 2p doublet measured on the Virgin electrode array is very similar to that of the etched film, with a slightly larger low-binding energy component.
The O 1s emission lines of the pristine and etched $SrTi_{0.95}Fe_{0.05}O_3$ film are shown in figure 8.18 a) in red and green, respectively, as well as the difference spectrum in cyan. In contrast to the emission lines of the cations, the etched $SrTi_{0.95}Fe_{0.05}O_3$ film shows additional spectral weight on the high binding energy side of the O 1s line. This broad feature is marked 'B' in the figure and is probably induced by the etching process. In contrast, the O 1s line measured on the Virgin electrodes (black) shows a distinct shift of the main line ('A') that can be interpreted as an additional contribution on the low binding energy side ('C'). Feature 'B' is also strongly enhanced in the Virgin spectrum, whereas the small contribution of feature 'C' in the etched spectrum is likely an artifact due to the different energy calibrations of the spectra.
It is important to consider that the trenches in between the electrodes are etched by the same treatment as the etched film, and therefore the Virgin spectra can be seen as combinations of the etched film and the spectral contributions that arise from beneath the electrodes. The difference that is observable between 'etched' and Virgin can therefore be attributed to the area under the electrodes. The low binding energy components in all the spectra are shifted by 0.6 eV to lower binding energies, which can be explained by the band-bending at the Rh / $SrTi_{0.95}Fe_{0.05}O_3$ interface. Assuming that this is the case, then the conduction band offset (or barrier height) can be evaluated to 0.7 ± 0.1 eV, which is comparable to the 0.9 eV found for Pt (section 5.3.1). Since these electronically shifted contributions

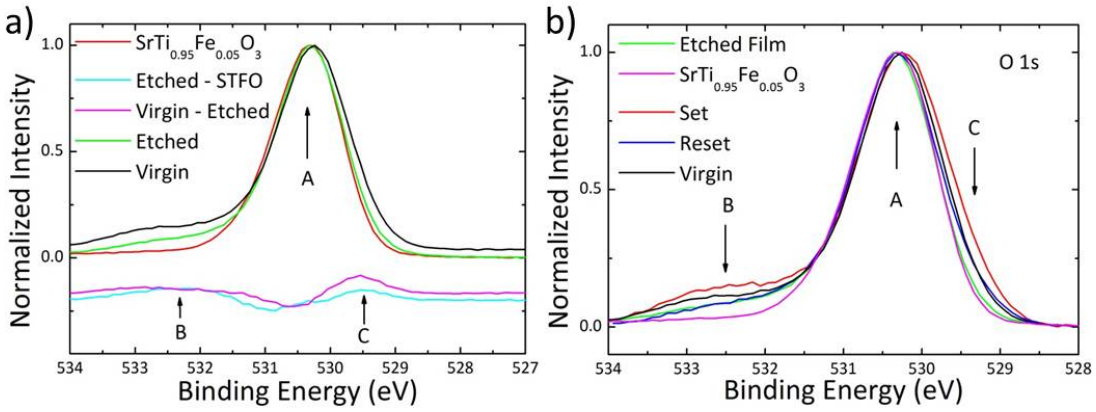

Figure 8.18: a): O 1s photoemission spectra from an $SrTi_{0.95}Fe_{0.05}O_3$ film (red), an etched $SrTi_{0.95}Fe_{0.05}O_3$ film (green) and the Virgin electrode array (black). The difference spectrum of the pristine and the etched $SrTi_{0.95}Fe_{0.05}O_3$ is shown in cyan and the difference of Virgin and etched $SrTi_{0.95}Fe_{0.05}O_3$ in magenta. b): O 1s photoemission lines of all three electrode arrays (SET: red, RESET: blue, Virgin: black), as well as the pristince $SrTi_{0.95}Fe_{0.05}O_3$ (magenta) and the etched $SrTi_{0.95}Fe_{0.05}O_3$ (green) films.

are strongest at the interface and decay with distance from the interface, the large escape depth of the photoelectrons actually minimizes the overall contribution of these components to the spectral envelope because the photoelectrons escaping from deeper layers in the sample have smaller or no electronic shifts. This and the fact that the *chemical* shifts induced by etching and the *electronic* shifts caused by the interface barrier have the same sign significantly complicate the analysis.
As a last point, the feature marked 'B' in the difference spectrum of the O 1s line is strongly enhanced in the Virgin spectrum. This energy position is often assigned to surface contaminations and physisorbants. From the above conclusions, a small part of this feature is due to the reduced, etched film, and the rest is likely a result of the sample handling during the automated switching and residual photoresist that was not removed at the electrode edges.
According to the systematic evolution of the spectra, the following conclusions can be drawn for the Virgin array: similar to the etched film, both Sr and Ti emission lines show spectral contributions on the low binding energy side. The O 1s emission line of the Virgin array is unlike the etched $SrTi_{0.95}Fe_{0.05}O_3$ film in that the etched film shows spectral weight on the high E_b side only, whereas the Virgin array shows spectral weight in both high and low E_b sides. For the cationic emission lines, the low E_b contribution is larger in the Virgin array than for the etched film. The shifts in the etched film are mainly due to oxygen removal and therefore a chemical reduction, and the observed peak shifts are *chemical* shifts. The opposite sign of the shift for cations and anions is a good indication. For the Virgin array, both cationic and anionic emission lines show a large contribution

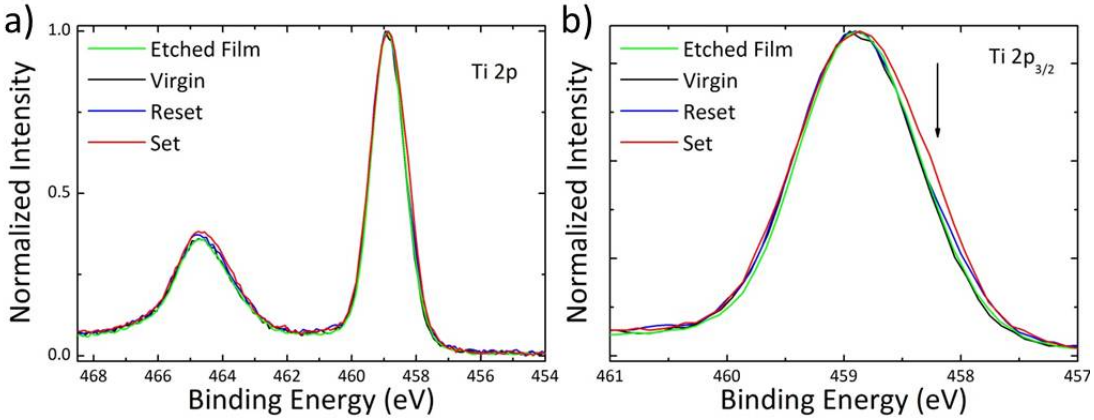

Figure 8.19: a): Ti 2p photoemission spectra of the three electrode arrays and the etched $SrTi_{0.95}Fe_{0.05}O_3$ film. The spectra are almost identical, but the slightly increased intensity of the low E_b shoulder in the SET spectrum can be seen in the magnified display of the Ti $2p_{3/2}$ line in b).

at the low E_b side, which points to an *electronic* shift as it is induced by surface band-bending. This is a consequence of the Schottky-type contact between Rh and $SrTi_{0.95}Fe_{0.05}O_3$.

Switched arrays

The O 1s spectra recorded on the SET and RESET electrodes (red and blue, respectively) are compared to the pristine (magenta) and etched (green) films and the Virgin electrodes (black) on the right-hand side of figure 8.18. The spectral feature 'B' scales with the electrode separation, with the intensity of Virgin (1.5 μm) in between that of SET (2 μm) and RESET (1 μm). However, the superposition of any 'real' features with contaminants on the surface renders an interpretation futile. Feature 'A' is likewise highest in the SET spectrum, but shows virtually identical intensity for Virgin and RESET. A similar observation can be made on the low E_b side of the Ti $2p_{3/2}$ line shown on the right side of figure 8.19. The SET - spectrum (red) shows a clear shoulder at 458.25 eV binding energy, shifted away from the Ti^{4+} position by -0.75 eV. The same shoulder, but with smaller intensity, can be seen in the RESET - spectrum (blue), whereas it is absent in the Virgin - spectrum and the etched film. While the spectral changes for the Ti 2p and O 1s emission lines are rather small, the difference in the shape of the Sr 3d envelope can be seen without magnification. Figure 8.20 shows the Sr 3d spectra for the Virgin, RESET and SET electrodes (from left to right) with components 1, 2 and 3 used to fit the spectral envelope. While Virgin and RESET are again very similar, the SET spectrum shows an appreciably larger contribution from the low binding

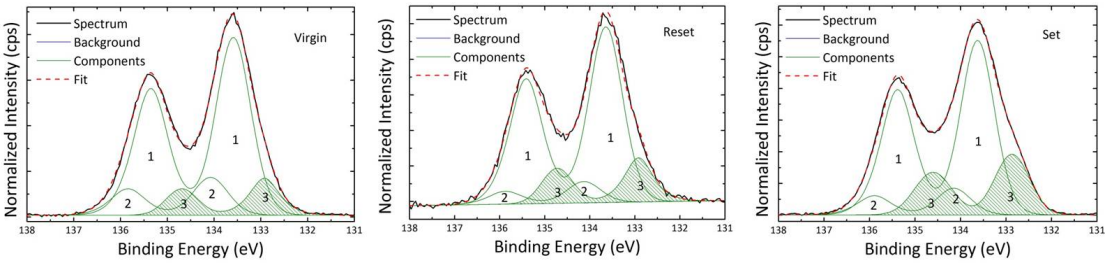

Figure 8.20: Sr 3d spectra and their constituent components as determined by peak-fitting analysis for the Virgin, RESET and SET electrodes (left to right). Lineshape parameters (LG-mix, FWHM) were fixed to values determined for Nb:STO for components 1 and 2, while component 3 was allowed slight variations.

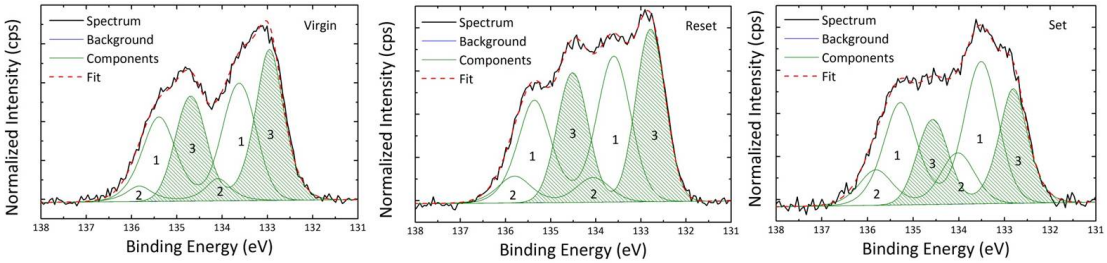

Figure 8.21: Sr 3d spectra recorded under a TOA of 45° for the three electrode arrays Virgin, RESET and SET (left to right). Fitted components 1 and 2 were fixed to the values obtained form the Nb:STO fit.

energy component 3. The peak parameters for components 1 and 2 were fixed to those obtained from fitting the Sr 3d doublet of Nb:STO (see section 5.3.1), while slight variations were allowed for component three. While the SET array has the largest trench-area and therefore the largest contribution from the etched film, the spectral weight of component 3 is much larger than observed in the etched spectrum. The consequence is again that the additional intensity must arise from the area under the electrodes. The energy positions of all three components are identical for all spectra, within the measurement uncertainty (< 100 meV). Sr 3d spectra were also recorded under a take-off angle of 45° to increase the sensitivity to the interface between Rh and $SrTi_{0.95}Fe_{0.05}O_3$Figure 8.21 shows the Sr 3d spectra of the Virgin, RESET and SET electrode arrays from left to right: Again Virgin and RESET are very similar while SET is drastically different. The main difference between Virgin and RESET is that the energy position of component 3 is shifted to slightly lower E_b in the RESET spectrum. The SET spectrum, however, shows a significant decrease in the intensity of component 3 compared to RESET or Virgin, while at the same time component 2 seems increased.

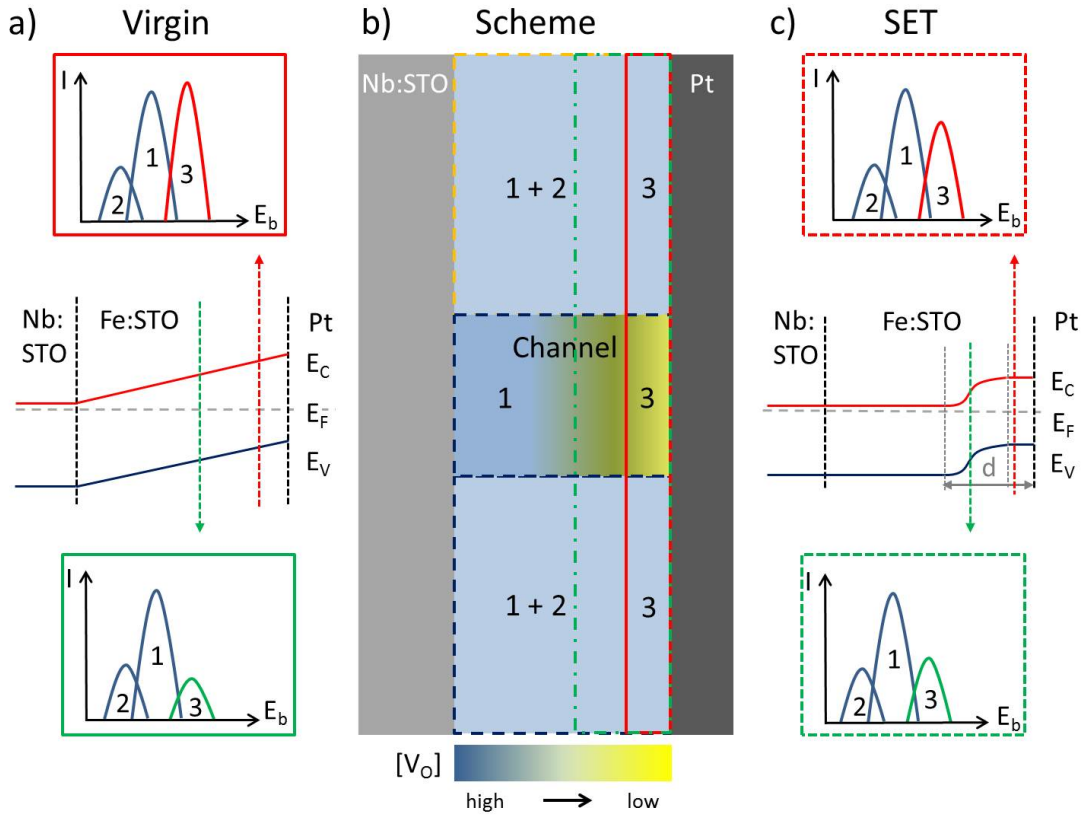

Figure 8.22: Schematic representation of the switching mechanism in thin $SrTi_{1-x}Fe_xO_3$ films. See text for a detailed description.

Discussion

The core-level spectra consistently show an increase of the low binding energy component for all core-levels in the SET spectra. The intensity of the additional spectral contributions places the RESET spectra in-between the SET and Virgin spectra. This is in agreement with the way the resistance is written during switching: first the resistance is lowered during SET, and then raised again during RESET. Since the RESET resistance is almost as high as the Virgin resistance, the close similarity of the Virgin and RESET spectra underline the impression that during RESET, the chemical changes induced during SET are reversed. This is in agreement with the picture of a reversible resistance change in the structure.
The origin of the additional spectral components is depicted schematically in figure 8.22. The center (b) depicts a schematic cross-section through a MIM-structure in the SET state: a resistively switched channel is embedded into an insulating periphery. The insulating film (marked in light blue) contributes spectral components 1 and 2 to the measured spectra. The $Rh/SrTi_{0.95}Fe_{0.05}O_3$ interface contributes

component 3, with the maximum intensity directly at the interface and smaller relative contributions for larger escape depth. This is sketched for the Virgin state in figure 8.22 a) for an interface sensitive spectrum (red box) with a large relative contribution of component 3 and for a bulk sensitive spectrum (green box) with a small relative contribution of component 3. The relative intensities of the three contributions are schematically depicted as bell-shaped curves, reproducing the relative contributions to the Sr $3d_{5/2}$ line.
The situation changes for the SET spectrum, as sketched in figure 8.22 c). In addition to the spectral contributions from the insulating matrix (same as Virgin), the presence of the channel modifies the SET spectra. The intensity of component 3 is reduced close to the interface, but not shifted in energy (see sketched spectrum in the dashed red box). This is a consequence of a *lateral* inhomogeneity due to the conducting channel, as seen with PEEM in section 8.1. At the same time, component 3 is increased in the bulk (dashed green box). This implies that the region of the sample giving rise to this component in the SET spectrum provides more intensity further away from the interface and extends into the bulk, whereas the interface barrier decays quickly with distance from the interface (see schematic band diagrams in figure 8.22 a) and c)). One explanation is an oxidized region that is depleted of oxygen vacancies, and therefore the difference E_C - E_F is larger than in the bulk to the film, which is enriched in oxygen vacancies. The corresponding accumulation of oxygen vacancies in the film underneath effectively reduces the width of the tunnel barrier d and decreases the resistance of the cell, in agreement with the mechanism proposed in section 6.2.6.

Chapter 9

Conclusions and Outlook

The scope of this thesis is the clarification of the switching mechanism by the application of advanced spectroscopy techniques on resistively switched MIM cells fabricated from $SrTi_{1-x}Fe_xO_3$ thin films. From a technological point of view, the key challenge is to explore and establish suitable sample systems that are tailored to suit each technique. Following up on this, a detailed investigation of the physical and structural state using several spectroscopy techniques was performed.

Investigations of the Thin Film Growth

Using Pulsed Laser Deposition (PLD) to grow epitaxial doped $SrTiO_3$ layers for resistive switching offers great advantages such as high versatility and flexibility. To optimize the growth parameters for resistive switching and spectroscopy, the influence of growth pressure and laser energy on the crystal structure of the films was examined and an optimal parameter set established. In addition, the substrate miscut angle was shown to influence the strain relaxation of thick, heteroepitaxial films: long terraces (small miscut angle) favor strain relaxation, while small terraces (large miscut angle) favor the growth of strained films. An important observation is also that the Fe-content of the ceramic target directly influences the growth rate and lattice expansion of the thin films, and therefore presumably influences the defect structure of the films.

Incorporation of Fe into $SrTiO_3$

In order to understand the chemical and nanoionic changes that cause the resistive switching phenomenon, a detailed understanding of the active switching material in its pristine state is extremely important. Despite nominally identical composition and crystal structure, $SrTiO_3$ thin films have been shown to differ significantly from the single crystalline material in terms of defect structure and physical properties [6, 30, 31]. One of the focal points of this thesis was therefore the understanding of Fe incorporation into Fe-doped $SrTiO_3$ thin films. The most important tool for this task is spectroscopy, analyzing the local structure around the Fe dopant (XAFS) and the electronic structure and chemical states of the thin film (HAXPES) after deposition. Despite dopant concentrations as high as 5% site fraction ($SrTi_{0.95}Fe_{0.05}O_3$), no unequivocal evidence for the formation of Fe-rich clusters was found.
An electrocolored, Fe-doped single crystal yielded an excellent reference for the defect configuration of Fe centers in $SrTiO_3$. Using EPR, Raman and XAFS, it was possible to identify and describe the respective Fe centers in the oxidized and reduced regions that are generated by the concentration polarization. With these

references, it was shown that PLD grown thin films do not contain any Fe^{4+} in the pristine state, but only Fe^{3+} with a high concentration of Fe-$V_O^{\bullet\bullet}$ centers for all Fe concentration (x = 0.5%, 1%, 2% and 5%).
Increased Fe doping could be linked to a decrease of the free charge carrier concentration in the system via photoemission spectroscopy, and confirmed by transport properties across the $SrTi_{1-x}Fe_xO_3$ / Pt interface. A high yet non-degenerate electron concentration was found for undoped $SrTiO_3$ films, induced by a strong oxygen deficiency. It needs to be clarified in the future whether the lower electron concentration in Fe-doped $SrTiO_3$ is caused by acceptor-like behavior of Fe and a charge compensation mechanism in the solid state, or if the Fe sufficiently alters the plasma-plume of the PLD deposition so that the growing film is more highly oxidized and therefore less oxygen vacancies are present.

Electroforming of thick $SrTi_{1-x}Fe_xO_3$ films

Concerning the long-term DC voltage treatment that is necessary to break down the high initial resistance ('electroforming') MIM cells fabricated from thick ($\geq$50 nm) $SrTi_{1-x}Fe_xO_3$ films, it was found that the forming times can be significantly shortened by the presence of growth defects - presumably screw dislocations - under the electrode. Switching properties of these 'defective' cells are very similar to those of conventionally formed cells, showing both switching polarities observable in thick $SrTi_{1-x}Fe_xO_3$ films.
The location of the conducting filament in an electroformed MIM cell with 100×100 μm dimensions could be found by XAFS with a microfocused X-ray beam using the spectroscopical footprint established for Fe-$V_O^{\bullet\bullet}$ centers. The local structure of the Fe dopants in the filament is different from that in reduced $SrTiO_3$, pointing to a clustering of multiple oxygen vacancies in the first shell around Fe. Interestingly, the $V_O^{\bullet\bullet}$ concentration increases homogeneously under the whole electrode during forming, even though the switching is localized at the filament only. This supports the model that the filament is nucleated and grows in a location where the propagation of the virtual cathode is faster than in the surrounding area. The large spread in electroforming times that was observed implies that the formation of the filament itself is a process that is limited by nucleation, and therefore a stochastic process. This has interesting consequences when the film thickness is reduced so far that the homogeneous front grows across most of the MIM cell in a time less than the average nucleation time, where the formation of a filament cannot be expected.

Thin $SrTi_{1-x}Fe_xO_3$ films

Indeed, 20 nm $SrTi_{1-x}Fe_xO_3$ films do not require a dedicated DC electroforming step and do not show the switching polarity that is associated with the conducting

filament in thick films (called 'filamentary' or 'counter-eightwise'), but only the switching polarity called 'eightwise' (or 'homogeneous'). These thin films were found to perform reliably, with yields up to 100%, and show multilevel switching properties than can be continuously tuned by the voltage amplitude. Chemically sensitive images of the switching craters of a Au/$SrTi_{0.95}Fe_{0.05}O_3$ /Nb:STO sample -recorded by Photoemission Electron Microscopy (PEEM) - supply evidence for a chemical demixing in the center of the crater, probably mediated by a high local temperature. Local spectroscopy indicates redox-reaction in the craters during SET and RESET.
The increased reliability was utilized to fabricate large arrays, consisting of thousands of MIM cells, that could be analyzed by spectroscopy without spatial resolution. Photoelectron spectroscopy of these arrays yielded information about the interface barrier height between metal electrode and insulator, which are in good agreement with barrier heights calculated from current-voltage analysis. In addition, the decreased initial resistance of MIM cells, which can be observed when reactive electrodes such as Ti are deposited above a certain thickness, was shown to be caused by a redox-reaction at the interface where the metal electrode is oxidized and the missing oxygen induces additional charge carriers into the $SrTi_{1-x}Fe_xO_3$ film.
With noble metal electrodes such as Pt and Rh, the analysis of core-level emission lines shows no observable changes in the Ti 2p doublet that would suggest Ti^{3+}, and instead suggests changes at the Sr doublet. Small changes in the line shape and width of all core-level emission lines are interpreted as a fingerprint of a oxygen vacancy-depleted (or oxidized) region close to the top interface. Together with the temperature-dependent analysis of the current-voltage characteristics of a Pt/$SrTi_{0.95}Fe_{0.05}O_3$ /Nb:STO cell, a switching model is suggested based on the modulation of the width of a tunneling barrier close to the top electrode. This barrier consists of a narrow region of highly oxidized $SrTi_{1-x}Fe_xO_3$ that has been depleted of oxygen vacancies by electrical stimuli.

Outlook

For future work, there are two promising experiments that could significantly expand our understanding of resistive switching in MIM-cells. The first of these techniques is Hard X-ray Photoemission Electron Microscopy (HAXPEEM), which is identical to PEEM but uses hard x-rays for excitation. Preliminary experiments have determined an electron attenuation length of 8 nm for 4.5 keV electrons (see figure 9.1). A spatial resolution of ∼410 nm could be obtained at 6.5 keV excitation energy (for full details see [117]). The advantage over PEEM using soft x-rays is the enhanced information depth, and the possibility to record spectra with increasing excitation energy, corresponding to a depth profile. However, intensity is expected to be a problem since the orbital cross-sections for photoexcitation

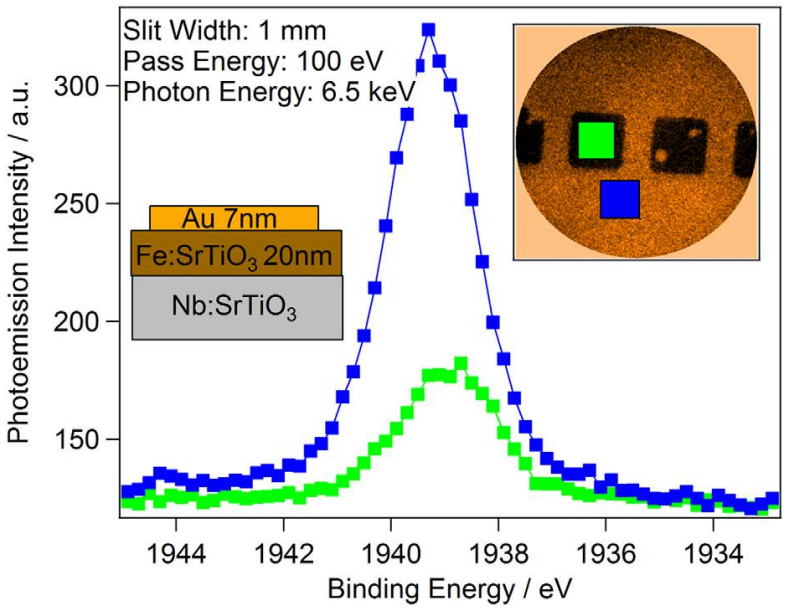

Figure 9.1: Sr $3p_{3/2}$ core level spectra recorded at 6.5 keV excitation energy form the marked regions of interest. The shift to lower binding energy underneath the Au electrode can be seen as an indication of band bending in the $SrTiO_3$ layer.

decrease with increasing photon energy. The second issue is that at present, there is no experimental endstation anywhere in the world that offers the possibility to do these experiments. A HAXPEEM endstation is currently being constructed at PETRA III in Hamburg.

Another promising technique for the characterization of MIM-cells is electron holography in a TEM, which is also presented in chapter 6 to support the suggested switching model. This technique is sensitive to local electric fields in the solid, and can yield quantitative information about the inner potential across switched MIM cells. The phase shift of an electron passing through the sample is compared to a reference beam, and can be evaluated in terms of a local potential. Figure 9.2 shows electron holography phase images (recorded by D. Cooper at CEA LETI, Grenoble) of two Nb:STO/$SrTi_{0.99}Fe_{0.01}O_3$ /Pt stacks in the SET (On-) state (a) and RESET (Off-) state (b). The false color plots correspond to the phase shift measured in both samples. The green region close to the interface in (a) corresponds to the $SrTi_{0.99}Fe_{0.01}O_3$ film, which is not visible in the phase image of the RESET sample (b). The two phase shifts along a line perpendicular (sketched in white) to the interface are shown in the diagram next to the images.

The phase is approximately constant across the Nb:STO substrate, and shows a sharp decrease in the $SrTi_{0.99}Fe_{0.01}O_3$ of the SET-sample (onset of $SrTi_{0.99}Fe_{0.01}O_3$ is marked with dashed blue line). This shift corresponds to acceptor doping and was evaluated to 0.8 V. These findings are in agreement with the model presented

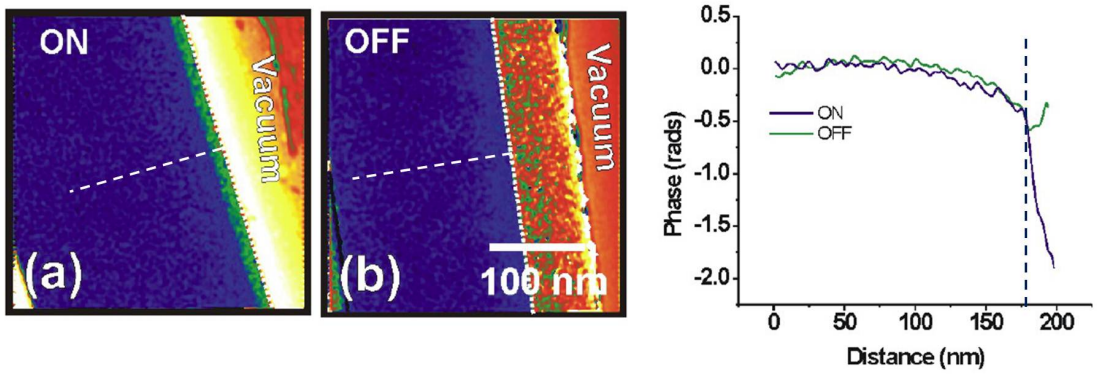

Figure 9.2: (a) and (b): electron holography phase images recorded on a Nb:STO/$SrTi_{0.99}Fe_{0.01}O_3$ /Pt sample in the SET (On) and RESET (Off) state, respectively. The phase along the dashed white lines is shown in the diagram, showing a change corresponding to 0.8 V in the SET (On-) sample whereas the potential is almost flat in the RESET (Off) case. Measurements performed by D. Cooper at CEA LETI.

in 6.2.6, but it should be mentioned that the spatial resolution is 3 nm and the region close to the interface to Pt is difficult to analyze. The polycrystalline nature of the Pt electrode make it impossible to utilize this technique in the region where Pt is found. However, the possibility to access changes in the crystal potential is a very powerful tool, especially for *pn*-type contacts and band bending at interfaces. The downside is that the samples need to be prepared by focused ion beam milling (FIB).

Appendix

Table 9.1: Line-shape parameters for the Sr 3d doublet measured on a Nb:STO single crystal.

Line	FWHM	LG-mixing	$A_{\frac{i+2}{2}}/A_{\frac{i}{2}}$	$\Delta E_{splitting}$
Sr $3d_{5/2}$	0.91 eV	0.3	1.36	1.76 eV
Sr $3d_{3/2}$	0.92 eV	0.569		

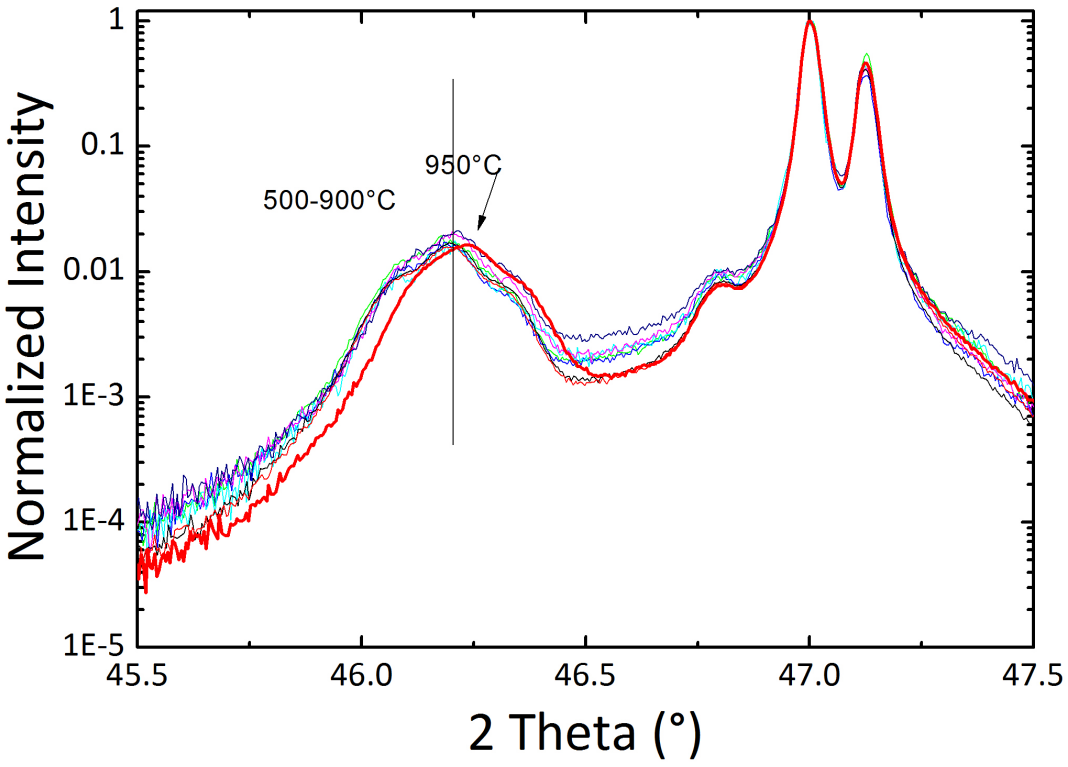

Figure 9.3: X-ray diffraction of a $SrTi_{0.99}Fe_{0.01}O_3$ film on $NdGaO_3$ after annealing in air at temperature ranging from 500°C - 950°C. Relaxation of the heteroepitaxial strain cannot be observed below 950°C.

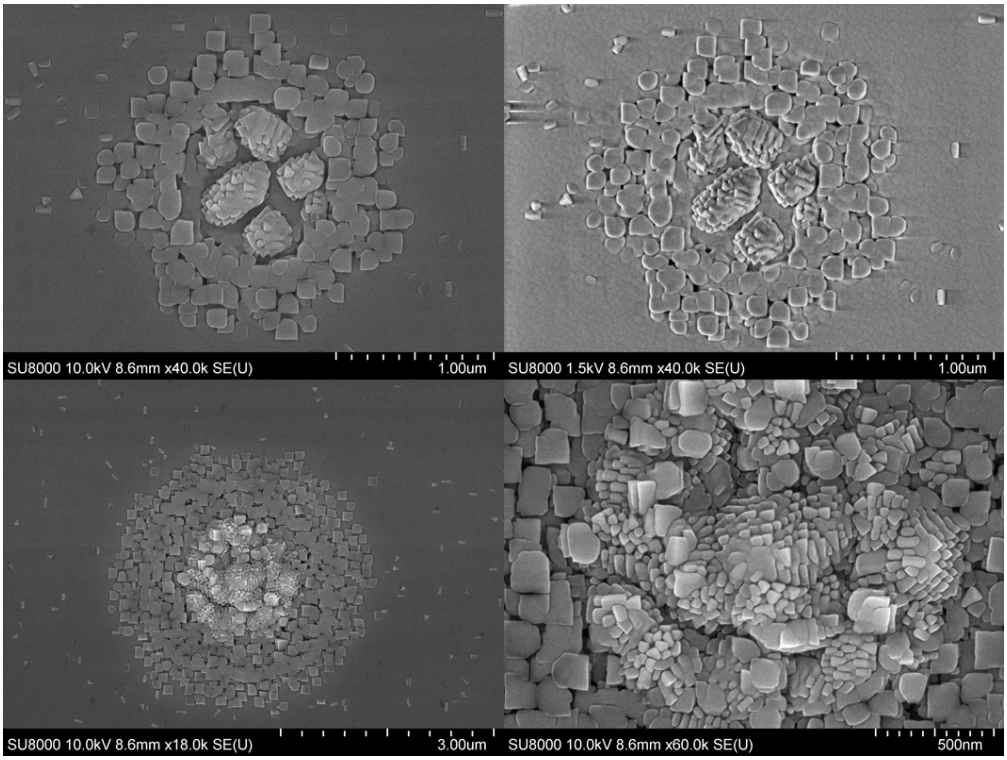

Figure 9.4: SEM micrographs recorded on a 100 nm thick $SrTi_{0.95}Fe_{0.05}O_3$films grown on Nb-doped $SrTiO_3$. Defective areas of different size can be found on the film, ranging from a few tens of nm to several μm in size.

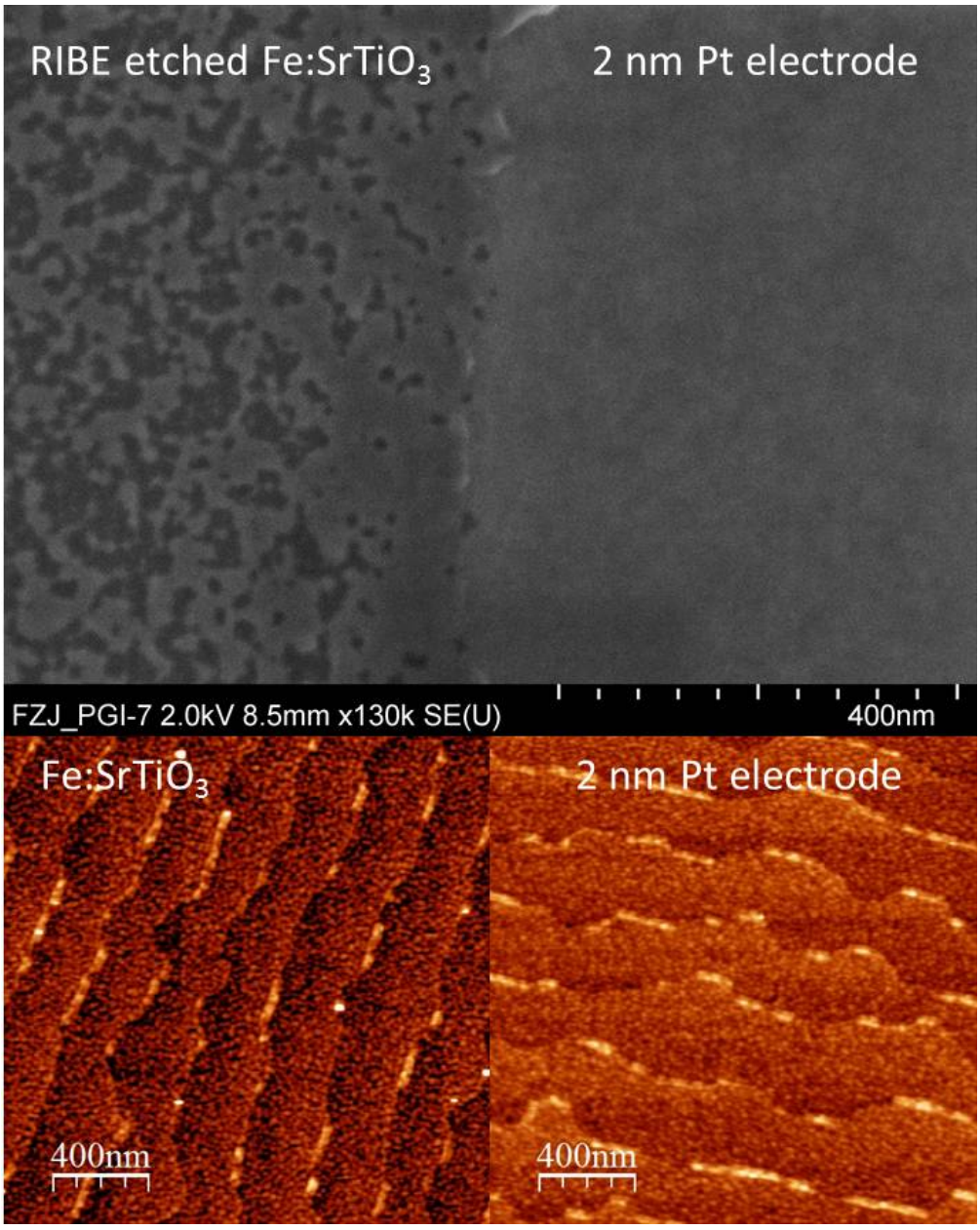

Figure 9.5: Top: SEM micrograph of a 2 nm Pt layer sputtered on top of a $SrTi_{0.95}Fe_{0.05}O_3$film. Bottom: AFM topography of the as-grown film and the Pt electrode. The RMS roughness is in both cases $\sim$ 0.25 nm.

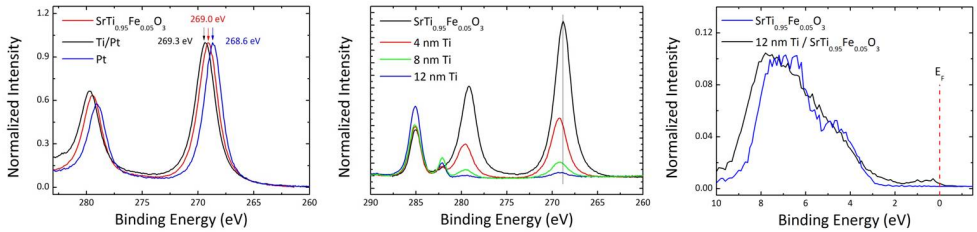

Figure 9.6: Left: Energy shift in the Sr 3p emission doublet of a Ti/Pt and a Pt covered $SrTi_{0.95}Fe_{0.05}O_3$film, compared to a reference. The observed shift in the Sr lines is within 100 meV of the shift observed at the O 1s line and confirms the band-line up at the Pt interface and the shift of the Fermi level in the $SrTi_{0.95}Fe_{0.05}O_3$/ Ti / Pt structure. Center: Sr 3p emission doublets from a bare $SrTi_{0.95}Fe_{0.05}O_3$film (black) and the same film covered with 4, 8 and 12 nm Ti, respectively (red, green and blue). Spectra are aligned to the C 1s emission line at 285.07 eV. The progressive shift in binding energy confirms the findings at the O 1s line of a shift of the reference level. Right: Comparison of the valence band of a bare $SrTi_{0.95}Fe_{0.05}O_3$film and one covered with a 12 nm Ti layer. The Fermi edge emission of the TiO_x layer is clearly observable, indicating electrical conductivity in the oxidized layer.

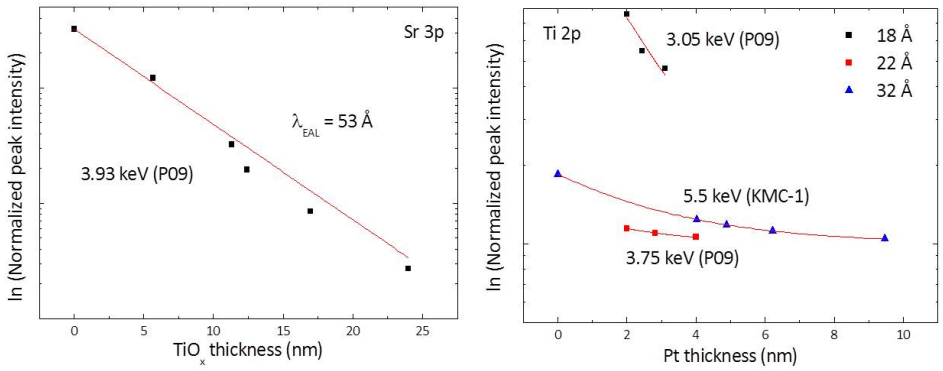

Figure 9.7: Effective attenuation length values determined by angular dependence of the photoemission intensity for TiO_x (Sr 3p, left) and Pt (Ti 2p line, right). The EAL values are determined by exponential fits of the type $I \propto exp(-t/EALcos\alpha)$ where t is the overlayer thickness and α the emission angle.

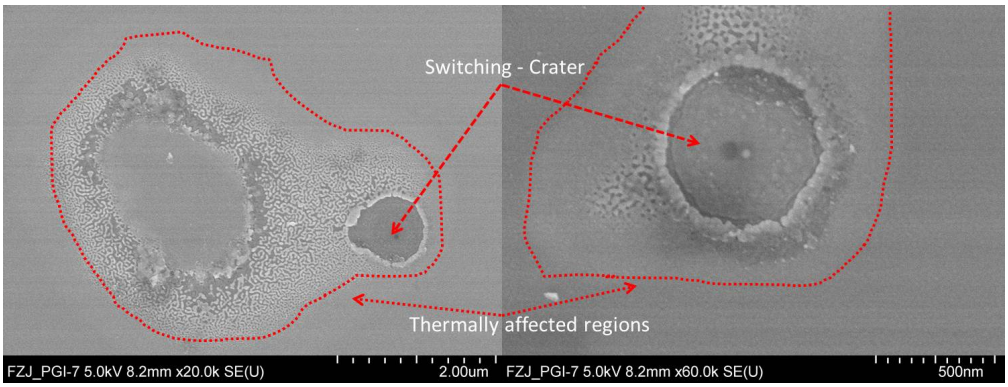

Figure 9.8: SEM images of two 5 nm Rh/ $SrTi_{0.95}Fe_{0.05}O_3$/ Nb:STO electrode pads in the RESET-state. Both pads show a distinct, circular switching crater, and in addition a region where the microstructure of the Rh electrode has been altered. The Rh film shows clear signs of recrystallization, with pinholes appearing in the structure due to increased temperature (and correspondingly, surface diffusivity) and the fact that the volume free energy of Rh is much more negative than the interface free energy of the Rh/oxide surface. The latter is a typical characteristic of a noble metal.

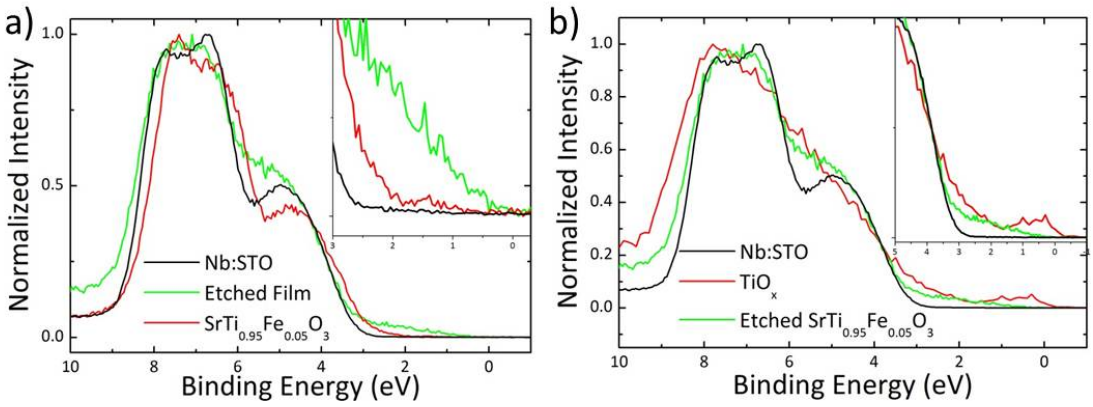

Figure 9.9: a:) HAXPES spectra taken from the valence band of a Nb:STO single crystal (black), an Ar etched $SrTi_{0.95}Fe_{0.05}O_3$ film (green) and an as-deposited $SrTi_{0.95}Fe_{0.05}O_3$ film. Inset: Magnification of the band-gap region. Note that the $SrTi_{0.95}Fe_{0.05}O_3$ spectrum is shifted by ∼400 meV to lower E_b because the position of the Fermi-level in the band-gap is different. b): VB spectra from etched $SrTi_{0.95}Fe_{0.05}O_3$ (green) and a TiO_x layer (red) grown by sputtering metallic Ti onto a $SrTi_{0.95}Fe_{0.05}O_3$ thin film, and Nb:STO crystal (black=. Note how the etched film seems to be a combination of both types of VB.

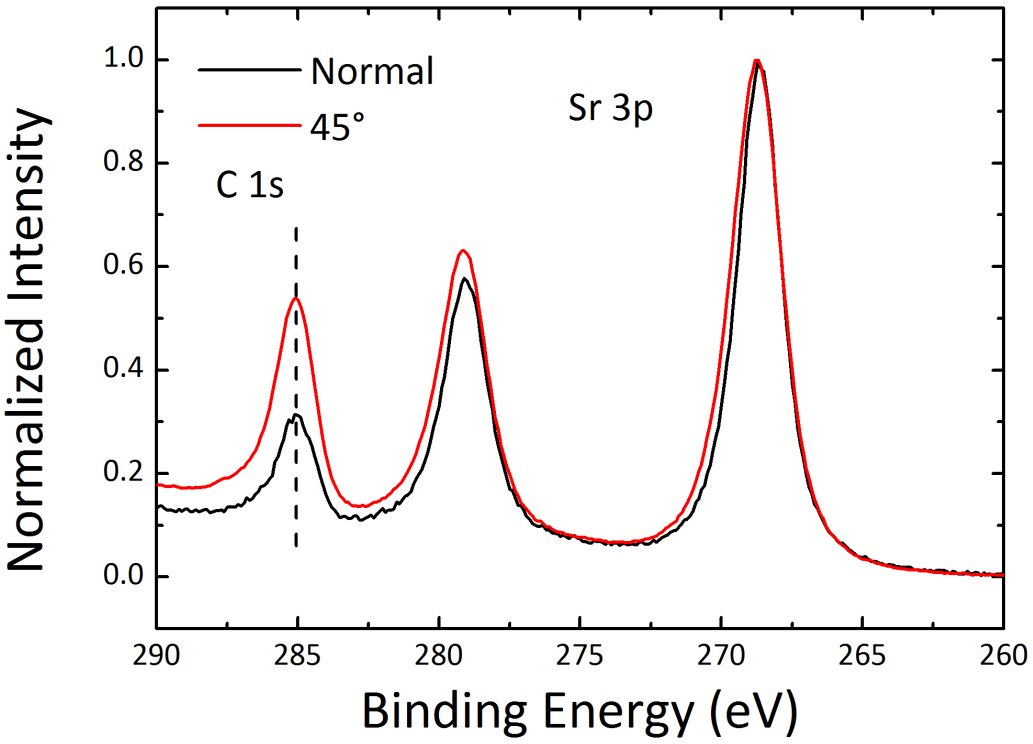

Figure 9.10: Comparison of Sr 3p spectra taken from a 2 nm Pt/ $SrTi_{0.95}Fe_{0.05}O_3$ structured sample. The spectra have been energy calibrated using the C 1s line of adventitious carbon. The peak broadening visible in the Sr doublet cannot be seen in the C 1s peak.

Bibliography

[1] R. Waser, R. Dittmann, G. Staikov, and K. Szot, *Adv. Mater.* **21**, 2632 (2009).

[2] R. Williams, *Oral presentation at the MRS Spring Meeting 2012, San Francisco, CA* (2012).

[3] *International Technology Roadmap for Semiconductors* (2011).

[4] A. Sawa, *Materials Today* **11**, 28 (2008).

[5] M. Janousch, G. I. Meijer, U. Staub, B. Delley, S. F. Karg, and B. P. Andreasson, *Adv. Mater.* **19**, 2232 (2007).

[6] C. Lenser, A. Kuzmin, J. Purans, A. Kalinko, R. Waser, and R. Dittmann, *J. Appl. Phys.* **111**, 076101 (2012).

[7] J. P. Strachan, D. B. Strukov, J. Borghetti, J. J. Yang, G. Medeiros-Ribeiro, and R. S. Williams, *Nanotechnology* **22** (2011).

[8] R. Dittmann, R. Muenstermann, I. Krug, D. Park, T. Menke, J. Mayer, A. Besmehn, F. Kronast, C. Schneider, and R. Waser, *submitted to IEEE* (2012).

[9] J. P. Strachan, G. Medeiros-Ribeiro, J. J. Yang, M.-X. Zhang, F. Miao, I. Goldfarb, M. Holt, V. Rose, and R. S. Williams, *Appl. Phys. Lett.* **98**, 242114 (2011).

[10] P. Calka, E. Martinez, D. Lafond, S. Minoret, S. Tirano, B. Detlefs, J. Roy, J. Zegenhagen, and C. Guedj, *J. Appl. Phys.* **109**, 124507 (2011).

[11] S. Stille, C. Lenser, R. Dittmann, A. Koehl, I. Krug, R. Muenstermann, J. Perlich, C. Schneider, U. Klemradt, and R. Waser, p. 223503.

[12] J. Simmons and R. Verderber, *Proc. Roy. Soc. A* **301**, 77 (1967).

[13] A. Beck, J. G. Bednorz, C. Gerber, C. Rossel, and D. Widmer, *Appl. Phys. Lett.* **77**, 139 (2000).

[14] R. Waser and M. Aono, *Nat. Mater.* **6**, 833 (2007).

[15] L. Chua, *IEEE Trans. Circuit Theory* **18**, 507 (1971).

[16] Y. Kin and J. Lee, *J. Appl. Phys.* **104**, 114115 (2008).

[17] S. Liu, N. Wu, and A. Ignatiev, *Appl. Phys. Lett.* **76**, 2749 (2000).

[18] D. Smyth, *The defect chemistry of metal oxides*, Oxford University Press, New York, 2000.

[19] R. Merkle and J. Maier, *Angew. Chem.-Int. Edit.* **47**, 3874 (2008).

[20] R. Waser, T. Baiatu, and K. Hardtl, *J. Am. Ceram. Soc.* **73**, 1654 (1990).

[21] K. Szot, W. Speier, G. Bihlmayer, and R. Waser, *Nat. Mater.* **5**, 312 (2006).

[22] S. Menzel, M. Waters, A. Marchewka, U. Bttger, R. Dittmann, and R. Waser, *Adv. Funct. Mater.* (2011).

[23] J. Borghetti, D. B. Strukov, M. D. Pickett, J. J. Yang, D. R. Stewart, and R. S. Williams, *J. Appl. Phys.* **106**, 124504 (2009).

[24] D. S. Jeong, H. Schroeder, and R. Waser, **10**, G51.

[25] S. Lee, W. Kim, S. Rhee, and K. Yong, *J. Electrochem. Soc.* **155**, H92 (2008).

[26] P. C. Joshi and S. b. Krupanidhi, *J. Appl. Phys.* **73**, 7627 (1993).

[27] K. van Benthem, C. Elsaesser, and R. French, **90**.

[28] S. Thiess, T. L. Lee, F. Bottin, and J. Zegenhagen, *Solid State Commun.* **150**, 13 (2010).

[29] F. A. Kroeger, *Chemistry of Imperfect Crystals*, North-Holland, Amsterdam, 1972.

[30] D. Keeble, S. Wicklein, R. Dittmann, L. Ravelli, R. Mackie, and W. Egger, *Phys. Rev. Lett.* **105**, 226102 (2010).

[31] K. Szot, R. Dittmann, W. Speier, and R. Waser, *Phys.stat.sol. (RRL)* **1**, 86 (2007).

[32] R. Muenstermann, T. Menke, R. Dittmann, and R. Waser, *Adv. Mater.* , 4819 (2010).

[33] T. Menke, R. Dittmann, P. Meuffels, K. Szot, and R. Waser, *J. Appl. Phys.* **106**, 114507/1 (2009).

[34] B. P. Andreasson, M. Janousch, U. Staub, T. Todorova, B. Delley, G. I. Meijer, and E. Pomjakushina, *Phys. Rev. B* **80**, 212103 (2009).

[35] R. Merkle and J. Maier, *Phys. Chem. Chem. Phys.* **5**, 2297 (2003).

[36] A. Rothschild, W. Menesklou, H. Tuller, and E. Ivers-Tiffee, *Chem. Mater.* **18**, 3651 (2006).

[37] D. Chrisey and G. K. Hubler, *Pulsed Laser Deposition of Thin Films*, John Wiley and Sons, New York, 1994.

[38] E. Chason and T. Mayer, *Crit. Rev. Solid State* **22**, 1 (1997).

[39] B. Lengeler, *X-ray Absorption and Reflection in the Hard X-ray Range*, 1988.

[40] G. Binnig, C. Quate, and C. Gerber, *Phys. Rev. Lett.* **56**, 930 (1986).

[41] S. N. Magonov and D. Reneker, *Annu. Rev. Mater. Sci.* **27**, 175 (1997).

[42] S. Huefner, *Photoelectron Spectroscopy*, Springer-Verlag (1995).

[43] K. Okada and A. Kotani, *J. Electron Spectrosc. Relat. Phenom.* **62**, 131 (1993).

[44] http://mooni.fccj.org/ ethall/cobalt/d-orb2.gif.

[45] B. Ravel, Hephaestus v0.18, http://cars9.uchicago.eud/ ravel/software/.

[46] J. Jaklevic, J. Kirby, M. Klein, A. Robertson, G. Brown, and P. Eisenberger, *Sol. State Comm.* **23**, 679 (1977).

[47] S. Tanuma, A. C. Powell, and D. Penn, *Surf. Interface Anal.* **43**, 689 (2011).

[48] A. Jablonski and C. Powell, *J. Electron Spectrosc.* **100**, 137 (1999).

[49] M. Sacchi, F. Offi, P. Torelli, A. Fondacaro, C. Spezzani, M. Cautero, G. Cautero, S. Huotari, M. Grioni, R. Delaunay, M. Fabrizioli, G. Vanko, G. Monaco, G. Paolicelli, G. Stefani, and G. Panaccione, *Phys. Rev. B* **71**, 155117 (2005).

[50] J. R. Zuazo and G. Castro, *Surface and Interface Analysis* **40**, 1438 (2008).

[51] C. Fadley, *Nuclear Instruments and Methods in Physics Research A* **547**, 24 (2005).

[52] Z. Hussain, S. Kono, and C. Fadley, *Phys. Rev. B* **22**, 3750 (1980).

[53] Y. Iijima, K. Miyoshi, and S. Saiton, *Surf. Interf. Anal.* **27**, 35 (1999).

[54] J. Jaklevic, J. Kirby, M. Klein, and A. Robertson, *Solid State Commun.* **23**, 679 (1977).

[55] J. Rehr and R. Albers, *Rev. Mod. Phys.* **72**, 621 (2000).

[56] B. K. Teo, *EXAFS: Basic Principles and Data Analysis*, Springer-Verlag, 1985.

[57] B. Ravel and M. Newville, *J. Synchrotron Rad.* **12**, 537 (2005).

[58] M. Newville, *J. Synchrotron Rad.* **8**, 322 (2001).

[59] O. Bunau and Y. Joly, *J. Phys.-Condes. Matter* **21**, 345501 (2009).

[60] Y. Joly, *Phys. Rev. B* **63**, 125120 (2001).

[61] Inorganic Crystal Structure Database, http://www.fiz-karlsruhe.de/icsd.html.

[62] R. Dirsyte, J. Schwarzkopf, G. Wagner, J. Lienemann, M. Busch, H. Winter, and R. Fornari, *Appl. Surf. Sci.* **255**, 8685 (2009).

[63] T. Onishi, M. Lippmaa, T. Yamamoto, S. Meguro, and H. Koinuma, *Appl. Phys. Lett.* **87**, 241919 (2005).

[64] T. Onishi, K. S. T. Yamamoto, and M. Lippmaa, *J. Appl. Phys.* **103**, 103703 (2008).

[65] H. Christen and G. Eres, *J. Phys.: Condens. Matter* **20**, 264005 (2009).

[66] S. Wicklein, *private comm.* (2012).

[67] C. Xu, *Master Thesis at RWTH Aachen University* (2011).

[68] E. Breckenfeld, R. Wilson, J. Karthik, A. R. Damodaran, D. G. Cahill, and L. W. Martin, *Chem. Mater.* **2**, 331 (2012).

[69] J. Blanc and D. Staebler, *Phys. Rev. B* **4**, 3548 (1971).

[70] T. Baiatu, R. Waser, and K. Hardtl, *J. Am. Ceram. Soc.* **73**, 1663 (1990).

[71] R. Moos, W. Menesklou, and K. H. Hardtl, *Appl. Phys. A-Mater. Sci. Process.* **61**, 389 (1995).

[72] A. Kuzmin, R. Kalendarev, A. Kursitis, and J. Purans, *Latvian Journal of Physics and Technical Sciences* **2**, 66 (2006).

[73] M. Vracar, A. Kuzmin, R. Merkle, J. Purans, E. A. Kotomin, J. Maier, and O. Mathon, *Phys. Rev. B* **76**, 174107 (2007).

[74] A. Kuzmin, *Physica B* **208**, 175 (1995), 8th International Conference on X-Ray Absorption Fine Structure (XAFS VIII), BERLIN, GERMANY, AUG 28-SEP 01, 1994.

[75] A. L. Ankudinov, B. Ravel, J. J. Rehr, and S. D. Conradson, *Phys. Rev. B* **58**, 7565 (1998).

[76] C. Lenser, A. Kalinko, A. Kuzmin, D. Berzins, J. Purans, K. Szot, R. Waser, and R. Dittmann, *Phys. Chem. Chem. Phys.* **13**, 20779 (2011).

[77] V. E. Alexandrov, J. Maier, and R. A. Evarestov, *Phys. Rev. B* **77**, 075111 (2008).

[78] J. Hodges, S. Short, J. Jorgensen, X. Xiong, B. Dabrowski, S. Mini, and C. Kimball, *J. Solid State Chem.* **151**, 190 (2000).

[79] K. A. Mueller, *Helv. Phys. A* **31**, 173 (1958).

[80] E. S. Kirkpatrick, R. S. Rubins, and K. A. Muller, *Phys. Rev.* **135**, A86 (1964).

[81] B. Faughnan, *Phys. Rev. B* **4**, 3623 (1971).

[82] R.-A. Eichel, *Phys. Chem. Chem. Phys.* **13**, 368 (2011).

[83] J. Blasco, B. Aznar, J. Garcia, G. Subias, J. Herrero-Martin, and J. Stankiewicz, *Phys. Rev. B* **77**, 054107 (2008).

[84] I. Levin, V. Krayzman, J. Woicik, A. Tkach, and P. Vilarinho, *Appl. Phys. Lett.* **96**, 052904 (2010).

[85] D. Smyth, *Ann. Rev. Mater. Sci.* **15**, 329 (1985).

[86] A. Koehl, D. Kajewski, J. Kubacki, K. .Szot, A. Kuzmin, C. Lenser, P. Meuffels, R. Dittmann, R. Waser, and J. Szade, *In preparation* (2012).

[87] J. Woicik, E. Shirley, C. Hellberg, K. Andersen, S. Sambasivan, D. Fischer, B. Chapman, E. Stern, P. Ryan, D. Ederer, and H. Li, *Phys. Rev. B* **75**, 140103 (2007).

[88] R. Greegor, F. Lytle, G. Arnold, and R. Ewing, *Journal of Non-Crystalline Solids* **122**, 121 (1990).

[89] S. Chambers, T. Droubay, T. Kaspar, M. Gutowski, and M. van Schilfgaarde, *Surf. Sci.* **554**, 81 (2004).

[90] K. Szot, W. Speier, J. Herion, and C. Freiburg, *Appl. Phys. A* **64**, 55 (1997).

[91] K. Szot, W. Speier, U. Breuer, R. Meyer, J. Szade, and R. Waser, *Surf. Sci.* **460**, 112 (2000).

[92] F. Morin and J. Oliver, *Phys. Ref. B* **8**, 5847 (1973).

[93] R. Berney and D. Cowan, *Phys. Rev. B* **23**, 37 (1981).

[94] F. Michel-Calendini and K. Muller, *Solid State Commun.* **40**, 255 (1981).

[95] J. Dashdorj, M. Zvanut, and L. Stanley, *J. Appl. Phys.* **107**, 083513 (2010).

[96] N. McIntyre and D. Zetaruk, *Anal. Chem.* **49**, 1521 (1977).

[97] A. Grosvenor, B. Kobe, M. Biesinger, and N. McIntyre, *Surf. Interface Anal.* **26**, 1564 (2004).

[98] T. Fuji, Y. Takada, M. Nakanishi, J. Takada, M. Kimura, and H. Yoshikawa, *J. Phys.* **100**, 012043 (2008).

[99] R. Moos and K. Hrdtl, *J. Am. Ceram. Soc.* **80**, 2549 (1997).

[100] R. A. de Souza, *Phys. Chem. Chem. Phys.* **11**, 9939 (2009).

[101] T. Menke, *Dissertation at RWTH Aachen University* (2010).

[102] G. Gottstein, *Physikalische Grundlagen der Materialkunde*, Springer Verlag, 2001.

[103] S. Sze, *Physics of Semiconductor Devices*, Wiley, New York, 1981.

[104] G. Dietz and R. Waser, *Thin film solids* , 53 (1997).

[105] D. B. Strukov, G. S. Snider, D. R. Stewart, and R. S. Williams, *Nature* **453**, 80 (2008).

[106] S. Saraf, M. Markovich, and A. Rothschild, *Phys. Rev. B* **82**, 245208 (2010).

[107] F. de Groot, J. Fuggle, B. Thole, and G. Sawatzky, *Phys. Rev. B* **41**, 928 (1990).

[108] G. Radtke, S. Lazar, and G. A. Botton, *Phys. Rev. B* **74**, 155117 (2006).

[109] R. Brydson, H. Sauert, W. Engelt, and F. Hofer, *J. Phys.: Condens. Matter* **4**, 3429 (1992).

[110] F. de Groot, M. Grioni, J. Fuggle, J. Ghijsen, G. Sawatzky, and H. Petersen, *Phys. Rev. B* **40**, 5715 (1989).

[111] R. L. geb. Muenstermann, *Dissertation at RWTH Aachen University* (2011).

[112] E. Kraut, R. W. Grant, J. Waldrop, and S. Kowalczyk, *Phys. Rev. Lett.* **44**, 1620 (1980).

[113] A. Carley, P. Chalker, J. Riviere, and M. Roberts, *J. Chem. Soc., Faraday Trans.* **83**, 351 (1987).

[114] B. Psiuk, J. Szade, H. Schroeder, H. Haselier, M. Mlynarczyk, R. Waser, and K. Szot, *Appl. Phys. A* **89**, 451 (2007).

[115] M. Alonso, R. Cimino, and K. Horn, *Phys. Rev. Lett.* **64**, 1947 (1990).

[116] B. Psiuk, J. Szade, M. Pilch, and K. Szot, *Vacuum* **83**, S69 (2009).

[117] C. Wiemann, M. Patt, S. Cramm, M. Escher, M. Merkel, A. Gloskovskii, S. Thiess, W. Drube, and C. Schneider, *Appl. Phys. Lett.* **100**, 223106 (2012).

Acknowledgements

This thesis would never have been possible without the assistance and support of numerous people, the most important of which I want to thank explicitly.

First of all, I want to thank Professor Dr. Georg Roth for agreeing to be my first reader, and for his help throughout the whole thesis procedure. His support always gave me confidence in myself.

I would like to thank Professor Dr. Rainer Waser for the opportunity to conduct my research in the Institute of Solid State Research 6 / Peter Grünberg Institute 7, and for his confidence and support throughout my time in Jülich.

Special thanks go to my supervisor Professor Dr. Regina Dittmann, whose expertise and support was invaluable to me during the entire time. Her ability to dismantle complex problems into solvable tasks and her systematic approach to science taught me much. In addition to her scientific professionalism, her tendency toward brevity in written documents proved the perfect complement to my own difficulty with this concept.

The many techniques used during my studies have brought me into contact with a large number of people in the context of scientific cooperations. I would like to thank our friends from the EXAFS laboratory in Riga, Professor Dr. Juris Purans, Dr. Alexei Kuzmin and Dr. Alexander Kalinko, for the numerous beamtimes we managed together and the excellent, fruitful scientific cooperation.

For their involvement with the HAXPES beamtimes and the PEEM projects, my special thanks go to Marten Patt, who spent many nights battling counting statistics in pursuit of iron. Furthermore, I would like to thank Dr. Carsten Wiemann, Dr. Ingo Krug, Dr. Astrid Besmehn, Dr. Andrei Gloskovskii, Dr. Sebastian Thieß and Professor Dr. Claus M. Schneider for their involvement in this project, as well as Professor Charles "Chuck" Fadley for sharing some of the very first beamtime at P09, PETRA III.

I would like to thank the PLD-group and my colleagues at the PGI-7 and the EMRL for the relaxed and supportive atmosphere that facilitates cooperation and learning. Among these people who have contributed the most to my thesis, Annemarie Köhl deserves special thanks for the extraordinary cooperation on the topic of spectroscopy on resistive switching films, and the countless discussions and shared experiments.

I would further like to gratefully acknowledge the cooperations with Dr. David Keeble and Dr. David Cooper.

And in the position of honor, I want to express my boundless gratitude to my family - my parents, whose role in my life is so fundamental that it cannot be adequately described in a few words, but whose support enabled me to get this far. My brother and his family, for acting like an older sibling should and lighting

the way in so many ways (and setting the bars so high to keep me motivated). My grandparents, who helped lay down the foundation of the person I am today, and whose faith in my abilities kept me on track. And most importantly, to my wonderful wife, Cate Morgan - your love and support sustained me in the effort to finish this enormous challenge. Together with our wonderful son Freddy, you two make sure that there is always one place where the sun is shining every day - even in Jülich.